# Multiferroic Properties of Magnetoelectrically Coupled Lithium-Copper-Nickel-Zinc Ferrite and Rare Earth Substituted Barium-Dysprosium-Titanate Composites

Mithun Kumar Das

Department of Physics

BANGLADESH UNIVERSITY OF ENGINEERING AND TECHNOLOGY

DHAKA-1000

# Multiferroic Properties of Magnetoelectrically Coupled Lithium-Copper-Nickel-Zinc Ferrite and Rare Earth Substituted Barium-Dysprosium-Titanate Composites

by

Mithun Kumar Das

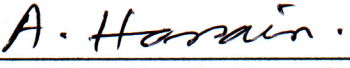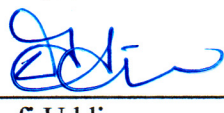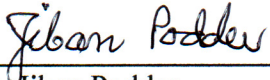Roll No: 0416144001F

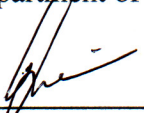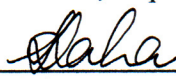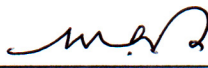Session: April 2016

DOCTOR OF PHILOSOPHY

Department of Physics

BANGLADESH UNIVERSITY OF ENGINEERING AND TECHNOLOGY

March 2021

The thesis titled **"Multiferroic Properties of Magnetoelectrically Coupled Lithium-Copper-Nickel-Zinc Ferrite and Rare Earth Substituted Barium-Dysprosium-Titanate Composites"** submitted by **Mithun Kumar Das,** Roll No.: **0416144001F**, Session: **April-2016,** has been accepted as satisfactory in partial fulfillment of the requirement for the degree of **Doctor of Philosophy (Ph.D.)** on 6 March, 2021.

## BOARD OF EXAMINERS

1. (_____)      Chairman
   Dr. A. K. M. Akther Hossain (Supervisor)
   Professor, Department of Physics, BUET, Dhaka.

2. (_____)      Member
   Dr. Md. Rafi Uddin     (Ex-Officio)
   Professor and Head, Department of Physics, BUET, Dhaka.

3. (_____)      Member
   Prof. Dr. Md. Abu Hashan Bhuiyan
   48/5A, BUET Teachers Quarter (Tower Bhaban), BUET,
   Dhaka-1000.

4. (_____)      Member
   Dr. Jiban Podder
   Professor, Department of Physics, BUET, Dhaka.

5. (_____)      Member
   Dr. Md. Feroz Alam Khan
   Professor, Department of Physics, BUET, Dhaka.

6. (_____)      Member
   Dr. Md. Abdullah Zubair
   Assistant Professor, Department of GCE, BUET, Dhaka.

7. (_____)      Member
   Dr. Supriya Saha
   Professor, Department of Physics, University of Dhaka,
   Dhaka-1000.

8. (_____)      Member
   Dr. Md. Abul Hossain     (External)
   Professor, Department of Physics, Jahangirnagar University,
   Savar, Dhaka-1342.

# CANDIDATE'S DECLARATION

It is hereby declared that this thesis or any part of it has not been submitted elsewhere for the award of any degree or diploma.

\-\-\-\-\-\-\-\-\-\-\-\-\-\-\-\-\-\-\-\-\-\-\-\-\-\-\-\-\-\-\-\-\-\-\-\-\-\-\-
Mithun Kumar Das

*Dedicated*

*To*

*My Beloved*

*Family Members*

# Acknowledgments

<div align="right">
The Author<br>
Mithun Kumar Das
</div>

# ABSTRACT

Multiferroic $x$Li$_{0.1}$Ni$_{0.3}$Cu$_{0.1}$Zn$_{0.4}$Fe$_{2.1}$O$_4$+(1-$x$)Ba$_{0.95}$R$_{0.05}$Ti$_{0.95}$Dy$_{0.05}$O$_3$ composites (where, R = Sm and Gd; $x$ = 0.00, 0.10, 0.20, 0.30, 0.40, 0.50, 0.60, and 1.00) were prepared by the conventional solid-state reaction technique. The structural, real part of initial permeability, *M-H* hysteresis loop, dielectric properties, ac conductivity, impedance spectroscopy, ferroelectric property, and magnetoelectric voltage coefficient of the composites have been studied in detail. The phase identification of ferrite and perovskite structure was executed by the Rietveld refinement analysis of the XRD patterns. The ferrite phase of Li$_{0.1}$Ni$_{0.3}$Cu$_{0.1}$Zn$_{0.4}$Fe$_{2.1}$O$_4$ forms a cubic spinel structure. On the other hand, ferroelectric phases of Ba$_{0.95}$Sm$_{0.05}$Ti$_{0.95}$Dy$_{0.05}$O$_3$ and Ba$_{0.95}$Gd$_{0.05}$Ti$_{0.95}$Dy$_{0.05}$O$_3$ show tetragonal perovskite structure. There is a slight change in the lattice parameters in the composites results from the stress between these phases. The density decreases and the average grain diameter increases with ferrite content in the composites. The real part of initial permeability and relative quality factor enhance with increasing ferrite phase because of high magnetic LNCZFO. Nevertheless, the composites with Sm show relatively higher real part of initial permeability compared to the composites with Gd. Saturation magnetization is found to increase with increasing ferrite content of the composites. The dispersive dielectric nature is observed in the low-frequency region due to Maxwell-Wagner type interfacial polarization. In lower frequency regions (20 Hz-10$^4$ Hz) some composites have a higher dielectric constant than the constituent phases due to large interfacial polarization created from the heterogeneous interface of the constituents. The shifting of the ferroelectric transition temperature in the composites confirmed the interaction between the constituent phases. The ac conductivity of the studied composites result from small polaron hopping mechanism and satisfied the Jonscher's power law. Non-Debye type relaxation is found in the studied composites because each composite exhibits a depressed semicircle. The presence of Ni and heterogeneity have a significant effect on the ferroelectric properties of the composites. The maximum magnetoelectric voltage coefficient ($\alpha_{ME}$) of 172 mV/cmOe is obtained for 0.10LNCZFO+0.90BGTDO composites. This value of $\alpha_{ME}$ may be a suitable alternative to Pb-based multiferroics for the application of modern multifunctional devices.

# Contents

## CHAPTER 1: INTRODUCTION

## CHAPTER 2: LITERATURE REVIEW

## CHAPTER 3: SAMPLE PREPARATION AND EXPERIMENTAL TECHNIQUES

## CHAPTER 4: RESULTS AND DISCUSSION

## CHAPTER 5: CONCLUSIONS

# List of figures

(where, R= Eu, Gd, and Tb).

# List of tables

# List of Symbols and Abbreviations

| | |
|---|---|
| **ME** | Magnetoelectric |
| **LNCZFO** | $Li_{0.1}Ni_{0.3}Cu_{0.1}Zn_{0.4}Fe_{2.1}O_4$ |
| **BSTDO** | $Ba_{0.95}Sm_{0.05}Ti_{0.95}Dy_{0.05}O_3$ |
| **BGTDO** | $Ba_{0.95}Gd_{0.05}Ti_{0.95}Dy_{0.05}O_3$ |
| **BT** | $BaTiO_3$ |
| **BCTO** | $Ba_{0.8}Ca_{0.2}TiO_3$ |
| **NCZFO** | $Ni_{0.2}Cu_{0.3}Zn_{0.5}Fe_2O_4$ |
| **XRD** | X-ray Diffraction |
| **FESEM** | Field Emission Scanning Electron Microscopy |
| **EDS** | Energy Dispersive Spectroscopy |
| **VSM** | Vibrating Sample Magnetometer |
| $N_A$ | Avogadro's number |
| $\mu_B$ | Bohr magneton |
| $T_C$ | Curie temperature |
| $T_N$ | Néel temperature |
| $\tau$ | Relaxation time |
| $T_s$ | Sintering temperature |
| $\rho_{th}$ | Theoretical density |
| $\rho_B$ | Bulk density |
| $P$ | Porosity |
| $\bar{D}$ | Average grain diameter |
| $L_0$ | Inductance of the winding coil without sample |
| $L_s$ | Self-inductance of the sample core |
| $\mu_i$ | Initial permeability |
| $\mu_i'$ | Real part of initial permeability |
| $f_r$ | Resonance frequency |
| $RQF$ | Relative quality factor |
| $tan\delta_M$ | Magnetic loss factor |
| $B$ | Magnetic induction |
| $H$ | Magnetic field |

| | |
|---|---|
| $M$ | Magnetization |
| $M_s$ | Saturation magnetization |
| $M_r$ | Remanent magnetization |
| $H_c$ | Coercivity |
| $E$ | Electric field |
| $C_s$ | Capacitance with dielectric |
| $C_o$ | Capacitance of free space |
| $\varepsilon'$ | Dielectric constant |
| $\varepsilon_0$ | Permittivity of free space |
| $tan\delta_E$ | Dielectric loss factor |
| $Z^*$ | Complex impedance |
| $Z'$ | Real part of the complex impedance |
| $Z''$ | Imaginary part of the complex impedance |
| $\sigma_{ac}$ | ac conductivity |
| $\sigma_{dc}$ | dc conductivity |
| $n$ | Frequency exponent factor |
| $C_g$ | Capacitance of grain |
| $C_{gb}$ | Capacitance of grain boundary |
| $R_g$ | Resistance of grain |
| $R_{gb}$ | Resistance of grain boundary |
| $M^*$ | Complex electric modulus |
| $M'$ | Real part of complex electric modulus |
| $M''$ | Imaginary part of complex electric modulus |
| $\alpha_{ME}$ | Magnetoelectric voltage coefficient |

# 1. INTRODUCTION

## 1.1 Introduction

Materials science and engineering have been at the prominent edge of technological development since the bronze and iron ages. Material having simultaneously ferroelectric and ferromagnetic/antiferromagnetic characteristics in the same phase is defined as multiferroics. The word "multiferroic" was first proposed by H. Schmid in 1994 [1] to define a material possessing two or more core ferroic properties which occur in the same phase. All multiferroic materials which have been studied to date grouped into two categories, namely single-phase materials, and composites. Single-phase multiferroics exhibit both piezoelectric and piezomagnetic characteristics in the same phase. In the case of single-phase multiferroics, multiferroicity is an intrinsic feature of the material and has identical structures. Natural single-phase multiferroics are limited and their magnetoelectric (ME) pairing influence, polarization, transition temperatures, and magnetization are insufficient for potential implementation. On the other hand, multiferroic composites (MFCs) are a mixture of various ferroic orders. MFCs have drawn great interest because of the co-existence of the constituent phases, the coupling between the ferroic phases, and emerging applications in various multifunctional devices (e.g. microwave phase shifters, data storage, actuators, multifunctional sensors, ME memory cells, broadband magnetic field sensors, etc.) [2-11]. The investigation and engineering of novel multifunctional materials, which exhibit different functionalities in the same phase, is one of the most fascinating challenges in today's solid-state physics. The use of these materials can increase the degree of flexibility and efficiency while at the same time reducing the expenses, size, and power consumption of possible integrated systems. In such conditions, complex oxides are very promising materials from a practical point of view, because they can show a broad range of properties: ferromagnetism, ferroelasticity, ferroelectricity, etc., and could be plastics, insulators, semiconductors, and superconductors. Besides, combining some of these characteristics may give rise to new promising applications. One of the most well-known examples is magnetoresistance (the combination of conductivity and magnetic order), which has enabled the development of basic physics within the spintronics system. The structure of the MFCs formed by the synthesis of two ferroic materials. In the case of

MFCs, the multiferroic order is not intrinsic and has different structures. The lack of single-phase multiferroic materials makes composites an effective alternative. Compared to single-phase multiferroic materials, composites are more attractive due to their improved properties, particularly at room temperature (RT).

In the most general perspective, the idea of multiferroics developed from the study of the ME mechanism [12]. Coupling interaction between different ferroic phases in MFCs could result in additional impacts, like the ME effect [13-15]. The combining effect between magnetic and electric properties in the matter was first introduced by Röntgen in 1888 [16] when he found that a dielectric material becomes magnetized with an electric field and, conversely, it becomes polarized with a magnetic field. This phenomenon was theoretically defined by Curie in 1894 [17]. The discovery of the origin of ferroelectricity was made by Valasek in 1920 [18]. Also, Fox and Scott [19] have demonstrated that ferroelectricity can generate a magnetic order and vice versa. The concept of ME was introduced by Debye in 1926 [20]. In 1972, the two-phase composite material was observed by van Suchtelen. He worked on composite $BaTiO_3/CoFe_2O_4$ and suggested the idea of a two-phase product property in the composite originating from an elastic interacting between the phases [21]. The ME impact in a composite with one magnetostrictive and one piezoelectric phase is one of these product properties. In this technique, the ME coupling is a mechanical method. The ME effect produced in this method may be approximately a hundred times greater than that obtained in a single-phase multiferroic system [22]. In the early 1990s, Russian scientists prepared particular ceramic composites of ferrites and $BaTiO_3$ (BT) or $Pb(ZrTi)O_3$ by standard sintering technique [23, 24]. The ME coupling can result from a combination of a few order parameters coupled with strain, such as electrostrictive and magnetostrictive, and so on. The multiferroic ME composites formed by mixing piezoelectric and piezomagnetic components have attracted interest in recent years because of their multi-functionality and large ME response [25, 26]. These ME composites have potential applications in multi-functional operating systems. Besides, MFCs can create a large coupling beyond RT that facilitates them to fit into high-tech applications.

**1.2 Motivation of the Present Research**

Multiferroic materials consist of a strain-coupled ME effect, which has attracted attention and encouraged a large number of research activities. They were of great interest for their promising technological applications in new multifunctional systems [1]. But single-phase multiferroics did not attract the researchers due to their practical limitations in multi-functional device applications. Such disadvantages might be overcome by the use of multiferroic composites. Composite materials were extensively used in modern electronic devices with a growing demand for new technology requiring high reliability, limited space, and multifunctional efficiency. Multiferroic composites are easy to process and have a greater ME voltage coefficient compared to single-phase materials such as $Cr_2O_3$ by two orders of magnitude [22]. Synthesized multiferroic composites exhibit strong ME effects at ambient temperature, which develop as a product-property of ferroic orders mediated by elastic deformation [21]. In the presence of the ME response, the external magnetic field can trigger electric polarization and the electric field can trigger magnetic order, which makes these materials technologically important. Suitable ferrite and ferroelectric mixture can produce an extremely good ME effect. The high magnetostriction coefficient of the ferrite phase and the prominent piezoelectric coefficient of the ferroelectric phase are fundamental requirements for obtaining a higher ME coefficient for multiferroic composites [27]. Thus, an appropriate combination of two different phases of the material, including magnetostrictive and piezoelectric phases, will result in a widely applicable extrinsic ME voltage coefficient in composites. Multiferroic properties of different composites based on Ni-Cu-Zn and $BaTiO_3$ were reported earlier [28-47]. To the best of our knowledge, no work has been reported on specific $x\text{Li}_{0.1}\text{Ni}_{0.3}\text{Cu}_{0.1}\text{Zn}_{0.4}\text{Fe}_{2.1}\text{O}_4 +$ $(1\text{-}x)\text{Ba}_{0.95}\text{R}_{0.05}\text{Ti}_{0.95}\text{Dy}_{0.05}\text{O}_3$ composites (where, R = Sm and Gd) based on a literature survey.

In this research, $\text{Li}_{0.1}\text{Ni}_{0.3}\text{Cu}_{0.1}\text{Zn}_{0.4}\text{Fe}_{2.1}\text{O}_4$ (LNCZFO) was chosen as the ferrite phase and $\text{Ba}_{0.95}\text{R}_{0.05}\text{Ti}_{0.95}\text{Dy}_{0.05}\text{O}_3$ (BRTDO) as the ferroelectric phase. The selection of these two materials was made based on the criteria for the high ME coefficient mentioned above. The Li-Ni ferrite doped with Jahn-Teller ions such as $Zn^{2+}$, $Cu^{2+}$ had a high magnetostriction coefficient as these ions have a high ME coupling

coefficient [48]. Nevertheless, enhanced RT saturation magnetization ($M_s$), complex initial permeability ($\mu_i$) with high resonance frequency ($f_r$), high relative quality factor (RQF), ambient Néel temperature ($T_N$), and large resistivity was also observed in $Li^{1+}$ doped Ni-Cu-Zn ferrites [49-51]. It is therefore quite important to figure out the possible improvements in the different physical properties of the different LNCZFO-BRTDO composites. On the other hand, BRTDO was chosen as a ferroelectric phase because rare-earth-doped BT has a high dielectric constant ($\varepsilon'$), low dielectric loss ($\tan\delta_E$), high resistance, good thermal stability, low leakage current density, low transition temperature ($T_C$), and high piezoelectric coefficient [52-54]. Therefore, it is quite interesting to find out possible changes in the various physical properties of a class of LNCZFO-BRTDO composites. Once these two-component phases can be successfully incorporated into the composites, it is expected that they might exhibit excellent magnetic, electrical, and ME properties. Lead-free materials are used for present MFCs due to the toxicity of lead and associated risks to health and the environment. The lead-free MFCs with the above two ferroic orders are expected to become a potential material for modern multifunctional device applications at RT.

## 1.3 Objectives

MFCs with LNCZFO and BRTDO are expected to have good magnetic, electrical, and ME properties for applications as an alternative to Pb-based multiferroics.

The main objectives of the present research are as follows:

- Synthesis of $x$LNZFO+(1-$x$)BRTDO composites (where R = Sm and Gd; $x = 0.00, 0.10, 0.20, 0.30, 0.40, 0.50, 0.60$ and 1).
- Structural characterization has been performed and hence theoretical density, the lattice constant, and porosity have also been calculated.
- Surface morphology and microstructure analysis have been performed.
- Complex initial permeability, loss tangent, RQF at RT in the frequency range 10 kHz to 120 MHz with compositional change have been performed.
- Measurements of the magnetization versus magnetic field ($M$-$H$) hysteresis loop of the samples.
- Dielectric properties, ac conductivity, complex impedance, and electric modulus spectroscopy with the variation of frequency have been performed.

- The temperature-dependent $\varepsilon'$ has been performed.
- Ferroelectric polarization versus electric field (P–E) hysteresis loops have been measured.
- Measurements of the ME coefficient as a function of the dc magnetic field.

## 1.4 Layout of the Thesis

- Chapter 1 deals with the introduction, motivation, and objectives of the present investigation.
- Chapter 2 described the literature review and review of earlier research.
- Chapter 3 deals with sample preparation and experimental techniques.
- Chapter 4 explained the results and discussion.
- Chapter 5 described the conclusions and suggestions for the future work of the present study.

# 2. LITERATURE REVIEW

## 2.1 Review of Earlier Research

A large number of researchers all over the world are working on the different properties of single-phase multiferroic and multiferroic composite consists of ferrite and ferroelectric phases [55-95]. A brief review of some of these is discussed below:

Islam et al. [49] looked into the magnetic behavior of polycrystalline $Li_{0.35-0.5x}Ni_{0.3}Zn_xFe_{2.35-0.5x}O_4$ spinel ferrites for various multifunctional applications. The X-ray diffraction (XRD) affirmed the presence of a single-phase spinel structure, as depicted in Fig. 2.1. (a). Fig. 2.1(b) shows the variation of density ($\rho$) with Zn content. The bulk density ($\rho_B$) and theoretical density ($\rho_{th}$) were enhanced as Zn content increased. Because of the increase in density, the porosity ($P$) decreases as the Zn content increases.
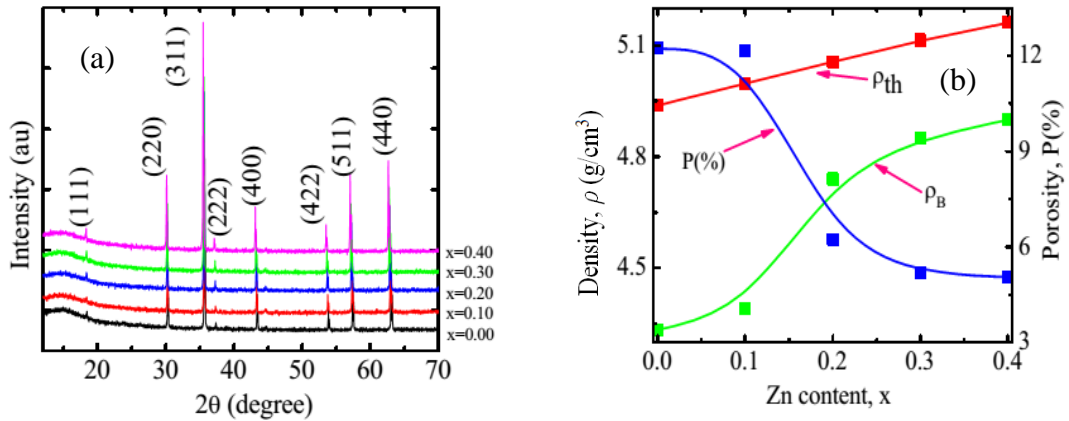


**Fig. 2.1(a)** The XRD patterns and (b) variation of $\rho_{th}$, $\rho_B$, and $P$ of various $Li_{0.35-0.5x}Ni_{0.3}Zn_x Fe_{2.35-0.5x}O_4$ [49].

The substitution of Zn accelerates grain growth and consistent grain allocation in the studied samples (Fig. 2.2). The mean grain diameter ($\overline{D}$) enhances as Zn concentration rises, which acting a vital role in enhancinges the $\mu_i'$, RQF, and $M_s$. The highest magnitude of $\mu_i'$ ($= 254$) is obtained for $Li_{0.15}Ni_{0.3}Zn_{0.4}Fe_{2.15}O_4$ sample, which is greater than 6 times as much as the parent sample. The maximum RQF and $M_s$ are also obtained for the $Li_{0.15}Ni_{0.3}Zn_{0.4}Fe_{2.15}O_4$ sample. With an increase in the Zn content, $\mu_i'$ and $M_s$ enhance up to their maximum magnitude for $x = 0.4$. This is

described by the cation distribution and super-exchange activity between A- and B-sites. Fig. 2.4(a) dipicts the variance of $\tan\delta_M$ with frequency and the minimum value is obtained for the $Li_{0.15}Ni_{0.3}Zn_{0.4}Fe_{2.15}O_4$ sample, which is 6 times smaller than the parent sample.
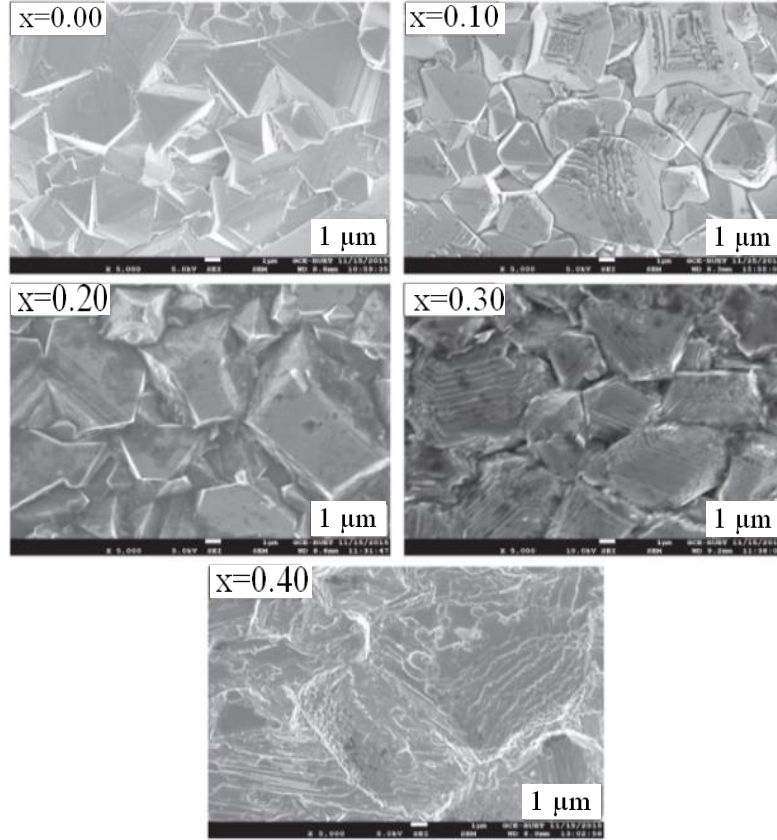


**Fig. 2.2** Micrograph images for various $Li_{0.35-0.5x}Ni_{0.3}Zn_xFe_{2.35-0.5x}O_4$ [49].
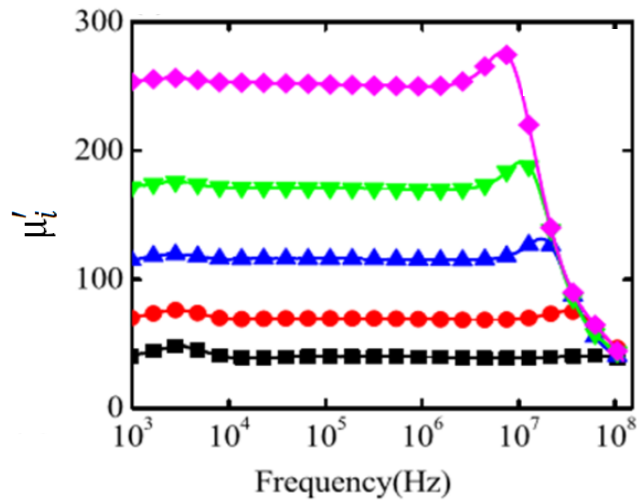


**Fig. 2.3** Variation of $\mu_i'$ as a function of frequency for several $Li_{0.35-0.5x}Ni_{0.3}Zn_xFe_{2.35-0.5x}O_4$ [49]
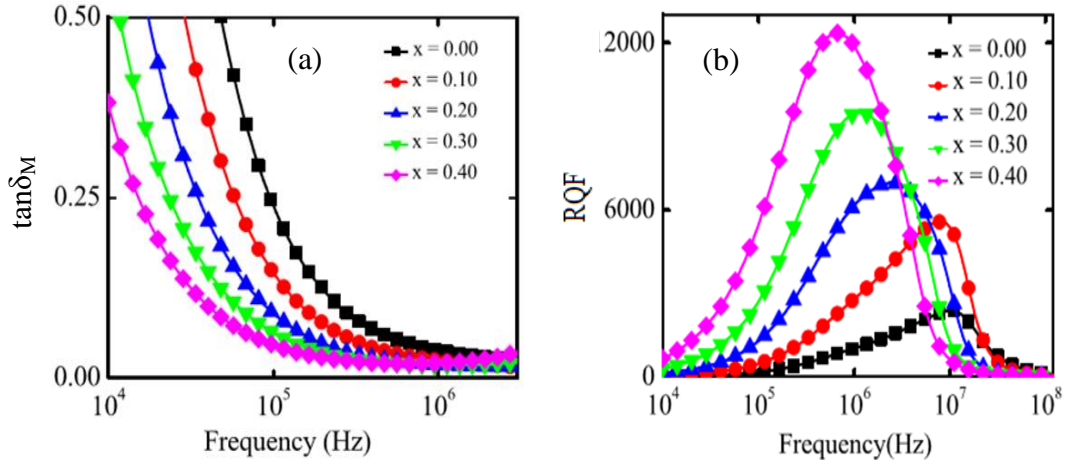
**Fig. 2.4** Variations of (a) $\tan\delta_M$, and (b) RQF for various $Li_{0.35-0.5x}Ni_{0.3}Zn_xFe_{2.35-0.5x}O_4$ [49].
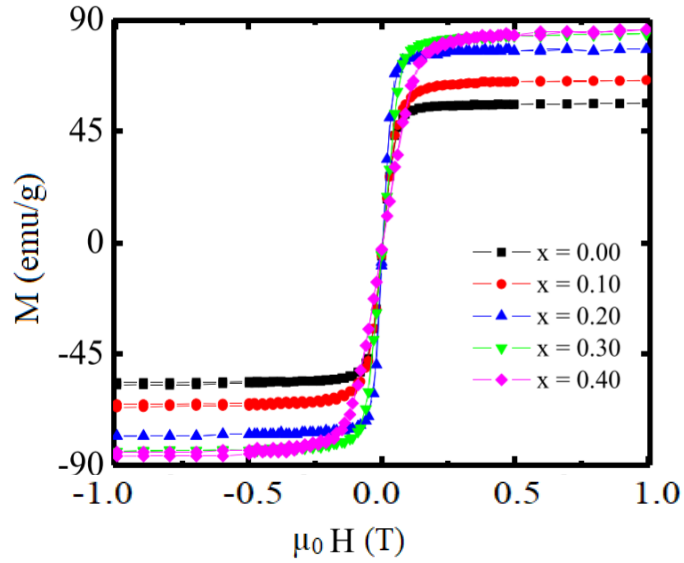


**Fig. 2.5** *M-H* hysteresis loops for various $Li_{0.35-0.5x}Ni_{0.3}Zn_xFe_{2.35-0.5x}O_4$ [49].

Parvin et al. [50] studied the microstructural, magnetic, and dielectric characteristics of $Li_xCu_{0.1}Co_{0.1}Zn_{0.8-2x}Fe_{2+x}O_4$ ferrites. The XRD patterns of these samples affirmed the existence of a single-phase spinel structure (Fig. 2.6a). Both ρth and ρB decline just a similar manner as Li content enhances in distinct $Li_xCu_{0.1}Co_{0.1}Zn_{0.8-2x}Fe_{2+x}O_4$ exclude $x = 0.10$, as illustrated in Fig. 2.6b. The $\rho_B$ enhances enhancing Li up to $x = 0.10$, after which it declines and the *P* reduces. This finding can be described in aspects of the atomic weights of the elements. The atomic weight of Zn (65.38 amu) is higher than that of Li (6.941 amu) and Fe (55.845 amu). Zn is replaced by both Li and Fe.
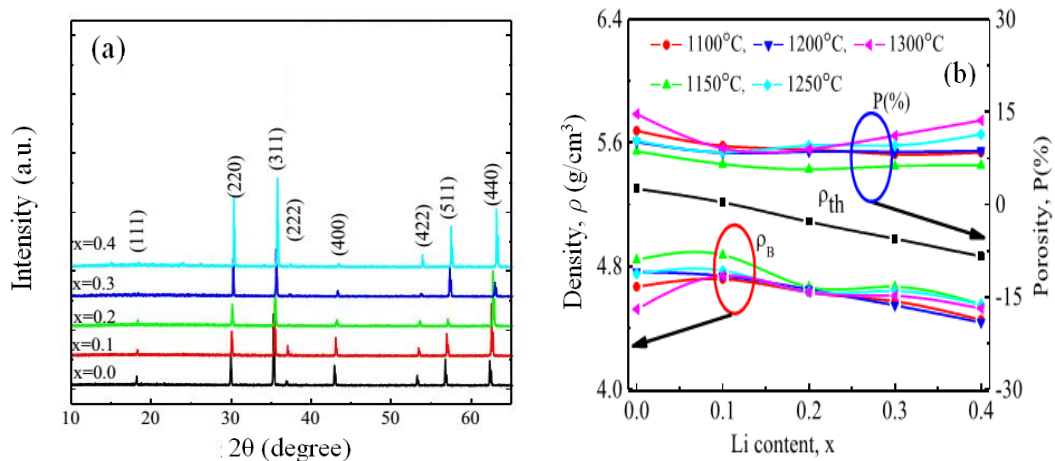
**Fig. 2.6**(a) The XRD patterns and (b) $\rho_{th}$, $\rho_B$ and $P$ with content for various $Li_xCu_{0.1}Co_{0.1}Zn_{0.8-2x}Fe_{2+x}O_4$ [50].

The $\overline{D}$ enhances with enhancing Li substitution since a small quantity of Li promotes grain growth (Fig. 2.7). It was observed that $\mu_i'$ enhances up to a specific amount of Li concentration and then decline with further enhancement of Li content. The effect of Li substitution improves the $\mu_i'$ from 18 to 61 for $x = 0.10$ sample. Both $\mu_i'$ and RQF are found to have a maximum value for the $x = 0.10$ due to the highest dense sample (in Fig. 2.8).
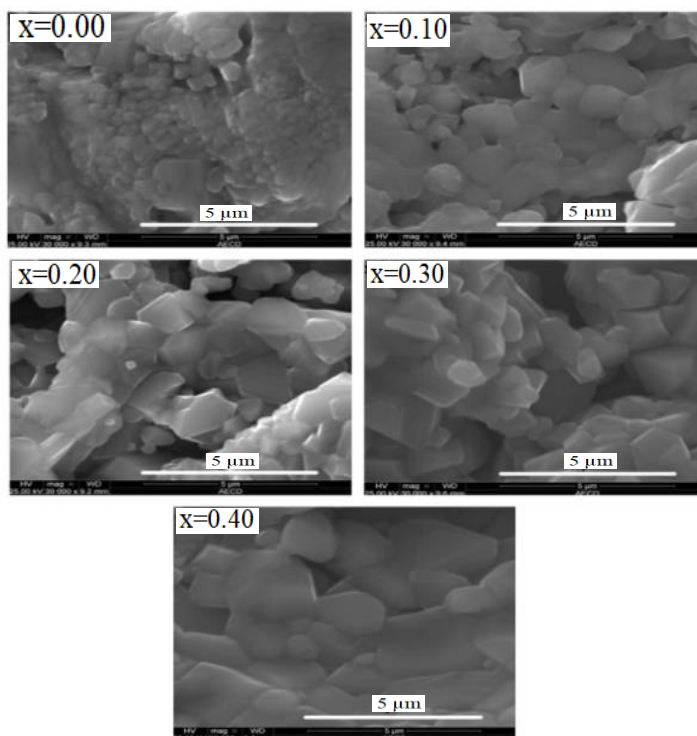


**Fig. 2.7** Micrograph images for polycrystalline $Li_xCu_{0.1}Co_{0.1}Zn_{0.8-2x}Fe_{2+x}O_4$ [50].
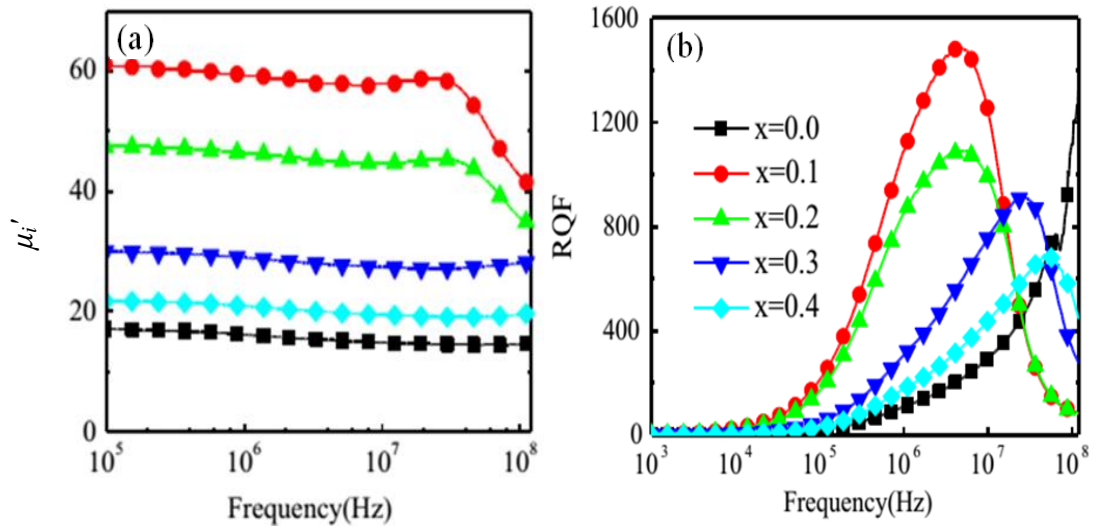
**Fig. 2.8** The variation of (a) $\mu_i'$, and (b) RQF for several $Li_xCu_{0.1}Co_{0.1}Zn_{0.8-2x}Fe_{2+x}O_4$ [50].

Fig. 2.9 shows the *M-H* curves for $Li_xCu_{0.1}Co_{0.1}Zn_{0.8-2x}Fe_{2+x}O_4$ ferrite. The substitution of Li content affects the magnetic characteristics owing to the modification of the cation distribution. The magnetization of the samples enhances linearly with enhancing imposed magnetic field strength up to 0.1 T. Magnetization gradually enhances additional than 0.1 T and eventually reaches saturation. The $M_s$ and $\mu_B$ enhance up to $x = 0.30$ attributable to the strengthening of the A-B interplay in the $AB_2O_4$ spinel ferrites (in Fig. 2.9). The $\varepsilon'$ declines with frequency, being faster at lower frequency regime and slower at higher frequencies, possibly wing to Maxwell-Wagner interfacial polarization (Fig. 2.10a). The minimum $\tan\delta_E$ for the $x = 0.10$ sample is obtained (Fig. 2.10b).
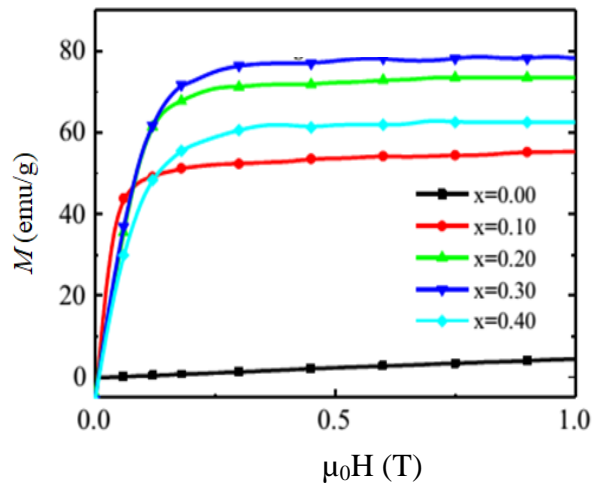


**Fig. 2.9** The *M-H* loops for $Li_xCu_{0.1}Co_{0.1}Zn_{0.8-2x}Fe_{2+x}O_4$ [50].
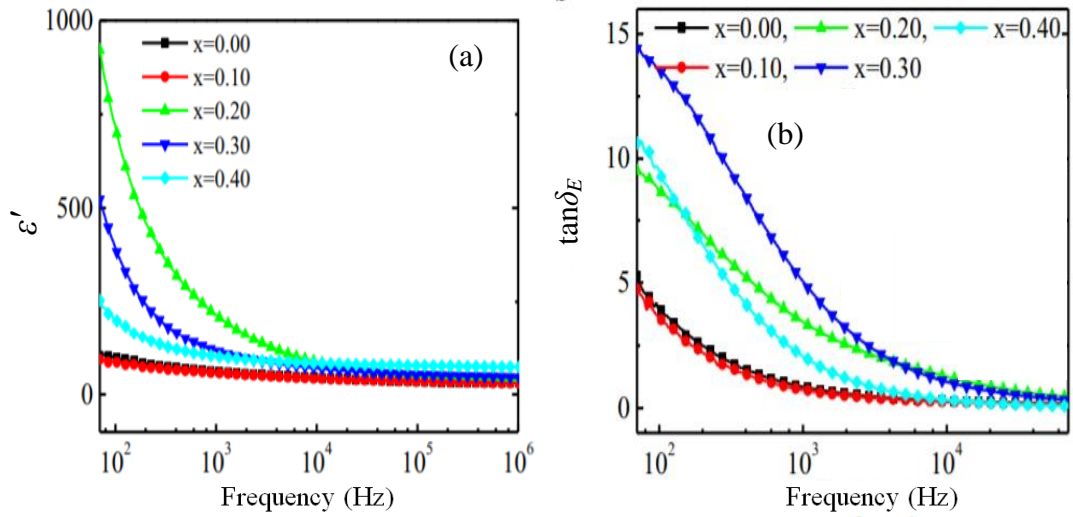
**Fig. 2.10** Variation of (a) $\varepsilon'$, and (b) $\tan\delta_E$ with frequency for distinct $Li_xCu_{0.1}Co_{0.1}Zn_{0.8-2x}Fe_{2+x}O_4$ [50].

Hossain et al. [51] investigated the structural and magnetic characteristics of Cu substituted $Ni_{0.50-x}Cu_xZn_{0.50}Fe_2O_4$ ferrites. The XRD patterns of these samples revealed the creation of a single-phase spinel structure (Fig. 2.11a). The $\rho_B$, $\rho_{th}$, and $P$ are displayed in Fig. 2.11(b). The $\rho_{th}$ rises with a rise in Cu content since the molecular weight of every sample rises considerably with the enhance of Cu content. The $\rho_B$ enhances with enhancing in Cu content up to $x = 0.10$, after which it declines.
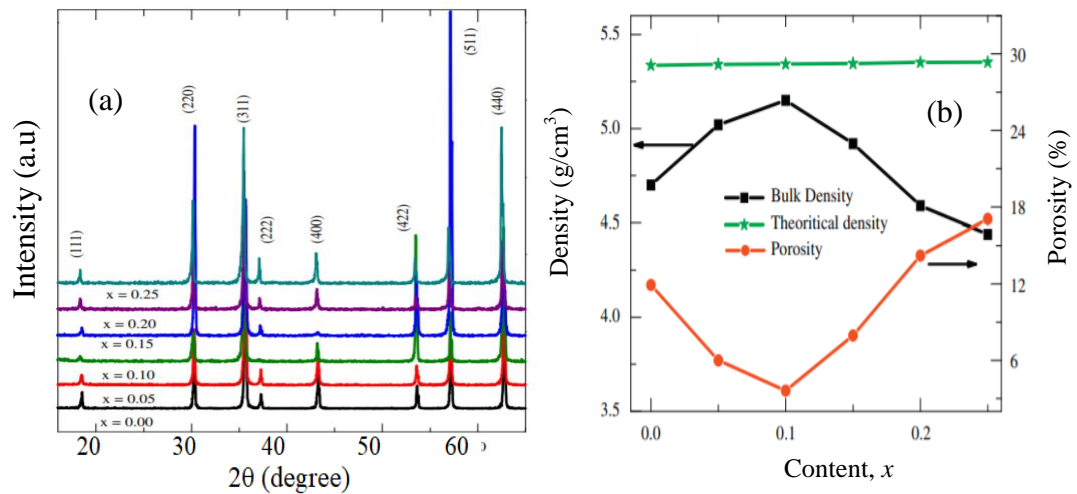


**Fig. 2.11**(a) The XRD patterns, and (b) the variation of $\rho_{th}$, $\rho_B$, and $P$ with content for various $Ni_{0.50x}Cu_xZn_{0.50}Fe_2O_4$ [51].

Besides, the $P$ of the sample exhibits the inverse trend. The rise in $\rho_B$ could be related to the variation in atomic weight between the initial and replaced cations (the atomic

weight of Cu (63.55 amu) is greater than Ni (58.71 amu)). The decline in density could be attributed to intergranular/intragranular porosity caused by discrete grain growth.
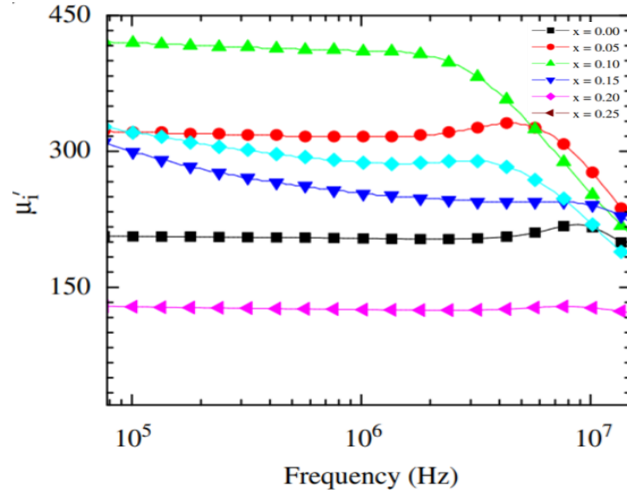


**Fig. 2.12** The variation of $\mu_i'$ with frequency for different $Ni_{0.50-x}Cu_xZn_{0.50}Fe_2O_4$ [30].

Fig. 2.12 displays the distinction of $\mu_i'$ with frequency for different $Ni_{0.50-x}Cu_xZn_{0.50}Fe_2O_4$ ferrites. From Fig. 2.12 it is evident that the $\mu_i'$ increases randomly with the enhance of Cu content and the maximum magnitude is obtained for $x = 0.10$ sample because it comprises the highest density. Beyond this magnitude of Cu substitution, $\mu_i'$ declines due to the decline in density.

From the *M-H* graph (Fig. 2.13), it is evident that all the samples are in a ferromagnetic state. The *M* enhances with an enhancement of the imposed magnetic field strength up to 0.2 T. Above this imposed field M rises deliberately and then reaches saturation. The $M_S$ reduces linearly with increasing Cu up to $x = 0.15$, after which it enhances. It is described by cation distribution and exchange interply because distribution of cations in the A- and B-sites impacts the magnetic characteristics of ferrites. The probable cation distribution could be presented as $(Zn_{0.50}^{2+}Fe_{0.50}^{3+})_A[Ni_{0.50}^{2+}Cu_x^{2+}Fe_{1.50}^{3+}]_BO_4^{2-}$ in the ideal case in which all cations are in their specified position. The probable cation distribution can be expressed as an ideal case in which all cations are in their appropriate locations. Substitution of Cu at the octahedral site rather than Ni declines the net magnetic moment at B-site. Subsequently the magnetic moment of Cu ($1\mu_B$) is smaller than that of Ni ($2\mu_B$). Furthermore, owing to the unaffected diamagnetic Zn content, the magnetization of

the A-site is assumed to be constant. As a consequence of weakening the A-B interaction of these NiCuZn ferrites, the net magnetization (MS = MB-MA) decreases.
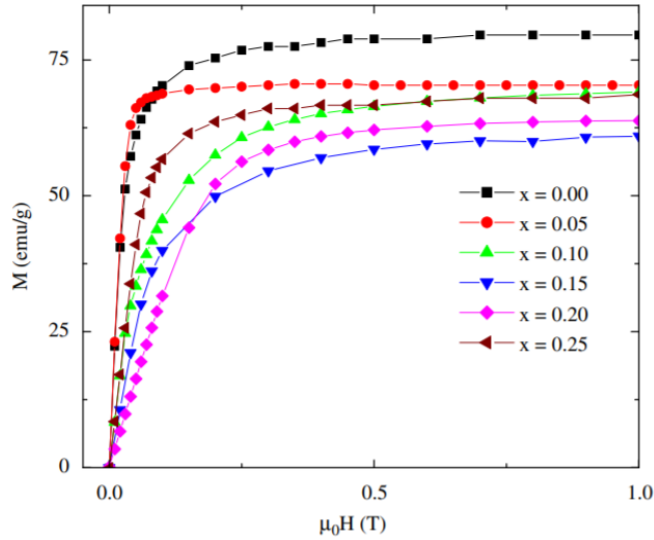


**Fig. 2.13** *M-H* hysteresis loops for different $Ni_{0.50-x}Cu_xZn_{0.50}Fe_2O_4$ [51].

Lu et al. [52] synthesized multiferroic $Eu^{3+}$, $Gd^{3+}$, $Tb^{3+,}$ and $Dy^{3+}$ doped BT ceramics by solid-state reaction method. The XRD patterns of the $(Ba_{0.94}R_{0.06})(Ti_{0.94}Dy_{0.06})O_3$ (BRTD) (where, R = Eu, Gd, Tb) ceramics displayed a tetragonal perovskite structure without any secondary phase except the perovskite phase. This XRD study reveals that *R* ions could be combined entirely into the host BT lattice using co-doping with $Dy^{3+}$ ions. The tetragonality of BRTD is noticed by two separate (002) and (200) peaks around 45⁰, as shown in the inset of Fig. 2.14. These two typical peaks are more distinct in the BTTD.
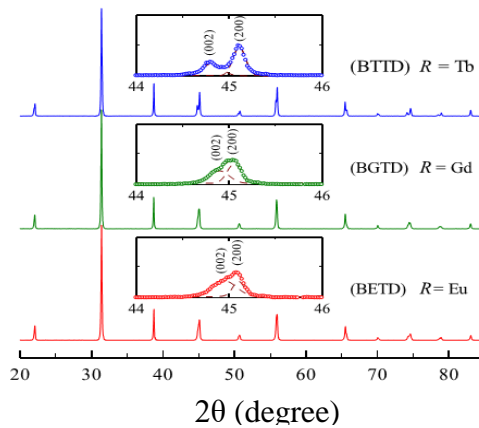


**Fig. 2.14** XRD patterns of $(Ba_{1-x}R_x)(Ti_{1-x}Dy_x)O_3$ ceramics. Gaussian-fitting to the XRD peaks in the region of 45⁰ [52].

The SEM images of BRTD became denser for the reason of co-doping of double rare earth, and these ceramics showed a medium $\bar{D}$. The $\bar{D}$ of BETD, BGTD, and BTTD were 0.25, 0.30, and 0.31 μm, accordingly, i.e. $\bar{D}$ grew gradually with atomic number (AN) (Fig. 2.15). Fig. 2.16 shows the temperature-dependent $\varepsilon'$ and $\tan\delta_E$ for BRTD measured at 1 kHz. It shows a diffuse phase transform performance and a nonlinear shift in $T_C$ with ion doping. The impact of mixed-valence states allied with site occupation is accountable for this irregular $T_C$-shift rate.
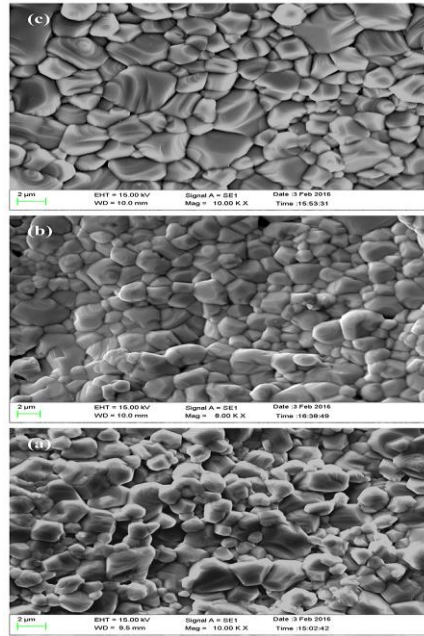


**Fig. 2.15** SEM images of (a) $(Ba_{0.94}Eu_{0.06})(Ti_{0.94}Dy_{0.06})O_3$, (b) $(Ba_{0.94}Gd_{0.06})(Ti_{0.94}Dy_{0.06})O_3$, and (c) $(Ba_{0.94}Tb_{0.06})(Ti_{0.94}Dy_{0.06})O_3$ ceramics [52]
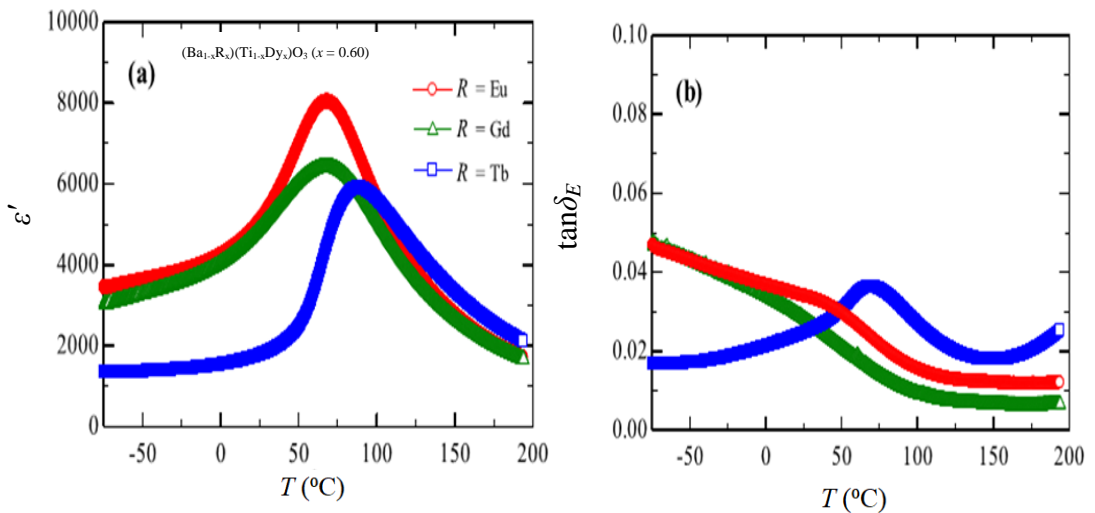


**Fig. 2.16** Temperature dependences of (a) $\varepsilon'$ and (b) $\tan\delta_E$ for BRTD (where, R= Eu, Gd, and Tb) measured at 1 kHz [52].

The frequency-dependent $\varepsilon'$ and $\tan\delta_E$ for BRTD are demonstrated in Fig. 2.17. The $\varepsilon'$ of BRTD decreased slowly up to $10^6$ Hz and then reduced rapidly. Nevertheless, the BGTD sample demonstrated higher $\varepsilon'$ at a higher frequency region compare to the other samples. The BGTD displayed a very low $\tan\delta_E$. Therefore, to attain larger $\varepsilon'$ at higher frequency with low $\tan\delta_E$, the co-doping with $Gd^{3+}$ and $Dy^{3+}$ ions in BT is the best option, which can enhance the dielectric implementation at a high frequency.
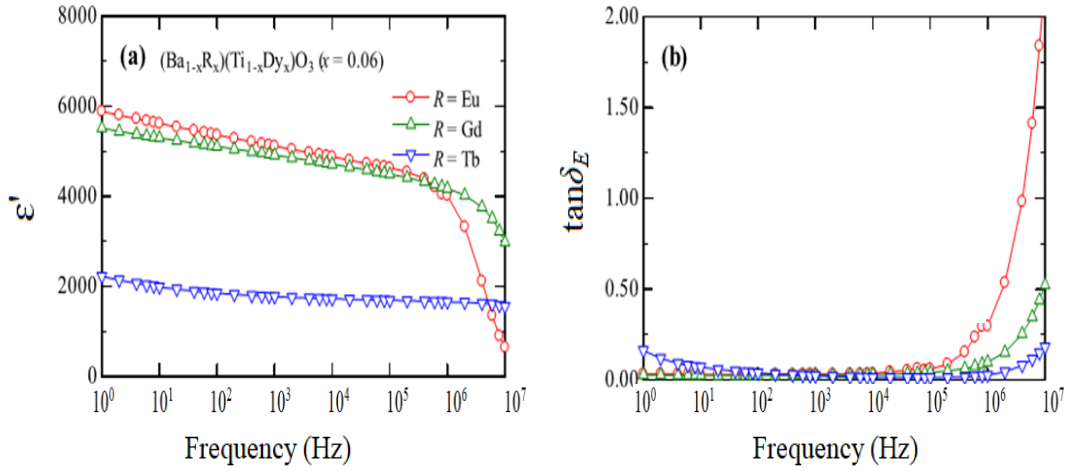


**Fig. 2.17** Frequency dependences of (a) $\varepsilon'$ and (b) $\tan\delta_E$ for BRTD
(where, R= Eu, Gd, and Tb) [52].

Borah et al. [53] prepared Gd doped BT samples by solid-state reaction process. The XRD patterns are revealed in Fig. 2.18(a). The diffraction patterns are shown perovskite structure of BT. Nevertheless there is a transition of the (110) peak to a lower Bragg angle with doping, no extra peaks contributing to any by-products or other intermediate products, including BaO were evidenced in the XRD patterns (in Fig. 2.18.a).
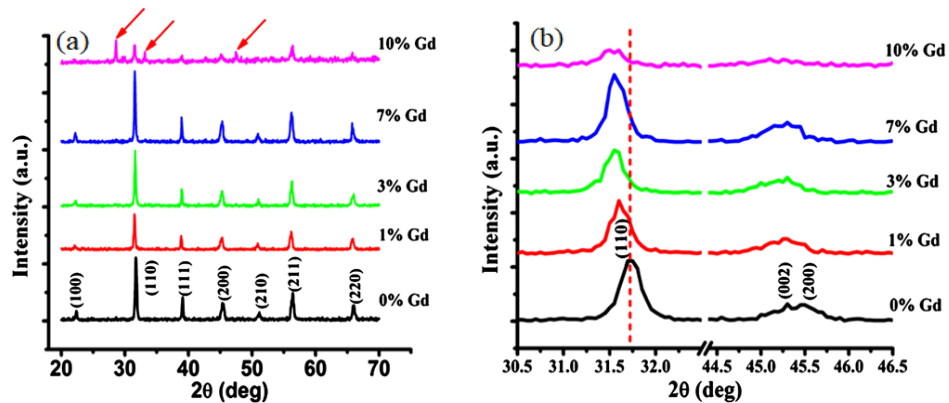


**Fig. 2.18** (a) XRD patterns of un-doped and Gd-doped $BaTiO_3$ perovskite (b) typical peak shifting of Gd doping [53].

15

The dielectric characteristics of a solid-state method generally correspond to its charge-holding capability at a specified frequency. Fig. 2.19 shows the frequency-dependent variation of $\varepsilon'$ and $\tan\delta_E$. As a common trend, the Gd-doped BT perovskite would have a higher charge-accumulation capacity than their un-doped counterparts. The impact of Gd doping on the frequency-dependent $\varepsilon'$ of BT is shown in Fig. 2.19(a). At lower frequency, all forms of polarization respond, but as the imposed frequency enhances, polarization (excluding for electronic polarization) disappears and, as a consequence, the magnitude of $\varepsilon'$ is decreased. Besides at a higher frequency, electric dipoles cannot capable to follow an ac frequency and appear to be mobile, thus suppressing the capacitive response. The $\tan\delta_E$ of a dielectric order is associated with the energy dissipation procedure in the dielectric system. The frequency-dependent $\tan\delta_E$ of undoped and Gd-doped BT arrangements are presented in Fig. 2.19(b). The $\tan\delta_E$ of these samples declines rapidly at lower frequencies but slowly at higher frequencies. The decrement in $\tan\delta_E$ with a frequency increment could be discussed by the decrement in polarization with an increase in frequency. It can be seen that, at lower frequencies, the magnitude of $\tan\delta_E$ was very high in comparison to its un-doped state. Nevertheless, at high-frequency region, $\tan\delta_E$ appears to be invarient of doping concentration.
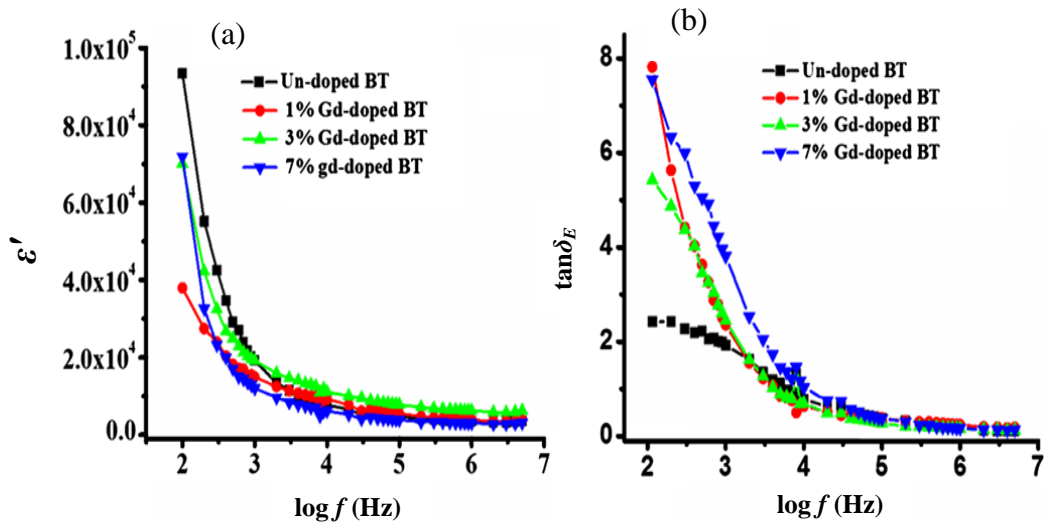


**Fig. 2.19** The frequency-dependent variation of (a) $\varepsilon'$ and (b) $\tan\delta_E$ [53].

Ganguly et al. [54] prepared $Ba_{1-x}Sm_{2x/3}TiO_3$ ceramics by solid-state reaction route. They investigated the XRD analysis, microstructural, dielectric property, and

ferroelectric property of the prepared samples. Fig. 2.20 demonstrates the XRD patterns of $Ba_{1-x}Sm_{2x/3}TiO_3$ ceramic powders. The findings of the single-phase perovskite structure can be seen in all of the samples. The presence of peaks (002) and (200) in all compositions indicates tetragonal symmetry.Shifting the peak to a higher angle implies a decline in the lattice constants with enhancing Sm element.
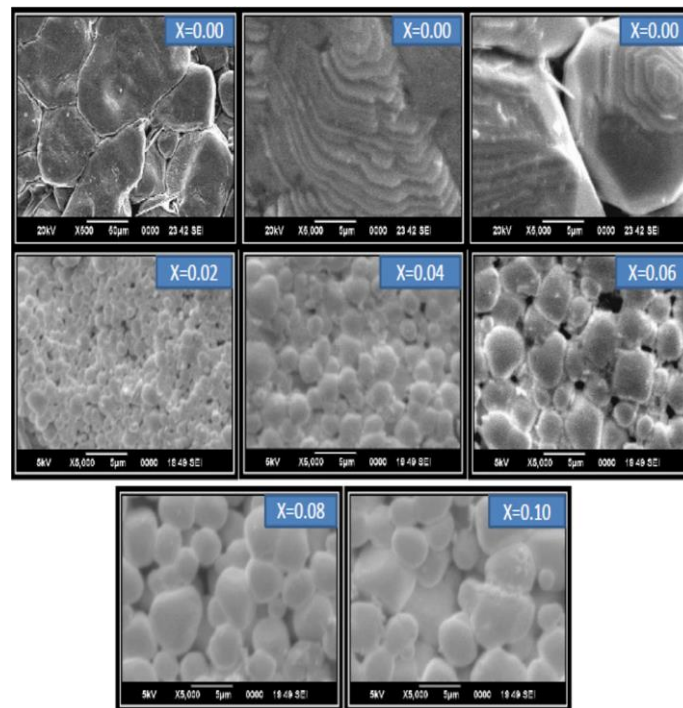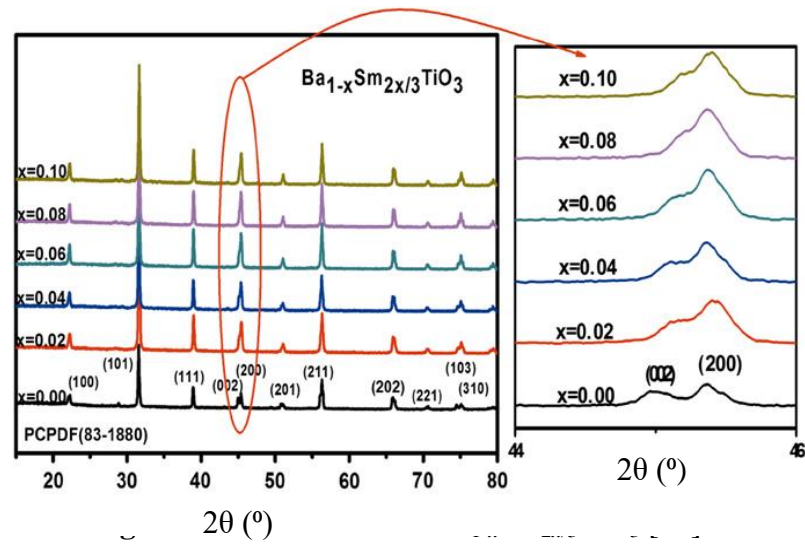




**Fig. 2.21** FESEM micrographs of $Ba_{1-x}Sm_{2x/3}TiO_3$ [54].

The radius of Ba ion is 0.16 nm whereas that of Sm is 0.124 nm for +2 valence state with co-ordination number 12. It is therefore evident that replacement of lower radii

Sm at the higher radii Ba site effects in a reduction in cell parameters and therefore in cell size. In doping, a rapid decrease in $\bar{D}$ is noticed compared to pure BT (Fig. 2.21).
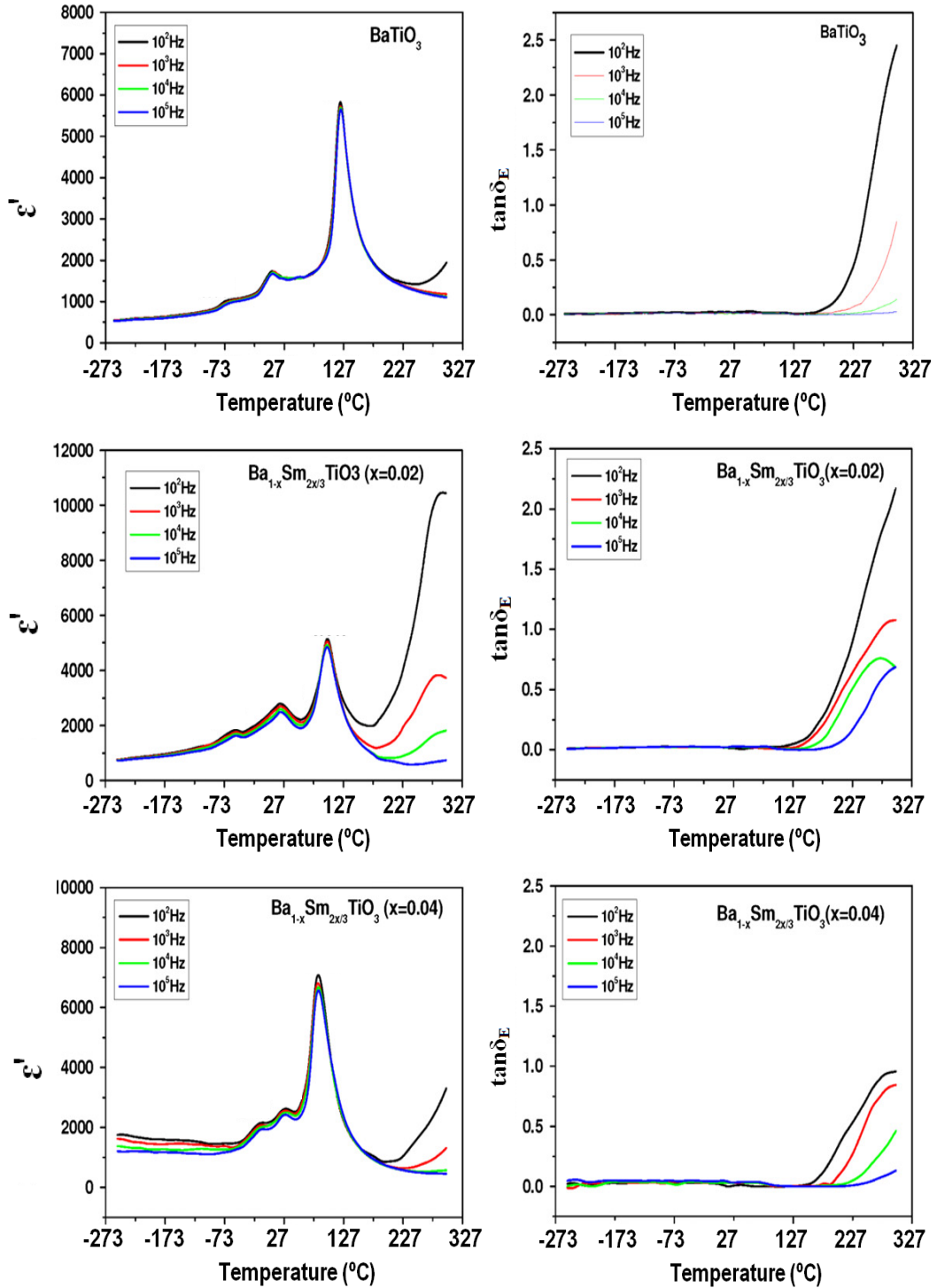


**Fig. 2.22** Variation of $\varepsilon'$ and $\tan\delta_E$ as a function of the temperature of $Ba_{1-x}Sm_{2x/3}TiO_3$ at different frequencies for samples with $x = 0.00$-$0.04$ [54].
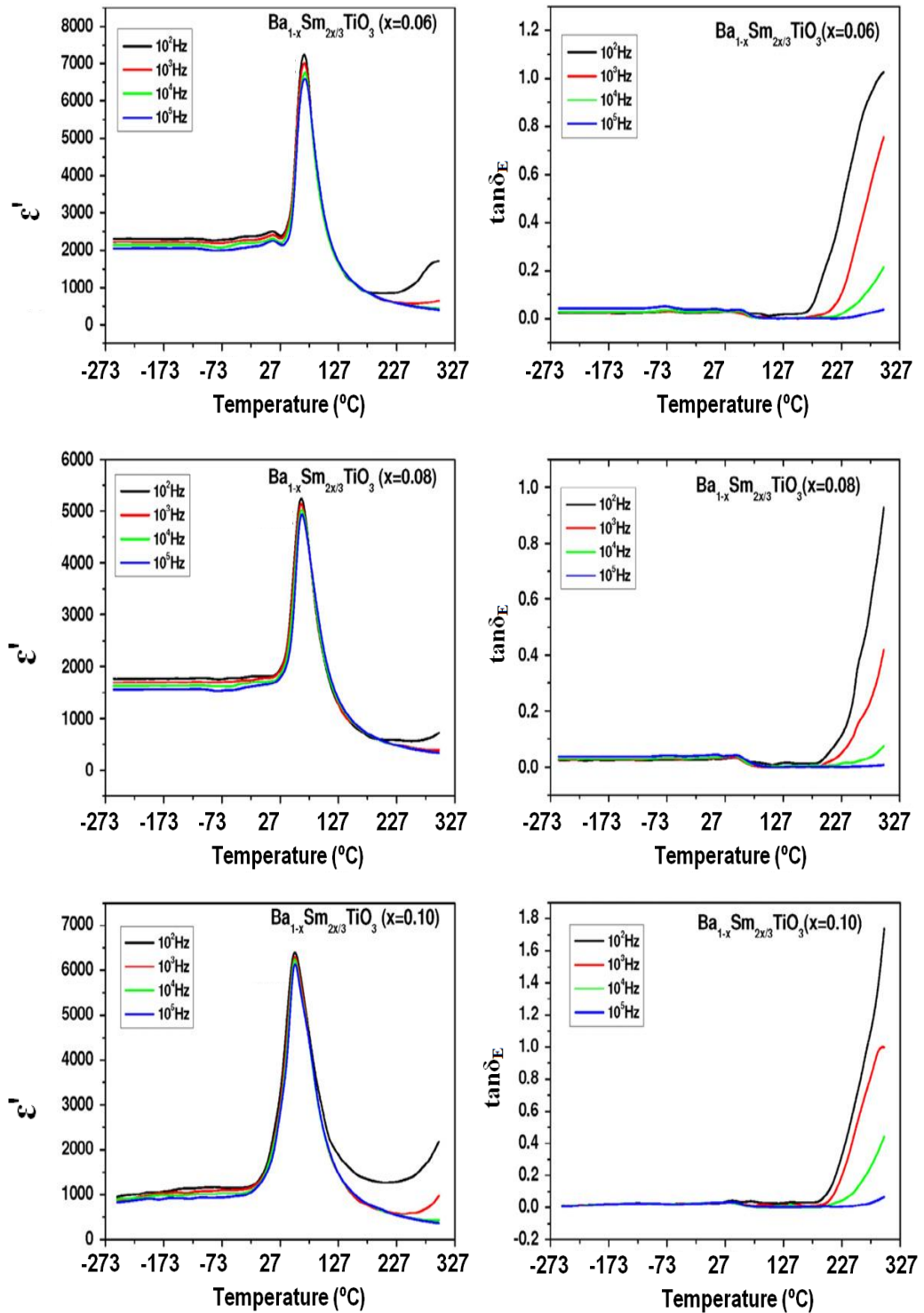
**Fig. 2.23** Variation of $\varepsilon'$ and $\tan\delta_E$ as a function of the temperature of $Ba_{1-x}Sm_{2x/3}TiO_3$ at different frequencies for samples with $x = 0.06$-$0.10$ [54].

Figures 2.22 and 2.23 show the dielectric nature as a variation of temperature at various frequencies. A rapid decrement in $T_{c-t}$ (cubic to tetragonal transition temperature) is found while an enhance in the $T_{t-o}$ (tetragonal to orthorhombic) and

the $T_{o-rh}$ (orthorhombic to rhombohedral) transition temperatures is noticed with enhancing Sm content. For all the samples the $T_{c-t}$ remains beyond RT. It can, therefore, be established that the un-doped BT and the doped materials reveal tetragonal uniformity at RT. The decline in $T_{c-t}$ in the circumstance of rare earth, such as Sm doping in BT suggests a reduction in tetragonality. Substituting $Ba^{2+}$ with $Sm^{3+}$ creats an A-site deficit to retain charge neutrality. This enhances with an enhance in Sm. Also, the tetragonal unit cell parameters decline. The unit cell shrinks as the $Ti^{4+}$ ion moves away from the octahedral site. Therefore the pairing between the $TiO_6$ octahedral weakens. This causes a significant decrease in $T_{c-t}$ ($T_{c-t}$ is related directly to the cation's shift from the core of the octahedral site to its position in the polar phase). Though the existence of an A-site vacancy provokes disorder in the structure, the long-range ferroelectric property is not eliminated. The temperature-dependent $\tan\delta_E$ decreases with the increase of Sm concentration ant the minimum magnitude is obtained for $x = 0.08$ sample.
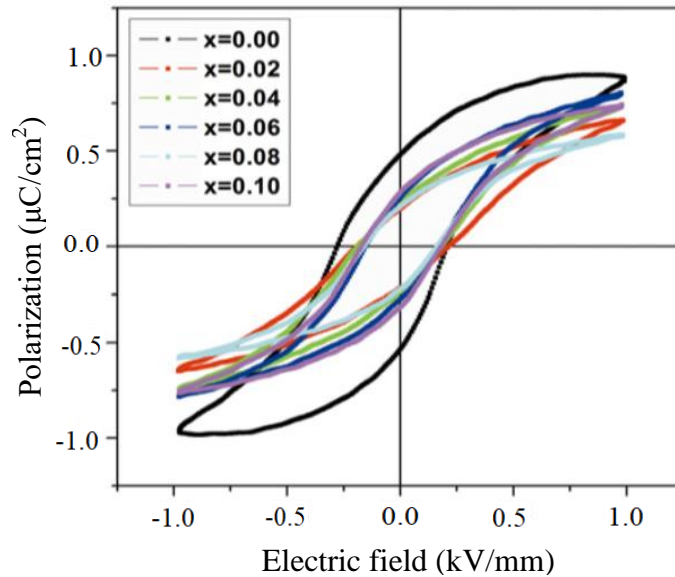


**Fig. 2.24** *P–E* hysteresis loop of $Ba_{1-x}Sm_{2x/3}TiO_3$ [54].

The *P-E* hysteresis loops of pure BT and doped samples are presented in Fig. 2.24. This ferroelectric behavior was evaluated at a frequency of 50 Hz with a maximum imposed electric field of 1 kV/mm. It is evident that polarizations are approaching saturation in such an electric field. Doping causes loops to become slimmer, as well as an irregular decline in remanent polarization but a very regular reduce in coercive

parameter. Dilution in the ferroelectric nature of BT is noticed with consecutive Sm doping. Reduced remnant polarization and a smaller coercive field were attributed to the effect of enhanced domain pinning by retained vacancies.

Sadhana et al. [38] synthesized and investigated the different properties of $x$Ba$_{0.8}$Ca$_{0.2}$TiO$_3$ (BCTO)+(1-$x$)Ni$_{0.2}$Cu$_{0.3}$Zn$_{0.5}$Fe$_2$O$_4$ (NCZFO) ($x$ = 0, 0.1, 0.3, 0.5, 0.7, 0.9, and 1) composites. Fig. 2.25 displays the XRD study of $x$BCTO+ (1-$x$)NCZFO composites. The co-existence of ferromagnetic and ferroelectric phases is visible in the XRD results. There were no other phases identified, revealing that there was no obvious reaction between the two phases. The lattice parameters intended for tetragonal BCTO are $a$ = 0.402 nm, $c$ = 0.398 nm, and cubic NCZFO ferrite is $a$ = 0.832 nm. The inset of Fig. 2.25 also illustrates that as x enhanced up to 0.3, the (311) peak shifted to a lower angle, whereas as x enhanced further, the peak shifted to a higher angle. It demonstrates that as x enhances up to 0.3, the composite is confined to stress generated by piezoelectric BCTO, which is effeciently shifted to the ferrite phase.
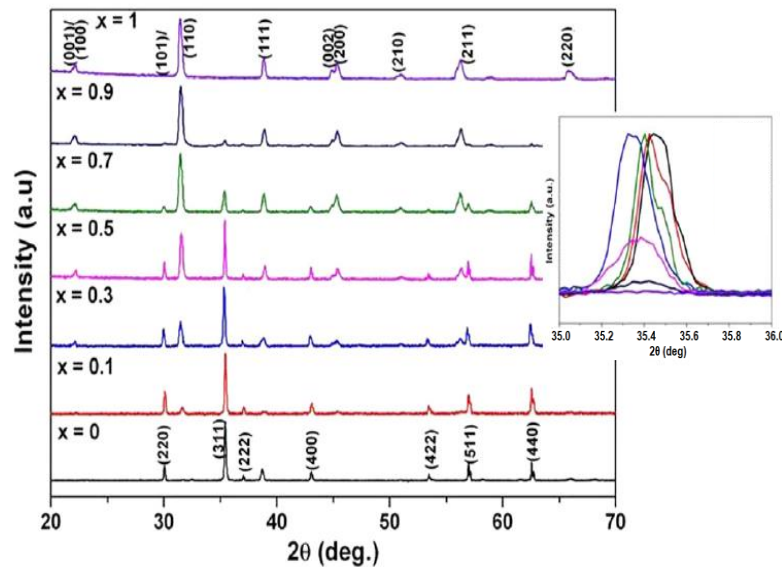


**Fig. 2.25** XRD patterns of $x$BCTO+(1-$x$)NCZFO ferrite composites ($x$ = 0.00-1.00). The inset: XRD of (311) plane for all compositions [38].

Fig. 2.26(a) shows the magnetization loops of $x$BCTO+(1-$x$)NCZFO composites. The disparity of $M_s$ and the coercive field ($H_c$) for all composites are displayed in Fig. 2.26(b). The maximum $M_s$ of 61 emu/g is found for the parent ferrite phase. It is evident that as the proportion of $x$ enhances, the Ms decliend because of the existence

of nonmagnetic phase and interface impacts, which modify the distribution of magnetic ions and their spin orientation, affecting the magnetic interactions. The $H_c$ enhances with x up to 0.3, then declines for 0.5, and afterwards enhances again with an additional increment of $x$, which may be contributed to domain wall pinning owing to the ferrite phase.
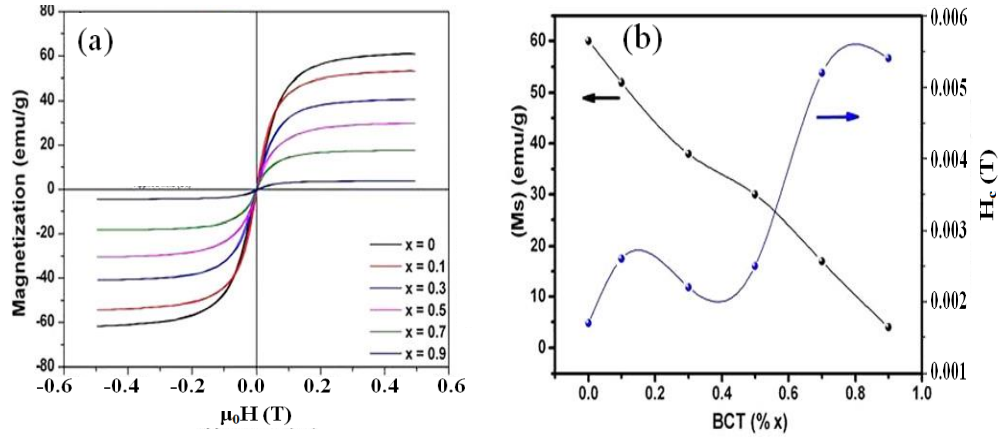


**Fig. 2.26**(a) *M-H* loops of $x$BCTO+(1-$x$)NCZFO composites, (b) $M_s$ and $H_c$ variation with BCTO fraction [38].
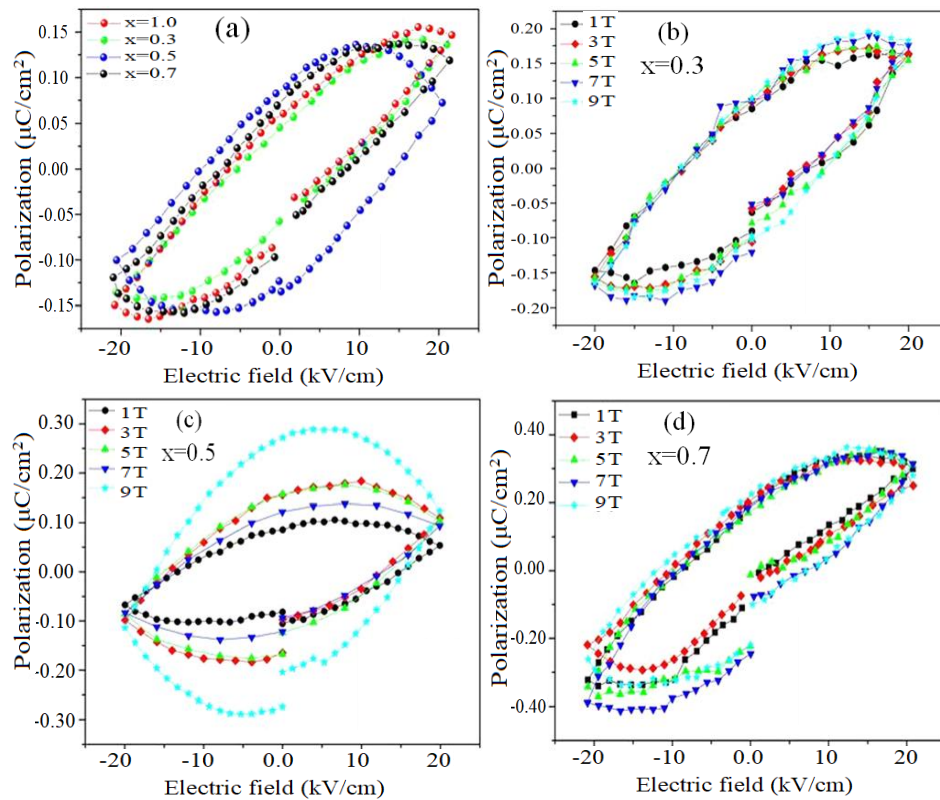


**Fig. 2.27**(a) *P-E* loops for several compositions of BCTO percentage, and (b)-(d) magnetic field induced polarization loops for $x$ = 0.3, 0.5, and 0.7, respectively [38].

Fig. 2.27(a) shows the *P-E* loops with numerous percentage of *x*. It is evident that *x*BCTO+(1-*x*)NCZFO composites exhibited ferroelectric nature. Polarization values increased with an increase in *x* content and the $E_c$ decreased owing to the reduction of leakage current. Fig. 2.27(b-d) depicts the magnetic field influenced polarization for *x* = 0.3, 0.5, and 0.7. Even when the magnetic field was applied, the ferroelectric loops has not demonstrate saturation, however, the leakage was evident to be large. The cause may be a voltage drop through the ferrite that affects the impedance of the BCTO+NCZFO interface. Once the electric field is imposed, the electrical phase separation happens in the NCZFO ferrite causing in a voltage drop through the interface that influences the ferroelectric transferring activity of the *x*BCTO+(1-*x*)NCZFO composites.
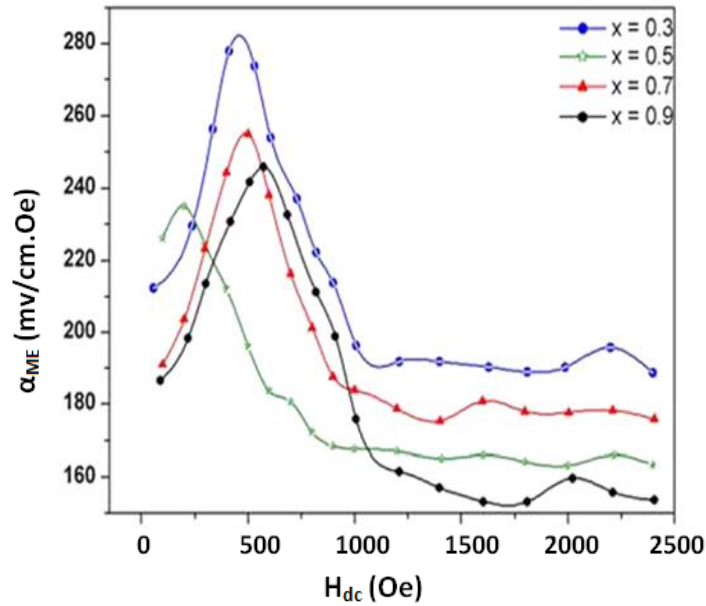


**Fig. 2.28** Variation of ME coefficient with dc magnetic field for *x*BCTO+(1-*x*)NCZFO composites [38].

Fig. 2.28 depicts the variation of ME response with dc biased magnetic field of for *x* = 0.3, 0.5, 0.7, and 0.9. It evident that ME response enhanced with a bias field and decreases after reaching the maximum value with the further enhance of the field. It is assumed that magnetostriction rises slowly and reaches the maximum limit with the magnetic field. This highest magnetostriction produces a large strain that transfers through the interface to the ferroelectric phase at which the voltage is generated. Thus, at this point, the ME output displays the highest value.

Kanakadurga et al. [96] investigated the different properties of $x$BaTiO$_3$+ $(1-x)$Mg$_{0.48}$Cu$_{0.12}$Zn$_{0.4}$Fe$_2$O$_4$ (MCZ) composites. The XRD patterns reveal that the composites are made of the MCZ ferrite phase with spinel structure and the BT phase with perovskite structure (in Fig. 2.29). It is also observed from the XRD patterns that both constituent phases coexist in the composites. The intensity of significant peaks, including (311) for MCZ and (110) for BT, relies on the quantity of their portion in the composite material. With an increment of $x$, the strength of BT peaks enhances, whereas the strength of ferrite peaks declined.
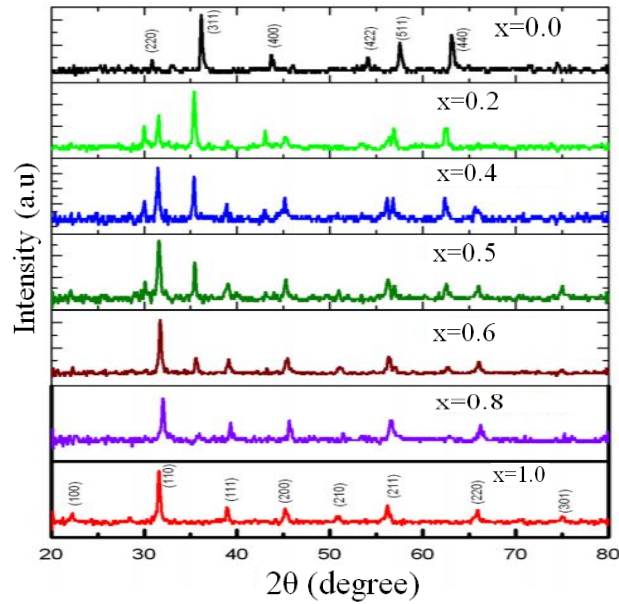


**Fig. 2.29** XRD patterns of vatrious $x$BaTiO$_3$+$(1-x)$Mg$_{0.48}$Cu$_{0.12}$Zn$_{0.4}$Fe$_2$O$_4$ composites [96].
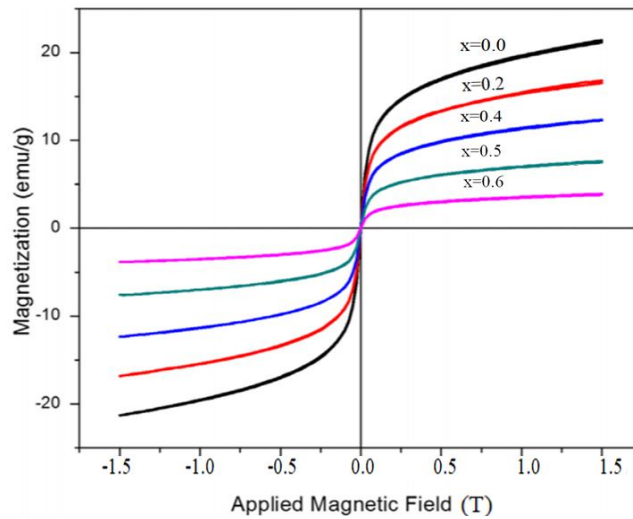


**Fig. 2.30** $M$-$H$ curves for various $x$BaTiO$_3$+$(1-x)$Mg$_{0.48}$Cu$_{0.12}$Zn$_{0.4}$Fe$_2$O$_4$ composites [96].

Fig. 2.30 reveals magnetic hysteresis loops of $x$ = 0.0, 0.2, 0.4, 0.5, and 0.6 at RT. Samples display standard magnetic hysteresis, suggesting that the composites are magnetically well-ordered. From the figure, it can be shown that coercivity rises with the enhance of the BT phase up to $x$ = 0.4. This suggests that the magnetization capacity is weakened by the presence of the non-magnetic BT phase, at where domain wall pinning happens, which contributes to enhanced $H_c$. When $x$ exceeds 0.4, the $H_c$ reduces, suggesting that no domain wall pinning exists. The maximum $M_s$ is obtained for the parent ferrite phase. Besides $M_s$ of the composites gradually declines with the rise of the BT phase.

Fig. 2.31 demonstrates the *P-E* loops for the composites. It is evident from Fig. 2.30 that the composites show the usual *P-E* loop implying that the materials are spontaneously polarized under the imposed electric field. The ferroelectric nature of the hysteresis loops gradually weakened by a reduction in BT content owing to a comparatively low electrical resistance of MCZ ferrite. The ferroelectric coercivity declines with a rise in the BT phase, which indicates that the composites become readily polarized by the imposed electric field.
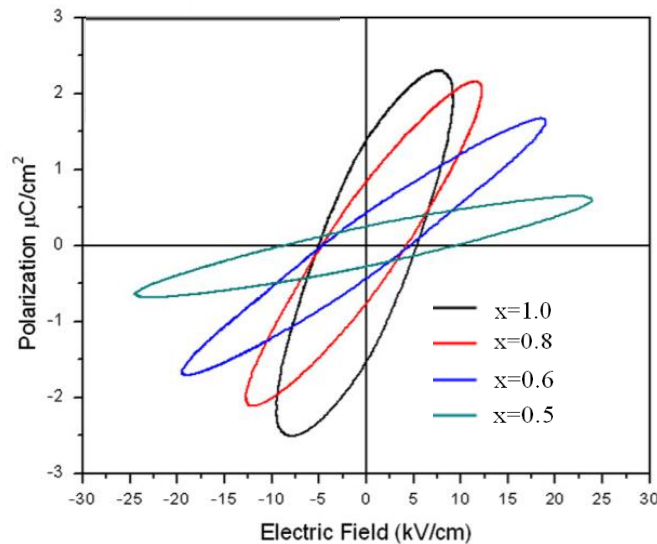


**Fig. 2.31** *P-E* loops of various $x$BaTiO$_3$+(1-$x$)Mg$_{0.48}$Cu$_{0.12}$Zn$_{0.4}$Fe$_2$O$_4$ composites [96].

Fig. 2.32 shows the change of the ME voltage coefficient on the dc magnetic field for composite materials. The figure reveals that the magnetic bias dependency of $\alpha_{ME}$ is

considered to be identical for each composites. It is evident that, for $x = 0.8$ sample, $\alpha_{ME}$ improves with a magnetic field rise of up to 700 µV/cm Oe and declines with more rise of $H$ and eventually saturates at a bias level. The maximum ME magnitude is found for the 1.5 kOe dc region. At this dc field, the ferromagnetic phase has achieved a saturation value generating a constant electric field in the ferroelectric phase, causing in a decrease of $\alpha_{ME}$ with the rising magnetic field. It indicates that magnetic saturation happens at low stimulation and that the materials are ideally suitable to a comparatively weak magnetic field.
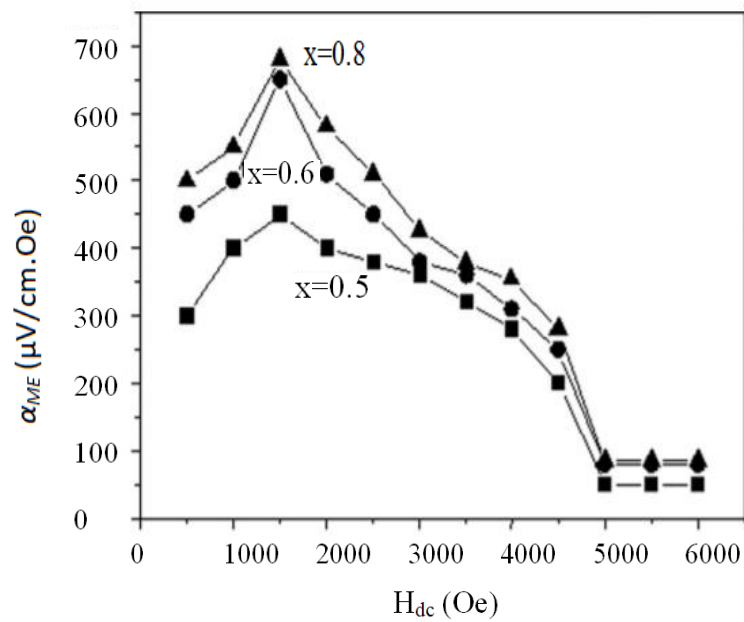


**Fig. 2.32** The variation of $\alpha_{ME}$ with applied dc magnetic field for various $x$BaTiO$_3$+ $(1-x)$Mg$_{0.48}$Cu$_{0.12}$Zn$_{0.4}$Fe$_2$O$_4$ composites [96].

# 3. SAMPLE PREPARATION AND EXPERIMENTAL TECHNIQUES

## 3.1 Sample Preparation

### 3.1.1 Introduction

Synthesizing polycrystalline composites with optimal favorable characteristics is indeed a complicated process, and controlling chemical composition, homogeneity, and microstructure is important. Since most of the characteristics required for composite applications are not inherent but extrinsic, the preparation of samples has to be made more complex. It is well established that approximately all composites decompose at high temperatures if we want to melt them under normal circumstances. Nowadays, a large number of composite powders are prepared by the conventional ceramic method or by the standard solid-state reaction methodology. The majority of non-conventional techniques involve the production of the powder using a wet process. Some of those approaches include [97, 98]:

(i) Co-precipitation

(ii) Organic precursors

(iii) Spray-drying

(iv) Freeze-drying

(v) Combustion synthesis

(vi) Glass crystallization

The standard solid-state reaction procedure used in this research work has been described here.

### 3.1.2 Chemical composition of the ceramic powders

Various ferroelectric and ferromagnetic ceramics with different chemical compositions were reported in the literature for use as components of ME ceramic composites. The following specific compositions were selected in the present study to produce ME composites:

Ferromagnetic phase: $Li_{0.10}Ni_{0.30}Cu_{0.10}Zn_{0.40}Fe_{2.10}O_4$

Ferroelectric phase: $Ba_{0.95}R_{0.05}Ti_{0.95}Dy_{0.05}O_3$ (where R = Sm and Gd).

### 3.1.3 Standard solid-state reaction technique

The solid-state reaction is often a high-temperature direct reaction among raw materials (typically powders). Ambient temperature delivers the energy required for the reaction. In general, solid-state reactions are slow, as a large number of bonds dissociate and ions moved through a strong gas-phase and solutions during reactions. Diffusion is the most common controlling factor for solid-state reactions. The diffusion of cations via product layer is thus the step that regulates the speed of a solid-state reaction. The solid-state reaction accelerates with increasing temperature, and it usually does not happen before the reaction temperature exceeds at least two-thirds of the melting temperature of one of it's molecules.

In a solid-state reaction system, raw elements are weighed as per the stoichiometry of the composition. Raw materials are mechanically combined, and then the grinding process is conducted to control the size of the particles and mix homogeneously. For this reason, the milling process may decrease the particle size to the 1-10 μm varieties [99]. An effort to minimize the particle size can further impact the homogeneity and purity of the sample. Acetone is taken as a medium because it is inexpensive, of high purity, and non-flammable. The next step is the solid-state reaction between the components of the raw materials at an appropriate temperature. This technique is called firing or calcination. The ground powders are calcinated in air or oxygen at a temperature of between 700 and 1000ºC for 5 hours. The calcination process may be performed till the mixture has been converted to the desired crystalline form. The calcined powders are smashed once more into finer particles. These calcined powders are formed into pellets and toroid samples via die-punch operation or hydrostatic or isostatic pressure. Then the prepared samples are sintered at an appropriate temperature to dense the compositions [100-102]. Fig. 3.4 demonstrates the flow chart of preparing composite material by the solid reaction method.

### 3.1.4 Details of calcining, pressing, and sintering
### 3.1.4.1 Calcination
Calcination is the process of heating a substance to an ambient temperature in air or oxygen a little below the melting point, resulting in moisture loss, reduction or

oxidation, obtaining a homogeneous, and phase pure composition of mixed powders of carbonates and any other compounds. A calciner is a steel cylinder that twists in a heated furnace and executes indirect high-temperature operation under controlled circumstances. The calcination procedure can be repeated as many times to achieve the highest standards of homogeneity. Powders that have been calcined are squashed into fine powders. The desired features of fine powders are [38]:

(i) Particles of a small size (sub-micron)

(ii) Narrow distribution in particle size

(iii) Dispersed particles

(iv) The equiaxed shape of particles

(v) High purity

(vi) Homogeneous composition.

Because of the narrow size distribution of the reactant granules, there is a considerable contact area for initiating the solid-state reaction; diffusion paths are reduced, resulting in more effective reaction finalization. The narrow allocations of spherical particles, and indeed the scattered state, are essential for powder compaction since the development of the green material. Grain growth throughout sintering might be a little more controlled if the preliminary size is small and homogeneous.

**3.1.4.2 Pressing**
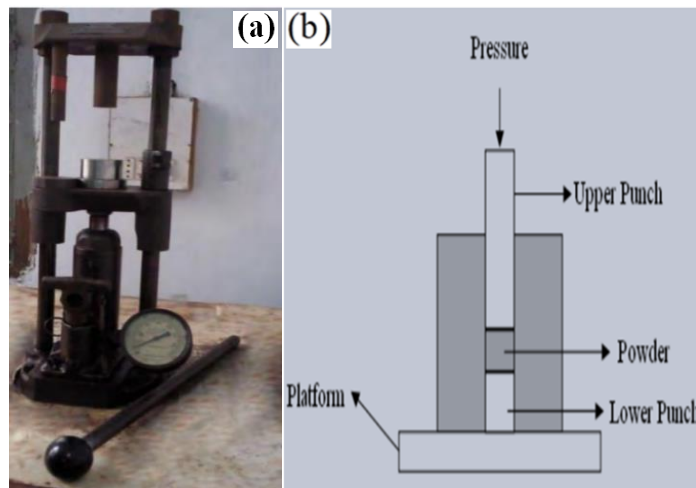


**Fig. 3.1** (a) Uniaxial press machine, and (b) uniaxial pressing mechanism.

A binder is applied before compaction, at a concentration below 5 wt% [38]. Polyvinyl alcohol is the most widely used binder. The binder promotes the movement of particles during compaction and increases the bonding between the particles, possibly through the formation of particle-binder-particle type bonds. Throughout sintering, binders are decomposed and extracted from the composite. Pressures are used for the compaction of calcined powders, typically several tons per square inch (using Fig. 3.1). To make a pellet of 90 g and a toroid shaped ring of 80 g powders are taken from the calcined powders and pressed by a hydraulic press.

### 3.1.4.3 Sintering

Sintering is a procedure that compresses green elements into strong and dense polycrystalline materials using the furnace depicted in Fig. 3.3. Throughout sintering at a significant temperature, the atomic movement becomes more prominent and the region between grains in contact opposite owing to the thermal expansion of the grains and lastly, only one interface between two grains persists. The decline in the surface free energy of the powder is the driving force behind sintering. In the polycrystalline body, some of this energy is transformed into interfacial energy (grain boundaries) [98, 103]. Densified ceramics result from atoms on grain surfaces being influenced in all directions by adjacent atoms in this state [104]. Sintering temperature, time, and the furnace environment play a vital role in the electric and magnetic characteristics of the materials. The objectives of the sintering mechanism are as follows:

(i) to bind the particles together to give adequate strength

(ii) to densify materials by removing pores

(iii) to homogenize the material by finishing the reactions during the calcination process.

The sintering of crystalline solids is done by Coble and Burke [105], who explained the scientific relationship with the rate of grain growth, is given below:

$$\bar{D} = k t_s^n \qquad (3.1)$$

where $n$ is around $\frac{1}{3}$, $t_s$ is the sintering time and $k$ is the temperature-dependent parameter.

There are three stages to sintering:

phase 1. the contact area among particles enhances

phase 2. the porosity shifts from open to closed.

phase 3. pore volume shrinks, and grains expand.
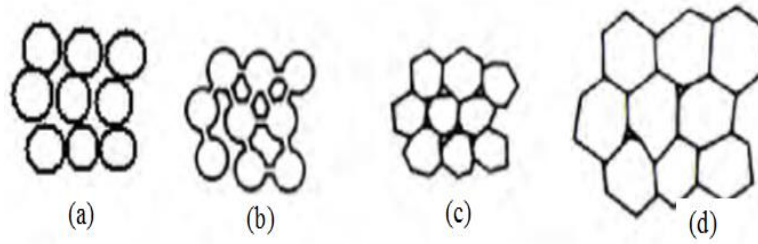


**Fig. 3.2** Sintering phases are depicted in a diagram: (a) green body, (b) initial phase, (c) intermediate phase, and (d) final phase [99].



**Fig. 3.3** Furnace (Nobertherm, HTC 08/14, Germany).

At the earliest stages of the sintering system, rather than at high temperatures, the lattice distortion, and internal strain are declined by atomic diffusion, and this is often referred to as the recovery process. A recrystallization process occurs by atomic diffusion during the further rise of temperature. Throughout recrystallization, a new crystal nucleus develops and grows at the grain boundary and in other regions within the grain with greater free energies. In the meantime, some grains grow by inhaling some smaller grains. Grain growth is typically understood through the movement of grain boundaries in the recrystallization stage. The higher the sintering temperature ($T_s$), the more grains could grow as the development of grain results from atomic diffusion that decreases with the rise in $T_s$. The density of the ceramic sample is influenced by the $T_s$ and time in a more complex manner. Whether the $T_s$ is too high or the sintering time is too long, the density of alkaline-based ceramics is reduced

due to $BaCO_3$ evaporation at high temperatures. Even though grain growth is triggered by nuclear diffusion, it confirms that higher $T_s$ and a longer hold time results in larger grains.

### 3.1.5 The stages in the preparation of sample

The flow chart for the preparation of samples using a solid-state reaction method is presented in Fig. 3.4.
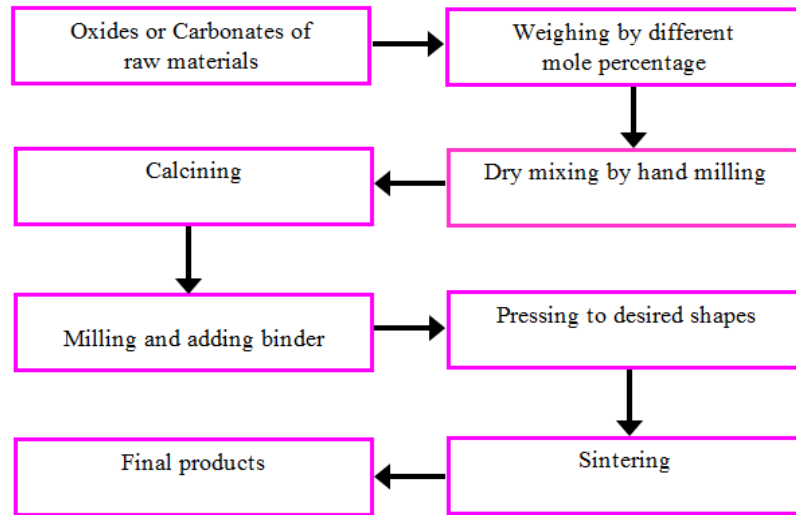


**Fig. 3.4** Flow chart of the sample preparation by solid-state reaction technique.

### 3.1.6 Preparation of samples for the present research

Multiferroic $x$LNCZFO+(1-$x$)BRTDO composites (where R = Sm and Gd; $x$ = 0.00, 0.10, 0.20, 0.30, 0.40, 0.50, 0.60 and 1.00) were amalgamated by the conventional solid-state reaction technique. The magnitudes of $x$ were chosen for a clear conception of the variations in the physical characteristics of composites with the ferrite phase. High purity $Li_2CO_3$ (99.0%), NiO (99.9%), CuO (99.99%), ZnO (99.9%) and $Fe_2O_3$ (99.95%) powders were taken to fabricated the LNCZFO constituent. Raw materials of $BaCO_3$ (99.9%), $Sm_2O_3$ (99.9%), $Gd_2O_3$ (99.9%), $TiO_2$ (99.9%), $Dy_2O_3$ (99.9%) were taken to fabricated the BRTDO phases. Stoichiometric amounts of raw materials were mixed with an agate mortar and pestle in an acetone medium. The mixed ferrite and ferroelectric powders were calcined at 700 and 1000⁰C, respectively. The ground powders of the constituent phases were then mixed in an acetone medium for 5h according to the formula $x$LNCZFO+(1-$x$)BRTDO. A granulation binder of 10% PVA was then mixed into the powders. The mixed

powders were uniaxially pressed to make disk- and ring-shaped samples. The optimum properties of the compositions are found at optimum $T_s$ which are typically between 1200 and 1250⁰C. The samples were sintered at various temperatures within this range to determine the optimum $T_s$. The optimum $T_s$ values were obtained as follows: 1250⁰C for $x = 0.00$, 0.10, 1225⁰C for $x = 0.20$, 0.30, 0.40, 0.50, 0.60, and 1200⁰C for $x = 1.00$ for composites with R = Sm. Besides, optimum $T_s$ values were obtained as follows: 1250⁰C for $x = 0.00$, 1225⁰C for $x = 0.10$, 0.20, 0.30, 0.40, 0.50, 0.60, and 1200⁰C for $x = 1.00$ for composites with R = Gd.

## 3.2 Characterization Techniques

### 3.2.1 X-ray diffraction

The XRD is a efficient method for the survey of crystal structures and the atomic spacing of powder and solid samples of any material shown in Fig. 3.5. The XRD works by using the constructive interference of monochromatic X-rays and crystalline samples. A cathode ray tube generates the X-rays, which are then filtered to generate monochromatic radiation, collimated to focus, and directed at the sample. Interaction of the incident rays with the sample generates constructive interference when the conditions agree with Bragg's law:

$$2d_{hkl}\sin\theta = n\lambda \tag{3.2}$$

where $d_{hkl}$ and $n$ are the distance between crystal planes and the positive integer which signifies the diffraction order, respectively. Equation (3.2) is referred to as the Bragg law. This law implies that diffraction can only be accomplished if the condition of $\lambda \leq 2\ d_{hkl}$ is satisfied.
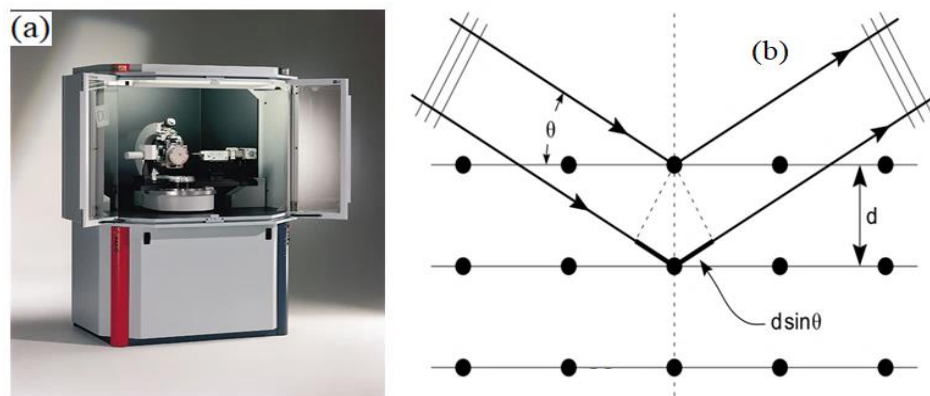


**Fig. 3.5** (a) Bruker's XRD D8-discover instrument and (b) Bragg law of diffraction [106].

X-ray spectra are made up of various components, the most useful of which are $K_\alpha$ and $K_\beta$. Specific wavelengths are the characteristics of the target material (such as Cu, Fe, Mo, Cr). Among these materials, Cu is the best common target element for single-crystal diffraction, with Cu$K_\alpha$ radiation of wavelength 0.1542 nm. The lattice parameters were calculated by Rietveld refinement analysis [107].

### 3.2.2 Density measurement

The $\rho_B$ of the sintered samples is evaluated with the Archimedes technique. First, each sintered sample was weighed ($W_d$) by the precision balance (Shimadzu AX 120). After that, the pellet was inserted into a beaker filled with distilled water with a small hanger and weighed ($W_w$). Using the above data, the $\rho_B$ of a sample was determined using the following formula:

$$\rho_B = \frac{W_d}{W_d - W_w} \times \rho_w \tag{3.3}$$

The $\rho_{th}$ (constituent phases) was computed by applying relationship:

$$\rho_{th} = \frac{nM_A}{N_A V} \tag{3.4}$$

where $n$ denotes the atoms per unit cell, $M_A$ denotes the molecular weight, $N_A$ denotes Avogadro's number, and $V$ denotes the unit cell volume. The $\rho_{th}$ of the composites was computed by applying relationship:

$$\rho_{th}(composite) = \frac{n}{N_A} \times \frac{xM_1 + (1-x)M_2}{V_1 + V_2} \tag{3.5}$$

where $M_1$ denotes molecular weight of LNCZFO and $M_2$ denotes molecular weight of BRTDO. The unit cell volume of ferrite and ferroelectric constituents in the composites are $V_1 = \frac{n}{N_A} \times \frac{xM_1}{\rho_{th}(ferrite)}$ and $V_2 = \frac{n}{N_A} \times \frac{(1-x)M_2}{\rho_{th}(ferroelectric)}$, respectively.

### 3.2.3 Field Emission Scanning Electron Microscopy

A Field Emission Scanning Electron Microscopy (FESEM) microscope works with electrons (particles with a negative charge) rather than light, as shown in Fig. 3.6. These electrons are liberated by the source of field emission. Electrons scan the object in a zigzag pattern. FESEM introduces topographical and elemental details at magnifications at magnifications of 10× to 300000×, with virtually unlimited depth of field. A scanning electron microscope's electron gun with a field-emission cathode provides narrower scanning beams at low as well as high electron energy, resulting

in both enhanced visual resolution and reduced sample charging and damage.FESEM contains the Schottky field emission gun that uses electric field emissions to reduce the efficiency and increased the thermionic emission of tungsten. The field emission gun generated an electron beam and enhanced current density or brightness. JSM 7610F equipped with Gentle Beam mode generates high-resolution images though at low voltage acceleration from 100 V to 3.9 kV without damaging the surface of the material. Therefore the signal is amplified and then used to exhibit the relevant sample statistics. The resolution of a FESEM image depends on the beam diameter on the surface of the sample. Though the effective resolution relies on the characteristics of the sample, the samples synthesized process, and many operational factors, including lens to surface distance of the sample, the beam intensity, scanning speed, accelerating voltage, and the angle of the sample for the detector. A resolution of 1 nm can be obtained under optimum conditions.



**Fig. 3.6** FESEM instrument (Model No. JEOL JSM 7600F).

### 3.2.4 Energy Dispersive Spectroscopy

Energy Dispersive Spectroscopy (EDS) is an analytical method used for the elementary analysis of a material. It is a type of X-ray fluorescence spectroscopy that investigates a substance using electromagnetic radiation and matter interactions. The pulse processor, X-ray detector, and analyzer are the three main components of an EDS system, and they must all be programmed to work together to obtain the best outcomes. X-rays are detected and converted into electronic signals by the X-ray

detector. After which the pulse operating system tests the electric signals to evaluate the energy of all X-ray observed. At last, the analyzer exhibits and interprets data from X-rays.

The present research was carried out using the EDS analysis system provided by the JSM 7610F FESEM.

### 3.2.5 Magnetic properties measurements

### 3.2.5.1 Complex initial permeability

The $\mu_i'$, $\tan\delta_M$ and RQF were evaluated using the Wayne Kerr 6500B impedance analyzer. The Toroid-shaped sample was used for the determination of complex permeability at RT in the frequency spectrum of 10 kHz-120 MHz presented in Fig. 3.7. The $\mu_i'$ was determined using the following relation:

$$\mu_i' = \frac{L_s}{L_0},$$ 
(3.6)

where $L_s$ is the self-induction of the winding coil with the sample, $L_0$ ($= \frac{\mu_0 N^2 S}{\bar{d}}$) is the inductance of the coil without sample, $N$ is the number of turns in the coil ($N = 4$), $S$ is the cross-sectional area and $\bar{d}$ is the mean diameter of the sample. The RQF was determined using the formula:

$$RQF = \frac{\mu_i'}{tan\delta_M},$$ 
(3.7)



**Fig. 3.7** Toroid shaped sample for $\mu_i'$ measurement.

### 3.2.5.2 *M-H* hysteresis loops

The *M-H* curve for materials was determined using the Vibrating Sample Magnetometer (VSM) shown in Fig. 3.8. VSM is a scientific instrument that measures magnetic behavior by placing the specimen inside a uniform magnetic field. The induced voltage due to the magnetic moment in the pickup coil made by

physically vibrating the sample is proportionate to the sample magnetization but is independent of the magnetic field applied. The magnetic field-dependent magnetization hysteresis curve of the materials can thus be evaluated by identifying the induced voltage.
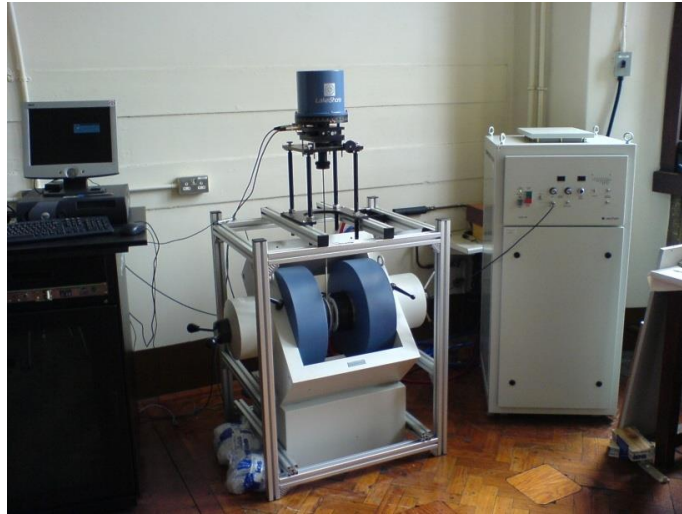


**Fig. 3.8** Vibrating Sample Magnetometer.

### 3.2.6 Dielectric properties measurements
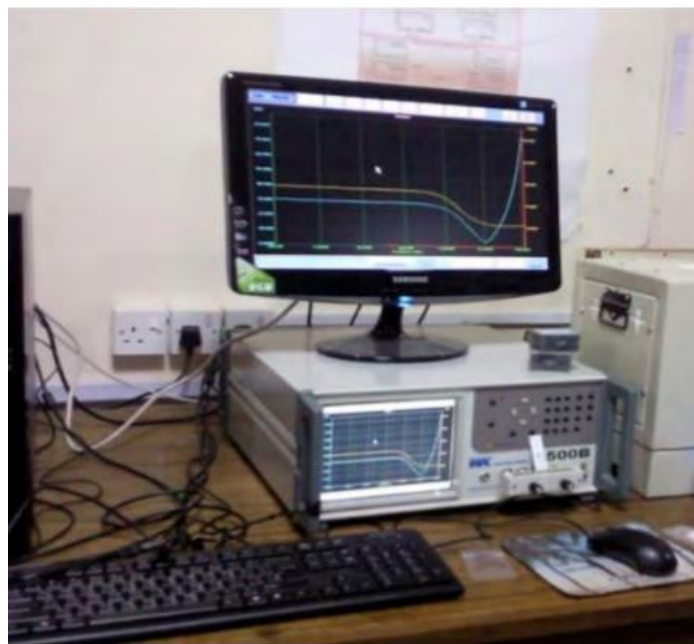


**Fig. 3.9** Wayne Kerr Impedance Analyzer (Model No. 6500B).

Frequency-dependent dielectric characteristics, ac conductivity, impedance spectroscopy, and temperature-dependent $\varepsilon'$ were measured using Impedance

Analyzer. Fig. 3.9 demonstrates the experimental setup of the Wayne Kerr 6500B Impedance Analyzer. Measurements of dielectric characteristics typically implicate the measurement of the change in capacitance and loss of a capacitor in the existence of dielectric materials. The operation of the measurement technique can be explained as follows: Firstly considered an ideal lossless air capacitor of capacitance $C_0$. The capacitance is changed when the dielectric component is inserted into the air medium. The RT dielectric and electrical properties (ac conductivity and impedance) measurements on disk-shaped samples are performed for all the compositions in the frequency spectrum of 20 Hz-5 MHz.

The $\varepsilon'$ is calculated using the following relations [100],

$$\varepsilon' = \frac{C}{C_0}, \tag{3.8}$$

where $C$ represents the capacitance of the composition and

$$C_0 = \frac{\varepsilon_0 A}{d} \tag{3.9}$$

where $C_o$, $d$ and $A$ represent the capacitance without dielectrics, the thickness of the capacitor, and the cross-sectional area of the disk-shaped sample, respectively. To ensure better electrical contact for the evaluation of $\varepsilon'$, the samples were painted on both sides with silver paste. The ac conductivity ($\sigma_{ac}$) is measured at RT in the frequency area of 20 Hz-5 MHz to investigate the conduction procedure of the samples. The $\sigma_{ac}$ of the samples is calculated using the following equation [108]:

$$\sigma_{ac} = \omega\varepsilon_0\varepsilon' tan\delta_E, \tag{3.10}$$

where $\varepsilon_0 = 8.85 \times 10^{-12}$ Fm$^{-1}$, $\omega$ and $tan\delta_E$ reflect angular frequency, and is the loss of the dielectric material, individually.

### 3.2.7 Complex impedance spectroscopy analysis

The electrical characteristics of complex perovskite oxides can be studied using complex impedance spectroscopy. The ac measurements are often performed to analyze impedance spectroscopy using a Wheatstone bridge form of device (Impedance Analyzer or LCR meter), wherein $R$ and $C$ of the samples are evaluated

and balanced with respect to the variable resistors and condensers. Impedance |Z| (~Z*) and the phase discrepancy ($\theta$) among the voltage and current are determined as a function of frequency. Therefore the data is examined by plotting the imaginary part of impedance, $Z'' = |Z|\cos\theta$ against the real part of impedance, $Z' = |Z|\sin\theta$ on such a complex plane recognized as impedance plot. The impedance for a parallel RC circuit is demonstrated using the relationship given below:

$$Z^* = Z' - jZ'' = \frac{R}{1+(\omega RC)^2} - j\frac{\omega R^2 C}{1+(\omega RC)^2} \tag{3.11}$$

One obtains after simplifying

$$(Z' - \frac{R}{2})^2 + Z''^2 = (\frac{R}{2})^2 \tag{3.12}$$

This shows the equation of the circle with the radius $R/2$ and the center at $(R/2, 0)$. Thereby, a plot of $Z'$ versus $Z''$ (as a function of $\omega$) for a polycrystalline material results in two semicircles (Fig. 3.10). This plot is often referred to as the Cole-Cole plot.
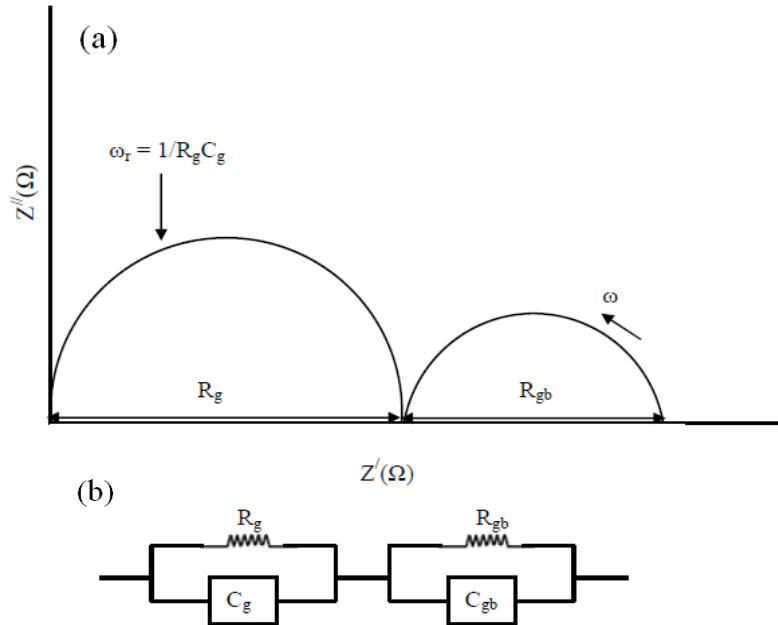


**Fig. 3.10** (a) The impedance plot for an ideal polycrystalline sample and (b) the corresponding equivalent circuit.

Using the given formula, the composites' complex electric modulus (*M\**) was estimated:

$$M^*(\omega) = \frac{1}{\varepsilon^*} = \frac{1}{\varepsilon' - j\varepsilon''} = \frac{\varepsilon'}{\varepsilon'^2 + \varepsilon''^2} + j\frac{\varepsilon''}{\varepsilon'^2 + \varepsilon''^2} = M'(\omega) + jM''(\omega), \tag{3.13}$$

where $\varepsilon^*$ and $\varepsilon''$ depict the complex dielectric constant and its imaginary part, respectively.

Simplifying and substituting $\varepsilon''$ by $\varepsilon' tan\delta_E$, we get

$$M^*(\omega) = M'(\omega) + jM''(\omega) = \frac{1}{\varepsilon'(1+tan^2\delta_E)} + \frac{j(tan\delta_E)}{\varepsilon'(1+tan^2\delta_E)},$$ (3.14)

where $M'$ and $M''$ dipict the real and imaginary parts of $M^*$, respectively.

### 3.2.8 Ferroelectric property measurements

Precision multiferroic test system (Model: P-PMF, Radiant Tech. Inc., USA) attached with 10 kV high voltage interface (Model. P HVI210KSC, amplifier (Model. Trek 609B) was used to describe the electrical characteristics of samples shown in Fig. 3.11. The electric field and frequency-dependent electric polarization, $\varepsilon'$, and tan$\delta_E$ can be determined by this device.



**Fig. 3.11** Ferroelectric loop tracer.

The basic *P-E* test system is based on Sawyer Tower (S-T) circuit depicted in Fig. 3.12. The circuit contains two capacitors, one owing to sample (*C*) and the other to a linear known valued internal capacitor (*C_o*) connected in series. The principle is simple when two capacitors are associated in series and ac voltage is imposed on both in series, the charge on both will be the same. To achieve complete saturation, the internal capacitance must be greater than the sample capacitance.
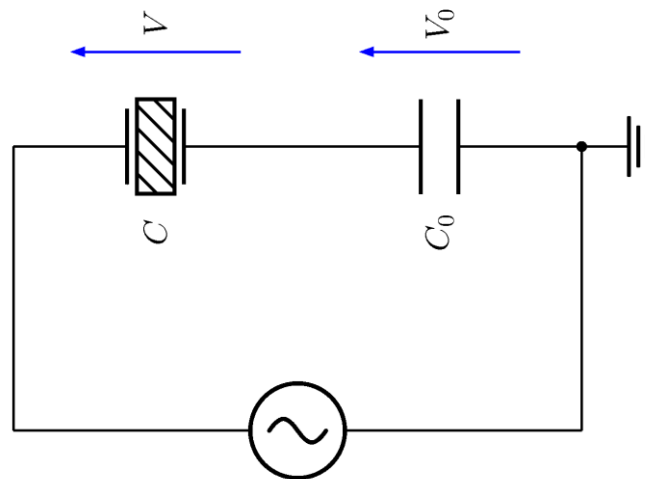
**Fig. 3.12** Sawyer Tower (S-T) circuit.

### 3.2.9 Magnetoelectric coefficient measurement
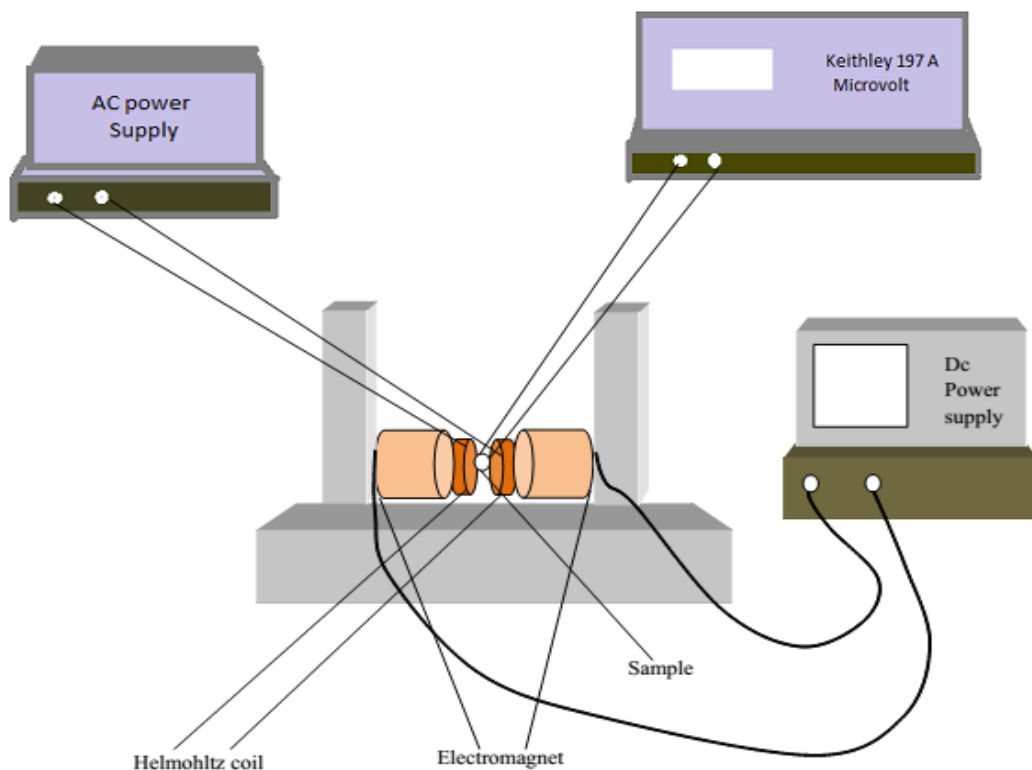


**Fig. 3.13** Experimental setup for the measurement of the ME coefficient.

The sides of the pellet are connected to a Keithley electrometer (model 197A) to measure the ME coefficient, which gives the output voltage value shown in Fig. 3.13. The sample is then inserted between the two poles of the electromagnet. Another pair of coils known as Helmholtz-coil is placed between the poles of the electromagnet.

The Helmholtz coil is attached to an ac power supply and creates an ac magnetic field. The magnetic field of the electromagnet is changed by changing the current and voltage of the dc power supply and the sample experience different magnetic fields. This effect results in a change in the output voltage. The ME coefficient of the materials is evaluated using the following relation [109]:

$$\alpha_{ME} = \left(\frac{dE}{dH}\right)_{H_{ac}} = \frac{V_0}{h_0 d} \tag{3.15}$$

where $V_0$, $d$, and $h_0$ represent the ME voltage established within the sample, the effective thickness of the sample, and the amplitude of the applied ac field, respectively.

# 4. RESULTS AND DISCUSSION

## 4.1 Characterization of *x*LNCZFO+(1-*x*)BSTDO Composites

### 4.1.1 Structural characterization, density, and porosity
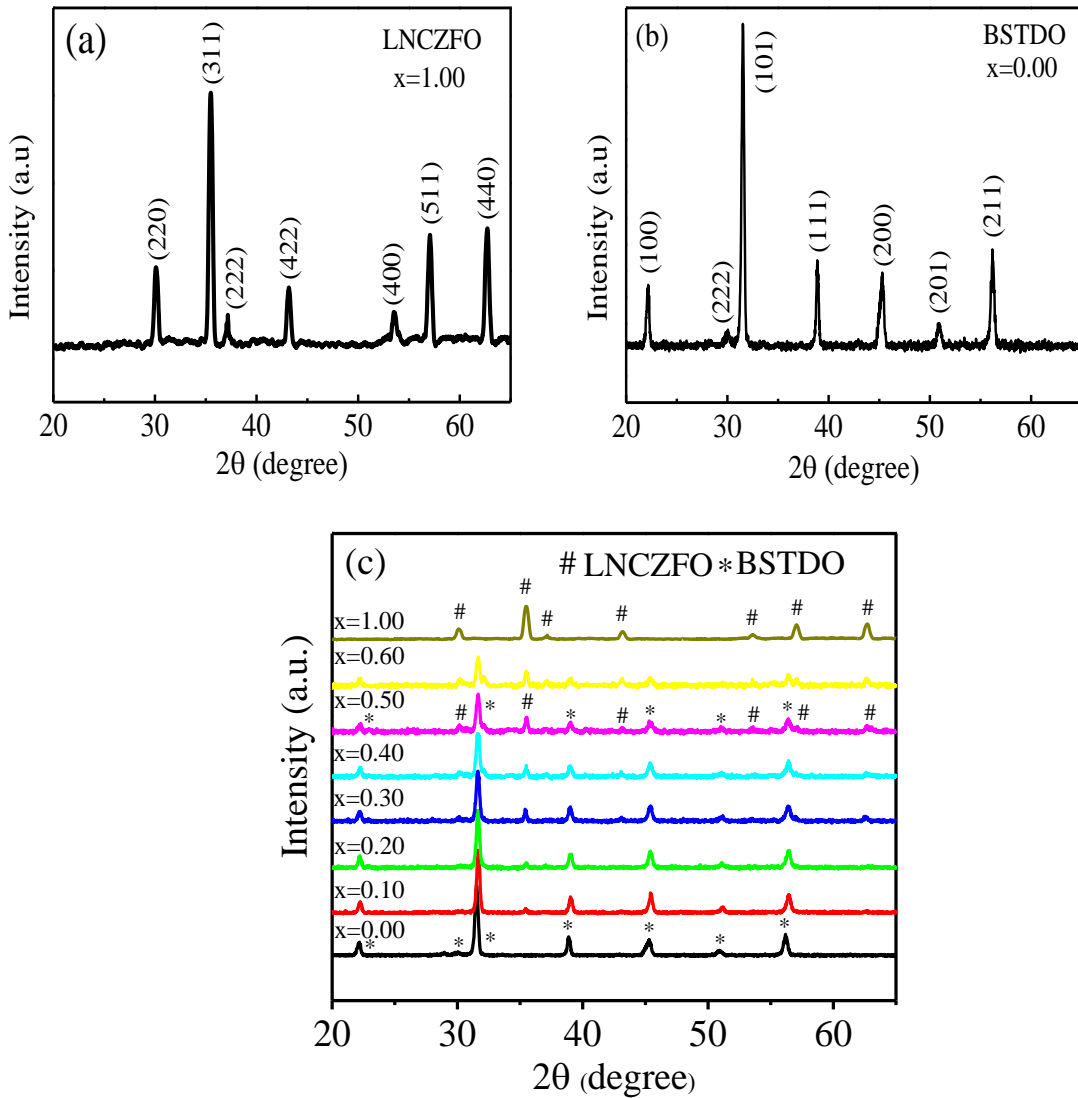


**Fig. 4.1** XRD patterns of (a) LNCZFO, (b) BSTDO, and (c) various
*x*LNCZFO+(1-*x*)BSTDO composites.

The XRD pattern of LNCZFO is shown in Fig. 4.1(a) confirms the single-phase
cubic spinel structure, while the pattern of BSTDO shown in Fig. 4.1(b) is a
characteristic feature of the single-phase tetragonal perovskite structure. The XRD
peaks have been identified with their corresponding Miller indices. The positions of
all peaks in the XRD pattern match well with previously reported results [49, 54].

Fig. 4.1(c) shows the XRD patterns of various $x$LNCZFO+(1-$x$)BSTDO composites. No third phase is observed in the XRD pattern, indicating that there was no chemical reaction between the phases. It is seen that, with increasing ferrite content in the composites, the intensity of the ferrite peaks increases while perovskite peaks decrease. This implies that the intensity of XRD peaks and the number of peaks depend on the concentration of constituent phases in the composites.

Fig. 4.2 demonstrates the Rietveld refined XRD patterns of the studied composites. The presence of constituents (LNCZFO and BSTDO) and the absence of intermediate phases confirm the excellent formation of composites. The Rietveld refinement also confirms the cubic spinel crystal structure with $Fd\bar{3}m$ space group of LNCZFO phase and tetragonal perovskite structure with *P4mm* space group of BSTDO phase [110]. In the figure, the black line and red circle represent the observed and calculated intensity, respectively. Short vertical lines with a red color below the patterns determine the position of the Bragg diffraction and the lower continuous line is the difference between the observed and the calculated intensity. It is evident that there is a good agreement in the observed and calculated XRD patterns that are also verified by the observation of the difference pattern. Parameters including R-factors (R = reliability) and goodness of fit index were analyzed to assess the reliability and fitting quality of experimental data, respectively. The best fit of the experimental diffraction data is obtained since these parameters have attained their lower value and therefore the respective crystal structure is regarded to be satisfactory [33]. There is no significant change in the refined lattice parameters (shown in Table 4.1) of the individual phases in the composites, which indicates that there is no structural change in the individual phases during the formation of the composites. Slight changes in the lattice parameters result from the stress between the two ferroic orders [30]. The values of the lattice parameter obtained from the Rietveld refinement analysis [107]. The cubic ferrite phase consists of $a = 0.8443$ nm, while $a = b = 0.4032$ nm and $c = 0.4035$ nm for the tetragonal perovskite phase of $x = 0.50$ composite. The results obtained are well satisfied with the results reported earlier [22-25, 111-119].
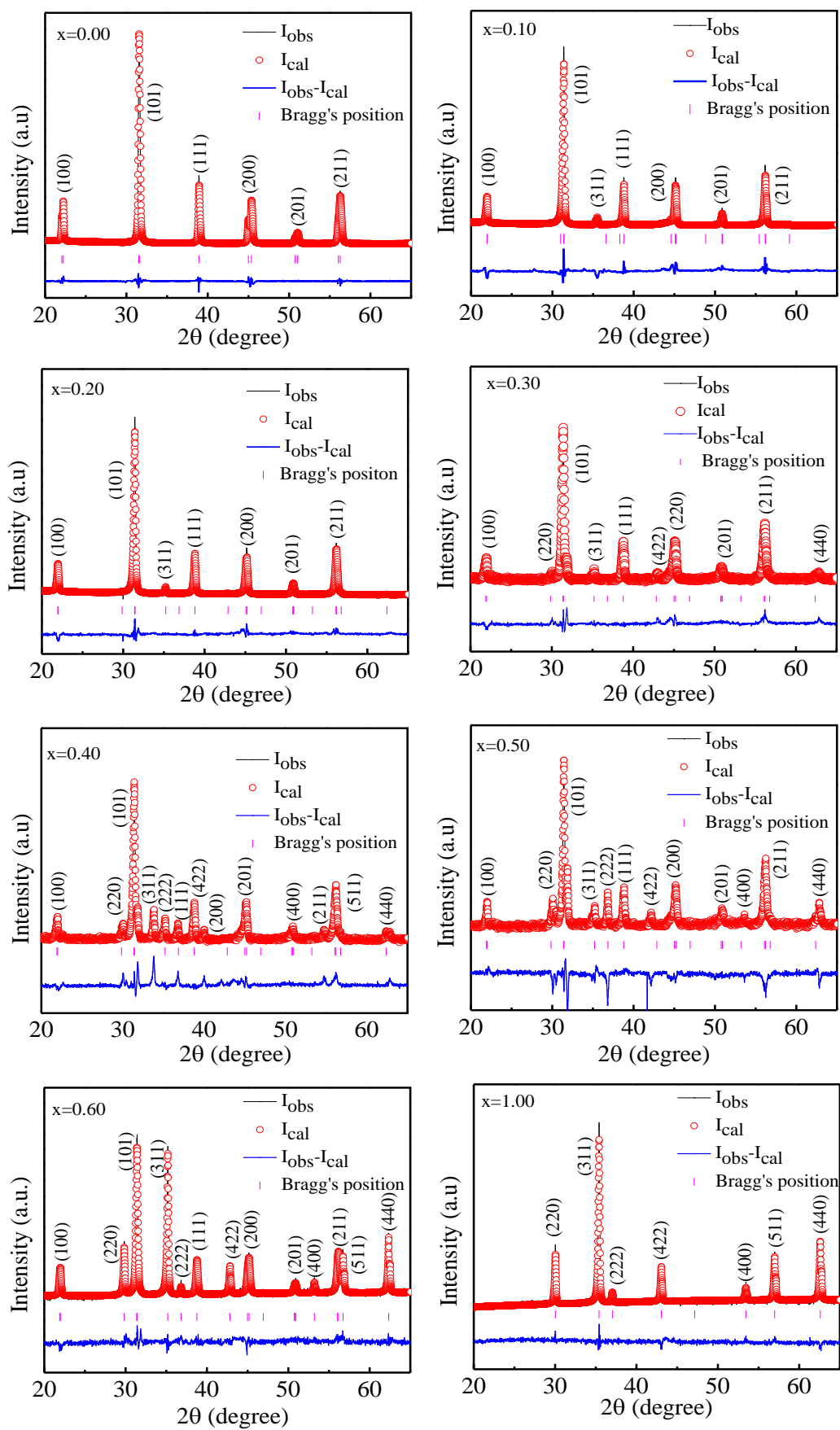
**Fig. 4.2** Rietveld refinement of various of *x*LNCZFO+(1-*x*)BSTDO composites.

**Table 4.1** The space group, lattice parameter, reliability factor ($R$), and goodness of fit (GOF) for various $x$LCNZFO+(1-$x$)BSTDO composites.

| Content ($x$) | Space group | | Lattice parameter (nm) | | | $R$ (%) | | |
|---|---|---|---|---|---|---|---|---|
| | Ferrite | Ferroelectric | Ferrite | Ferroelectric | | $R_e$ | $R_p$ | GOF |
| | | | $a$ | $a$ | $c$ | | | |
| 0.00 | $Fd\bar{3}m$ | $P4mm$ | ------- | 0.4035 | 0.4037 | 4.66 | 4.27 | 1.22 |
| 0.10 | $Fd\bar{3}m$ | $P4mm$ | 0.8377 | 0.4034 | 0.4036 | 5.44 | 8.57 | 1.97 |
| 0.20 | $Fd\bar{3}m$ | $P4mm$ | 0.8384 | 0.4033 | 0.4037 | 5.08 | 6.74 | 1.70 |
| 0.30 | $Fd\bar{3}m$ | $P4mm$ | 0.8382 | 0.4036 | 0.4038 | 4.59 | 6.87 | 1.84 |
| 0.40 | $Fd\bar{3}m$ | $P4mm$ | 0.8385 | 0.4037 | 0.4039 | 4.30 | 5.94 | 1.96 |
| 0.50 | $Fd\bar{3}m$ | $P4mm$ | 0.8379 | 0.4032 | 0.4035 | 4.03 | 6.50 | 1.99 |
| 0.60 | $Fd\bar{3}m$ | $P4mm$ | 0.8388 | 0.4031 | 0.4034 | 3.69 | 3.84 | 1.35 |
| 1.00 | $Fd\bar{3}m$ | $P4mm$ | 0.8443 | ------- | ------- | 2.63 | 2.61 | 1.26 |

Fig. 4.3 demonstrates the variation of $\rho_B$, $\rho_{th,}$ and $P$ as a function of the ferrite content. The $\rho_B$ of the sintered samples was measured using the Archimedes method. The $\rho_B$ initially increases with the ferrite content (for $x = 0.10$) because the small-sized grains of BSTDO fill the intergranular pores of the LNCZFO phase thereby increasing $\rho_B$. Also, the high interaction between the constituent phases for $x = 0.10$ samples confirmed by the $\alpha_{ME}$ is responsible for the higher $\rho_B$. Then $\rho_B$ decreases with an increase in the ferrite content as the molecular weight of the LNCZFO (232.08 amu) is lower than that of the BSTDO (239.58 amu). The $\rho_{th}$ decreases almost linearly according to the sum rule. It also appeared that, for all the composites, the value of $\rho_B$ is lower than the corresponding value of $\rho_{th}$. This can be explained by the influence of pores that might be created and developed throughout the sintering of bulk samples. There are two sources of porosity in ceramic samples: intergranular and intragranular porosity [120, 121]. Thus, total porosity is expressed as,

$$P = P_{inter} + P_{intra.} \tag{4.1}$$

As a result of these intergranular and intragranular pores, $\rho_B$ is smaller than $\rho_{th}$ in the composites.
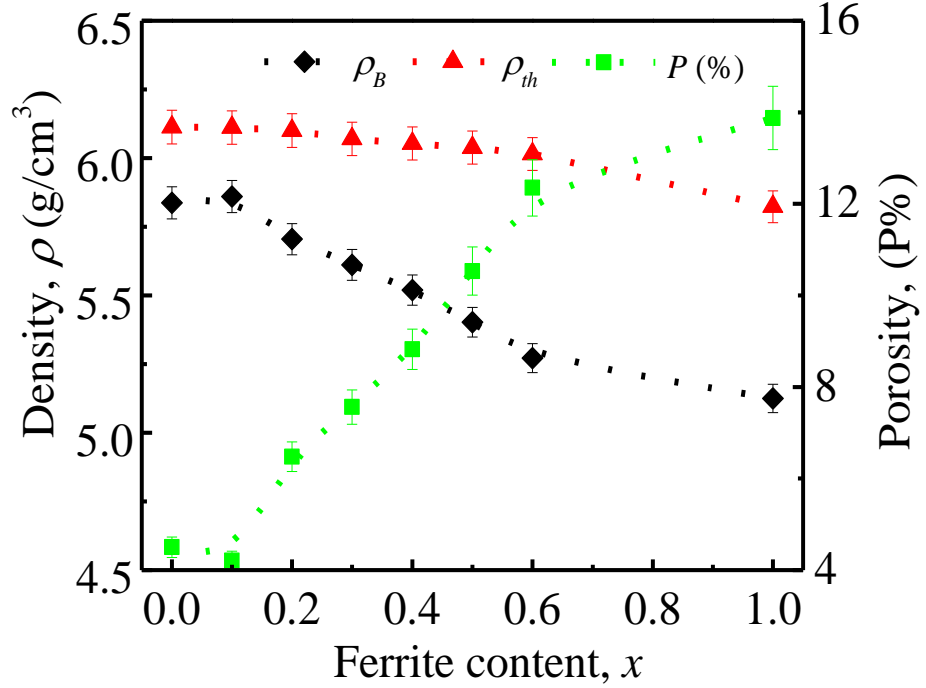


**Fig. 4.3** Variation of $\rho_B$, $\rho_{th,}$ and $P$ as a function of ferrite content of various $x$LNCZFO+(1-$x$)BSTDO composites.

### 4.1.2 Surface morphology and EDS analysis

The microstructure of multiferroic materials plays an important role not only for electrical and magnetic properties but also for ME coupling. The distribution of the grains along with fitted curves as presented in Fig. 3.4 to evaluate the grain sizes of LNCZFO and BSTDO ferroics in the composites. The two ferroic phases can be easily identified from the FESEM images. From FESEM image analysis it was observed that the relatively larger grains are the ferromagnetic phase. The number of these grains increases as the $x$ value increases. It is observed from the micrographs that the multiferroic composites have a fine crystalline structure. Micrographs show the inhomogeneous grain size due to the different growth rates of the individual phases in the composites. The average grain diameter ($\overline{D}$) of the compositions, calculated by fitting the data based on the Gaussian distribution function. With the increase of LNCZFO ferrite in composites, the $\overline{D}$ increased due to a higher $\overline{D}$ of LNCZFO than BSTDO. The reduction of stress due to an increase in porosity with an

increase in the ferrite phase in the composite also may be responsible for this increase in $\bar{D}$ with the ferrite phase.
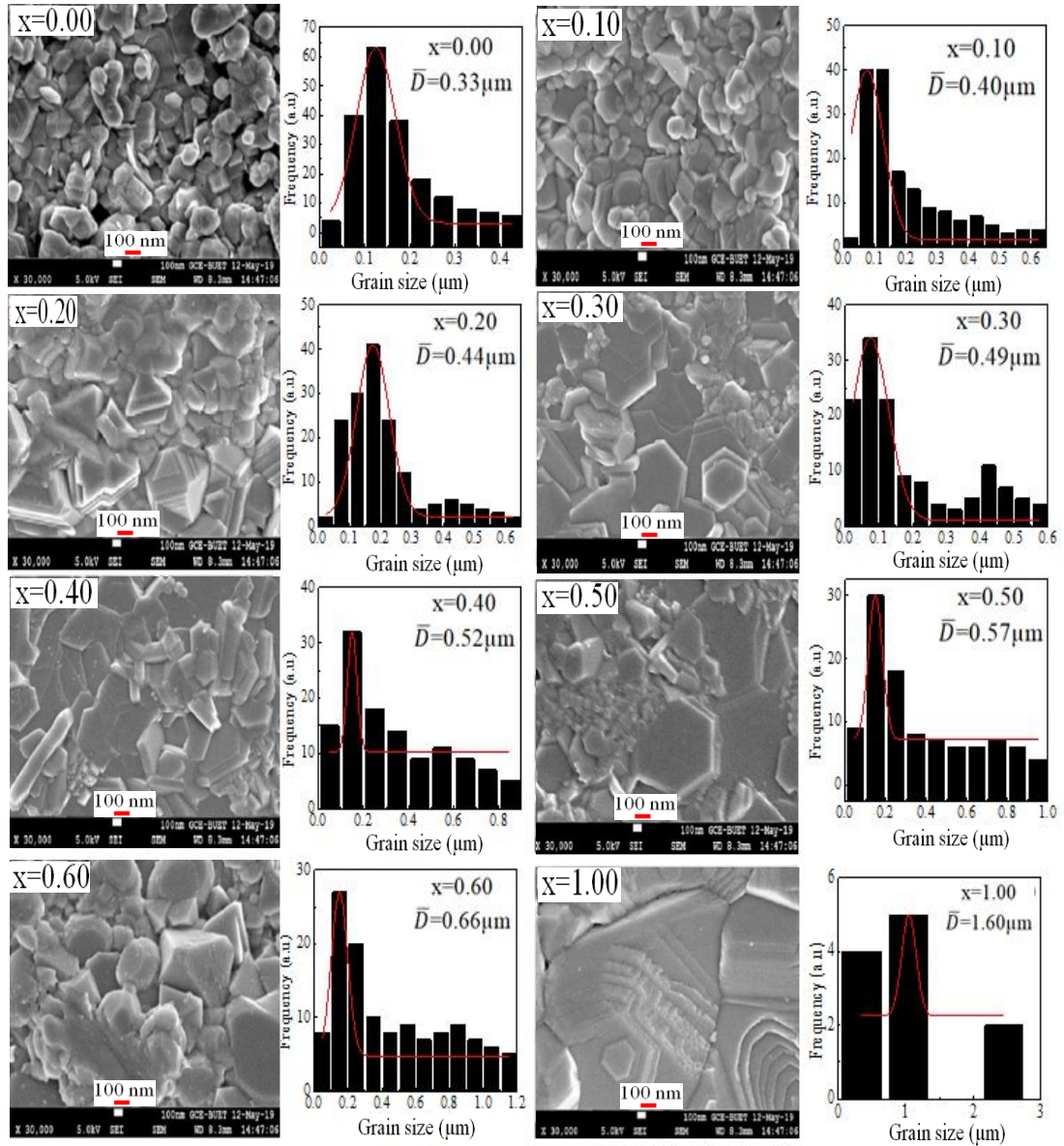


**Fig. 4.4** FESEM images along with grain distribution histogram of various $x$LNCZFO+(1-$x$)BSTDO composites.

To evaluate the chemical composition of different $x$LNCZFO+(1-$x$)BSTDO composites, EDS spectra are recorded from FESEM as depicted in Fig. 4.5. The EDS spectrum shows that the proportion of the elements in the constituent phases is well compatible with the nominal composition of the composite phases, except for

oxygen. This is because the oxygen deficiency can be created during the high sintering temperature.
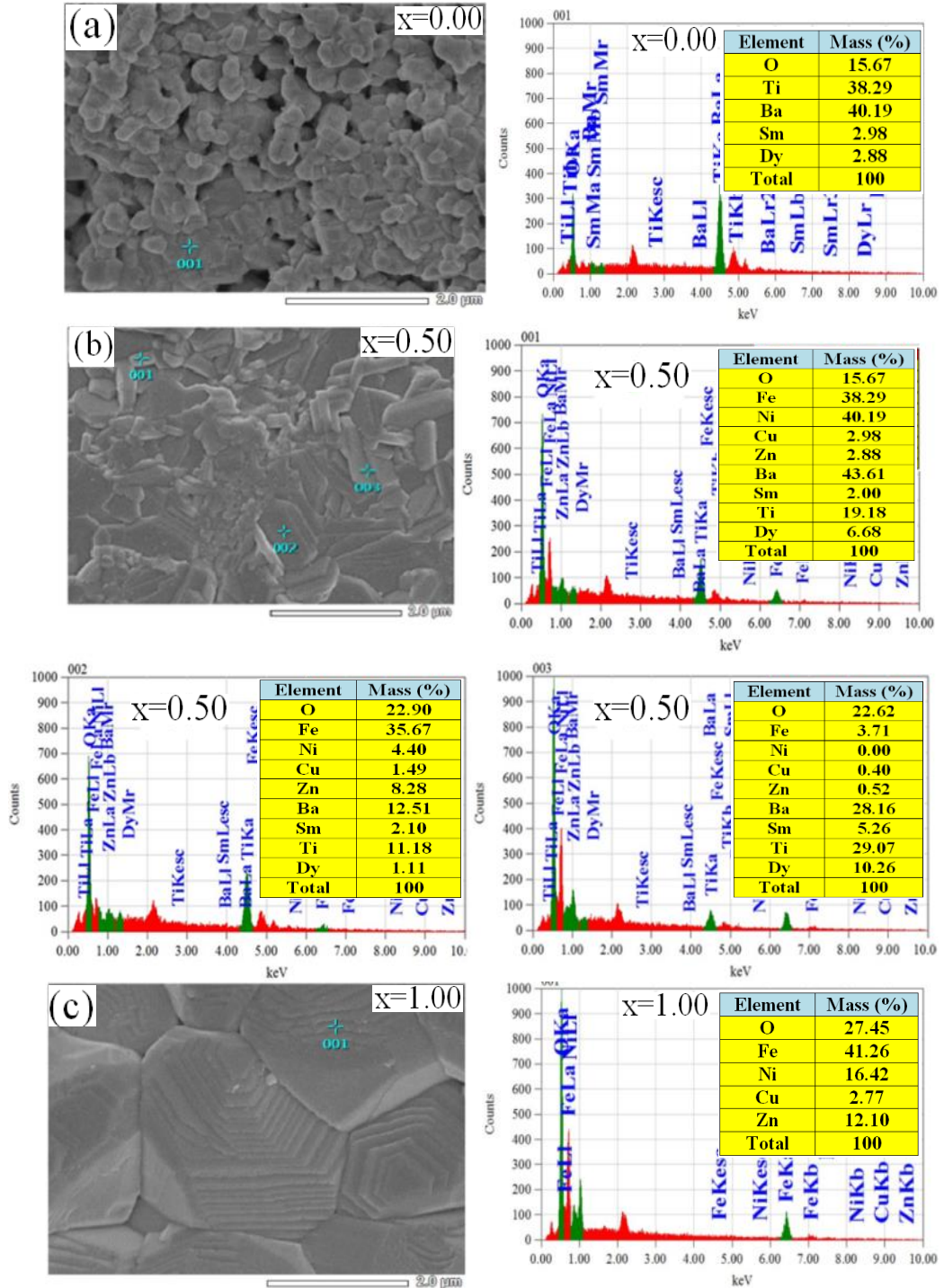


**Fig. 4.5** FESEM image and EDS spectrum of (a) $x = 0.00$, (b) $x = 0.50$, and (c) $x = 1.00$ samples of $x$LNCZFO+(1-$x$)BSTDO composites.

## 4.1.3 Initial permeability
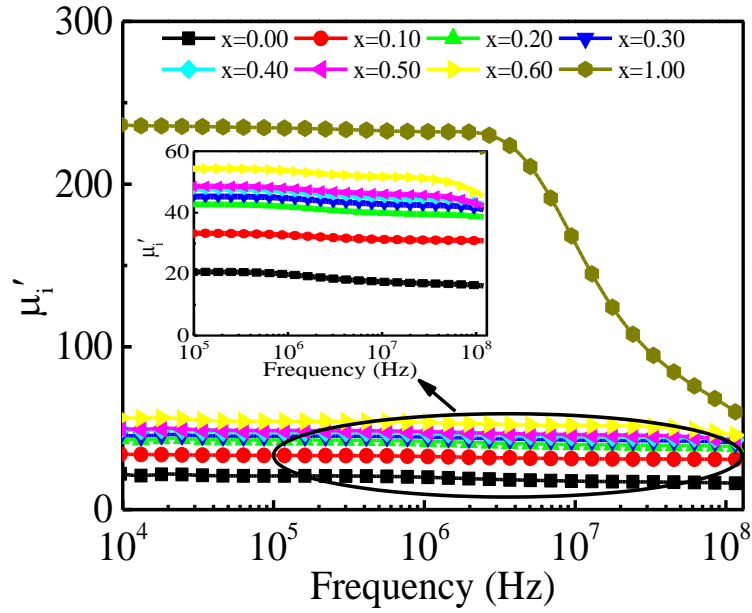


**Fig. 4.6** Variation of $\mu_i{}'$ as a function of frequency for various $x$LNCZFO+(1-$x$)BSTDO composites.

Information on the mechanism behind the magnetic properties of the composites and their capability in high-frequency applications is reflected by the value of $\mu_i{}'$. Fig. 4.6 demonstrates the variation of $\mu_i{}'$ with frequency for different $x$LNCZFO+ (1-$x$)BSTDO composites between 10 kHz and 120 MHz. The value of $\mu_i{}'$ increases with increasing LNCZFO phase in the composites because of high magnetic LNCZFO, while BSTDO exhibits weak ferromagnetic or antiferromagnetic behavior. For $x$ = 1.00, the value of $\mu_i{}'$ is very high compared to the other samples. The $\mu_i{}'$ of a polycrystalline ferrite is related to two separate processes of magnetization: (i) domain wall motion and (ii) spin rotation [122, 123], which is expressed as follows:

$$\mu_i^{'} = 1 + \chi_w + \chi_{spin} \tag{4.2}$$

where $\chi_w$ and $\chi_{spin}$ represent the domain wall motion and the spin rotation susceptibility of the material, respectively. The $\chi_w$ and $\chi_{spin}$ can be written as:

$$\chi_w = \frac{3\pi M_s^2 \overline{D}}{4\gamma} \tag{4.3}$$

$$\chi_{spin} = \frac{2\pi M_s^2}{K} \tag{4.4}$$

50

where $M_s$ is the saturation magnetization, $K$ is the anisotropy constant, and $\gamma$ is the domain wall energy. Therefore, it is seen that the motion of the domain wall is influenced by the $\overline{D}$ and strengthened with the increase of $\overline{D}$. In the case of normal grain growth, the relationship between $\mu_i'$ and $\overline{D}$ is directly proportional. Besides, from the $M$-$H$ hysteresis loop, it is also evident that the magnetization is very large for $x = 1.00$ sample. The $\mu_i'$ is directly proportional to the magnetization. The $\overline{D}$ and magnetization of $x = 1.00$ sample is greater than the other composites. As a result, the sample with $x = 1.00$ is much different from the rest. With an increase of frequency, the value of $\mu_i'$ remains almost constant for all composites up to $f_r$ and then decreases. The reason for the decrease of $\mu_i'$ beyond $f_r$ is the origination of pinning points from intragranular pores and impurities at a higher-frequency on the surface of the sample. These pining points obstruct the spin rotation and the motions of domain walls as a result reduce their contribution to $\mu_i'$ [124]. High $\mu_i'$ and high $f_r$ are mutually incompatible, according to Snoek's relation ($f_r\mu_i' = $ constant) [125]. Therefore, as LNCZFO increases in composites, $f_r$ decreases. No $f_r$ was found for $x = 0.00$ and $x = 0.10$ samples in the observed frequency range (inset of Fig. 4.6) as the $f_r$ occurs beyond this range. The increase of $\mu_i'$ with an increase of the LNCZFO content is expected as per the sum rule of the composite. The values of $\mu_i'$ are presented in Table 4.2.
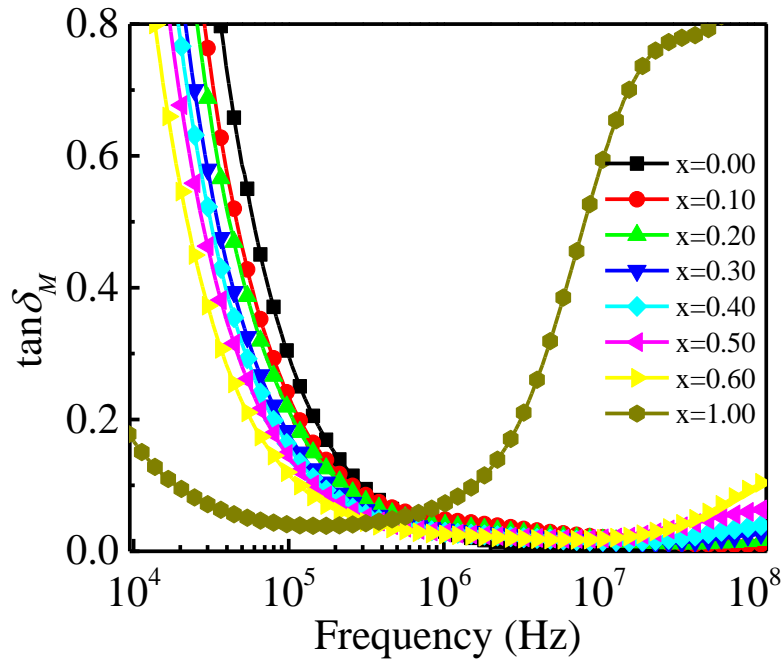


**Fig. 4.7** Variation of tan$\delta_M$ as a function of frequency for various
$x$LNCZFO+(1-$x$)BSTDO composites.

Fig. 4.7 demonstrates frequency variation of $\tan\delta_M$ for various $x$LNCZFO+ $(1-x)$BSTDO composites. The $\tan\delta_M$ arises by the latency of domain wall motion with applied ac field is ascribed to various defects, including domain wall bowing, non-uniform and non-repetitive domain wall motion, and domain wall annihilation [126]. It is extremely desirable from the implementation point of perspective to have this loss as small as possible. At the lower frequency region (up to $10^5$ Hz) the $\tan\delta_M$ decreases with the increase of ferrite phase due to the increase of $Q$ factor which is inversely proportional to the $\tan\delta_M$. The $\tan\delta_M$ of the composites at high-frequency (beyond $10^6$ Hz) is quite low. This is because of the insulating layers originating from BSTDO enveloping the LNCZFO particles, which significantly increase the resistivity of the material causing a reduction in the eddy current loss [127]. At higher frequency region, the $\tan\delta_M$ again increases due to the random motion of the domain wall which unable to follow the magnetic field. Moreover, at the higher frequency region, $\tan\delta_M$ also increases with increasing ferrite content due to the decrease of the $Q$ factor.
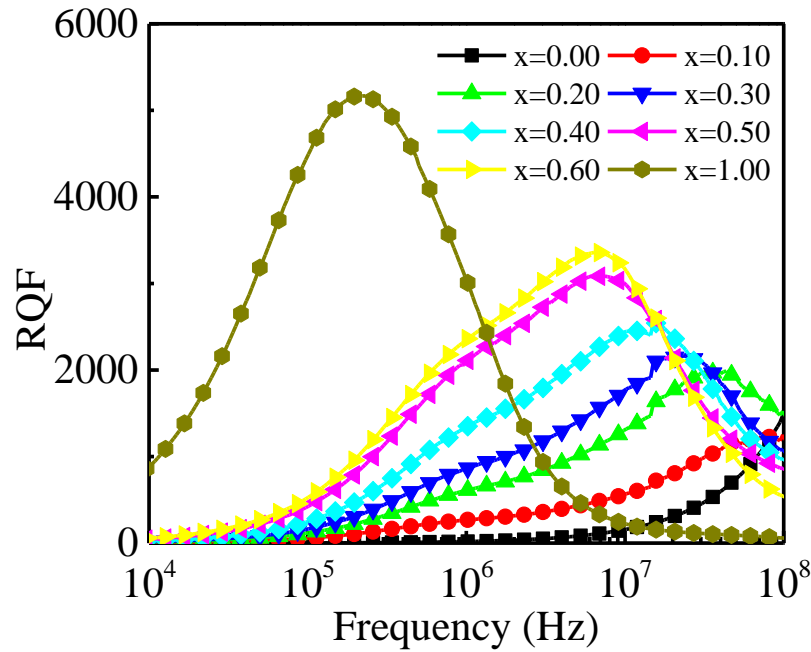


**Fig. 4.8** Variation of RQF as a function of frequency for various
$x$LNCZFO+$(1-x)$BSTDO composites.

The variation of the RQF as a function of the frequency is demonstrated in Fig. 4.8. The RQF is used as a performance indicator for practical applications. The RQF increases with the increase of ferrite content due to the increase of $\mu_i{'}$ which is

directly proportional to the RQF. The RQF increases with an increase in frequency up to a certain value and then decreases with the formation of a peak. RQF peaks shift towards the lower frequency region with the increase of ferrite content indicating the lowering of tan$\delta_M$. For LNCZFO, the peak is sharper but broadened by increasing the ferroelectric phase in the composite, increasing the frequency utility range.

**Table 4.2** The $\rho_{th}$, $\rho_B$, $P$, $\overline{D}$ and $\mu_i'$ (at 100 kHz) for various $x$LCNZFO+(1-$x$)BSTDO composites.

| Content ($x$) | $P_{th}$ (g/cm$^3$) | $\rho_B$ (g/cm$^3$) | $P$ (%) | $\overline{D}$ (μm) | $\mu_i'$ at 100 kHz |
|---|---|---|---|---|---|
| 0.00 | 6.12 | 5.83 | 5 | 0.34 | 25 |
| 0.10 | 6.11 | 5.86 | 4 | 0.40 | 38 |
| 0.20 | 6.10 | 5.72 | 7 | 0.44 | 43 |
| 0.30 | 6.07 | 5.61 | 8 | 0.49 | 45 |
| 0.40 | 6.05 | 5.52 | 9 | 0.52 | 48 |
| 0.50 | 6.04 | 5.41 | 11 | 0.57 | 49 |
| 0.60 | 6.02 | 5.28 | 12 | 0.66 | 54 |
| 1.00 | 5.82 | 5.13 | 14 | 1.60 | 231 |

### 4.1.4 Magnetic hysteresis

Magnetic hysteresis analysis is a significant factor for assessing the potential use of magnetic materials. Variation of magnetization with the applied magnetic field for different $x$LNCZFO+(1-$x$)BSTDO composites are presented in Fig. 4.9. The figure represents that the *M-H* loops are quite narrow for all samples. The magnetization of all samples significantly increases with an increase of the applied magnetic field up to 0.1 T. Magnetization above 0.1 T increases slowly and then obtained a saturation nature. The applied magnetic field above 0.2 T the *M-H* loops exhibit an independent nature, i.e. the magnetization of all samples reaches its saturation value. The $M_s$ of the samples enhances with an increase of the ferrite phase in the composites due to

the higher $\mu_i'$ of ferrite phase which is directly proportional to the $M_s$. Increased magnetization values with an increasing LNCZFO contributes to more ferrite grains than ferroelectric phase grains that also enhance the magnetic moment of the composite sample [128, 129]. The LNCZFO phase has higher $M_s$ because of the stimulation of migration of $Fe^{3+}$ into B-site as nonmagnetic $Zn^{2+}$ prefers to go to A-site. Such migration of $Fe^{3+}$ to B-site raises the magnetic moment of the B-site, leading to enhance A-B interaction. Enhanced A-B interaction causes an increase in net magnetization ($M_s = M_B - M_A$). The BSTDO exhibits a weak ferromagnetic behavior with a small magnitude of $M_r$ of 0.182 emu/g and incorporation of LNCZO and BSTDO into composite contributes to an enhancement of magnetization due to the interfacial strain leads to change the orientation of the spins [103]. The magnitude of $M_s$ for all samples is measured by the extrapolation of the magnetization curve to $H = 0$. The minimum $M_s$ of 2.420 emu/g is found for $x = 0.00$ sample. The $M_s$ enhances with an increase in ferrite content and reached a maximum value of ~80 emu/g for $x = 1.00$ sample. The composites comprise a large magnitude of reduced ($M_r/M_s$) magnetization relative to the parent LNCZFO phase. This reduced magnetization is also referred to as the hysteresis loop squareness. The estimated range of these values is 0.094-0.026, which is appropriate for use in memory devices [130].
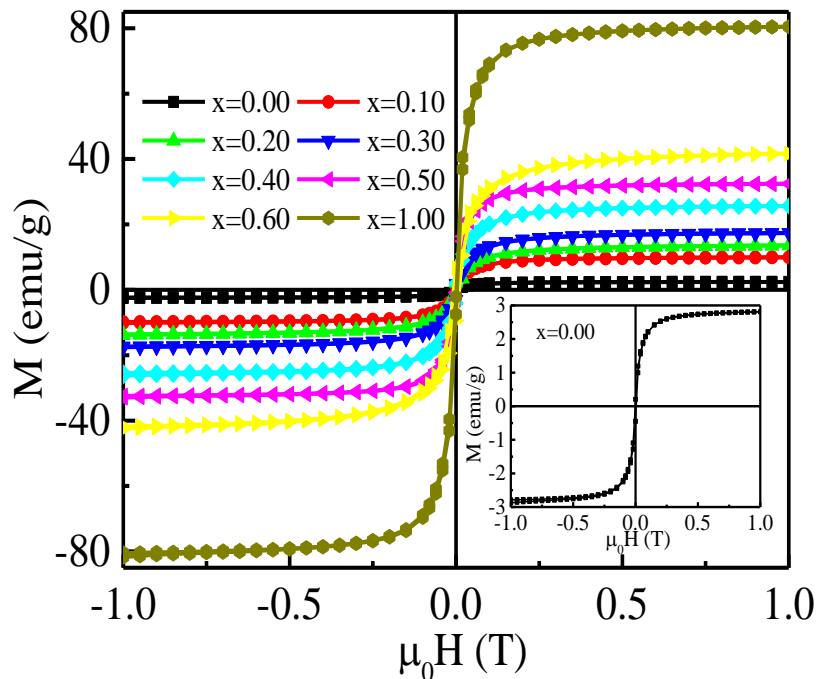


**Fig. 4.9** M-H hysteresis loops of various $x$LNCZFO+(1-$x$)BSTDO composites.

**Table 4.3** Measured magnetic parameters of $x$LNCZFO+(1-$x$)BSTDO composites.

| Content, $x$ | $M_s$ (emu/g) | $M_r$ (emu/g) | $H_c$ (T) |
|:---:|:---:|:---:|:---:|
| 0.00 | 2.43 | 0.33 | 0.0031 |
| 0.10 | 7.03 | 0.99 | 0.0032 |
| 0.20 | 11.63 | 2.59 | 0.0069 |
| 0.30 | 14.92 | 2.42 | 0.0075 |
| 0.40 | 22.80 | 2.94 | 0.0042 |
| 0.50 | 28.06 | 1.75 | 0.0034 |
| 0.60 | 32.66 | 6.71 | 0.0071 |
| 1.00 | 79.67 | 4.38 | 0.0034 |

### 4.1.5 Dielectric property

The $\varepsilon'$ signifies the efficiency of the dielectric material to store the electrical energy. Fig. 4.10 demonstrates the variation of $\varepsilon'$ with frequency. It is observed that $\varepsilon'$ decreases with the increase of frequency. Afterward, it remains almost constant for all composites. This low-frequency dielectric dispersion results, because at low-frequency all types of polarization (interfacial, dipolar, ionic, and electronic) are present in the samples [131]. However, on increasing frequency, some of the polarizations gradually disappear (except electronic and ionic) resulting in a rapid drop of $\varepsilon'$. It could be also happened due to the electric dipoles do not get enough time to line up and therefore cannot follow the rapid variation of the applied alternating electric field. In the lower frequency, the large value of $\varepsilon'$ also results from the interfacial polarization suggested by Maxwell-Wagner [132-134]. Interfacial polarization originates from the inhomogeneity of the sample arising from grain structure, impurity, interfacial defects, and porosity. This inhomogeneity is generated in the sample during the process of high-temperature calcination and sintering. The $\varepsilon'$ increases with increasing the ferrite content for some of the composites owing to the enlarged $\overline{D}$ of the samples. The grain boundary area decreases as $\overline{D}$ increases. The increase in interfacial polarization also resulted from the heterogeneity of composites [135, 136]. These heterogeneities are the interfaces between the ferrite and ferroelectric phases, where the conductivity and permittivity of the constituent phases are different. This gives rise to an interfacial polarization

and contributes to $\varepsilon'$ [137]. As a result of the presence of ferrite with large $\overline{D}$ and heterogeneity in the composites, $\varepsilon'$ was increased. In the present study, an enhanced $\varepsilon'$ was observed for $\overline{D}$ between 0.521-0.658 μm and a decreasing trend of $\varepsilon'$ was observed for other values of $\overline{D}$. These results agree with the earlier reports [138, 139]. The value of $\varepsilon'$, however, is decreased with an increase in the ferrite phase at a higher frequency for the reason that $\varepsilon'$ is smaller for LNCZFO compared to BSTDO.
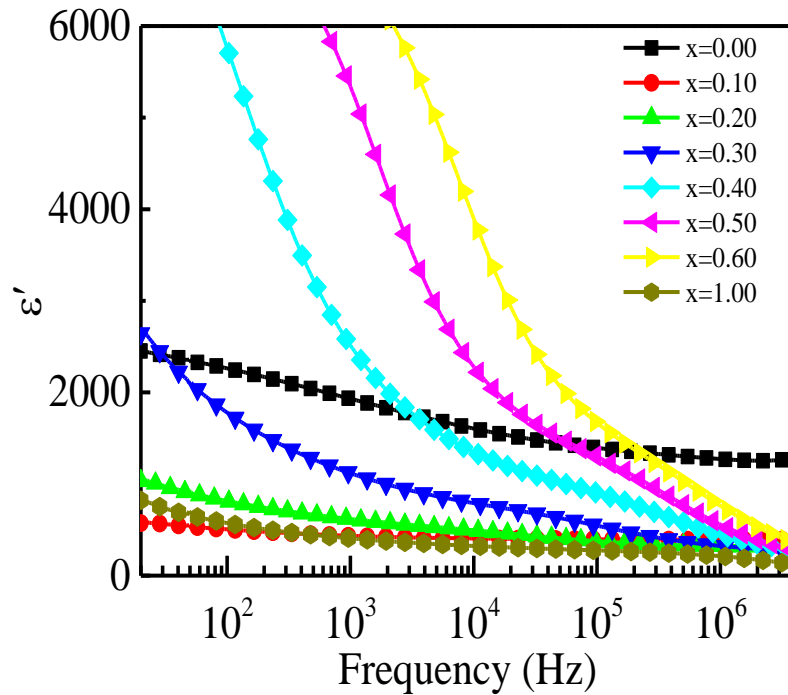


**Fig. 4.10** Variation of $\varepsilon'$ as a function of frequency for various $x$LNCZFO+(1-$x$)BSTDO composites.

The $\tan\delta_E$ is the dissipation of electrical energy in the form of heat energy. Fig. 4.11 reveals the variation of $\tan\delta_E$ as a function of frequency. This $\tan\delta_E$ is attributed to the resonance of the domain wall [51]. Frequency dispersion $\tan\delta_E$ occurs in both ends of the relaxation peak. It is observed that the composites exhibit the loss peaks according to the Debye relaxation theory. Such resonance loss peaks arise when the hopping frequency of the electrons between the different ionic states, becomes almost equal to the frequency of the applied field. That is when the condition $\omega\tau = 1$ is satisfied [33]. Similar behavior is also reported in earlier studies [140, 141]. Samples with $x$ = 0.40-0.60 show a double relaxation loss peak. The samples were prepared with a mixture of two ferroic phases of different electrical properties. In a

polycrystalline material, both grain and grain boundaries can be prominent. It is evident from the Nyquist plot of these samples that both grain and grain boundary effects exist. This double loss peak is originated from the grain and grain boundary contribution. The loss peak at the lower frequency area is for grain boundary contribution and the higher frequency is for grain contribution. The value of $\tan\delta_E$ increases with the increase of ferrite content due to the increase of the mobility of the charge carrier.
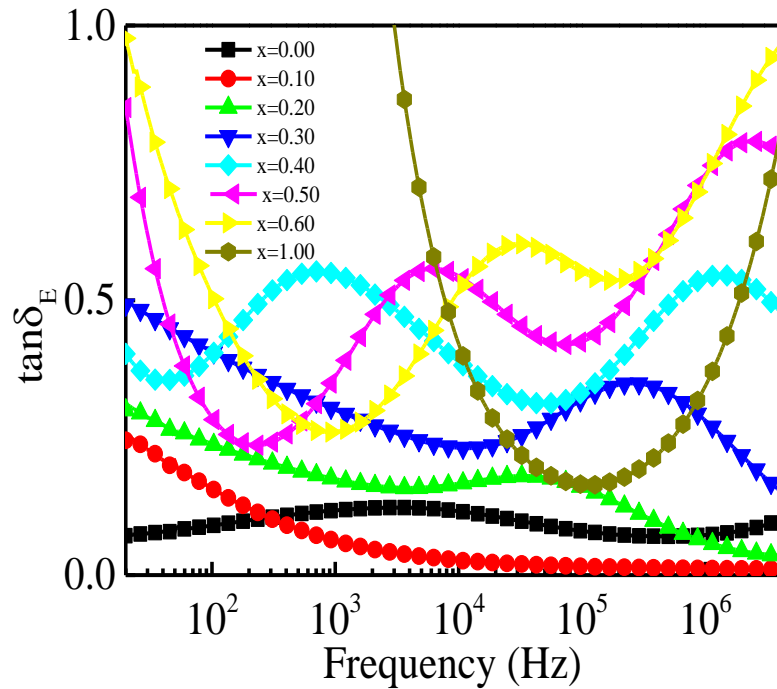


**Fig. 4.11** Variation of $\tan\delta_E$ as a function of frequency for various $x$LNCZFO+(1-$x$)BSTDO composites.

Fig. 4.12(a) demonstrates the temperature-dependent $\varepsilon'$ measured at a frequency of 100 kHz. A dielectric peak at around 132ºC is observed for the case of untainted BSTDO ceramics. The peak observed at about 194ºC might be the structural transition of the ferromagnetic phase. Different factors including structural transitions, the ME effect, or transitory interaction among oxygen ion vacancies and the $Fe^{3+}$ as well as $Fe^{2+}$ ions at the interface of polycrystalline materials can result in temperature-dependent dielectric peaks [142-144]. Fig. 4.12(b) shows the shifting of dielectric peaks to higher temperatures with increasing the ferrite phase in the composites due to the heterogeneity, defects, and strain produce between the constituent phases [145-147]. This can also be for the different $T_C$ of the constituent

phases. The shifting of the peak position implies the ME interaction between the constituent phases [148-150]. The broadening of the dielectric peak for some samples reveals the existence of diffuse phase transition.
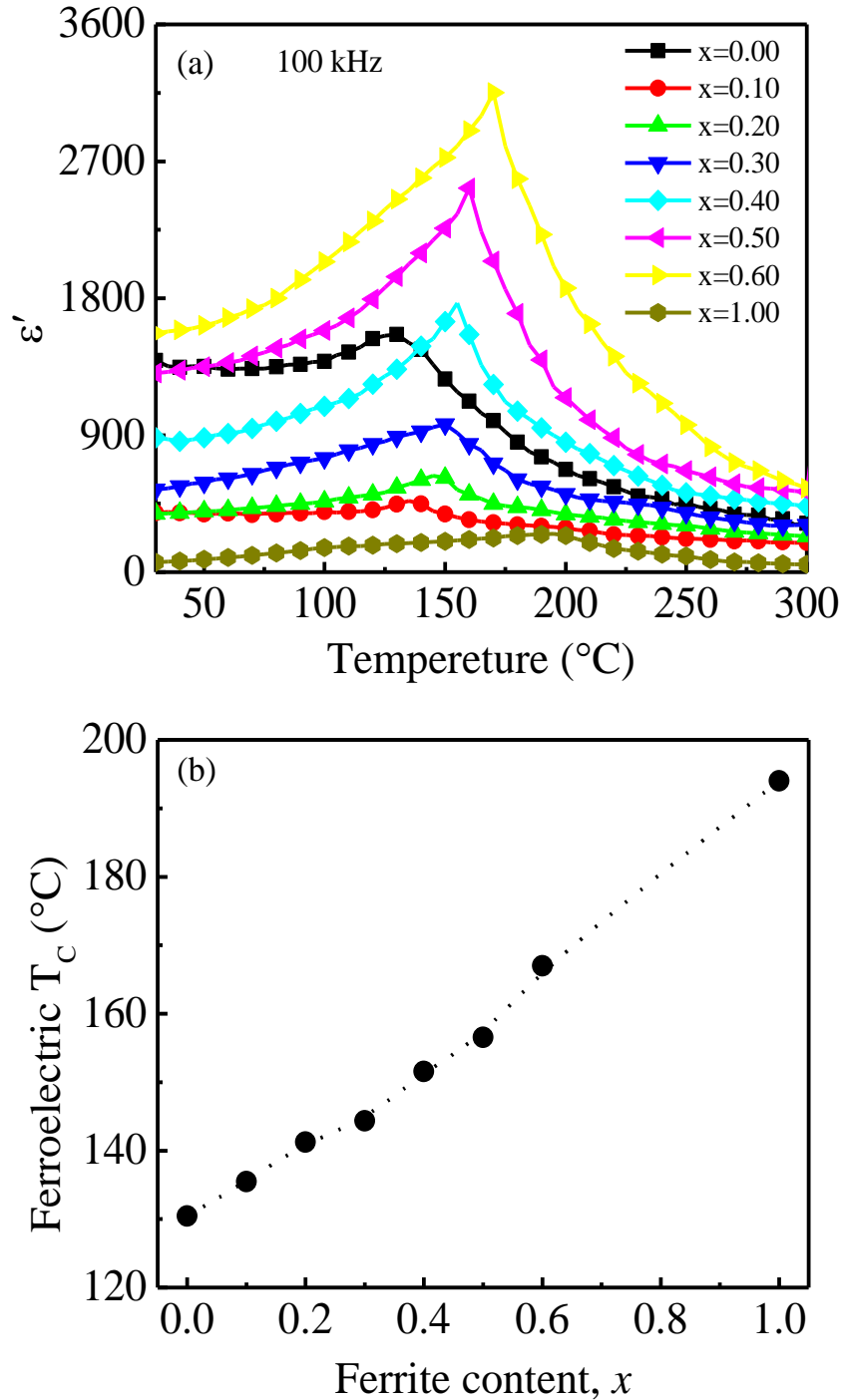


**Fig. 4.12** Variation of (a) $\varepsilon'$ as a function of temperature for various $x$LNCZFO+ $(1-x)$BSTDO composites at 100 kHz frequency, and (b) $T_C$ with ferrite content.

**4.1.6 Complex impedance spectra analysis**
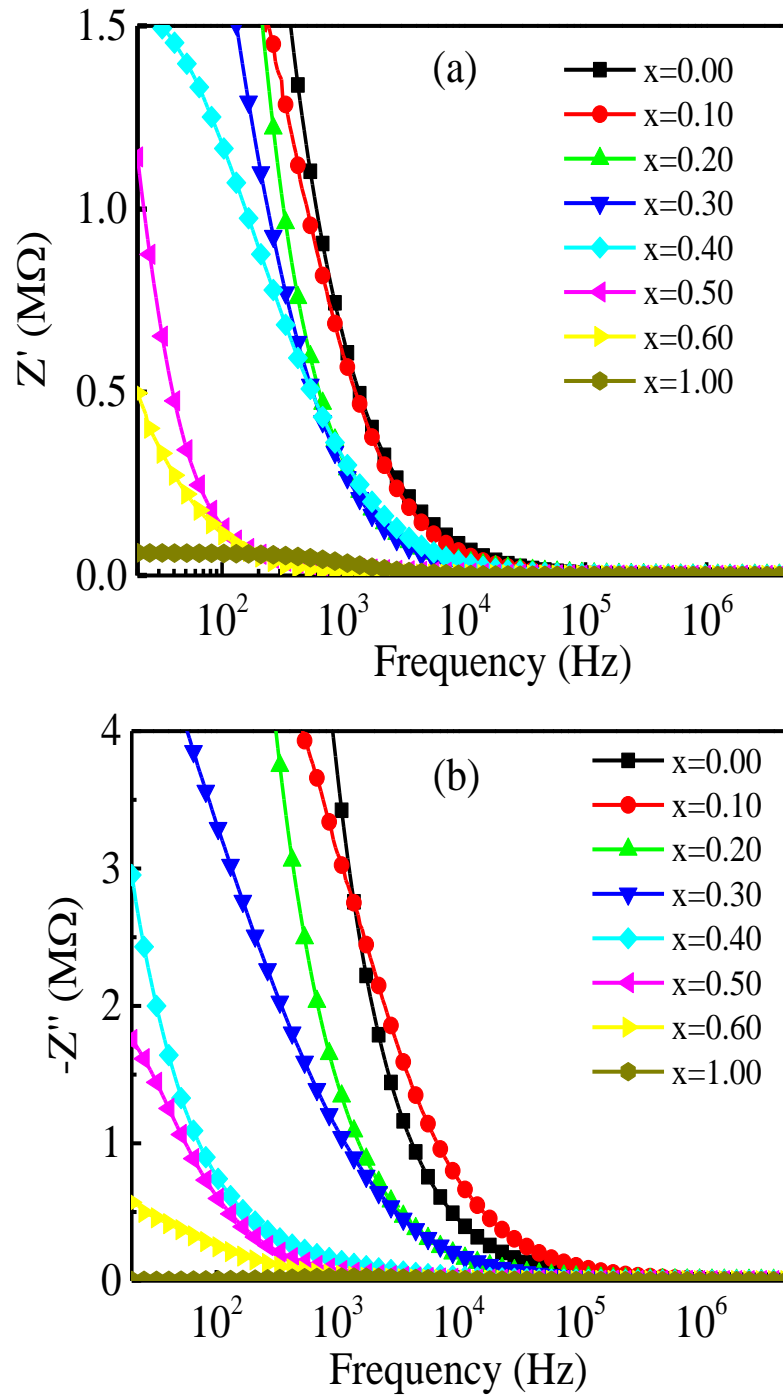


**Fig. 4.13** Frequency dependent variation of (a) $Z'$, and (b) $Z''$ for various $x$LNCZFO+ $(1-x)$BSTDO composites.

Frequency-dependent $Z'$ is shown in Fig. 4.13(a). The graphical representation shows that the magnitude of $Z'$ gradually decreases with an increase of frequency up to a certain value (10 kHz) which confirms the increase of conductivity in the composite.

At lower frequencies (up to $10^4$ Hz), the higher value of $Z'$ indicates that relaxors have larger polarization since all types of polarization exist in this region. In the lower frequency region, the $Z'$ decreases with the increase of ferrite content due to the lower resistive property of the ferrite phase. The plateau-like behavior of $Z'$ at higher frequencies indicates the possible release of space charge polarization at the boundaries of homogeneous phases in composites under the applied external field [151-153]. The merger behavior of $Z'$ at a higher frequency region (above $10^4$ Hz) is due to the reduction of the impedance of the sample. This is due to the capacitive reactance is inversely proportional to the frequency which contributes to the total impedance. The obtained results are well compatible with PZT+NZFO and CZFMO+PCT composites [154, 155]. Fig. 4.13(b) shows the identical variation of $Z''$ with frequency as that of $Z'$. The absence of the relaxation phase resulted from the static relaxation of the electron in the composites.

Fig. 4.14(a) shows the frequency-dependent $M'$ which is inversely proportional to $\varepsilon'$. In the low-frequency region (up to $10^3$ Hz), the value of $M'$ is quite low, indicating the presence of the polaron hopping and the relatively small influence of the electrode impact [156-158]. After a certain frequency, the value of $M'$ increases, because of the inability of some dipoles to follow the alternating electric field at higher frequencies. Therefore, $M'$ significantly increases with frequency for all samples. Fig. 4.14(b) demonstrates the frequency response $M''$. The $M''$ peak is obtained in different frequency regions for different composites due to the different relaxation times. The region below the peak frequency defines the range of motion of the charge carriers over long distances, i.e. between the grains. Beyond the peak frequency, the charge carrier moves within short distances, i.e. within the grains [159]. The region where the peak occurs indicates a shift from long to short-distance mobility of charge carriers. At both ends of the maxima, asymmetrical peak broadening is observed. Asymmetric peak broadening indicates that relaxation times are distributed at different time constants [160].
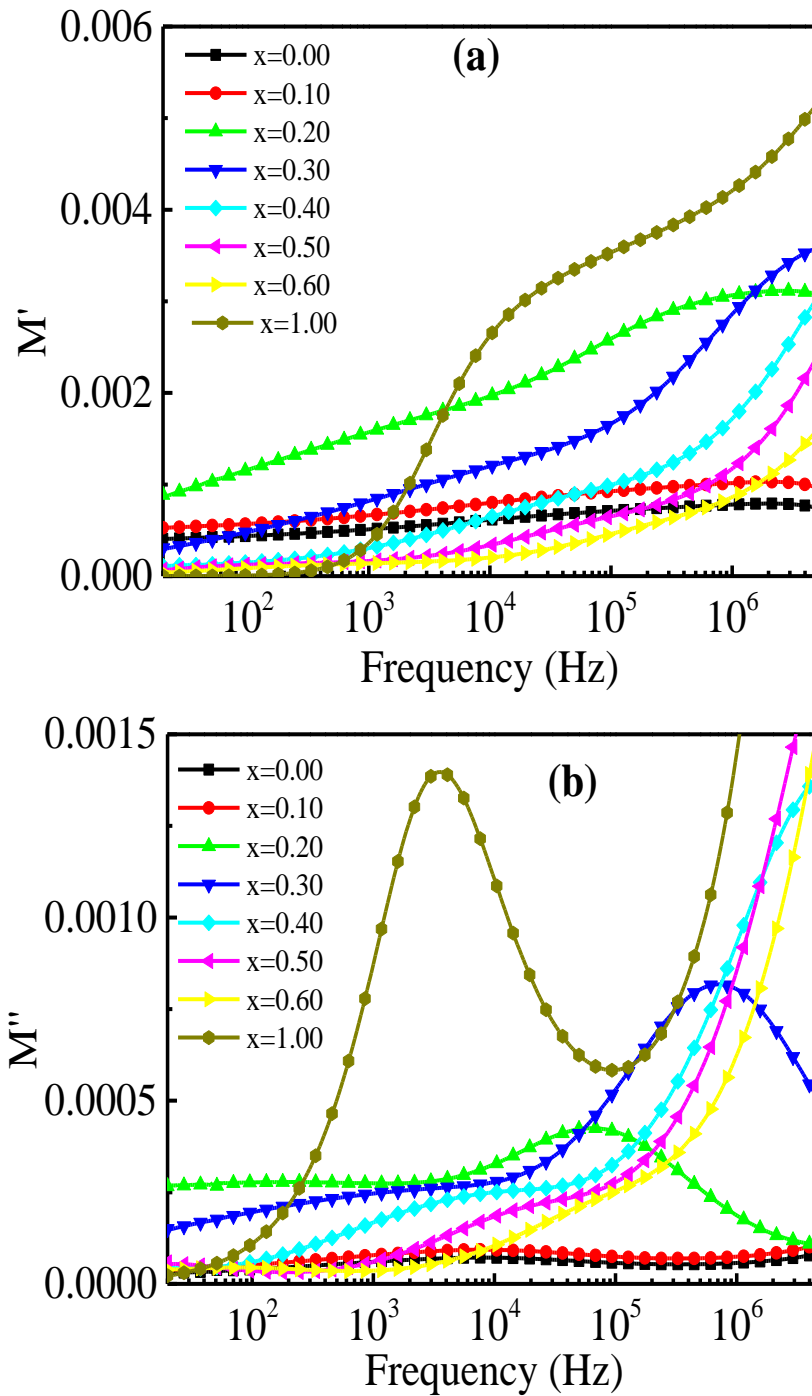
**Fig. 4.14** Electric modulus spectra of various $x$LNCZFO+(1-$x$)BSTDO composites: (a) for real part ($M'$), and (b) for imaginary part ($M''$).

Polycrystalline relaxors consisting of grains and grain boundaries can be modeled by an equivalent circuit according to the brick-layer model [161] consisting of three parallel RC circuits connected in series (Fig. 4.15.a). Each RC element of the equivalent circuit contributes a semicircle to the $Z'$ versus $Z''$ graph. The first semicircle indicates grain effects and the second semicircle indicates the presence of

grain boundary effects. If a third semicircle is present, it indicates the electrode effects.
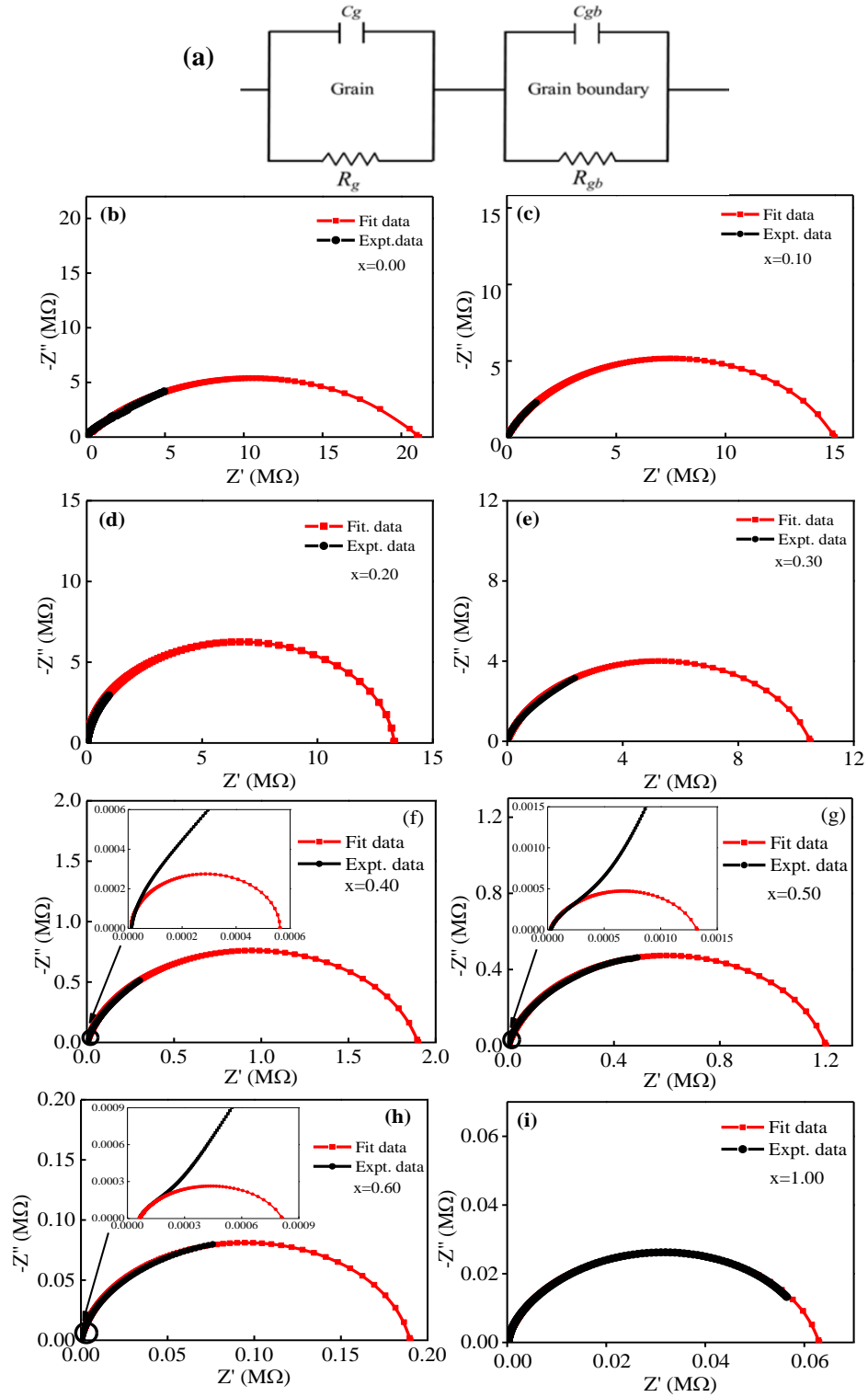


**Fig. 4.15** (a) Equivalent circuit model, and (b)-(i) Nyquist plot of various *x*LNCZFO+(1-*x*)BSTDO composites.

Fig. 4.15(b-i) demonstrates the Nyquist plot of different composites. In the impedance spectra, composites with $x = 0.00$, $0.10$, $0.20$, $0.30$, and $1.00$ have a single semicircular arc. This suggests that the materials have only a grain boundary effect on the conduction process [162]. The impedance spectra of composites $x = 0.40$, $0.50$, and $0.60$ consists of double semicircular arcs. In higher frequencies, these composites exhibit an asymmetrical semicircular arc that is caused by the superposition of semicircular arcs of the constituent phases. This may result from a slight difference in relaxation time for grains in the constituent phases. The equivalent circuit consists of two sub-circuits connected in series as shown in Fig. 4.15(a) can be used to describe this activity. The response of $R_g C_g$ and $R_{gb} C_{gb}$ corresponds to the high and low-frequency semicircular arcs, respectively. Here, $R_g$ and $R_{gb}$ are the grain and grain boundary resistance, $C_g$ and $C_{gb}$ are the grain and grain boundary capacitance, respectively. According to the equivalent circuit, impedance can be evaluated as follows:

$$Z^* = R_g - \frac{1}{i\omega c_g} + R_{gb} - \frac{1}{i\omega c_{gb}} \qquad (4.5)$$

Non-Debye-type relaxation is found in the studied composites because each composite exhibits a depressed/distorted semicircle. A perfect semicircle with its center at $Z'$-axis is observed for an ideal Debye-type relaxation [163]. The figure displays that with the increase of ferrite content the grain boundary resistance decreases. This may be ascribed to the less resistivity of the ferrite phase.

### 4.1.7 The ac conductivity

In material science, conductivity is an important topic. Electrical conductivity shows significant electrical features and is therefore essential to clarify its mechanism. Fig. 4.16 demonstrates the frequency-dependent variation of $\sigma_{ac}$. The frequency-dependent $\sigma_{ac}$ spectrum shows two different regions. The conductivity in the lower-frequency region is almost independent of the frequency referred to as dc conductivity ($\sigma_{dc}$), where the resistive grain boundaries are more active for dielectrics according to the Maxwell-Wagner double layer model [133, 164]. At the high-frequency region (above $10^4$ Hz), known as the hopping region, $\sigma_{ac}$ is increasing very rapidly and the transport phenomenon continues with hopping carriers resulting from the constituent elements. Conductive grains become more prominent at higher frequencies, thus increasing the hopping charge carrier and contributing to increased

conductivity. Hopping of 3d electrons between $Fe^{2+}$ and $Fe^{3+}$ as well as $Ni^{2+}$ and $Ni^{3+}$ could play a significant role in the conductivity system. The frequency-dependent $\sigma_{ac}$ can be written according to Jonscher's power law [165]:

$$\sigma_{ac}(\omega) = \sigma_{dc} + B\omega^n, \tag{4.6}$$

where $\sigma_{ac}(\omega)$ is the resultant conductivity, $B$ is the pre-exponential factor, $n$ is the frequency exponent. The exponent $n$ shows the degree to which the moving ions interact with the surrounding lattice. Both $n$ and $B$ depend on materials and temperature. The $n$ parameter specifies whereas the conduction is dependent on the frequency ($0 < n < 1$) or independent of the frequency ($n = 0$). The independent nature of $\sigma_{ac}$ at a lower frequency (up to $10^2$ Hz) and increasing trend at a higher frequency, indicating the shift of an ion from long-range hopping to short-range ion motion and thereby confirms the establishment of conductivity relaxation. The variation of $\sigma_{ac}$ can easily be explained by the polaron hopping mechanism proposed by Austin and Mott as a function of frequency [166]. In the small polaron model, $\sigma_{ac}$ increases with increasing the frequency, while the $\sigma_{ac}$ decreases with increasing the frequency in the large polaron hopping mechanism [167].
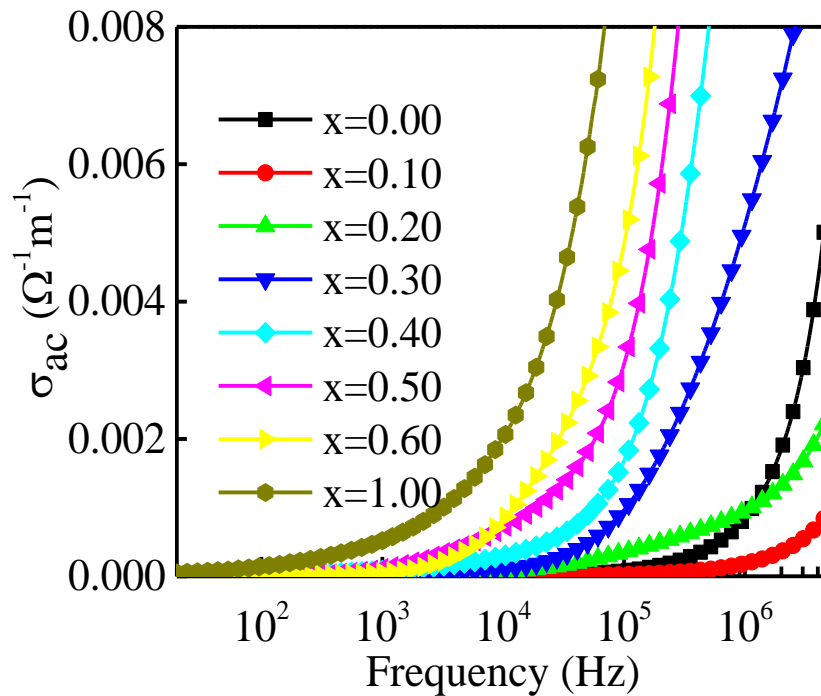


**Fig. 4.16** Frequency dependence of $\sigma_{ac}$ for various $x$LNCZFO+(1-$x$)BSTDO composites.
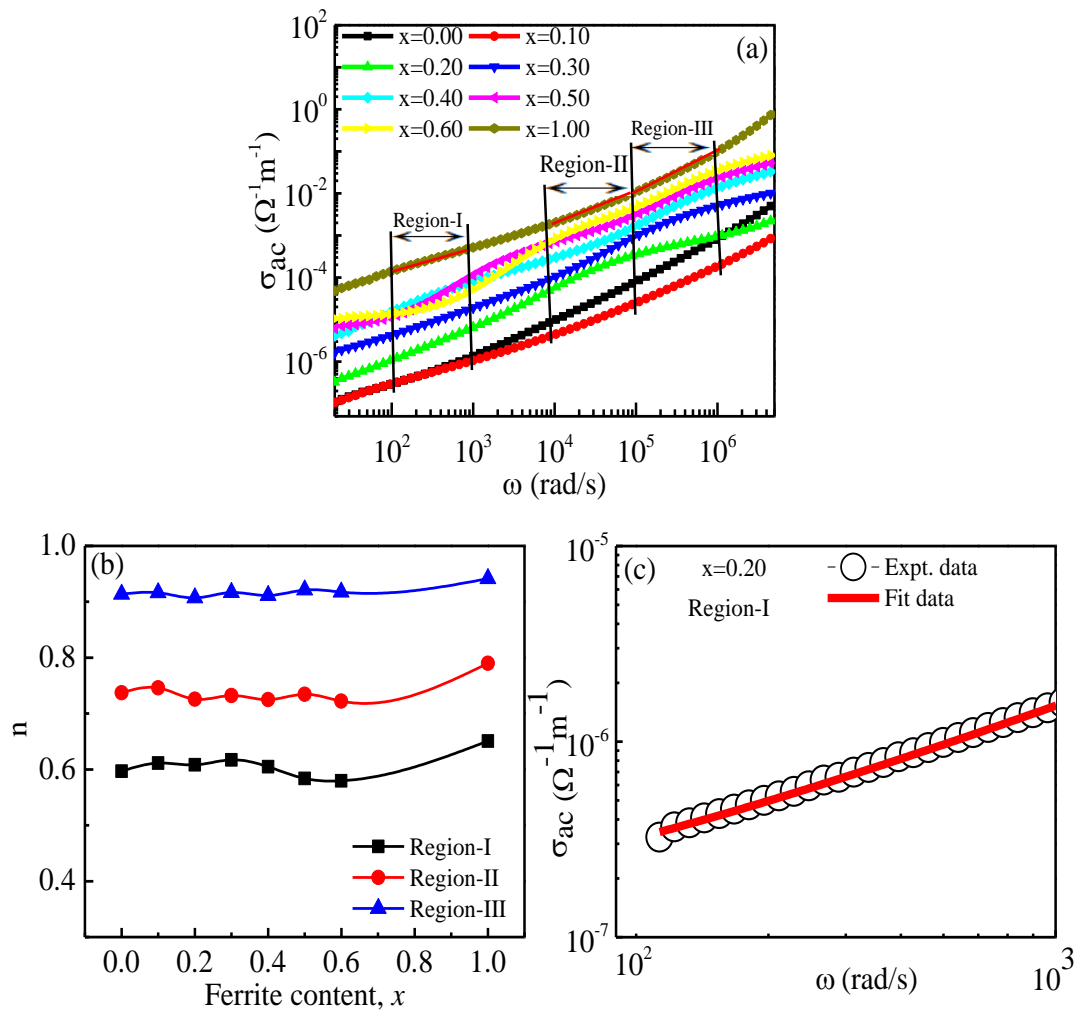
**Fig. 4.17** Variation of (a) $\sigma_{ac}$ with $\omega$, (b) $n$ with ferrite content, and (c) $\sigma_{ac}$ fitting according to the Jonschers power law for $x = 0.20$ sample in region-I.

Fig. 4.17(a) shows the variation of $\sigma_{ac}$ as a function of $\omega$. The $\sigma_{ac}$ increases almost linearly with increasing $\omega$, indicating the conduction process in the composites is caused by a small polaron hopping mechanism [168]. Fig. 4.17(b) demonstrates the variation of $n$ with the ferrite content. There are three different regions of $\sigma_{ac}$ were selected (in Fig. 4.17.a) and the value of $n$ is determined by the fitting of Jonscher power law for different frequency regions. Fig. 4.17(c) shows the fitting diagram of $\sigma_{ac}$ by the Jonschers power law for $x = 0.20$ composite in region-I. The value of $n$ in the region I ($10^2$-$10^3$ Hz) is found to be between 0.58-0.65. Moreover, the value of $n$ in region II ($10^4$-$10^5$ Hz) is in-between 0.72-0.79, and region III ($10^5$-$10^6$ Hz) is in-between 0.91-0.94. This result satisfied Jonscher's power law and the conduction is due to the small polaron hopping mechanism. The magnitude of $n$

increases with an increasing frequency indicating that the increase of mobility of charge carrier over a long distance to a short distance. The variation of $\sigma_{ac}$ with $\omega$ should be linear as per Jonscher's law. However, mixed polarons (small/large) conductions are responsible for the slight deviation of some composites from linearity [169, 170].

**4.1.8 Ferroelectric hysteresis**

The *P-E* curves were evaluated to assess the ferroelectric nature of the composites as shown in Fig. 4.18. In the figure, samples up to $x = 0.20$ show typical ferroelectric nature, indicating that the samples are polarized spontaneously. The maximum saturation polarization (0.39 $\mu C/cm^2$) is found for $x = 0.20$ among these samples. The remnant polarization of these samples is found to be between the ranges of 0.035-0.204 $\mu C/cm^2$, which is quite small. This may be the smallest $\bar{D}$ of the BSTDO phase [171]. The ferroelectric behavior of the composites gradually weakens with an increase in ferrite content as the LNCZFO provides a relatively lower electrical resistance than BSTDO perovskite. The *P-E* loops of the composites with $x = 0.50$ and 0.60 are almost rounded and the ferrite phase ($x = 1.00$) illustrates an almost rectangular loop, suggesting a very lossy and lower resistive sample from which nothing could be obtained from the intrinsic ferroelectricity. High leakage current, inappropriate electrode and barium volatilization may also be the possible reason for this. Similar behavior has been reported earlier [172]. The ferroelectric coercive field is minimum for $x = 0.10$ composite, which implies that the composite may easily be polarized under the appropriate electric field.
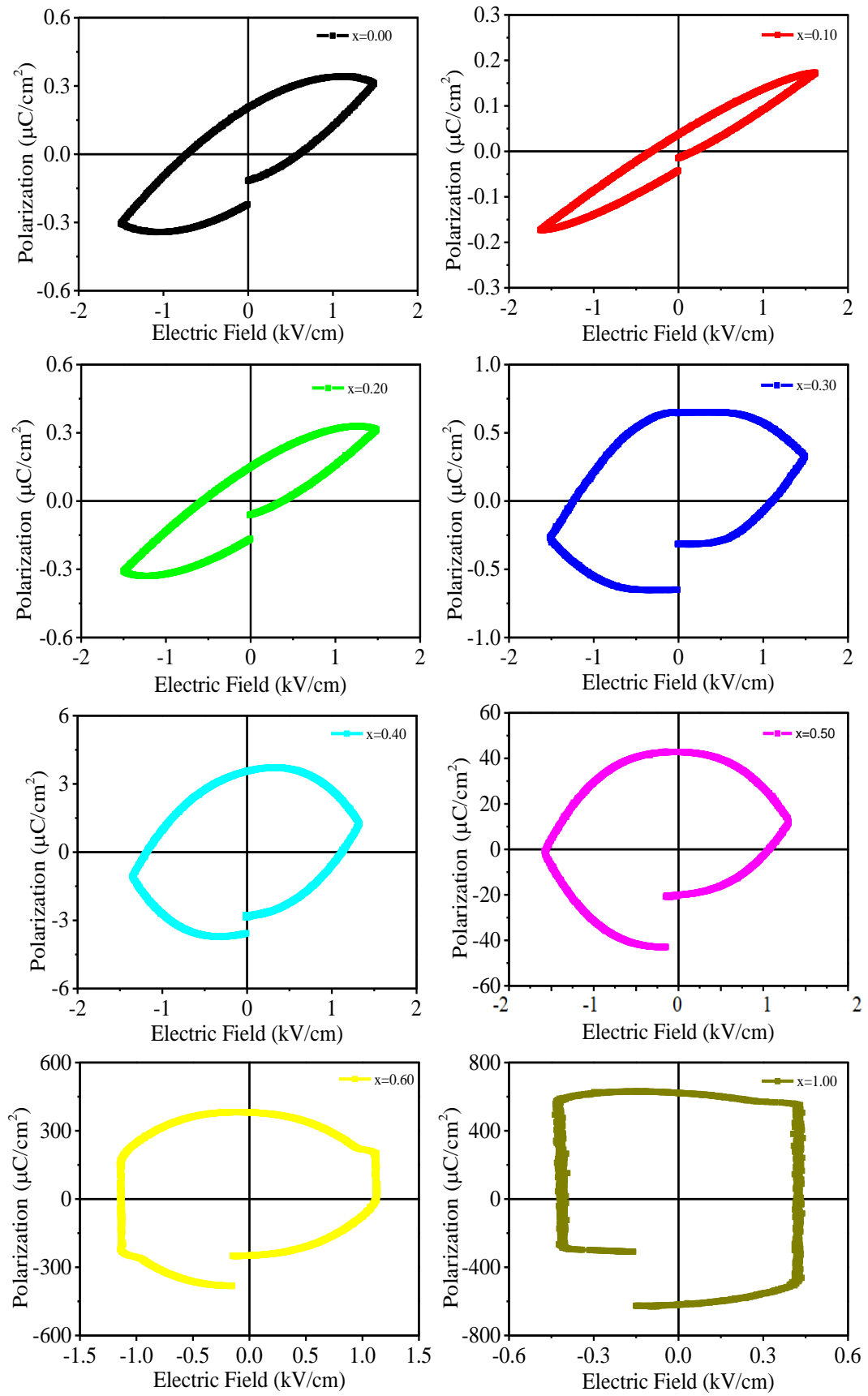
**Fig. 4.18** *P–E* loops of *x*LNCZFO+(1-*x*)BSTDO composites.

### 4.1.9 Magnetoelectric voltage coefficient
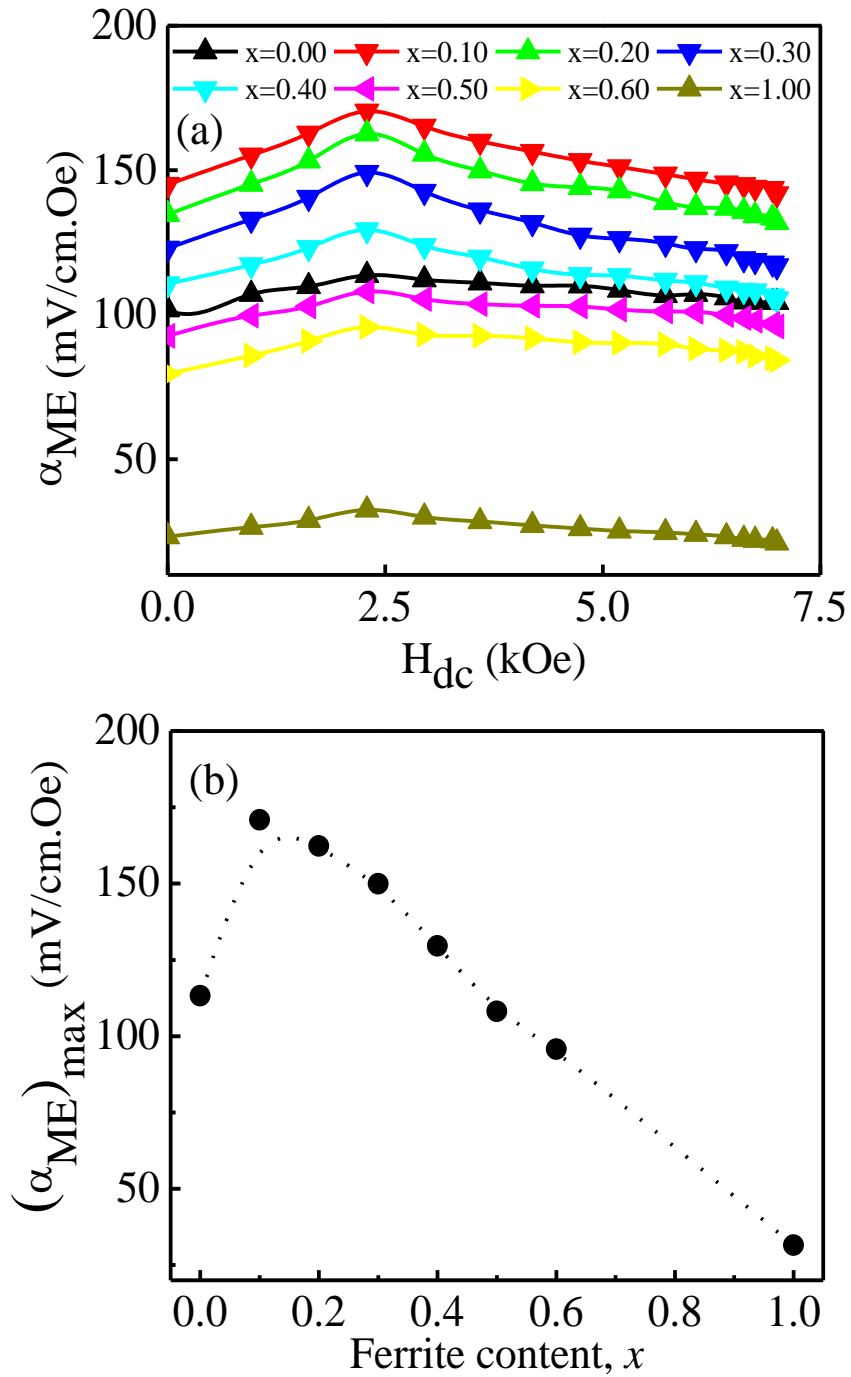


**Fig. 4.19** Variation of (a) $\alpha_{ME}$ with dc magnetic field for various $x$LNCZFO+ $(1-x)$BSTDO composites, and (b) maximum $\alpha_{ME}$ with the ferrite content.

The strain-mediated ME coupling effect in composites with constituent phases depends on the weight proportion of the component phases, the magnetization, polarization, and electrical resistivity of the ferroic phases [173]. The ME effect in

multiferroic materials arises from the interaction of the magnetic and ferroelectric domains. The applied magnetic field induces a large strain in the magnetic domains of the samples, which distort the ferroelectric domains. As a result, charges are induced in the grains. These charges would help to develop more voltage in the grain, which in turn produces a strong ME coupling. The variation of $\alpha_{ME}$ for the composites as a function of the applied dc magnetic field is demonstrated in Fig. 4.19(a). The value of $\alpha_{ME}$ is found to increase with the applied dc magnetic field due to the increase of magnetostriction in the ferromagnetic phase. At a certain value of the applied dc magnetic field, the $\alpha_{ME}$ obtained its maximum value because of obtaining the saturation state of the ferromagnetic phase. The $\alpha_{ME}$ gradually decreases after reaching the maximum value. The decrease in $\alpha_{ME}$ with the increase in the dc magnetic field is explainable by the fact that after reaching the saturation state ferromagnetic phase provides a constant voltage to the ferroelectric phase. As a result with increasing voltage after reaching saturation state causes lowering the voltage magnetic field ratio which reduces the value of $\alpha_{ME}$ [174]. The variation of maximum $\alpha_{ME}$ with ferrite content is shown in Fig. 4.19(b). The plot reveals that the maximum $\alpha_{ME}$ decreases with large grain ferrite content, which is responsible for a significant decrease in composite resistivity. The ME response of the composites depends on the piezoelectricity of the ferroelectric phase and the magnetostriction of the ferrite phase. Smaller grains are more effective in producing both piezomagnetic and piezoelectric coefficients than larger grains [175]. Moreover, to obtain a better ME effect in composites, two individual phases should be in equilibrium, and a mismatch between grains should not be present. Leakage charges are developed through the path of low resistive ferrite grain surrounding the ferroelectric grains. These leakage charges reduce the piezoelectric effect of the ferroelectric phase, which is one of the causes of the $\alpha_{ME}$ decrease. The increasing porosity with the increase of the ferrite phase is another possible reason for less ME coupling between the two phases in the composite. The increase in porosity results in a decrease in the net magnetization of the samples, which has a significant effect on the coupling interaction between the two phases. The maximum value of $\alpha_{ME}$ (170 mV/cmOe) is found for the $x = 0.10$ composite. Sample with $x = 0.10$ shows the maximum $\alpha_{ME}$ due to the well-connected grains, high density, low porosity, and high

resistivity. The results of the presented composites are relatively higher than previously reported results by other researchers [176-178].

## 4.1.10 Summary of $x$LNCZFO+(1-$x$)BSTDO Composites

Various $x$LNCZFO+(1-$x$)BSTDO multiferroic composites were synthesized and investigated the structural, morphological, magnetic properties, dielectric properties, electric modulus, conductivity, impedance spectroscopy, ferroelectric property, and ME voltage coefficient. The Rietveld refinement analysis of XRD patterns confirms the existence of both constituent phases without any third phase. The density decreases and $\bar{D}$ increases with the increase of the ferrite phase. The $\mu_i'$ and RQF increases with the enhancement of LNCZFO in the composite due to the increase of magnetic grains. The $M_s$ of the composites enhances with increasing ferrite content and obtained a maximum value of ~80 emu/g for $x = 1.00$ sample. Some composites show a higher $\varepsilon'$ than the constituent phases due to the space charge polarization results from a heterogeneity of the composites. The shift of temperature-dependent $\varepsilon'$ peak position has confirmed the ME interaction between the ferroic phases. The modulus and the $\sigma_{ac}$ of the composites reveal a polaron hopping conductivity. The linearity of $\sigma_{ac}$ versus $\omega$ graphs implies that the conductivity is due to the small polaron hopping mechanism and satisfied Joncher's power law. The non-Debye type relaxation occurs for all the composites that each composite has a distorted semicircle in the $Z'$ versus $Z''$ graph. Initially, the ferroelectric property increases with the increase of the ferrite content up to $x = 0.20$ then decreased due to the increase of low resistive and high porous ferrite phase. The $x = 0.10$ composite shows the highest $\alpha_{ME}$ of 170 mV/cmOe. The results obtained from the present study could be used to manufacture potential multifunctional devices for technological use and to explore the new family of composites.

## 4.2 Characterization of *x*LNCZFO+(1-*x*)BGTDO composites

### 4.2.1 Structural characterization, density, and porosity
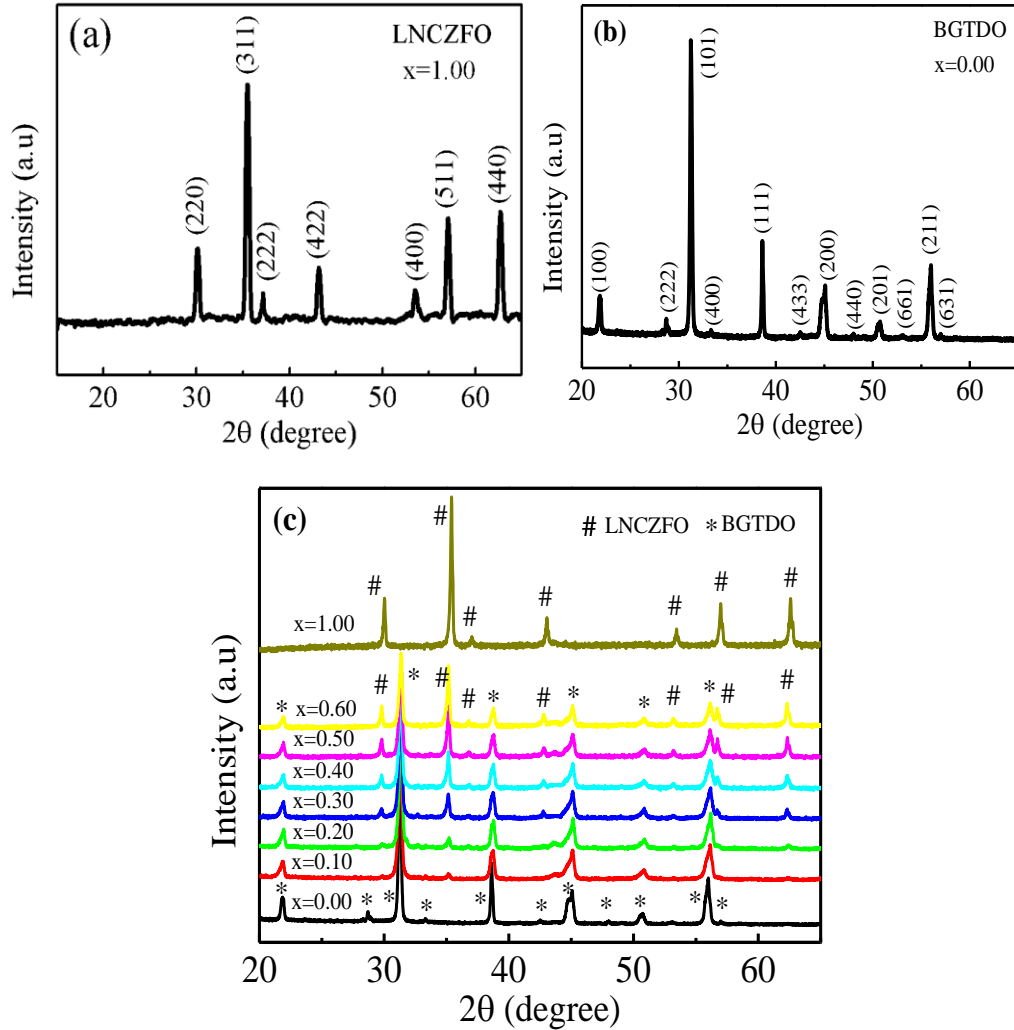


**Fig. 4.20** XRD patterns of (a) LNCZFO, (b) BGTDO, and (c) various
*x*LNCZFO+(1-*x*)BGTDO composites.

Fig. 4.20 illustrates the typical XRD patterns of LNCZFO, BGTDO, and different
*x*LNCZFO+(1-*x*)BGTDO composites. The XRD peaks were indexed with equivalent
Miller indices. No reflections except those relating to a cubic structure of the ferrite
material and tetragonal structure of the ferroelectric material were detected,
indicating that there were no chemical reactions between the two ferroics in the final
sintering stage [49, 54]. No non-indexed peaks correlated with the initial raw
materials were found that can attribute to the production of impurity. The existence
of both phases in the composite with no third phase confirmed the excellence of the

71

fabrication of composite material. When the ferrite phase increases, the ferrite peaks become more intense, while the perovskite peaks become less intense. The number and intensity of peaks in the XRD patterns depend on the number of ferroic orders in the composites.
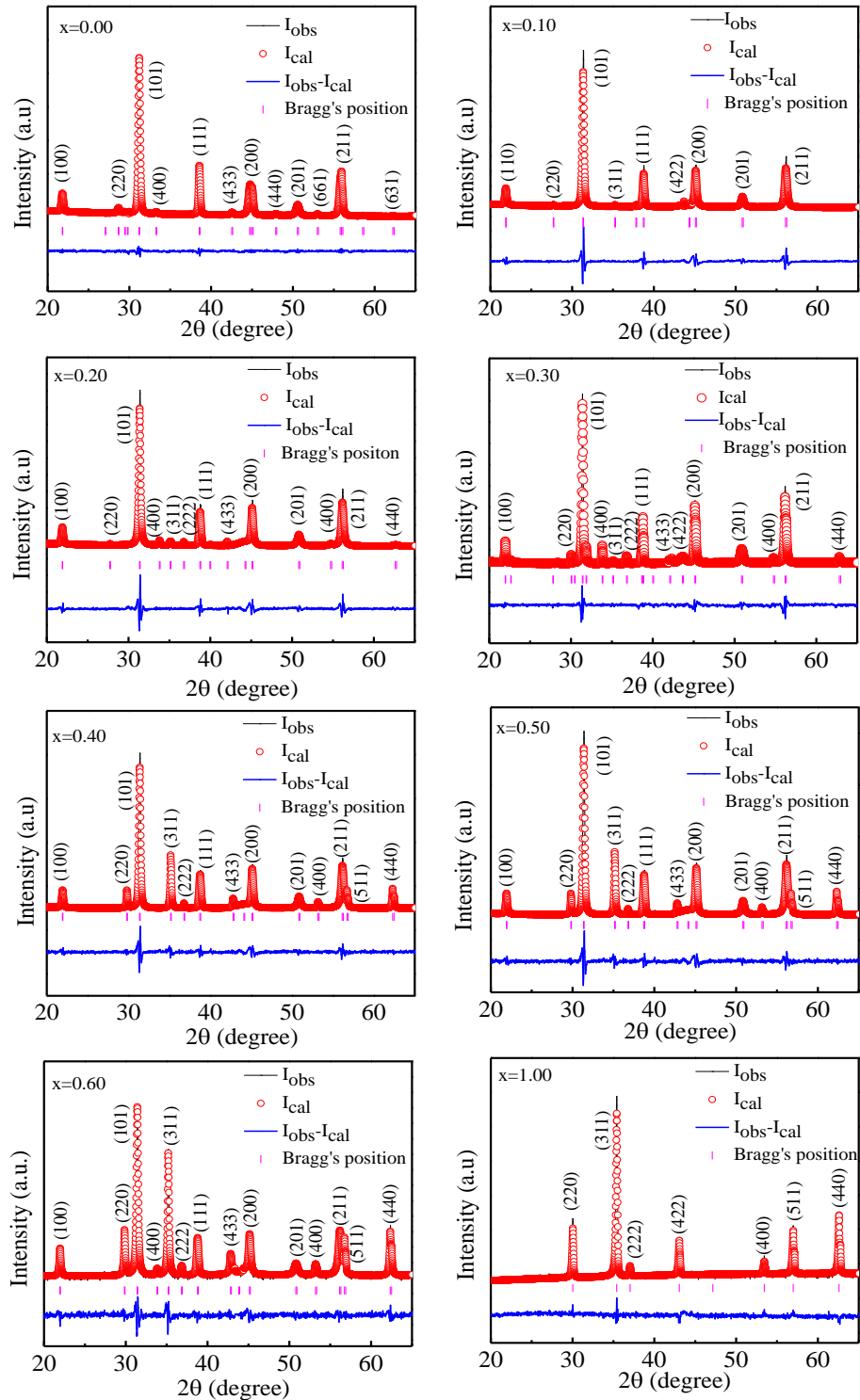


**Fig. 4.21** Rietveld refinement of various $x$LNCZFO+(1-$x$)BGTDO composites.

Fig. 4.21 demonstrates the Rietveld refined XRD patterns of the studied composites. The presence of constituents (LNCZFO and BGTDO) and the absence of intermediate phases confirm the excellent formation of composites. The Rietveld refinement also confirms the cubic spinel crystal structure with $Fd\bar{3}m$ space group of LNCZFO phase and tetragonal perovskite structure with *P4mm* space group of BGTDO phase. In the figure, the black line and red circle represent the observed and calculated intensity, respectively. Short vertical lines with a red color below the patterns determine the position of the Bragg diffraction and the lower continuous line is the difference between the observed and the calculated intensity. It is evident that there is a good agreement in the observed and calculated XRD patterns that are also verified by the observation of the difference pattern. Parameters including R-factors (R = reliability) and goodness of fit index were analyzed to assess the reliability and fitting quality of experimental data, respectively. The best fit of the experimental diffraction data is obtained since these parameters have attained their lower value and therefore the respective crystal structure is regarded to be satisfactory [32]. There is no significant change in the refined lattice parameters (shown in Table 4.4) of the individual phases in the composites, which indicates that there is no structural change in the individual phases during the formation of the composites. Slight changes in the lattice parameters result from the stress between the two ferroic orders [30]. The values of the lattice parameters were obtained from the Rietveld refinement analysis [107]. The cubic ferrite phase consists of $a = 0.8443$ nm, while $a = b = 0.3988$ nm and $c = 0.3999$ nm for the tetragonal perovskite phase of $x = 0.50$ composite. The results obtained are well satisfied with the results reported earlier [22-25].

**Table 4.4** The space group, lattice parameter, $R$, and GOF of various $x$LCNZFO+ $(1-x)$BGTDO composites.

| Content ($x$) | Space group | | Lattice parameter (nm) | | | $R$ (%) | | GOF |
| | Ferrite | Ferroelectric | Ferrite | Ferroelectric | | | | |
| | | | $a$ | $a$ | $c$ | $R_e$ | $R_p$ | |
| 0.00 | $Fd\bar{3}m$ | $P4mm$ | ------- | 0.3995 | 0.4026 | 5.91 | 4.63 | 1.03 |
| 0.10 | $Fd\bar{3}m$ | $P4mm$ | 0.8447 | 0.3986 | 0.3993 | 5.61 | 7.29 | 1.75 |
| 0.20 | $Fd\bar{3}m$ | $P4mm$ | 0.8444 | 0.3987 | 0.3998 | 5.13 | 6.09 | 1.59 |
| 0.30 | $Fd\bar{3}m$ | $P4mm$ | 0.8446 | 0.3985 | 0.4001 | 5.25 | 6.89 | 1.31 |
| 0.40 | $Fd\bar{3}m$ | $P4mm$ | 0.8445 | 0.3986 | 0.4003 | 4.54 | 4.21 | 1.22 |
| 0.50 | $Fd\bar{3}m$ | $P4mm$ | 0.8446 | 0.3988 | 0.3999 | 4.29 | 3.79 | 1.15 |
| 0.60 | $Fd\bar{3}m$ | $P4mm$ | 0.8444 | 0.3989 | 0.4004 | 3.76 | 3.26 | 1.13 |
| 1.00 | $Fd\bar{3}m$ | $P4mm$ | 0.8443 | ------- | ------- | 2.63 | 2.61 | 1.26 |

The graphical representation of $\rho_B$, $\rho_{th}$, and $P$ of the composites as a percentage of the ferrite component is shown in Fig. 4.22. The bulk density of all composites was estimated using the Archimedes principle. The maximum value of $\rho_B$ was obtained for $x = 0.10$ composite, as the small grains of the perovskite material fill the intergranular pores of the composition. Also, the high interaction between the constituent phases for $x = 0.10$ samples confirmed by the highest $\alpha_{ME}$ is responsible for the higher $\rho_B$. The $\rho_B$ decreases above $x = 0.10$ due to the atomic weight of LNCZFO (232.08 amu) which is lower than the atomic weight of BGTDO (239.92 amu). $\rho_B$ is lower than $\rho_{th}$ for all composites because, in the case of $\rho_{th}$ estimation, porosity is not considered which can be produced and grown well into the bulk samples during the sintering process. The $\rho_{th}$ declines just about linearly to comply with the mixture rule or the sum rule. In ceramic material, $P$ is derived from two sources, including intergranular pores and intragranular pores [121]. Due to the count of these intergranular and intragranular pores during the $\rho_B$ measurement, $\rho_B$ is lower than $\rho_{th}$.
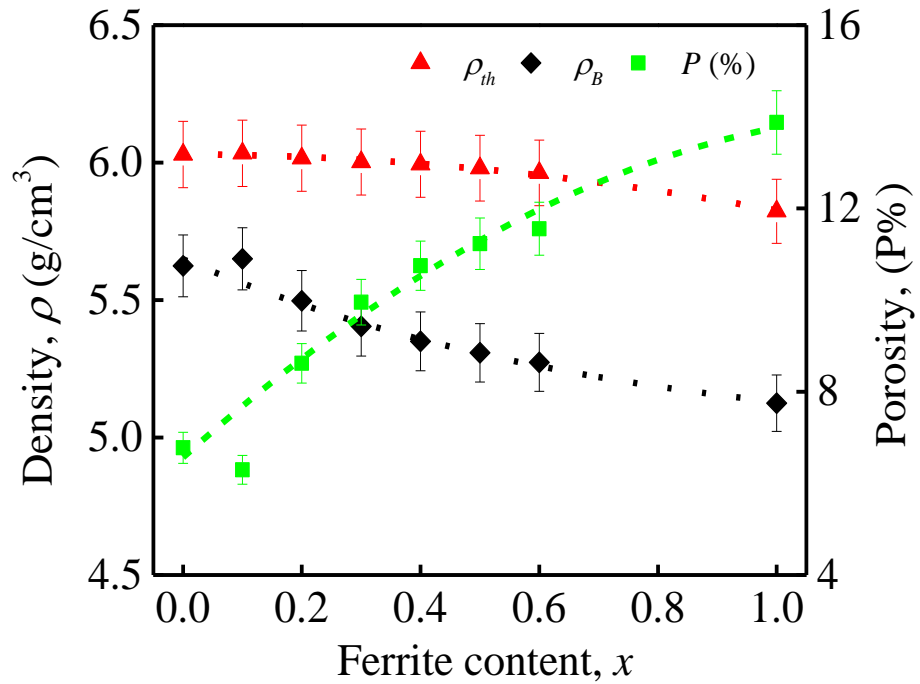
**Fig. 4.22** The $\rho_B$, $\rho_{th}$, and $P$ as a function of ferrite content of $x$LNCZFO+ $(1-x)$BGTDO composites.

### 4.2.2 Surface morphology and EDS analysis

The microstructure of MFCs plays an important role in the electric and magnetic behaviors, as well as the ME coupling. The FESEM associated with the EDS carried out the microstructural, surface morphology, and elemental distribution of all samples. The distribution of the grains along with fitted curves is presented in Fig. 4.23 to evaluate the grain diameter of LNCZFO and BGTDO ferroics in the composites. The ferroic phases can be easily identified from the FESEM images. From FESEM image analysis it was observed that the relatively larger grains are of the ferromagnetic phase. The number of these grains increases as the $x$ value increases. Micrographs exhibit the inhomogeneous grain development in the composites. This inhomogeneity of grain is due to the dissimilar growth of particular phases. The $\bar{D}$ of the composites were calculated by fitting the data based on the Gaussian distribution function [121]. The $\bar{D}$ values of the composites in the range of 0.319–1.597 μm were well consistent with the earlier report [179]. The increase in $\bar{D}$ with an increment in ferrite content in the composite might be the cause of the combination of large ferrite grains with small ferroelectric grains. The $\bar{D}$ value for the different samples is presented in Table 4.5. The porosity of the composites develops

with an increment in the LNCZFO phase, which agreed with the bulk density and porosity measured according to the Archimedes principle. The lower stress created from the high porosity of the ferrite element also leads to an increment in $\bar{D}$ with the ferrite content.
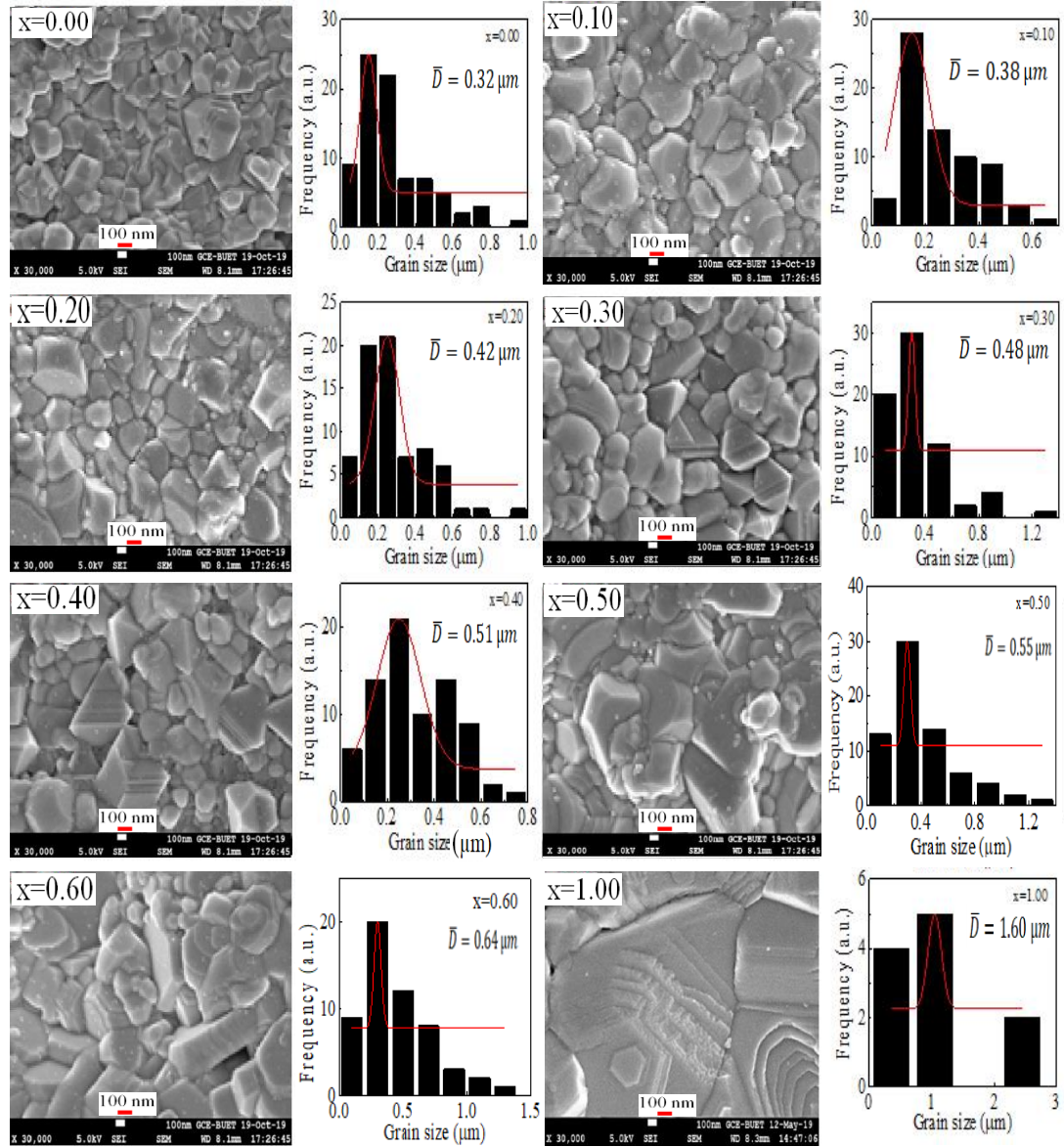


**Fig. 4.23** FESEM images and grain distribution histogram of various $x$LNCZFO+(1-$x$)BGTDO composites.

The EDS spectra were obtained from FESEM to evaluate the atomic percentage of the different $x$LNCZFO+(1-$x$)BGTDO composites, as shown in Fig. 4.24. The EDS spectra confirmed the incorporation of Ni, Cu, Zn, Fe, Ba, Gd, Ti, Dy, and O in the composites. The evaluated quantities of the elements are well-matched with the

approximate percentages of the different constituents, excluding oxygen. The oxygen vacancy can be created at high temperatures during the sintering.
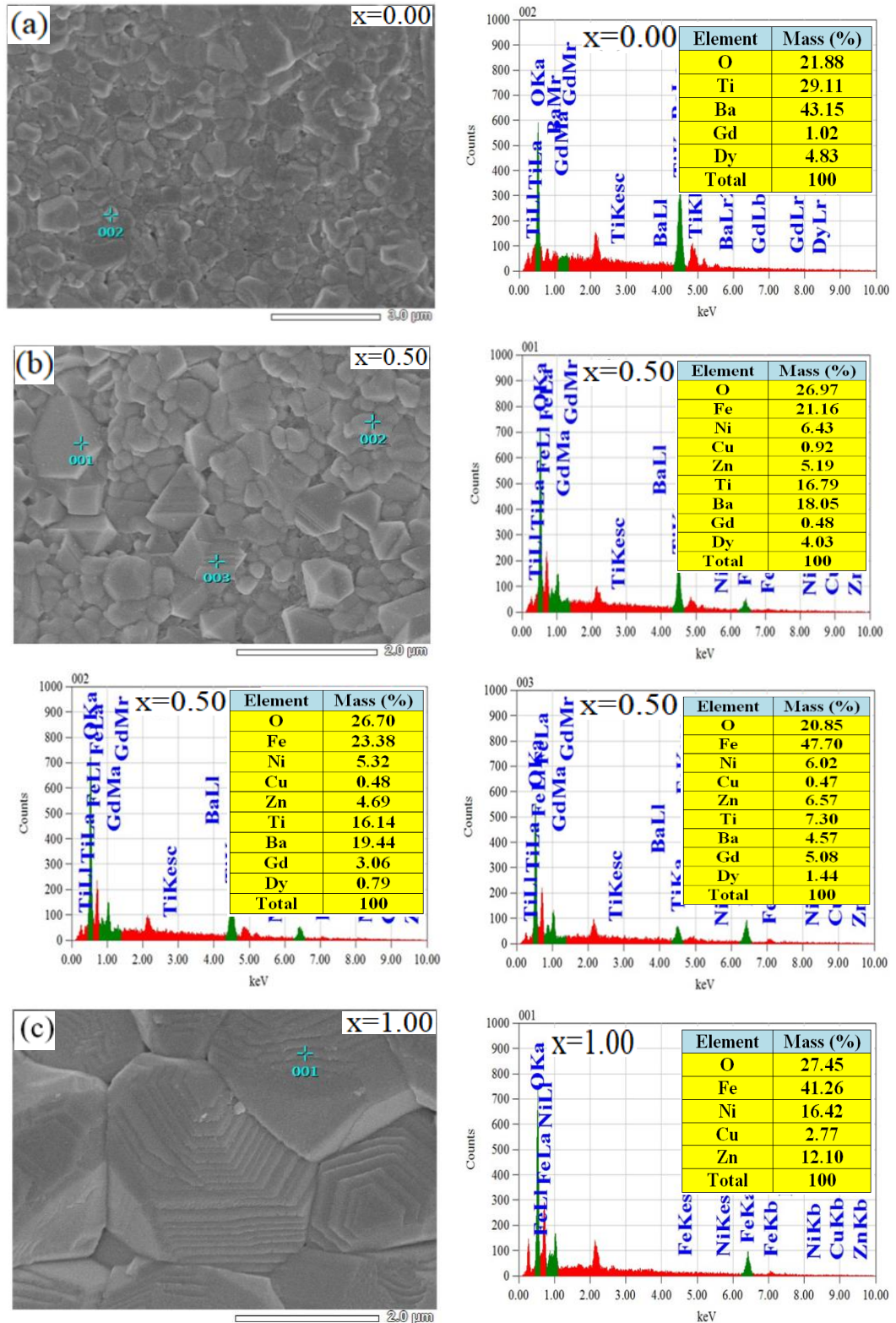


**Fig. 4.24** Micrographs and corresponding EDS spectra of (a) $x = 0.00$, (b) $x = 0.50$, and (c) $x = 1.00$ of $x$LNCZFO+(1-$x$)BGTDO composites.

### 4.2.3 Initial permeability
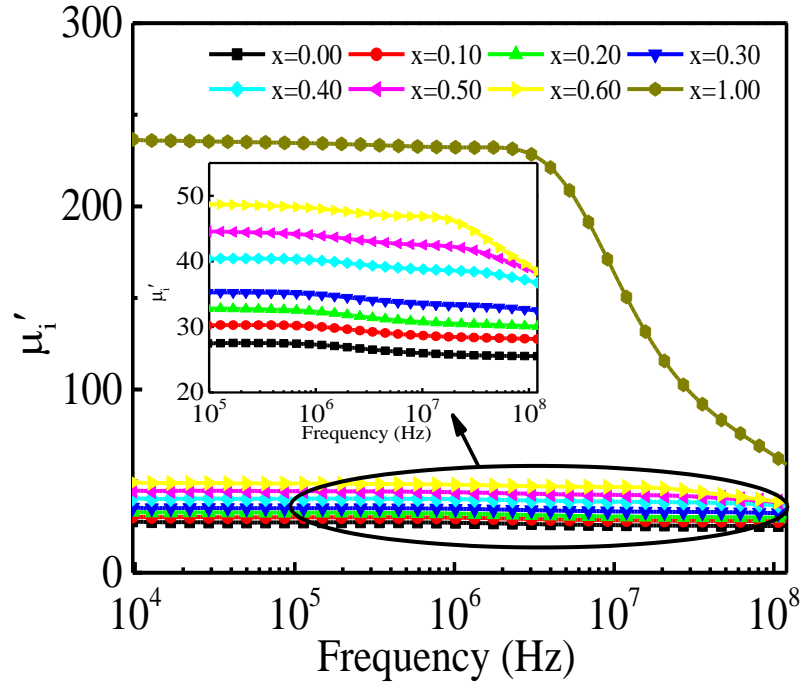


**Fig. 4.25** Variation of $\mu_i{}'$ as a function of frequency for various
$x$LNCZFO+(1-$x$)BGTDO composites.

The $\mu_i{}'$ represents the stored energy and demonstrates the part of magnetic induction in material under the ac magnetic field. Fig. 4.25 shows the variation of $\mu_i{}'$ with a frequency range of 10 kHz-120 MHz for various $x$LNCZFO+(1-$x$)BGTDO composites. The $\mu_i{}'$ is almost constant up to a certain frequency for the reason that magnetic moments are capable of following the alternate applied magnetic field in this region through the magnetization process [180]. This frequency independence nature is influential for different applications, including broadband transformer and wideband read-write head for video recording [181, 182]. The $\mu_i{}'$ increases with the ferrite content as the LNCZFO are highly magnetic, whereas the BGTDO is weakly ferromagnetic. The $\mu_i{}'$ for the LNCZFO phase is much larger than any of the other composites. The magnitude of $\mu_i{}'$ of a ferrite depends on two factors: (i) domain wall motion and (ii) spin rotation [122, 123]. For normal grain growth, the domain wall motion is proportional to the $\bar{D}$ of the material. The value of $\bar{D}$ increased by the increase of the domain walls per grain. As the motion of domain walls creates $\mu_i{}'$, any increase in the number of domain walls may lead to an increase in $\mu_i{}'$. The $\bar{D}$ for

$x = 1.00$ is much larger than the other composites. Besides, in the *M-H* hysteresis loop, it is also evident that the magnetization is very large for $x = 1.00$ sample. The $\mu_i'$ is directly proportional to the magnetization. Hence, $\mu_i'$ for $x = 1.00$ is quite different from the rest of the samples. The $\mu_i'$ decreases in the higher frequencies because of the creation of pinning points on the surface of the sample from impurities and intergranular pores, which obstructs the spin rotation and domain wall motion by lowering the contribution to enhancing $\mu_i'$ [124]. The maximum $\mu_i'$ and the corresponding $f_r$ are inversely proportional to each other as per the Snoek ($f_r\mu_i'$ = constant) relationship [125]. Thus, an increase of LNCZFO in composites causes a decrease in the magnitude of $f_r$. Hence, it is possible to control the $\mu_i'$ and $f_r$ of the composites by changing the LNCZFO or BGTDO content. No resonance peak was identified in the observed frequency range for $x = 0.00$, 0.20, and 0.30 composites as above the frequency studied. The $\mu_i'$ increases with LNCZFO content according to the sum rule of the composite and is reported in Table 4.5.

**Table 4.5** The $\rho_{th}$, $\rho_B$, $P$, $\overline{D}$, and $\mu_i'$ (at 100 kHz) for various $x$LCNZFO+(1-$x$)BGTDO composites.

| Content ($x$) | $P_{th}$ (g/cm$^3$) | $\rho_B$ (g/cm$^3$) | $P(\%)$ | $\overline{D}$ (μm) | $\mu_i'$ at 100 kHz |
|---|---|---|---|---|---|
| 0.00 | 6.03 | 5.63 | 7 | 0.32 | 26 |
| 0.10 | 6.04 | 5.65 | 6 | 0.38 | 30 |
| 0.20 | 6.02 | 5.50 | 9 | 0.42 | 32 |
| 0.30 | 6.00 | 5.40 | 10 | 0.48 | 35 |
| 0.40 | 5.99 | 5.35 | 11 | 0.51 | 41 |
| 0.50 | 5.98 | 5.31 | 12 | 0.55 | 45 |
| 0.60 | 5.96 | 5.27 | 13 | 0.64 | 48 |
| 1.00 | 5.82 | 5.13 | 14 | 1.60 | 231 |

Fig. 4.26 describes the frequency-dependent $\tan\delta_M$ of all composites. This $\tan\delta_M$ creates from the lack of domain wall motion with the applied ac magnetic field and is also attributed to different defects, like non-uniform and non-repetitive domain wall motion, and domain wall bowing [126]. At the lower frequency region (up to $10^6$ Hz), the $\tan\delta_M$ decreases with the increase of the ferrite phase due to the increase of $Q$ factor which is inversely proportional to the $\tan\delta_M$. The $\tan\delta_M$ for all samples in high frequency (beyond $10^5$ Hz) is quite low due to the insulating layer created from BGTDO surrounding the LNCZFO elements, which can significantly enhance the resistive property of the materials and minimize the loss of eddy current [127]. At the higher frequency region, the $\tan\delta_M$ again increases due to the random domain wall motion and unable to follow the magnetic field. Besides, at the higher frequency region, $\tan\delta_M$ also increases with increasing ferrite content due to the decrease of the $Q$ factor.
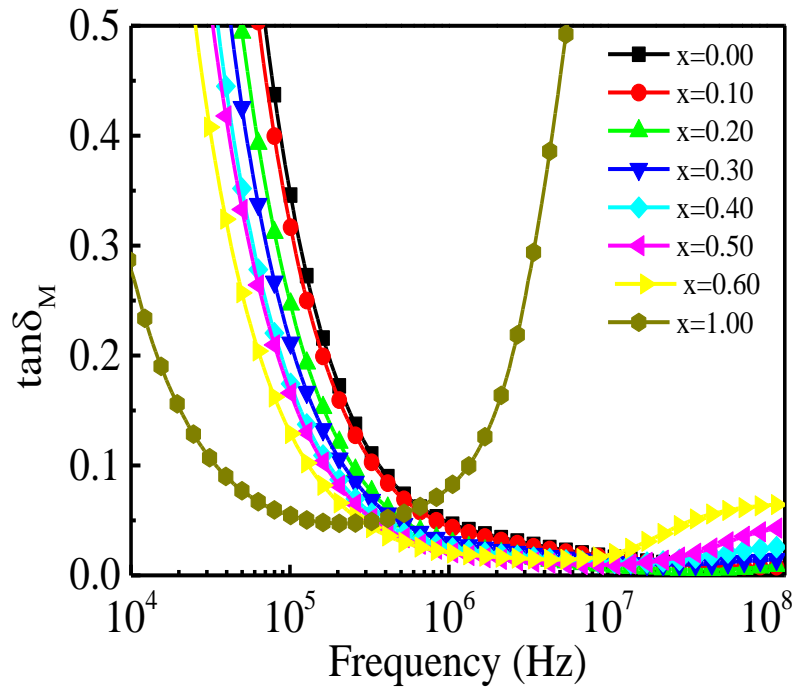


**Fig. 4.26** Variation of $\tan\delta_M$ with frequency for various $x$LNCZFO+(1-$x$)BGTDO composites.

The RQF is used as a performance assessment parameter of material for practical applications. Fig. 4.27 represents the frequency-dependent RQF of the samples. The RQF increases with the increase of ferrite content due to the increase of $\mu_i'$ which is directly proportional to the RQF. The RQF enhances as the frequency increases and

then decreases with the additional increment showing a peak. The maximum RQF and $f_r$ shifted to lower frequencies with an increase in the ferrite content indicating the lowering of $\tan\delta_M$. For the ferrite phase, the RQF peak is sharp but widens by enhancing the ferroelectric component in the composite, which increases the frequency band of the utility.
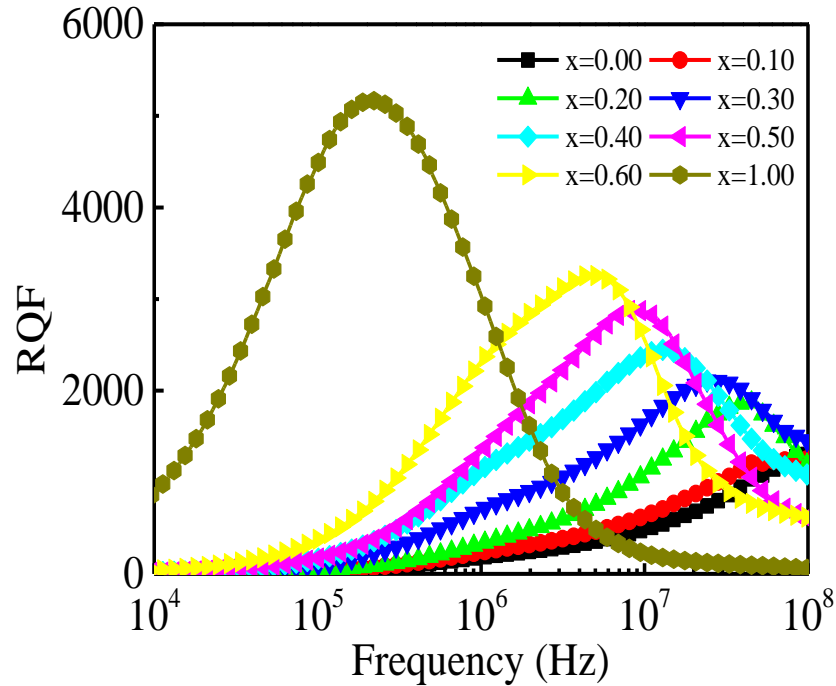


**Fig. 4.27** Variation of RQF with frequency for various $x$LNCZFO+(1-$x$)BGTDO composites.

### 4.2.4 Magnetic hysteresis

Magnetic hysteresis is a significant factor in the determination of the potential use of magnetic materials. Variability of magnetization at RT with the applied field for various $x$LNCZFO+(1-$x$)BGTDO composites is shown in Fig. 4.28. The figure describes that the *M-H* loops are quite thin for all samples. The magnetization of all samples considerably enhances with an addition of the implemented magnetic field up to 0.15 T. Magnetization beyond 0.15 T rises slowly, and then a saturation nature is achieved. The applied magnetic field higher than 0.25 T shows an independent structure of the *M-H* loops, i.e., the magnetization of all samples reaches the saturation state. The $M_s$ of the samples enhances with an increase of the LNCZFO phase in the composites due to the higher $\mu_i'$ which is directly proportional to the $M_s$.

Increased magnetization values with an increasing LNCZFO contributes to more magnetic grains than the BGTDO phase that also enhances the magnetic moment of the composites [128, 129]. The LNCZFO phase has more eminent $M_s$ because of the stimulation of migration of $Fe^{3+}$ into B-site as nonmagnetic $Zn^{2+}$ favors to go to A-site. This migration of $Fe^{3+}$ to the B-site increases the magnetic moment of the B-site, which strengthens the interaction of the A-B. Enhanced A-B interaction induces increased net magnetization ($M_s = M_B–M_A$). The BGTDO demonstrates a weak ferromagnetic performance with a low magnitude of $M_r$ of 0.32 emu/g and the inclusion of LNCZO and BGTDO into composite contributes to an enhancement of magnetization due to the interfacial strain leads to change in the orientation of the spins [159]. The magnitude of $M_s$ for all composites is evaluated by the extrapolation of the magnetization curve to $H = 0$. The minimum $M_s$ of 2.26 emu/g is observed for $x = 0.00$ sample. The $M_s$ increased with an increase in ferrite content and achieved a maximum value of ~80 emu/g for $x = 1.00$ sample. The composite consists of a significant amount of reduced magnetization ($M_r/M_s$) relative to the parent LNCZFO phase. This decreased magnetization is often called the squareness of the hysteresis loop. The determined range of these values is 0.057-0.247, which is suitable for use in memory devices [130].
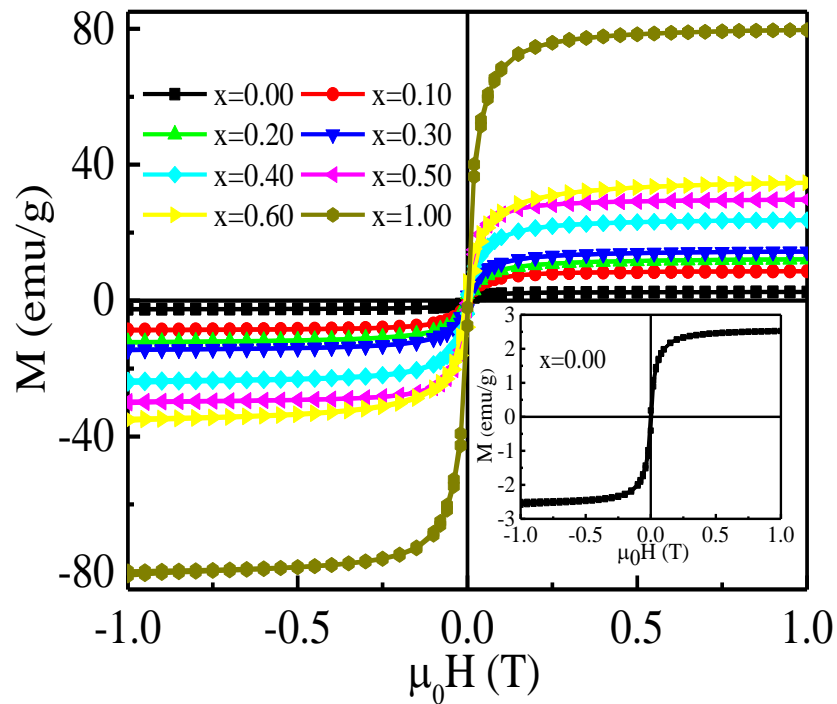


**Fig. 4.28** M-H hysteresis loops for various $x$LNCZFO+(1-$x$)BGTDO composites.

**Table 4.6** Measured magnetic parameters of $x$LNCZFO+(1-$x$)BGTDO composites.

| Content, $x$ | $M_s$ (emu/g) | $M_r$ (emu/g) | $H_c$ (T) |
|:---:|:---:|:---:|:---:|
| 0.00 | 2.26 | 0.32 | 0.0023 |
| 0.10 | 6.92 | 1.11 | 0.0047 |
| 0.20 | 9.89 | 2.44 | 0.0081 |
| 0.30 | 13.14 | 1.98 | 0.0047 |
| 0.40 | 20.55 | 2.86 | 0.0046 |
| 0.50 | 26.12 | 1.73 | 0.0023 |
| 0.60 | 31.85 | 7.59 | 0.0081 |
| 1.00 | 79.67 | 4.38 | 0.0034 |

### 4.2.5 Frequency-dependent dielectric property
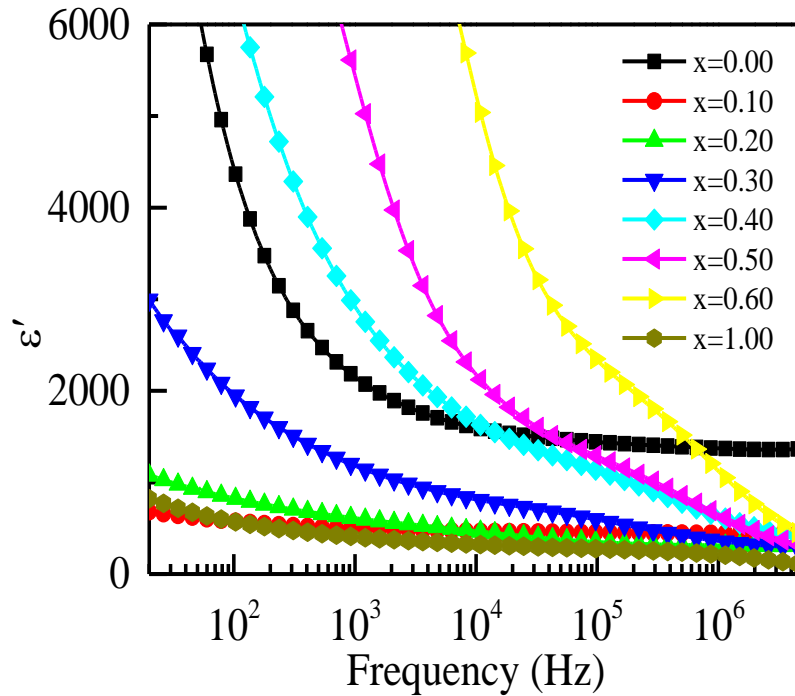


**Fig. 4.29** Variation of $\varepsilon'$ with frequency for various $x$LNCZFO+(1-$x$)BGTDO composites.

The $\varepsilon'$, also known as relative permittivity, is a unique parameter used to describe the dielectric behaviors of the materials. The $\varepsilon'$ is the amount of energy stored in the material. The frequency-dependent $\varepsilon'$ is represented in Fig. 4.29. The $\varepsilon'$ decreases to

certain values by increasing the frequency. After that, $\varepsilon'$ becomes almost constant for all the composites. The low-frequency dielectric dispersion occurs since all kinds of polarizations are present in the composites at low-frequency (up to $10^4$ Hz). But, as the frequency increases, some polarizations are significantly disappeared (except for electronic and ion) leading to a sharp fall of $\varepsilon'$. The $\varepsilon'$ is fairly small at higher frequencies (beyond $10^4$ Hz) because the electric dipoles do not get sufficient time to align and unable to follow the fast variation of the ac electric field. In the low-frequency region, the high magnitude of $\varepsilon'$ derived from the interfacial polarization proposed by Maxwell-Wagner [132, 133]. Interfacial polarization creates from inhomogeneity of the material, results through grain composition, porosity, interfacial defects, charges trapped by the defects at the grain boundaries, oxygen vacancies, and impurity. During the high-temperature calcination and sintering, this inhomogeneity formed in the sample. Besides, space charge polarization could also be caused by the Ba-volatility and the transition from $Fe^{3+}$ to $Fe^{2+}$ in LNCZFO. The $Fe^{3+}$ to $Fe^{2+}$ transition in LNCZFO takes place to maintain a charge balance, which may also contribute to the formation of oxygen vacancies [183]. The $\varepsilon'$ for some samples of $x = 0.40$, $0.50$, and $0.60$ enhances with the increase of LCNZFO content because of the large $\bar{D}$ for the LNCZFO phase. The area of the grain boundary reduces with the increase of $\bar{D}$. The heterogeneity of the composites also increased the interfacial polarization [135, 136]. The difference in conductivities and permittivity of the interface between the constituent phases forms this heterogeneity. When an electric field is implemented in the studied samples, the space charge is given by the LNCZFO phase. This charge accumulates at the interface of the two phases as a result of the existence of distinct conductivity and permittivity. It leads to the rise of the interfacial polarization and contributes to the $\varepsilon'$ [137]. The effect of large $\bar{D}$ of ferrite phase and heterogeneity of the composite contribute to an increase of $\varepsilon'$. In this investigation, enlarged $\varepsilon'$ found for samples with $\bar{D}$ values ranging from 0.521 to 0.659 μm and a declining pattern of $\varepsilon'$ observed for all other $\bar{D}$ values. The findings are well agreed with the previous reports [138, 139]. The studied composites also showed an immense frequency consistency of $\varepsilon'$ at the higher frequency region. Nevertheless, with an increment in the ferromagnetic phase at a higher frequency region, the value of $\varepsilon'$ is declined since $\varepsilon'$ is smaller for LNCZFO than for BGTDO.
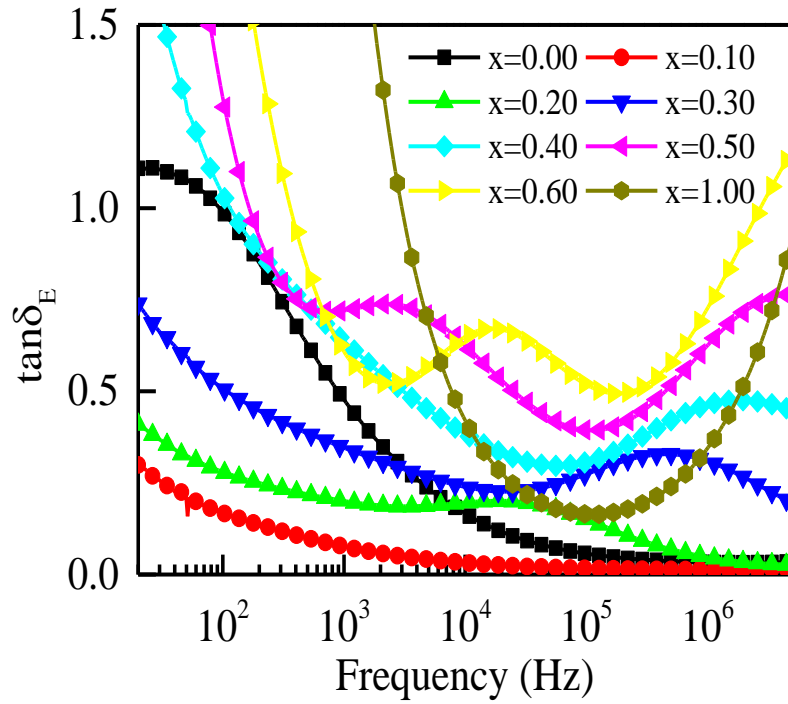
**Fig. 4.30** Variation of tan$\delta_E$ with frequency for various $x$LNCZFO+(1-$x$)BGTDO composites.

The tan$\delta_E$ variation, depending on frequency, is presented in Fig. 4.30. This tan$\delta_E$ resulted from the domain wall resonance [51]. The large tan$\delta_E$ of LNCZFO is due to some ion migrations and, in particular, to the loss of conductivity induced by hopping electrons between $Fe^{3+}$ and $Fe^{2+}$ ions [184]. As mentioned, the grains have higher conductivity than that of the grain boundaries in ferrite, while small grains are efficient for reducing the $Fe^{2+}$ concentration [184]. On the other hand, BGTDO ceramics could cause a decrement in $\overline{D}$, leading to a decline in conductivity. In both ends of the tan$\delta_E$ peak, frequency dispersion tan$\delta_E$ occurs. The composites show the loss peaks satisfying the Debye theory of relaxation. These relaxation tan$\delta_E$ peaks resulted from the momentary delay of molecular polarization of dielectric material with the ac electric field. In other terms, if the condition $\omega\tau = 1$ is satisfied [140]. In earlier studies, similar behaviors are also reported [51, 141]. The value of tan$\delta_E$ increases with the increase of LNCZFO content due to the increase of the mobility of the charge carrier.

### 4.2.6 Temperature-dependent dielectric property
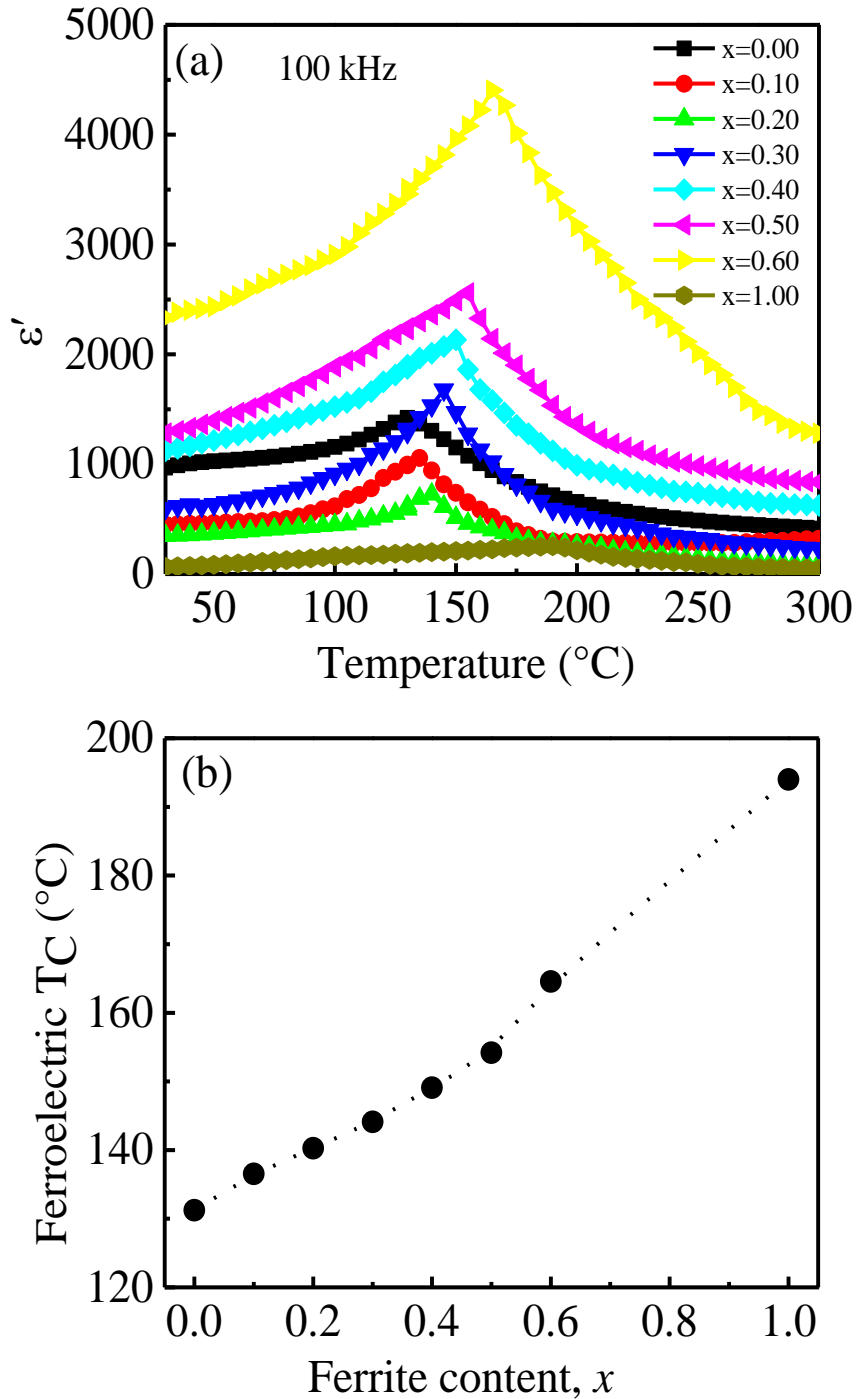


**Fig. 4.31** Variation of (a) $\varepsilon'$ as a function of temperature for various $x$LNCZFO+ (1-$x$)BGTDO composites at 100 kHz and (b) $T_C$ with ferrite content.

Fig. 4.31(a) demonstrates the temperature-dependent $\varepsilon'$ measured at a frequency of 100 kHz. A dielectric peak at around 130ºC is observed for the case of pure BGTDO ceramics. The peak observed at about 194ºC might be the structural transition of the

ferromagnetic phase. Different factors including structural transitions, the ME effect, or transitory interaction among oxygen ion vacancies and the $Fe^{3+}$ as well as $Fe^{2+}$ ions at the interface of polycrystalline materials can result in temperature-dependent dielectric peaks [142]. Fig. 4.31(b) shows the shifting of dielectric peaks to higher temperatures with increasing the LNCZFO phase in the composites due to the heterogeneity, defects, and strain produced between the constituent phases [145-1147]. This can also be for the different $T_C$ of the constituent phases. The shifting of the peak position implies the ME interaction between the constituent phases [148]. The broadening of the dielectric peak for some samples reveals the existence of diffuse phase transition.

### 4.2.7 Complex impedance spectra analysis

The frequency-dependent nature of $Z'$ is shown in Fig. 32(a). The value of $Z'$ decreases with an increase in frequency to a certain value, indicating that the charge carrier conductivity is increased up to this limit and then follows the frequency-independent nature. The larger $Z'$-value in the lower-frequency range (up to $10^4$ Hz) specifies that the relaxors comprise a higher polarization resulting from all types of polarization. The impedance spectroscopy study revealed that the $Z'$-values initially reduced by an increment in frequency to a certain value of $\leq 10^4$ Hz and attained a stable state at a frequency of $\geq 10^4$ Hz. The decline in $Z'$ may result from an increase in conductivity due to the presence of space charge polarization in the composites at higher frequencies [1151, 152, 185, 186]. The large value of $Z'$ at lower frequencies indicates that the polarization in the composites is larger. The merger of $Z'$ at higher frequencies indicates the possible release of space charge polarization or accumulation at the boundaries of homogeneous phases in the composites under the applied external field. The merger behavior of $Z'$ at a higher frequency region is due to the reduction of the impedance of the sample. This is due to the capacitive reactance which is inversely proportional to the frequency which contributes to the total impedance. Additionally, with the increase of LNCZFO content, the values of $Z'$ decline in the low-frequency region, and then they appear to merge in the high-frequency region. This suggests that the frequency at which the space charge becomes free also depends upon the LNCZFO phase. At the lower frequency region, the $Z'$ decreases with the increase of LNCZFO content due to the lower resistive

property. The decreasing trend of $Z'$ implies an increasing loss in resistive properties of the composites. This is the typical nature due to the existence of space charge polarization in the material. The findings are well agreed with earlier research [154, 155].
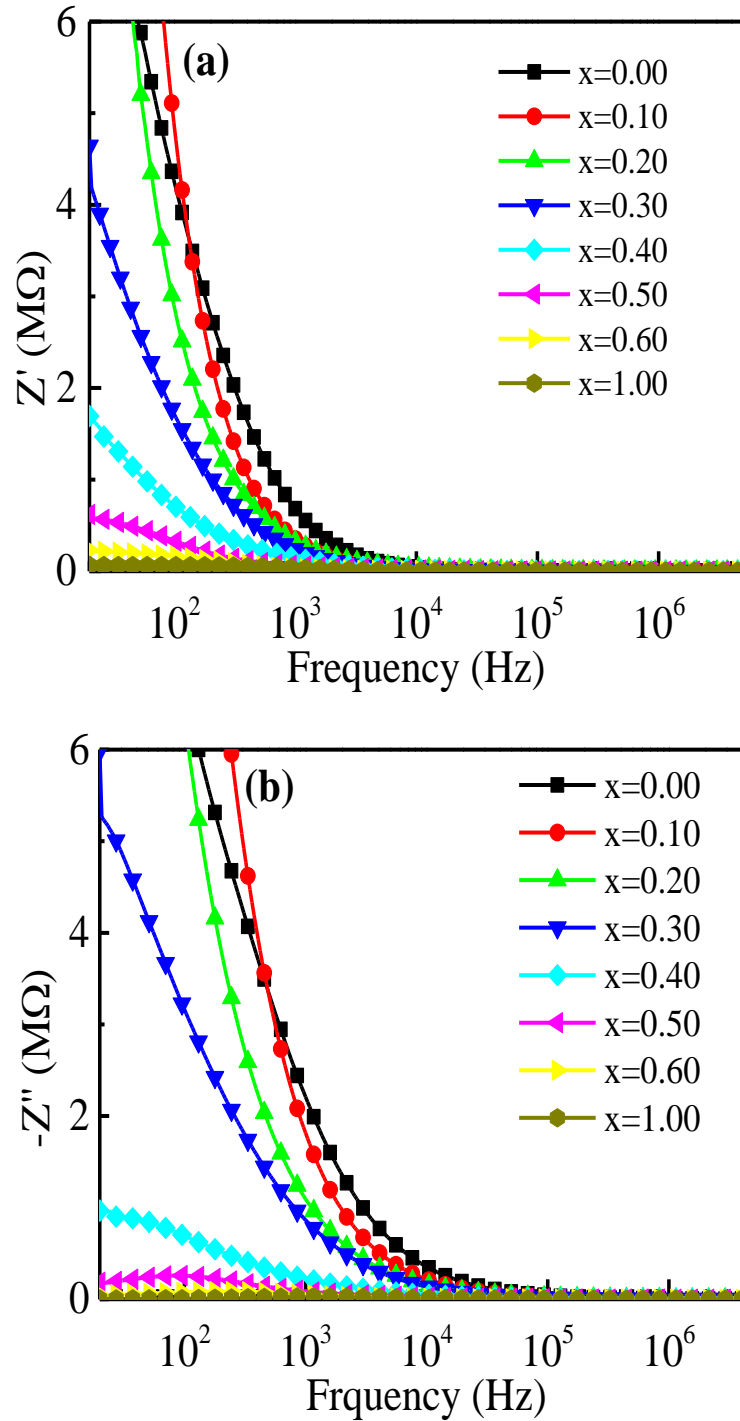


**Fig. 4.32** (a) Frequency dependence of $Z'$, and (b) $Z''$ for various $x$LNCZFO+(1-$x$)BGTDO composites.

The variation of $Z''$ with frequency is presented in Fig. 4.32(b). Fig. 4.32(b) shows the identical variation of $Z''$ with frequency as that of $Z'$. The absence of the relaxation phase resulted from the static relaxation of the electron in the composites.
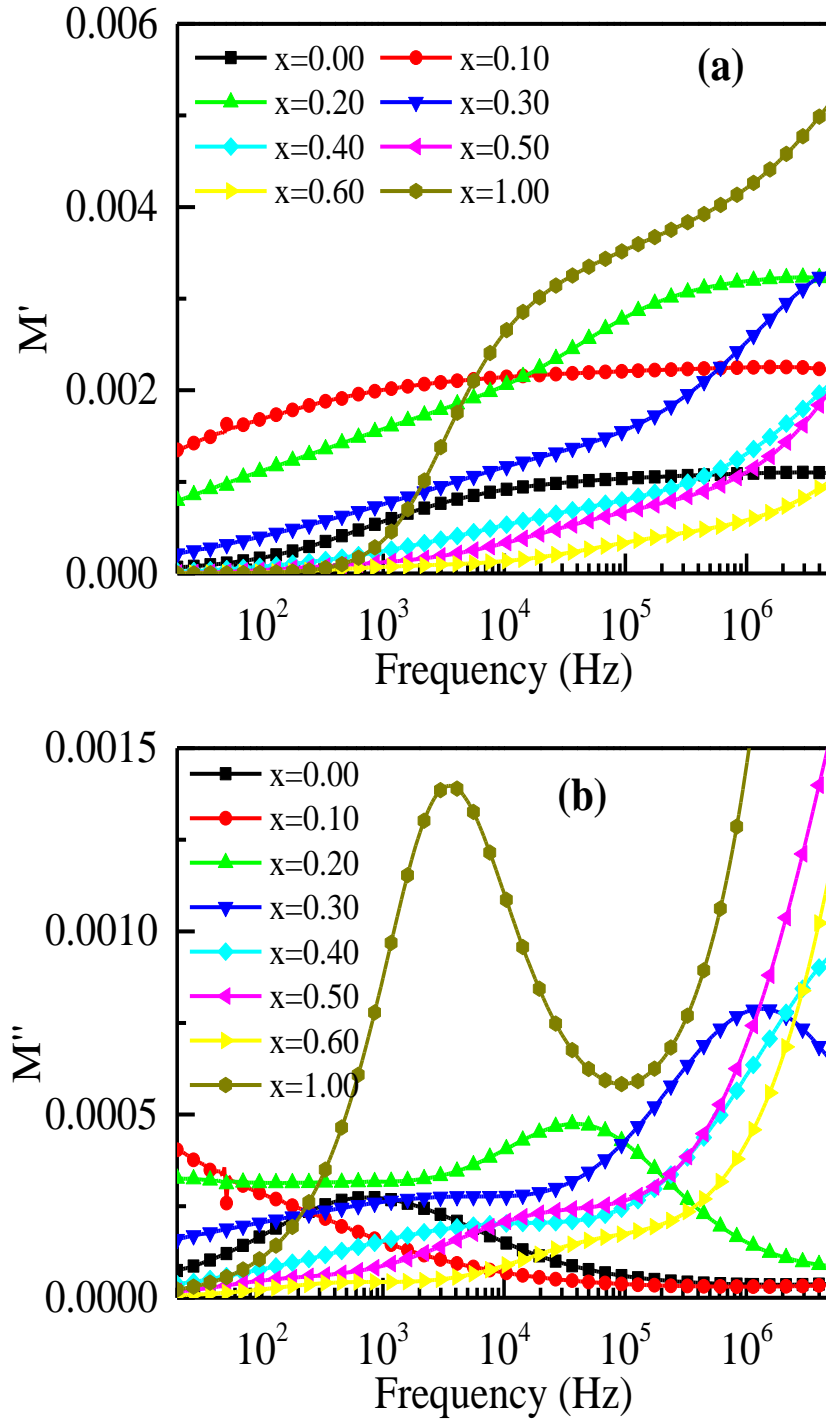


**Fig. 4.33** Electric modulus spectra of various $x$LNCZFO+(1-$x$)BGTDO composites: (a) for $M'$ and (b) for $M''$.

The bulk characteristics evident in the impedance investigation are associated with dipole relaxation and/or long-range conductivity. It is hard to distinguish this bulk characteristic with the help of impedance studies, for which electrical modulus analysis is used. Electric modulus, depending on the capacitance value, helps to understand the different relaxation and space charge aspects. Fig. 4.33(a) demonstrates the frequency variation of $M'$. The value of $M'$ is quite low in the lower-frequency region (up to $10^3$ Hz), suggesting the activity of polaron hopping and the relatively small influence of electrode effects [156, 187]. The $M'$ increases up to a certain frequency since various dipoles cannot follow the ac electric field near a higher frequency (beyond $10^3$ Hz). The $M'$ significantly enhanced for all samples with frequency and reaching high-frequency saturation. Dispersion is significant at low frequency, which shifts to higher-frequency for the distribution of relaxation times within the material. The frequency response of $M''$ is presented in Fig. 4.33(b). It is evident that $M''$ shows the maximum value at a certain frequency and varies with composites along with the frequency, confirming the different relaxation times for different samples. Asymmetrical peak broadening is found at both ends of the maxima, which indicates that periods of relaxation are divided into separate time constants [160]. The peak broadening results due to the distribution pattern of local conductivity and electrical response time as a result of the non-uniform microstructure of the material [188]. The frequency range below the peak specifies the mobility region of the charge carrier over long distances, i.e., between the grains. Above the peak frequency, the charges move within short-distances, i.e., within grains [129]. The peak represents the transition from long to short-distance mobility.

Impedance spectroscopy is a well-known method used to determine the influence of grain and grain boundary influences on polycrystalline materials. The Nyquist plots are particularly suitable for materials with one or more different relaxation mechanisms of similar magnitude and following the Cole-Cole functional methods. The equivalent circuit of the brick-layer model [161] with three parallel RC circuits paired in series can explain the relaxor's properties of the material containing the effect of grain, grain boundaries, and electrode.
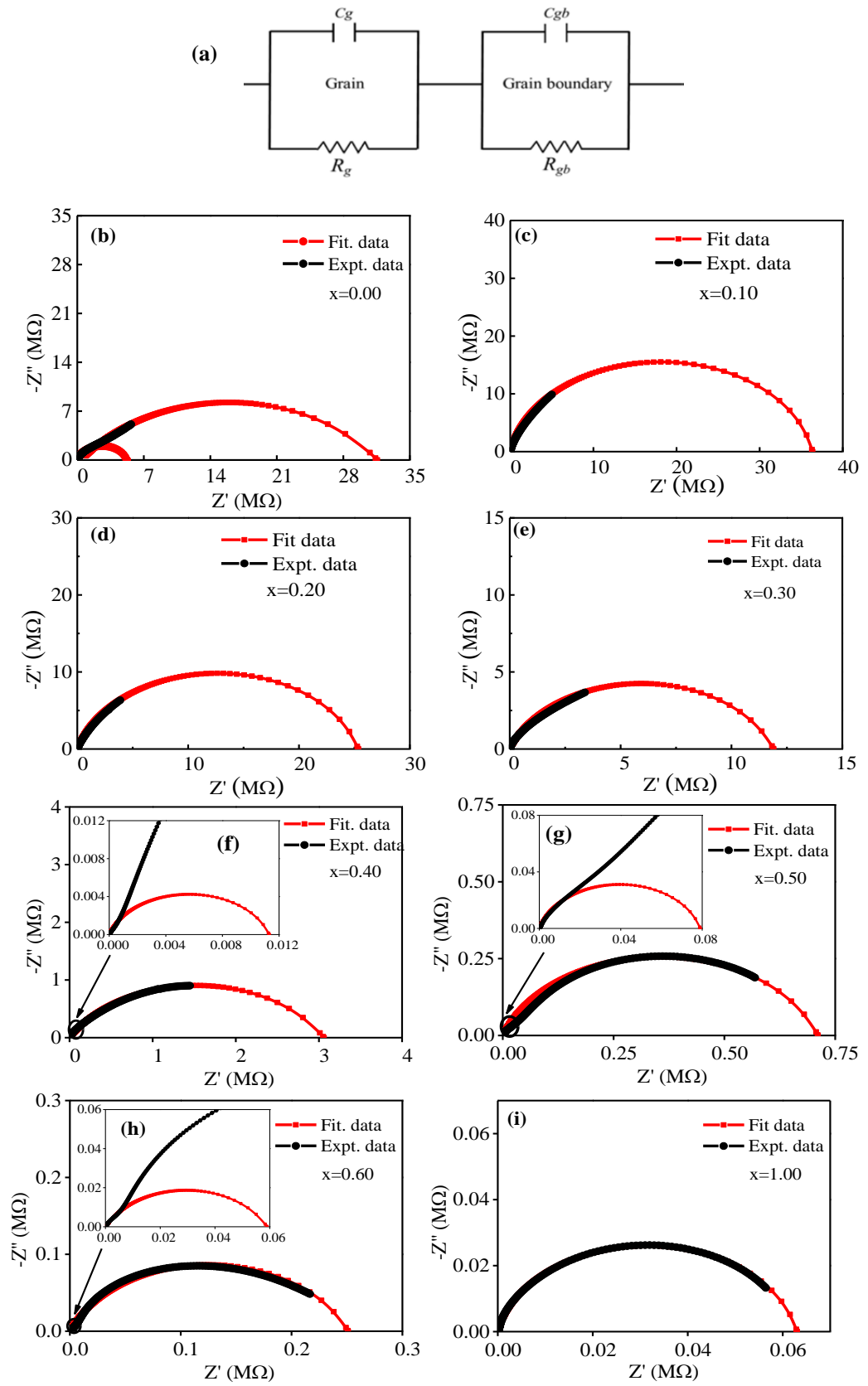
**Fig. 4.34** (a) Equivalent circuit model, and (b)-(i) Nyquist plot of various $x$LNCZFO+(1-$x$)BGTDO composites.

Depending on the electrical properties of the composite, the plot may have two semi-circles. The first semicircular arc at the lower frequency range and the second at the higher frequency region represent the resistance of grain boundary and grain, respectively [189]. In some cases, a relatively narrow semicircular arc is observed at a slightly lower frequency, which may be due to the influence of interfaces or electrodes [190]. The semicircular arc in the intermediate frequency region is due to the dominant grain boundary effect, resulting from the parallel arrangement of the grain resistance and grain capacitance of the material. On the other hand, arcs at larger frequencies reveal the grain influence creating from the parallel arrangement of grain resistance and capacitance of the sample [162]. Fig. 4.34(b-i) shows the complex impedance plots for all the composites. The points in the black line represent the experimental data and the points in the red line show the theoretical fit data in Fig. 4.34. In the present study, samples of $x = 0.10$, 0.20, 0.30, and 1.00 comprise only a single semicircle, suggesting that electrodes and grains do not have much impedance since this would produce an extra semicircular arc. A single semicircle in the impedance spectra demonstrates that only a grain boundary effect is dominant for the conduction of the composites. The samples of $x = 0.00$, 0.40, 0.50, and 0.60 exhibit double semicircle in their impedance spectra diagram. The impedance spectra with a double semicircular arc reveal the contribution of both grain and grain boundary resistance to the conduction process within the samples. The grain contribution arc usually lies in a frequency region higher than the grain boundary, as the grain boundary relaxation time is higher than the grain. This activity can be explained with an equivalent circuit comprising of two sub-circuits linked in series as presented in Fig. 4.34(a). If the center of the semi-circular arc lies on the $Z'$-axis, the Deby-type nature relaxation occurs [163]. Relaxation of the non-Debye pattern was obtained for the investigated composites, as each composite produces a depressed/distorted semicircle. The grain and grain boundary resistances were obtained from the fit for the studied composites. The grain boundary resistance of the samples decreases with ferrite content (except $x = 0.10$) due to the enhanced grain inhomogeneity in the composites. The small grain boundary resistance is found for the pure LNCZFO phase compared to the rest of the samples as a result of the conductive ferrite phase.

### 4.2.8 The ac conductivity
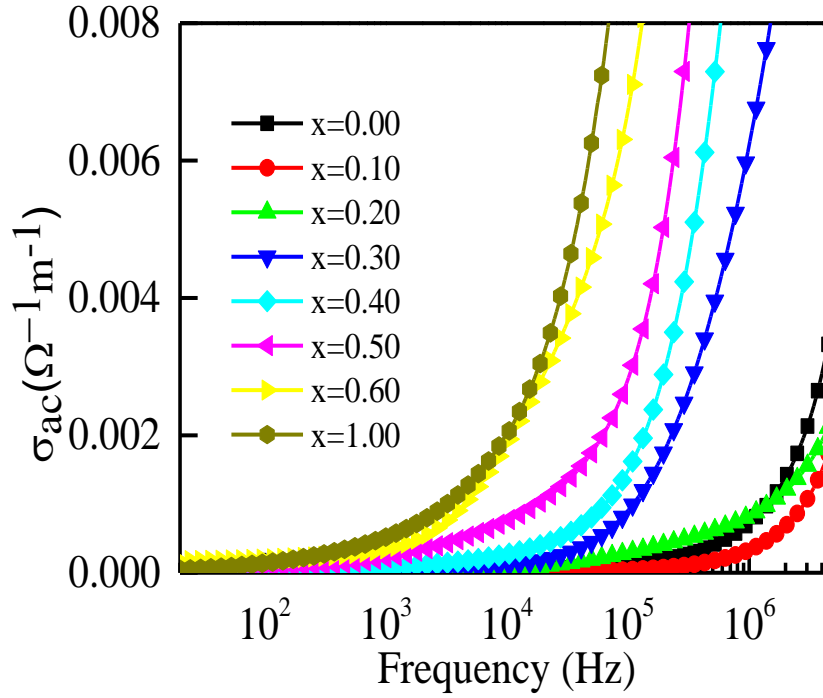


**Fig. 4.35** Variation of $\sigma_{ac}$ with frequency for various $x$LNCZFO+(1-$x$)BGTDO composites.

The frequency-dependent $\sigma_{ac}$ of MFCs stated by the polaron hopping mechanism depends on the free charges available in the composites. When the electric field is applied, the mobility of negative charges in oxide metals begins to distort or polarize the adjacent lattice to form a polaron. If distortions within lattice are of the order of the lattice constant, small polaron developed, while the distortions are equal or above the lattice constant, large polarons are created. It is also possible to describe the $\sigma_{ac}$ by the Austin and Mott polaron models [164]. The large polaron happens when the $\sigma_{ac}$ decreases as the frequency increases, while the small polaron happens when the $\sigma_{ac}$ increases with the frequency [165]. Fig. 4.35 illustrates the variation of frequency-dependent $\sigma_{ac}$. There are two different regions in the frequency-dependent $\sigma_{ac}$ spectrum. In the low-frequency region (up to $10^2$ Hz), the conductive behavior is independent of the frequency defined as $\sigma_{dc}$, in which the grain boundary effect becomes more prominent to dielectrics according to the Maxwell-Wagner double layer model [133, 166]. In the high-frequency hopping region (beyond $10^4$ Hz), $\sigma_{ac}$ increases rapidly, and hopping carriers from the components are continuing to

develop. Conductive grains at higher frequencies become more dominant, increasing the hopping carrier and conductivity. Hopping 3d electrons between $Ni^{2+}$ and $Ni^{3+}$ also between $Fe^{2+}$ and $Fe^{3+}$ might play an influential role in the conduction mechanism. By the Jonscher power law [167], the frequency-dependent $\sigma_{ac}$ expressed as $\sigma_{ac}(\omega)_= \sigma_{dc}+B\omega^n$. The independent nature of $\sigma_{ac}$ at a lower frequency and increasing trend at a higher frequency, indicating the shift of an ion from long-range to short-range mobility and thereby confirms the establishment of conductivity relaxation.
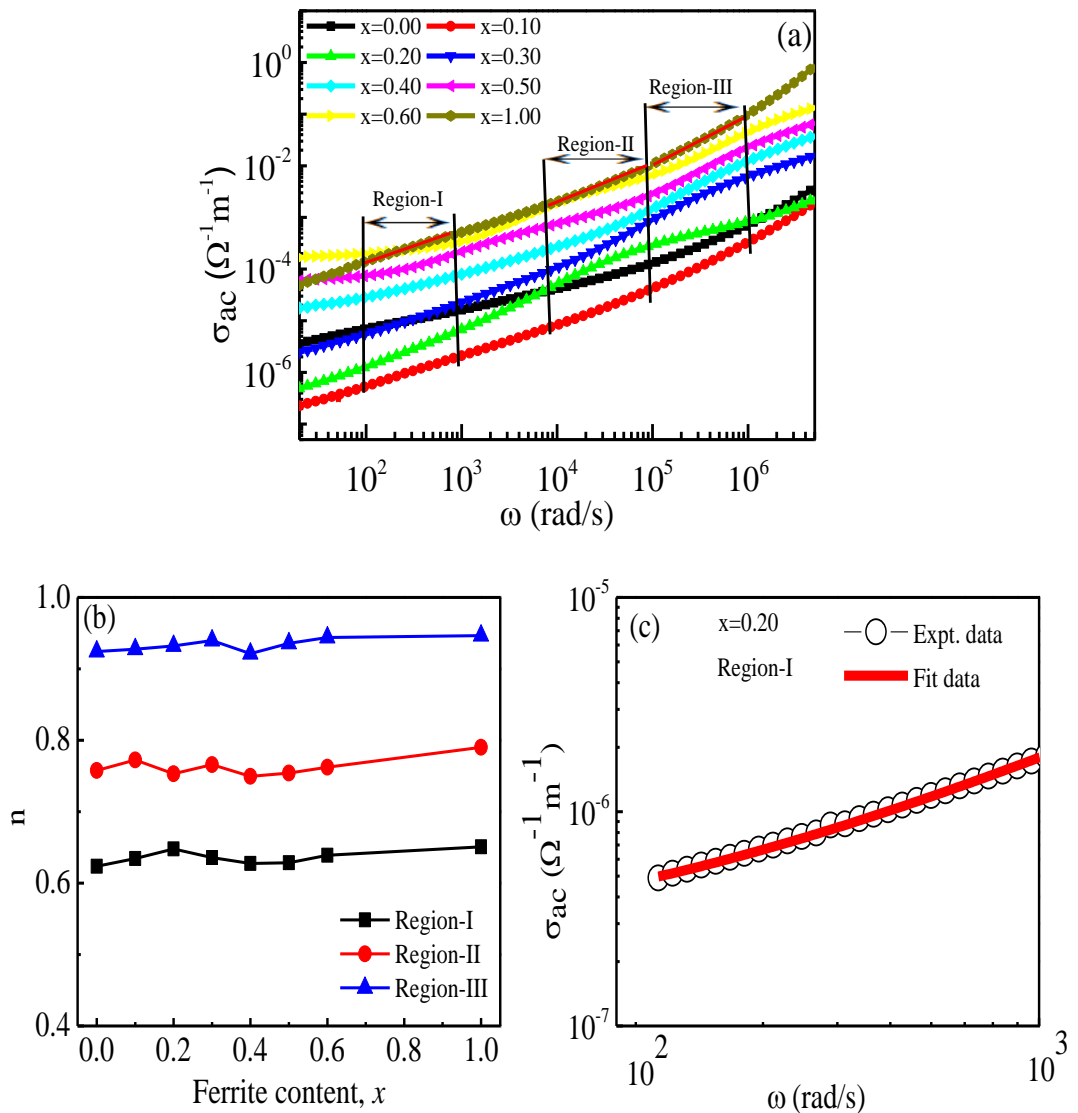


**Fig. 4.36** Variation of (a) $\sigma_{ac}$ with $\omega$, (b) $n$ with ferrite content, and (c) $\sigma_{ac}$ fitting according to the Jonscher's power law for $x = 0.20$ sample in region-I.

Fig. 4.36(a) shows the variation of $\sigma_{ac}$ as a function of $\omega$. The $\sigma_{ac}$ increases almost linearly with increasing $\omega$, indicating the conduction process in the composites is caused by a small polaron hopping mechanism [168]. Fig. 4.36(b) demonstrates the variation of $n$ with the ferrite content. There are three different regions of $\sigma_{ac}$ were selected (in Fig. 4.36.a) and the value of $n$ is determined by the fitting of Jonscher power law for different regions. Fig. 4.36(c) shows the fitting diagram of $\sigma_{ac}$ by the Jonschers power law for $x = 0.20$ composite in region-I. The value of $n$ in the region I ($10^2$-$10^3$ Hz) is found to be between 0.62-0.66. Moreover, the value of $n$ in region II ($10^4$-$10^5$ Hz) is in-between 0.74-0.79, and region III ($10^5$-$10^6$ Hz) is in-between 0.92-0.95. This study satisfied Jonscher's power law of conductivity and the conduction is due to the small polaron hopping mechanism [165]. The magnitude of $n$ increases with an increasing frequency indicating that the increase of mobility of charge carrier over a long distance to a short distance. The variation of $\sigma_{ac}$ with $\omega$ should be linear as per Jonscher's law. However, mixed polaron (small/large) conductions are responsible for the slight deviation of some composites from linearity [169, 170].

### 4.2.9 Ferroelectric hysteresis

The ferroelectric behavior of the composites evaluated by *P-E* curves is demonstrated in Fig. 4.37. Composites up to $x = 0.30$ show typical ferroelectric characteristics, signifying spontaneous polarization under the applied electric field. These samples display a *P-E* hysteresis loop, which is not fully saturated. Besides, the typical polarization increases with an increase in the ferrite content up to $x = 0.30$, and the highest polarization of 0.34 $\mu C/cm^2$ is obtained for $x = 0.30$ of these samples. The remanent polarization increases with an increase in LNCZFO content. This increase in polarization may be due to the space charge polarization created by the heterogeneity of the interface between the LNCZFO and BGTDO phases. The contribution to polarization due to space charge increases with an increase of LNCZFO content in the composites. This confirms that the presence of nickel ferrite in the composite has a significant effect on the ferroelectric properties of the barium titanate phase. Similar results were reported earlier [191, 192]. The composites of $x = 0.40$ and 0.50 exhibited almost rounded shaped loops, whereas samples of $x = 0.60$ and 1.00 showed a nearly rectangular-shaped loop, suggesting lower

resistive and highly lossy samples from which no inherent ferroelectricity can be found. The significant reason for the lack of ferroelectricity of the samples could be the high leakage current, improper electrode, and barium volatilization. These findings are well compatible with the results reported earlier [172, 179]. The sample of $x = 0.00$ comprises the minimum coercive field, which signifies that the samples can be polarized easily by an adequate electric field.
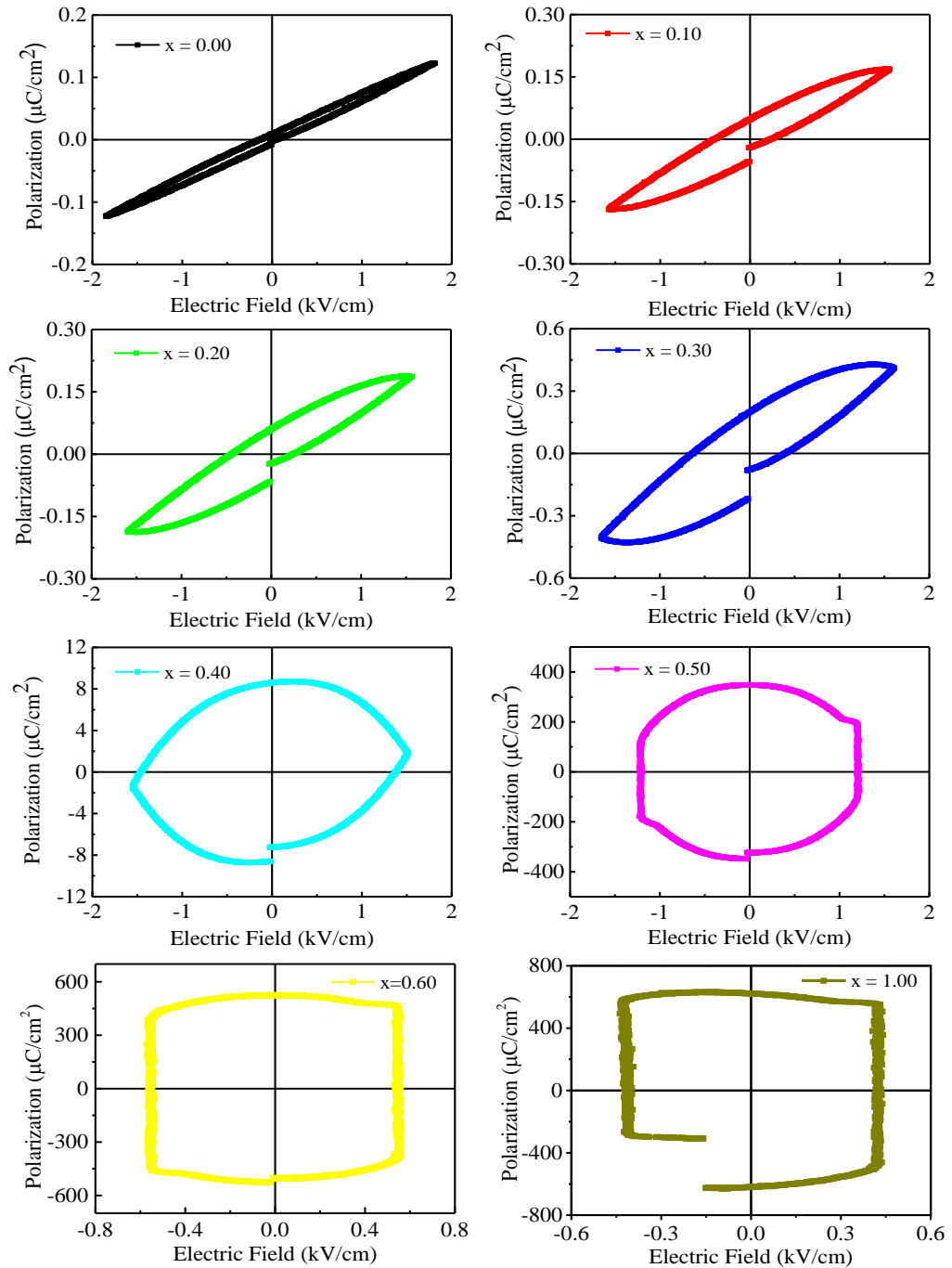


**Fig. 4.37** P-E loops for various $x$LNCZFO+(1-$x$)BGTDO composites.

## 4.2.10 Magnetoelectric voltage coefficient
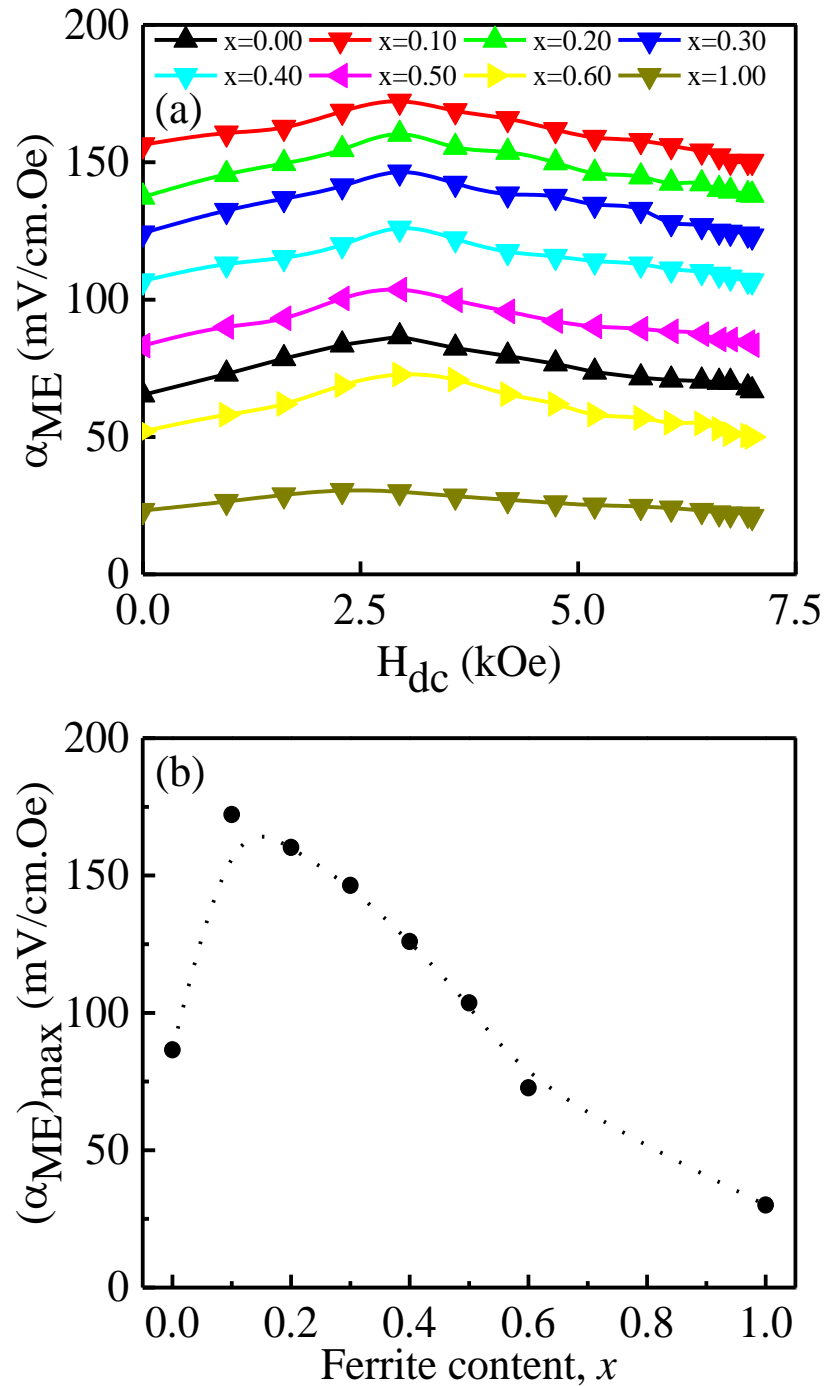


**Fig. 4.38** Variation of (a) $\alpha_{ME}$ with dc magnetic field for various $x$LNCZFO+ $(1-x)$BGTDO composites, and (b) maximum $\alpha_{ME}$ with the ferrite content.

The ME effect is generated in multiferroic materials by the coupling between the ferromagnetic and ferroelectric domains of the materials. The ME response is an interface that incorporates ferroelectric and ferromagnetic phases by the elastic

interactions between them [193]. The strain-mediated ME response was observed depending on the mole percentage of the constituent phases, polarization, electric resistance, and the magnetization of the ferroic phases [173]. The applied magnetic field and the coupling between ferromagnetic and ferroelectric domains establish strain in magnetic domains, which leads to stress in ferroelectric domains. This stress causes polarization of the ferroelectric domains, which creates a voltage in the grains. The $\alpha_{ME}$ variation for all samples with the applied dc magnetic field is shown in Fig. 4.38(a). The figure shows that $\alpha_{ME}$ increases with the applied dc magnetic field reaches a peak and then gradually decreases. A similar result was reported by another researcher [194]. The increase in elastic interaction between the ferroic orders may contribute to this initial increase in $\alpha_{ME}$. The highest ME value for all the composites observed in the 2.8 kOe dc field, suggesting that the LNCZFO phase has reached a saturation state creating a steady electric field in the BGTDO phase, resulting in a decrement of $\alpha_{ME}(= \frac{V_0}{h_0 d})$ with an increment of the magnetic field [156]. Fig. 4.38(b) demonstrated the variation of the maximum $\alpha_{ME}$ of each sample with ferrite content. This figure shows that the maximum $\alpha_{ME}$ decreases with an increase in ferrite of large grain owing to a significant reduction in composite resistivity. The $\alpha_{ME}$ depend on the magnetostriction and piezoelectricity of the ferromagnetic and ferroelectric phases, respectively. Smaller grains are more efficient than larger grains for the enhancement of piezomagnetic and piezoelectric coefficients [175]. However, to achieve a better result in composites, two particular components would be similar, and there would be no disparity between grains. The decreasing of the $\alpha_{ME}$ with an increasing concentration of the LNCZFO phase due to the low resistive ferrite provides poor strain and also establishes a path for the charges created in the ferroelectric phase. Besides, leakage charges are formed by the low-resistive ferrite grain through the mentioned path, which plays an important role to decrease the $\alpha_{ME}$. The higher porosity of the ferrite phase may be another potential reason for decreasing the $\alpha_{ME}$ with the ferrite content. However, the shift of stress between the ferromagnetic and the ferroelectric phases plays an influential role in obtaining high resistance. The maximum $\alpha_{ME}$ of about 172 mV/cmOe was found for $x = 0.10$ composites at 2.8 kOe applied dc magnetic field, which is relatively higher than the results reported earlier [176-178]. Sample with $x = 0.10$ shows the maximum $\alpha_{ME}$ due to the well-connected grains, high density, low porosity, and high resistivity.

**Table 4.7** Comparison of the maximum $\alpha_{ME}$ of various composites prepared by standard solid-state reaction technique with the present composites.

| ME composite | $\alpha_{ME}$ (mV/cm.Oe) | Reference |
|---|---|---|
| $0.15Ni_{0.85}Cd_{0.2}Cu_{0.05}Fe_2O_4+0.85BaTiO_3$ | 17 | [195] |
| $0.2Ni_{0.5}Cu_{0.3}Zn_{0.2}Fe_2O_4+0.8BaTiO_3$ | 141 | [196] |
| $0.1Ni_{0.8}Zn_{0.2}Fe2O4+0.9BaTiO_3$ | 152 | [197] |
| $0.3NiFe_2O_4+0.7PbZr_{0.47}Ti_{0.53}O_3$ | 0.5 | [198] |
| $0.1Ni_{0.8}Zn_{0.2}Fe_2O_4+0.9PbZr_{0.52}Ti_{0.48}O_3$ | 40 | [199] |
| $0.7CuFe_2O_4+0.3BaTiO_3$ | 15 | [200] |
| 0.1LNCZFO+0.9BSTDO | 170 | Present |
| 0.1LNCZFO+0.9BGTDO | 172 | study |

### 4.2.11 Summary of *x*LNCZFO+(1-*x*)BGTDO Composites

The standard solid-state reaction technique was used to synthesize the mixed spinel-perovskite structured $x$LNCZFO+(1-$x$)BGTDO MFCs. The phases of spinel-perovskite were identified by Rietveld refinement analysis of XRD spectra. The $\bar{D}$ enhances with an enhancement of LNCZFO, while the density decreased with an increment of LNCZFO in MFCs. A significant improvement of $\mu'_i$ was observed due to the substitution of BGTDO by strong magnetic LNCZFO. The typical low-frequency (up to $10^6$ Hz) dielectric dispersal behavior is observed due to the Maxwell-Wagner interfacial polarization. The independent nature of $\varepsilon'$ in the high-frequency range (beyond $10^6$ Hz) is due to a lack of response to the fast variation of the applied field by the electric dipoles with higher relaxation time. The sample of $x = 0.60$ is comprised of the maximum dielectric constant of about $10^4$ at 1 kHz. The linearity of the $\sigma_{ac}$ versus $\omega$ plots proves that the conductivity is for a small polaron hopping process. Complex impedance spectroscopy showed that samples of $x = 0.10$, 0.20, 0.30, and 1.00 only have a grain boundary contribution, whereas samples of

$x$ = 0.00, 0.40, 0.50, and 0.60 showed grain and grain boundary effect on the conductivity of the material. Excellent intrinsic ferroelectric properties were obtained for samples up to $x$ = 0.30. The maximum ME coefficient was obtained to be 172 mV/cmOe for the composite of $x$ = 0.10. These results suggest that $x$ = 0.10 may be useful for engineering in lead-free multifunctional devices in the broad frequency ranges.

# 5. CONCLUSIONS

## 5.1 Conclusions

The significant findings of this research work are as follows:

- Multiferroic composites (i) $x$LNCZFO+(1-$x$)BSTDO and (ii) $x$LNCZFO+(1-$x$)BGTDO were prepared by the standard solid-state reaction method.

- The Rietveld refinement of XRD patterns of the composites exhibits both ferrite and ferroelectric phases with no third phase confirmed the excellence of the manufacturing of composite material. The LNCZFO shows a cubic spinel structure. Besides, BSTDO and BGTDO show tetragonal perovskite structure.

- The value of $\rho_B$ increased for $x = 0.10$ sample and then decreases with the addition of the ferrite phase in both $x$LNCZFO+(1-$x$)BSTDO and $x$LNCZFO+(1-$x$)BGTDO composites. Density decreased with the addition of the LNCZFO phase which might be attributed to the fact that the molecular weight of LNCZFO is lower than those of BSTDO and BGTDO. The value of $\rho_{th}$ was found to be higher than that of $\rho_B$. The maximum value of $\rho_B$ (5.87 g/cm$^3$) is found for the 0.10LNCZFO+0.90BSTDO composite.

- The $\bar{D}$ increases with increasing the ferrite phase due to the larger grain diameter of the ferrite phase compare to that of the ferroelectric phase. Lower stress is created due to the high porosity of the ferrite phase which may also lead to an increment in $\bar{D}$ with the ferrite content.

- The elements present in different compositions in EDS are well-matched with their nominal stoichiometry, which confirmed that the preparation condition completely favored the formation of the multiferroic composites.

- The $\mu_i'$ and RQF increase, while tan$\delta_M$ decreases with increasing ferrite content in both series of composites. The relatively larger value of $\mu_i'$ and RQF are obtained for the $x$LNCZFO+(1-$x$)BSTDO composites, and the maximum value of $\mu_i'$ (231) at 100 kHz is found for the LNCZFO sample.

- The $M_s$ increases with increasing ferrite content in both series of composites signifying the enhancement of the ferromagnetic property of the composites. The comparatively higher value of $M_s$ is obtained for the $x$LNCZFO+(1-$x$)BSTDO composites, and a maximum $M_s$ of ~80 emu/g is obtained for LNCZFO sample.

- At lower frequency regions some composites have higher $\varepsilon'$ than the constituent phases due to large interfacial polarization produced by the heterogeneity of the composites. The maximum $\varepsilon'$ of about $10^4$ at 1 kHz is obtained for 0.60LNCZFO+0.40BGTDO composite. The $\varepsilon'$ shows excellent high-frequency stability which can be appropriate for fabricating microwave devices.

- The position of temperature-dependent dielectric peaks shifts to higher temperature with the increase of the ferrite phase in both series of composites due to the heterogeneity, defects, and strain produce between the constituent phases. The shifting of the $T_C$ confirmed the interaction between the constituent phases.

- The contribution of grain and grain boundary in the conduction mechanism of the composites was identified by the complex impedance spectroscopy analysis. Some samples exhibit a single semi-circular arc due to the dominance of grain boundary resistance, whereas other samples show double arcs representing the dominance of grain and grain boundary effect on the conduction mechanism.

- The ac conductivity follows Joncher's power law and the present investigation is satisfied with the small polaron hopping mechanism.

- The *P-E* hysteresis loop of both series of composites was measured. Samples up to $x = 0.30$ for $x$LNCZFO+(1-$x$)BSTDO composites and up to $x = 0.20$ for $x$LNCZFO+(1-$x$)BGTDO composites show a typical ferroelectric nature and the rest of the samples show lossy behavior. The maximum typical polarization of 0.39 $\mu$C/cm$^2$ is obtained for 0.30LNCZFO+0.70BSTDO composite.

- The ME coupling between the magnetic and ferroelectric order of both series of composites was determined by the calculation of $\alpha_{ME}$. The maximum $\alpha_{ME}$ of 172 mV/cmOe is obtained for 0.10LNCZFO+0.90BGTDO composite.

**Table 5.1** Comparison of different properties of $\bar{D}$ in μm, $\mu_i'$ at 100 kHz, $M_s$ in emu/g, $\varepsilon'$ at 100 kHz, and $\alpha_{ME}$ in mV/cmOe of the present composites.

| Content, $x$ | $x$LNCZFO+(1-$x$)BSTDO | | | | | $x$LNCZFO+(1-$x$)BGTDO | | | | |
|---|---|---|---|---|---|---|---|---|---|---|
| | $\bar{D}$ | $\mu_i'$ | $M_s$ | $\varepsilon'$ | $\alpha_{ME}$ | $\bar{D}$ | $\mu_i'$ | $M_s$ | $\varepsilon'$ | $\alpha_{ME}$ |
| 0.00 | 0.33 | 25 | 2.43 | 1397 | 113 | 0.32 | 26 | 2.26 | 1452 | 86 |
| 0.10 | 0.40 | 38 | 7.03 | 401 | 170 | 0.38 | 30 | 6.92 | 455 | 172 |
| 0.20 | 0.44 | 43 | 11.63 | 379 | 162 | 0.42 | 32 | 9.89 | 388 | 160 |
| 0.30 | 0.49 | 45 | 14.92 | 554 | 149 | 0.48 | 35 | 13.14 | 594 | 146 |
| 0.40 | 0.52 | 48 | 22.80 | 904 | 129 | 0.51 | 41 | 20.55 | 1124 | 125 |
| 0.50 | 0.57 | 49 | 28.06 | 1299 | 108 | 0.55 | 45 | 26.12 | 1308 | 103 |
| 0.60 | 0.66 | 54 | 32.66 | 1658 | 95 | 0.64 | 48 | 31.85 | 2329 | 72 |

## 5.2 Suggestions for further research

Further studies on different aspects are possible for the fundamental interest of the studied materials.

- Neutron diffraction analysis and Mössbauer spectroscopy can be performed to know the cation distribution in A- and B-sites, and also to know the valence state of the ions.

- Transmission electron micrographs may be taken for a proper understanding of the domains.

- Different preparation techniques (e.g., sol-gel, Spray-drying, and auto-combustion) may be followed to prepare the samples for comparing the properties of the present study.

# Novelty of the Present Research

The novelty of this research is that composites formed from two ferroic phases exhibit large $\alpha_{ME}$ (172 mV/cmOe for $0.10Li_{0.1}Ni_{0.30}Cu_{0.1}Zn_{0.4}Fe_{2.1}O_4 + 0.90Ba_{0.95}Gd_{0.05}Ti_{0.95}Dy_{0.05}O_3$ composite) at RT, a suitable alternative of Pb-based multiferroics for the application of modern multifunctional devices.

# References

[1]     Schmid, H., "Multi-ferroic magnetoelectric", *Ferroelectrics*, vol.162, pp. 317-338, 1994.

[2]     Shin, K.H., Inoue, M., Arai, K.I., "Elastically coupled magneto-electric elements with highly magnetostrictive amorphous films and PZT substrates", *Smart Mater. Struct.*, vol. 9, pp. 357-361, 2000.

[3]     Nan, C.W., Bichurin, M.I., Dong, S., Viehland, D. and Srinivasan, G., "Multiferroic magnetoelectric composites: Historical perspective, status, and future directions", *J. Appl. Phys.*, vol. 103, 031101, 2008.

[4]     Smolenskiĭ, G.A., Chupis, I.E., "Ferroelectromagnets", *Sov. Phys. Usp.*, vol. 25, pp. 475-493, 1982.

[5]     Bibes, M., Barthélémy, A., "Multiferroics: towards a magnetoelectric memory", *Nat. Mater.*, vol. 7, pp. 425-426, 2008.

[6]     Palneedi, H., Annapureddy, V., Priya, S., Ryu, J., "Status and perspectives of multiferroic magnetoelectric composite materials and applications", *Actuators*, vol. 5, pp. 1-35, 2016.

[7]     Vopsaroiu, M., Blackburn, Muniz-Piniella, J.A., Cain, M.G., "Multiferroic magnetic recording read head technology for 1 Tbit/ in.2 and beyond", *J. Appl. Phys.*, vol. 103, pp. 07F506(1–3), 2008.

[8]     Wang, Y., Li, J., Viehland, D., "Magnetoelectrics for magnetic sensor applications: status, challenges and perspectives", *Mater. Today*, vol. 17, pp. 269-275, 2014.

[9]     Lu, C., Li, P., Wen, Y., Yang, A., "Zero-biased magnetoelectric composite $Fe_{73.5}Cu_1Nb_3Si_{13.5B9}$/Ni/Pb$(Zr_{1-x},Ti_x)O_3$ for current sensing", *J. Alloys Compd.*, vol. 589, pp. 498-501, 2014.

[10]    Scott, J., "Multiferroic memories", *Nat. Mater.,* vol. 6, pp. 256-257, 2007.

[11]    Vopson, M.M., "Fundamentals of multiferroic materials and their possible applications", *Crit. Rev. Solid State Mater. Sci.,* vol. 40, pp. 223-250, 2015.

[12]    Proceedings of the MEIPIC-3, edited by M. Bichurin, Novgorod, Russia, 16–20 September 1996 [*Ferroelectrics* 204 (1997)].

[13] Proceedings of the MEIPIC-4, edited by M. Bichurin, Novgorod, Russia, 16–19 October 2001 [*Ferroelectrics,* pp. 279–280 (2002)].

[14] Magnetoelectric Interaction Phenomena in Crystals, edited by M. Fiebig, V. V. Eremenko, and I. E. Chupis(Kluwer, Dordrecht, 2004); Proceedings of the MEIPIC-5, Sudak, Ukraine, 21–24 September 2003.

[15] Röntgen, W. C., "Description of the apparatus with which the experiments on the electrodynamic effect of moving dielectric were performed", *Ann. Phys.*, vol. 35, pp. 264-283, 1888.

[16] Cure, P., "First discussion of an intrinsic correlation between magnetic and electric properties", *J. Phys.*, vol. 3, pp. 393-417, 1894.

[17] Valasek, J., "Piezoelectric and allied phenomena in rochelle salt", *Phys. Rev.*, vol. 15, pp. 537-538, 1920.

[18] Fox, D. L., Scott, J. F., "Ferroelectrically induced ferromagnetism", *J. Phys. C*, vol. 10, pp. 329–331, 1977.

[19] Debye, P., "Remark on some new experiments on a magneto-electric directional effect," *Z. Phys.*, vol. 36, p. 300, 1926.

[20] Van, S. J., "Product Properties: A New Application of Composite Materials", *Philips Res. Rep.*, vol. 27, pp. 28-37, 1972.

[21] Lopatin, S., Lopatin, I., Lisnevskaya, I., "Magnetoelectric PZT/ferrite composite material", *Ferroelectrics*, vol. 162, pp. 63-68, 1994.

[22] Bichurin, M. I., Kornev, I. A., Petrov, V. M., Lisnevskaya, I., "Investigation of magnetoelectric interaction in a composite", *Ferroelectrics*, vol. 204, pp. 289-297, 1997.

[23] Cheong, S. W., Mostovoy, M., "Multiferroics: a magnetic twist for ferroelectricity", *Nat. Mater.*, vol. 6, pp. 13-20, 2007.

[24] Nan, C. W., "Magnetoelectric effect in composites of piezoelectric and piezomagnetic phases", *Phys. Rev.*, vol. B50, pp. 6082-6088, 1994.

[25] Erenstein, W., Mathur, N.D., Scott, J.F., "Multiferroic and magnetoelectric materials", *Nature*, vol. 442, pp. 759-765, 2006.

[26] Bammannavar, B.K., Naik, L.R., "Electrical properties and magnetoelectric effect in $(x)Ni_{0.5}Zn_{0.5}Fe_2O_4+(1-x)$BPZT composites", *Smart Mater. Struct.*, vol. 18, 085013, 2009.

[27] Ryu, J., Priya, S., Uchino, K., Kim, H-E., "Magnetoelectric Effect in Composites of Magnetostrictive and Piezoelectric Materials", *J. Electroceramics*, vol. 8, pp. 107–119, 2002.

[28] Hemeda, O.M., Tawfik, A., Amer, M.A., Kamal, B.M., El Refaay, D.E., "Structural, spectral and dielectric properties of piezoelectric–piezomagnetic composites", *J. Magn. Magn. Mater.*, vol. 324, pp. 3229-3237, 2012.

[29] Rahaman, Md. D., Saha, S.K., Ahmed, T.N., Saha, D.K., Hossain, A.K.M. Akther, "Magnetoelectric effect of $(1-x)Ba_{0.5}Sr_{0.5}Zr_{0.5}Ti_{0.5}O_3+ (x)Ni_{0.12}Mg_{0.18}Cu_{0.2}Zn_{0.5}Fe_2O_4$ composites", *J. Magn. Magn. Mater.*, vol. 371, pp. 112-120, 2014.

[30] Grigalaitis, R., Petrović, M.M. Vijatović, Bobić, J.D., Dzunuzovic, A., Sobiestianskas, R., Brilingas, A., Stojanović, B.D., Banys, J., "Dielectric and magnetic properties of $BaTiO_3+NiFe_2O_4$ multiferroic composites", *Ceram. Int.,* vol. 40, pp. 6165-6170, 2014.

[31] Sadhana, K., Murthy, S. R., Jie, S., Xie, Y., Liu, Y., Zhan, Q., Li, R. W., "Magnetic field-induced polarization and magnetoelectric effect of $Ba_{0.8}Ca_{0.2}TiO_3+Ni_{0.2}Cu_{0.3}Zn_{0.5}Fe_2O_4$ nanomultiferroic", *J. Appl. Phys.*, vol. 113, pp. 1-3, 2013.

[32] Duong, V., Groessinger, R., Turtelli, R., "Driving mechanism for magnetoelectric effect in $CoFe_2O_4+BaTiO_3$ multiferroic composite", *J. Magn. Magn. Mater.*, vol. 310, pp. 1157-1159, 2007.

[33] Su, L., Liu, P., He, Y., Zhou, J., Cai, L., Liu, C., Zhang, H., "Electrical and magnetic properties of low temperature sintered $xBa_{0.6}Sr_{0.4}TiO_3+(1-x)Ni_{0.2}Cu_{0.2}Zn_{0.62}O(Fe_2O_3)_{0.98}$ composite ceramics", *J. Alloys Compd.*, vol. 494, pp. 330-335, 2010.

[34] Shovon, O.G., Rahaman, M.D., Tahsinz, S., Hossain, A.K.M. Akther, "Synthesis and characterization of $(100-x)Ba_{0.82}Sr_{0.03}Ca_{0.15}Zr_{0.10}Ti_{0.90}O_3+ (x)Mg_{0.25}Cu_{0.25}Zn_{0.5}Mn_{0.05}Fe_{1.95}O_4$ composites with improved magnetoelectric voltage coefficient", *J. Alloys Compd*, vol. 735, pp. 291-311, 2018.

[35] Kitahara, N., Kageyama, H., Kawasaki, T., Abe, K., Itoh, H., Takahashi, J., "Low-temperature fabrication of NiCuZn Ferrite+(Ba$_{0.7}$Sr$_{0.3}$)TiO$_3$ composites using granulated powders", *J. Ceram. Soc. JAPAN J CERAM SOC JPN*, vol. 121, pp. 54-61, 2013.

[36] Qinghui, Y., Huaiwu, Z., Qiye, W., Yingli, L., "Electromagnetic properties of microwave sintered ferromagnetic-ferroelectric composites for application in low temperature co-fired ceramic devices", *J. Appl. Phys.*, vol. 109, 07D733, 2011.

[37] Jia, L., Zhang, H., Li, T., Liu, Y., Wen, Q., Shen, J., "Dielectric and magnetic properties of 0.4PZT+0.6NiCuZn-ferrite composites modified with P$_2$O$_5$-Co$_2$O$_3$", *J. Appl. Phys.*, vol. 107, 09E3093, 2010.

[38] Sadhana, K., Praveena, K., Murthy, S., "Magnetic properties of $x$Ni$_{0.53}$Cu$_{0.12}$Zn$_{0.35}$Fe$_{1.88}$O$_4$+(1-$x$)BaTiO$_3$ nanocomposites", *J. Magn. Magn. Mater.*, vol. 322, pp. 3729-3736, 2010.

[39] Miah, M., Khan, M., Hossain, A.K.M. Akther, "Synthesis and enhancement of multiferroic properties of ($x$)Ba$_{0.95}$Sr$_{0.05}$TiO$_3$+(1-$x$)BiFe$_{0.90}$Dy$_{0.10}$O$_3$ ceramics", *J. Magn. Magn. Mater.*, vol. 397, pp. 39-50, 2016.

[40] Miah, M., Khan, M., Hossain, A.K.M. Akther, "Weak ferromagnetism and magnetoelectric effect in multiferroic $x$Ba$_{0.95}$Sr$_{0.05}$TiO$_3$+(1-$x$)BiFe$_{0.9}$Gd$_{0.1}$O$_3$ relaxors", *J. Magn. Magn. Mater.*, vol. 401, pp. 600-611, 2016.

[41] Mudinepalli, V.R., Song, S-H., Li, J.-Q., Murty, B., "Magnetoelectric properties of lead-free Ni$_{0.93}$Co$_{0.02}$Mn$_{0.05}$Fe$_{1.95}$O$_4$+Na$_{0.5}$Bi$_{0.5}$TiO$_3$ multiferroic composites synthesized by spark plasma sintering", *J. Magn. Magn. Mater.*, vol. 386, pp. 44-49, 2015.

[42] Babu, S. N., Suryanarayana,S., Bhimasankaram, T., "Magnetic and magnetoelectric characterization of Ni$_{0.93}$Co$_{0.02}$Mn$_{0.05}$Fe$_{1.95}$O$_4$ and PZT composites", *J. Alloys Compd.*, vol. 473, pp. 418-422, 2009.

[43] Saha, S.K., Rahaman, M.D., Zubair, M., Hossain, A.K.M. Akther, "Structural, electrical, magnetic and magnetoelectric properties of (1-$x$)[Ba$_{0.6-x}$Ca$_x$Sr$_{0.4}$Zr$_{0.25}$Ti$_{0.75}$O$_3$]+($x$)[(Li$_{0.5}$Fe$_{0.5}$)$_{0.4}$Ni$_{0.18}$Cu$_{0.12}$Zn$_{0.3}$Fe$_2$O$_4$] composites", *J. Alloys Compd.*, Vol. 698, pp. 341-356, 2017.

[44] Lin, Y., Zhang, J., Yang, H., Wang, T., "Excellent piezoelectric and magnetoelectric properties of the $(K_{0.45}Na_{0.55})_{0.98}Li_{0.02}(Nb_{0.77}Ta_{0.18}Sb_{0.05})O_3$ +$Ni_{0.37}Cu_{0.20}Zn_{0.43}Fe_{1.92}O_{3.88}$ laminated composites". *J. Alloys Compd.*, vol. 692, pp. 86-94, 2017.

[45] Mudinepalli, V.R, Song, S., Murty, B., "Enhanced magnetoelectric properties in lead-free $Ni_{0.83}Co_{0.15}Cu_{0.02}Fe_{1.9}O_{4-\delta}$+$Na_{0.5}Bi_{0.5}TiO_3$ composites by spark plasma sintering", *Scr. Mater.*, vol. 82, pp. 9-12, 2014.

[46] Kulkarni, S., Kanamadi, C., Chougule, B., "Magnetic and dielectric properties of $Ni_{0.8}Co_{0.1}Cu_{0.1}Fe_2O_4$+PZT composites", *J Phys Chem Solids*, vol. 67, pp. 1607-1611, 2006.

[47] Kulawik, J., Guzdek, P., Szwagierczak, D., Stoch, A., "Dielectric and magnetic properties of bulk and layered tape cast $CoFe_2O_4$+$Pb(Fe_{0.50}Ta_{0.50})O_3$ composites", *Compos. Struct.*, vol. 92, pp. 2153-2158, 2010.

[48] Devan, R.S., Kanamadi, C.M., Lokare, S.A., Chougule, B.K., "Electrical properties and magnetoelectric effect measurement in $(x)Ni_{0.8}Cu_{0.2}Fe_2O_4$+ $(1-x)Ba_{0.9}Pb_{0.1}Ti_{0.9}Zr_{0.1}O_3$ composites", *Smart Mater. Struct.*, vol. 15, pp. 1877-1881, 2006.

[49] Islam, M.A., Hasan, Mehadi, Hossain, A.K.M. Akther, "Enhancement of initial permeability and reduction of loss factor in Zn substituted nanocrystalline $Li_{0.35-0.5x}Ni_{0.3}Zn_xFe_{2.35-0.5x}O_4$", *J. Magn. Magn. Mater.*, vol. 424, pp. 108-114, 2017.

[50] Parvin, Roksana, Momin, A.A., Hossain, A.K.M. Akther, "Improvement of microstructure, initial permeability, magnetization and dielectric properties of nanocrystalline $Li_xCu_{0.1}Co_{0.1}Zn_{0.8-2x}Fe_{2+x}O_4$", *J. Magn. Magn. Mater.*, vol. 401, pp. 760-769, 2016.

[51] Hossain, A.K.M. Akther, Rahman, M.L.," Enhancement of microstructure and initial permeability due to Cu substitution in $Ni_{0.50-x}Cu_xZn_{0.50}Fe_2O_4$ ferrites", *J. Magn. Magn. Mater.*, Vol-323, pp. 1954-1962, 2011.

[52] Lu, Da-Yong, Cui, Shu-Zhen, Liu, Qiao-Li, Sun, Xiu-Yun, "Dielectric properties and defect chemistry of barium titanate ceramics co-doped R and Dy ions (R = Eu, Gd, Tb)", *Ceram. Int.*, vol. 42, pp. 14364–14373, 2016.

[53] Borah, Manjit, Mohanta, Dambarudhar, "Effect of $Gd^{3+}$ doping on structural, optical and frequency-dependent dielectric response properties of pseudo-cubic $BaTiO_3$ nanostructures", *Appl. Phys. A.*, vol. 115, pp. 1057-1067, 2013.

[54] Ganguly, M., Rout, S.K., Woo, W.S., Ahn, C.W., Kim, I.W., "Characterization of A-site deficient samarium doped barium titanate", *Physica B*, vol. 411, pp. 26-34, 2013.

[55] Snelling, E. C., "Soft ferrites: Properties and Applications", First Edition. London: Ilife Books Ltd., 1969.

[56] Goldman, A., Modern Ferrite Technology, Van Nostrand Reinhold, New York, 1990.

[57] Heck, C., "Magnetic Materials and Their Applications", London: Butterworths, 1974.

[58] Van Run, A. M., Terrell, D. R., Scholing, J.H., "A site Grown Eutectic Magnetoelectric Composite Material Part 2 Physical Properties", *J. of mat. Sci.*, vol. 9, pp. 1710-1714, 1974.

[59] Goldman, A., "Modern ferrite technology", Springer Science+Business Media, Inc., Pittsburgh, USA, 2006.

[60] Cullity, B.D., "Introduction to Magnetic Materials", Addison-Wisley Publishing Company, Inc., California, 1972.

[61] Macedo, PB, Moynihan, CT, Bose, R, "Role of ionic diffusion in polarization in vitreous ionic conductors", *Phys. Chem. Glasses*, vol. 13, pp. 171-179, 1972.

[62] Liu, J.J, Duan, C.G, Yin, W.G., Mei, W.N, Smith, RW, Hardy, JR, "Dielectric permittivity and electric modulus in $Bi_2Ti_4O_{11}$", *J. Chem. Phys.*, vol. 119, pp. 2812-2819, 2003.

[63] Ganguli, M., Harish, M. Bhat, Rao, K.J., "Role of PbO in lithium ion transport in $Li_2O–PbO–B_2O_3$ glasses", *Mater. Res. Bull*, vol. 34, pp. 1757-1772, 1999.

[64] Bera, J., Rout, S. K., "Synthesis of $(Ba_{1-x}Sr_x)(Ti_{0.5}Zr_{0.5})O_3$ ceramics and effect of Sr content on room temperature dielectric properties", *J. Electroceram*, vol. 18, pp. 33-37, 2007.

[65] Bhaskar, S.y. Redd, Rao, K. Prasad, Ramachandra Rao, M. S., "Structural and dielectric characterization of Sr substituted $Ba(Zr, Ti)O_3$ based functional materials", *Appl. Phys. A.*, vol. 89, pp. 1011-1015, 2007.

[66] Hristoforou, E., Ktena, A., "Magnetostriction and magnetostrictive materials for sensing applications", *J. Magn. Magn. Mater.*, vol. 316, pp. 372–378, 2007.

[67] Patankar, V.L., Mathe, Mahajan, R.P., Patil, S.A., Reddy, R.M., Siva Kumar, K.V., "Dielectric behavior and magnetoelectric effect in $CuFe_2O_4+Ba_{0.8}Pb_{0.2}TiO_3$ composites," *Mater. Chem. Phys.*, vol. 72, pp. 23–29, 2001.

[68] Kittel, C. A., "Introduction to Solid State Physics", 7th ed., *John Wiley & Sons Inc.*, New York, 1996.

[69] Jaffe, B., Cook, W. R. and Jaffe, H., "Piezoelectric Ceramics", *Academic Press*, 1971.

[70] Hur, N., Park, S., Sharma, P.A., Ahn, J.S., Guha, S., Cheong, S.W., "Electric polarization reversal and memory in a multiferroic material induced by magnetic fields", *Nature*, vol. 429, pp. 392–395, 2004.

[71] Haertling, G. H., "Ferroelectric Ceramic: History and Technology", *J. Ame. Cera. Soci.*, vol. 82, pp. 797-818, 1999.

[72] Gabal, M.A., "Effect of Mg substitution on the magnetic properties of Ni-Cu-Zn ferrite nanoparticles prepared through a novel method using egg white", *J. Magn. Magn. Mater.*, vol. 321, pp. 3144-3148, 2009.

[73] Goldschmidt, V.M., "The laws of crystal chemisty" *Naturwissenschaften*, vol. 14, pp. 477-485, 1926.

[74] Wang, J., Neaton, J. B., Zheng, H., Nagarajan, V., Ogale, S.B., Liu, B., Viehland, D., Vaithyanathan, V., Schlom, D.G., Waghmare, U.V., Spaldin, N.A., Rabe, K.M., Wuttig, M., Ramesh, R., "Epitaxial $BiFeO_3$ multiferroic thin film heterostructures", *Science*, vol. 299, pp.1719-1722, 2003.

[75] Kimura, K., Goto, T., Shintani, H., Ishizaka, K., Arima, T., Tokura, Y., "Magnetic control of ferroelectric Polarization" *Nature*, vol. 426, pp. 55-58, 2003.

[76] Spaldin, N.A., Fiebig, M., "The Renaissance of magnetoelectric multiferroics", *Science*, vol. 309, pp. 391-392, 2005.

[77] Kao, K.C., "Dielectric phenomena in solids", *Elsevier Academic Press*, USA, 2004.

[78]  Pelaiz-Barranco, A, Guerra, J.D.S., "Dielectric relaxation phenomenon in ferroelectric perovskite-related structures", Edited by Indrani Coondoor, Published by In Tech, Rijeka, Croatia, 2010.

[79]  Fiebig, M. "Revival of the magnetoelectric effect", *J. Phys. D: Appl. Phys.,* vol. 38, pp. 123-129, 2005.

[80]  Tokura, Y., Seki, S.*,* Multiferroics with spiral spin orders", *Adv. Mater.,* vol. 22*,* pp. 1554-1565, 2010*.*

[81]  Suchtelen, J.V., "Product Properties: A New Application of Composite Materials", *Philips Res. Rep.*, vol. 27, pp. 28-37, 1972.

[82]  Fu, C., Yang, C., Chen, H., Wang, Y., Hu, L., "Microstructure and dielectric properties of $Ba_xSr_{1-x}TiO_3$ ceramics", *Mater. Sci. Eng: B*, vol. 119, pp. 185-188, 2005.

[83]  Kulkarni, S., Devan, R., Chougule, B., "Electrical and magnetoelectric properties of $Ni_{0.8}Co_{0.1}Cu_{0.1}Fe_2O_4+PbZr_{0.5}Ti_{0.5}O_3$ composites", *J. Alloys Compd*, vol. 455, pp. 336-339, 2008.

[84]  Panigrahi, M., Panigrahi, S., "Diffuse phase transition and dielectric study in $Ba_{0.95}Ca_{0.05}TiO_3$ ceramic", *Physica B Condens. Matter*, vol. 405, pp. 2556-2559, 2010.

[85]  Thakur, O., Prakash, C., Agrawal, D.K., "Dielectric behavior of $Ba_{0.95}Sr_{0.05}TiO_3$ ceramics sintered by microwave", *Mater. Sci. Eng. B:,* vol. 96, pp. 221-225, 2002.

[86]  Pahuja, P., Prakash, C., Tandon, R., "Comparative study of magnetoelectric composite system $Ba_{0.95}Sr_{0.05}TiO_3+Ni_{0.8}Co_{0.2}Fe_2O_4$ with ferrite prepared by different methods", *Ceram. Int.,* vol. 40, pp. 5731-5743, 2014.

[87]  Devan, R.S., Kolekar, Y.D., Chougule, B.K., "Magnetoelectric effect and electrical properties in $BTO+Ni_{0.93}Co_{0.02}Cu_{0.05}Fe_2O_4$ particulate composites", *J. Alloys Compd*, vol. 461, pp. 678-683, 2008.

[88]  Lokare, S.A., Devan, R.S., Chougule, B.K., "Structural analysis and electrical properties of ME composites", *J. Alloys Compd*, vol. 454, pp. 471-475, 2008.

[89] Chougule, S.S., Patil, D.R., Chougule, B.K., "Electrical conduction and magnetoelectric effect in ferroelectric rich $(x)Ni_{0.9}Zn_{0.1}Fe_2O_4+(1-x)PZT$ ME composites", *J. Alloys Compd*, vol. 452, pp. 205-209, 2008.

[90] Burange, N.M., Chougule, S.S., Patil, D.R., Devan, R.S., Kolekar, Y.D., Chougule, B.K., "Studies on structural, electrical and magnetic properties of $xNi_{0.5}Zn_{0.3}Co_{0.2}Fe_2O_4+(1-x)BaTiO_3$ composites", *J. Alloys Compd*, vol. 479, pp. 569-573, 2009.

[91] Lokare, S.A., Patil, D.R., Chougule, B.K., "Structural, dielectric and magnetoelectric effect in $xBaTiO_3+(1-x)Ni_{0.93}Co_{0.02}Mn_{0.05}Fe_2O_4$ ME composites", *J. Alloys Compd*, vol. 453, pp. 58-63, 2008.

[92] Patil, D.R., Lokare, S.A., Devan, R.S., Chougule, S.S., Kolekar, Y.D., Chougule, B.K., "Dielectric properties and magnetoelectric effect of $(x)NiFe_2O_4+(1-x)Ba_{0.8}Sr_{0.2}TiO_3$ composites", *J Phys Chem Solids*, vol. 68, pp. 1522-1526, 2007.

[93] Kanamadi, C.M., Chougule, B.K., "Studies on Electrical Properties and Magnetoelectric Effect of $(x)Ni_{0.8}Cu_{0.2}Fe_2O_4+(1-x)Ba_{0.8}Pb_{0.2}Ti_{0.8}Zr_{0.2}O_3$ Composites", *J. Electroceramics*, vol. 15, pp. 123-128, 2005.

[94] Yang, Haibo, Zhang, Ge, Lin, Ying, "Enhanced magnetoelectric properties of the laminated $BaTiO_3+CoFe_2O_4$ composites", *J. Alloys Compd*, vol. 644, pp. 390-397, 2015.

[95] Patil, D.R., Chougule, B.K, "Studies on magnetic and magnetoelectric properties of the $NiFe_2O_4+Ba_{0.7}Sr_{0.3}TiO_3$ composites", *J. Mater. Sci. Mater*, vol. 20, pp. 398-402, 2009.

[96] Kanakadurga, M., Raju, P., Murthy, S.R., "Preparation and characterization of $BaTiO_3+MgCuZnFe_2O_4$ nanocomposites", *J. Magn. Magn. Mater.*, vol. 341, pp. 112-117, 2013.

[97] Pahuja, P., Tomar, Amit, Tandon, R.P., "Modification in properties of barium titanate on $Sm^{3+}$ substitution", *Ferroelectrics*, vol. 516, pp. 127-130, 2017.

[98] Goldman, A., "Handbook of Modern Ferromagnetic Materials", Kulwer Acad. Pub, Boston, U.S.A, 1999.

[99] Valenzuela, R., "Magnetic Ceramics", Cambridge University Press, Cambridge, 1994.

[100] Moulson, A.J., Herbert, J.M., "Electroceramics: Materials, Properties, and Application", Chapman & Hall, UK, 1990.

[101] Baaziz, H., Maaloul, N.K., Tozri, A., Rahmouni, H., Mizouri, S., Khirouni, K., Dhahri, E., "Effect of sintering temperature and grain size on the electrical transport properties of $La_{0.67}Sr_{0.33}MnO_3$ manganite", *Chem. Phys. Lett*, vol. 40, pp. 77-81, 2015.

[102] Brook, R.J., "Sintering: An Overview", Concise Encyclopedia of Advanced Ceramic Materials, Pergamon Press, Oxford, vol. 438-440, 1991.

[103] Reijnen, P., "Science of Ceramics, Academic Press", London, 1967.

[104] Kingery, W.D., Bowen, H.K., Uhlman, D.R., "Introduction to Ceramics", 2nd edition, Wiley Interscience, New York, 1976.

[105] Xu, Y., "Ferroelectric materials and their applications", Elsevier Science Pub. Co., New York, USA, 1991.

[106] Kittel, C. A., "Introduction to Solid State Physics", 7th ed., John Wiley & Sons Inc., New York, 1996.

[107] McCusker, L.B., Von Dreele, R.B., Cox, D.E., Louërd D., Scardie, P., "Rietveld refinement guidelines", *J. Appl. Crystallogr*, vol. 32, pp. 36-50, 1999.

[108] Coble, R.L., Burke, J.E., "On the reactivity of solids", 4th Int. Symp., 30 May-4 June, *Amsterdam*, pp. 38-51, 1960.

[109] Grossinger, R., Duong, G.V., Sato-Turtelli, R., "The physics of magnetoelectric composites", *J. Magn. Magn. Mater.*, vol. 320, pp. 1972-1977, 2008.

[110] Kanamadi, C., Kim, J., Yang, H., Moon, B., Choi, B., Jeong, J., "Magnetoelectric effect and complex impedance analysis of $xCoFe_2O_4$+ $(1-x)Ba_{0.8}Sr_{0.2}TiO_3$ multiferroics", *J. Alloys Compd*, vol. 481, pp. 781-785, 2009.

[111] Qi, X., Zhou, J., Yue, Z., Gui, Z., Li, L., Buddhudu, S., "A ferroelectric ferromagnetic composite material with significant permeability and permittivity", *Adv. Funct. Mater.*, vol. 14, pp. 920-926, 2004.

[112] Ciomaga, C.E., Buscaglia, M.T., Buscaglia, V., Mitoseriu, L., "Oxygen deficiency and grain boundary-related giant relaxation in Ba(Zr, Ti)$O_3$ ceramics", *J. Appl. Phys.*, vol. 110, 114110, 2011.

[113] Kanamadi, C., Pujari, L., Chougule, B., "Dielectric behaviour and magnetoelectric effect in $x$Ni$_{0.8}$Cu$_{0.2}$Fe$_2$O$_4$+(1-$x$)Ba$_{0.9}$Pb$_{0.1}$Ti$_{0.9}$Zr$_{0.1}$O$_3$ ME composites", *J. Magn. Magn. Mater*, vol. 295, pp. 139-144, 2005.

[114] Badapanda, T., Rout, S., Panigrahi, S., Sinha, T., "Relaxor behavior of (Ba$_{0.5}$Sr$_{0.5}$)(Ti$_{0.6}$Zr$_{0.4}$)O$_3$ ceramics", *Bull. Mater. Sci.*, vol. 31, pp. 897-901, 2008.

[115] Rout, S., Barhai, P., Panigrahi, S., Kim, I., "Synthesis of (Ba$_{0.5}$Sr$_{0.5}$)(Ti$_{1-x}$Zr$_x$)O$_3$ ceramics: Effect of Zr content on room temperature electrical properties", *J. Electroceramics*, vol. 23, pp. 37-42, 2009.

[116] Rani, R., Singh, S., Juneja, J., Raina, K., Prakash, C., "Dielectric properties of Zr substituted BST ceramics", *Ceram. Int*, vol. 37, pp. 3755-3758, 2011.

[117] Li, W., Xu, Z., Chu, R., Fu, P., Zang, G., "High piezoelectric d$_{33}$ coefficient of lead-free (Ba$_{0.93}$Ca$_{0.07}$)(Ti$_{0.95}$Zr$_{0.05}$)O$_3$ ceramics sintered at optimal temperature", *Mater. Sci. Eng. B*:, vol. 176, pp. 65-67, 2011.

[118] Tavade, C.M., Sagar, R., Madolappa, S., Raibagkar, R., "Synthesis and structural parameters of (Ba$_{0.6}$Sr$_{0.4}$)(Zr$_{1-x}$Ti$_x$)O$_3$ ($x$ = 0.4 and 0.5) nanoceramics", *World J. Sci. Technol*, vol. 1, pp. 12-14, 2011.

[119] Sujatha, C., Reddy, K.V., Babu, K.S., Reddy, A.R., Rao, K., "Structural and magnetic properties of Mg substituted NiCuZn nano ferrites", *Physica B Condens. Matter*, vol. 407, pp. 1232-1237, 2012.

[120] Suchtelen, J. Van, "Coarsening of eutectic structures during and after unidirectional growth", *J Cryst Growth.*, vol. 43, pp. 28-46, 1972.

[121] Sattar, A.A., El-Sayed, H.M., El-shookrofy, K.M., El-Tabey, M.M., "The effect of Al-substitution on the structure and electrical properties of Mn-Ni-Zn ferrites" *J. Mater. Sci*, vol. 40, pp. 4873-4879, 2005.

[122] Nakamura, T., "Snoek's limit in high-frequency permeability of polycrystalline Ni–Zn, Mg–Zn, and Ni–Zn–Cu spinel ferrites", *J. Appl. Phys.*, vol. 88, pp. 348-353, 2000.

[123] Tsutaoka, T., Ueshima, M., Tokunaga, T., Nakamura, T., Hatakeyama, K., "Frequency dispersion and temperature variation of complex permeability of Ni-Zn ferrite composite materials", *J. Appl. Phys.*, vol. 78, pp. 3983-3991, 1995.

[124] Globus, A., Duplex, P., Guyot, M., "Determination of initial magnetization curve from crystallites size and effective anisotropy field", *IEEE Transactions on Magnetics*, vol. 7, pp. 617-622, 1971.

[125] Snoek, J.L., "Dispersion and absorption in magnetic ferrites at frequencies above one Mc/s", *Physica*, vol. 14, pp. 207-217, 1948.

[126] Haque, M. Manjurul, Huq, M., Hakim, M.A., "Influence of CuO and sintering temperature on the microstructure and magnetic properties of Mg–Cu–Zn ferrites", *J. Magn. Magn. Mater.*, vol. 320, pp. 2792-2799, 2008.

[127] Xuegang Lu, Gongying Liang, Yumei Zhang, Wei Zhang, "Synthesis of $FeNi_3/(Ni_{0.5}Zn_{0.5})Fe_2O_4$ nanocomposite and its high-frequency complex permeability", *Nanotechnology*, vol. 18, 015701, 2007.

[128] Pradhan, D.K., Puli, V.S., Tripathy, S.N., Scott, J.F., Katiyar, R.S., "Room-temperature multiferroic properties of $Pb(Fe_{0.5}Nb_{0.5})O_3+Co_{0.65}Zn_{0.35}Fe_2O_4$ composites", *J. Appl. Phys.*, vol. 114, 234106, 2013.

[129] Pattanayak, S., Choudhary, R.N.P., Das, P.R., Shannigrahi, S.R., "Effect of Dy-substitution on structural, electrical and magnetic properties of multiferroic $BiFeO_3$ ceramics", *Ceram. Int.*, vol. 40, pp. 7983–7991, 2014.

[130] Moon, K.W., Cho, S.G., Choa, Y.H., Kim, K.H., Kim, J., "Synthesis and magnetic properties of nano Ba-hexaferrite/NiZn ferrite composites", *Phy. Status Solidi A*, vol. 204, pp. 4141-4144, 2007.

[131] Rao, B.P., Rao, K., Trinadh, K., Caltun, O., "Dielectric behavior of Niobium doped Ni-Zn ferrites", *J. Optoelectron. Adv. Mater.*, vol. 6, pp. 951-954, 2004.

[132] Maxwell, J.C., "A Treatise on Electricity and Magnetism", Oxford University Press, London, 1873.

[133] Wagner, K., "Zur Theorie der unvollkommenen Dielektrika", *J. Ann. Phys.*, vol. 345, pp. 817-855, 1913.

[135] Upadhyay, S., Kumar, D., Parkash, O.M., "Effect of composition on dielectric and electrical properties of the $Sr_{1-x}La_xTi_{1-x}Co_xO_3$ system", *Bull. Mater. Sci.*, vol. 19, pp. 513–525, 1996.

[136] Kuldeep, V., Subohi, O., Kurchania, R., "Investigations on dielectric, electrical and ferroelectric properties of $xBaTiO_3+(1-x)NiFe_2O_4$ multiferroic composite ceramics", *Appl. Phys. A*, vol. 125, pp. 631-635, 2019.

[137] Sharma, R., Poonam, P., Tandon, R.P., "Structural dielectric ferromagnetic ferroelectric and ac conductivity studies of the $BaTiO_3+CoFe_{1.8}Zn_{0.2}O_4$ multiferroic particulate composites", *Ceram. Int.,* vol. 40, pp. 9027–9036, 2014.

[138] Shaw, T.M., Trolier- McKinstry, S., McIntyre, P.C., "The properties of ferroelectric films at small dimensions", *Annu. Rev. Mater. Sci.,* vol. 30, pp. 263-298, 2000.

[139] Arlt, G., Hennings, D., With, G.de, "Dielectric properties of fine-grained barium titanate ceramics", *J. Appl. Phys.,* vol. 58, pp. 1619-1925, 1985.

[140] Verma, Kavita, Kumar, Ashwini, Varshney, Dinesh, "Dielectric relaxation behavior of $A_xCo_{1-x}Fe_2O_4$ (A = Zn, Mg) mixed ferrites", *J. Alloys Compd.,* vol. 526, pp. 91-97, 2012.

[141] Mazumdar, S.C., Khan, M.N.I., Islam, Md. Fakhrul, Hossain, A.K.M. Akther, "Tuning of magnetoelectric coupling in $(1-y)Bi_{0.8}Dy_{0.2}FeO_3+yNi_{0.5}Zn_{0.5}Fe_2O_4$ multiferroic composites", *J. Magn. Magn. Mater.*, vol. 401, pp. 443–454, 2016.

[142] Prasad, N.V., Prasad, G., Bhimasankaram, T., Suryanarayana, S.V., Kumar, G.S., "Synthesis and Electrical Properties of $SmBi_5Fe_2Ti_3O_{18}$", *Mod. Phys. Lett. B.*, vol. 12, pp. 967-972, 1998.

[143] Adhlakha, N,. Yadav, K., "Study of structural, dielectric and magnetic behaviour of $Ni_{0.75}Zn_{0.25}Fe_2O_4+Ba(Ti_{0.85}Zr_{0.15})O_3$ composites", *Smart Mater. Struct.,* vol. 21, 115021, 2012.

[144] Chen, X., Gong, X., Li, T., He, Y., Liu, P., "Microstructure, dielectric and ferroelectric properties of $(1-x)(0.94Bi_{0.5}Na_{0.5}TiO_3+0.06BaTiO_3)+xBiFeO_3$ lead-free ceramics synthesized via a high energy ball milling method", *J. Alloys Compd.*, vol. 507, pp. 535-541, 2010.

[145] Rai, R., Bdikin, I., Valente, M.A., Kholkin, A.L., "Ferroelectric and ferromagnetic properties of Gd-doped $BiFeO_3+BaTiO_3$ solid solution", *Mater. Chem. Phys.*, vol. 119, pp. 539-545, 2010.

[146] Catalan, G., Scott, J.F., "Physics and applications of bismuth ferrite", *Adv. Mater.*, vol. 21, pp. 2463-2485, 2009.

[147] Uniyal, P., Lotey, G.S., Gautam, A., Verma, N.K., Yadav, K.L., "Multiferroic properties of $xBi_{0.9}Gd_{0.1}FeO_3+(1-x)BaTiO_3$ ceramics", *J. Supercond., Nov. Magn.*, vol. 27, pp. 569-574, 2014.

[148] Kumar, M.M., Srinivas, A., Suryanarayana, S.V., "Structure-property relations in $BiFeO_3/BaTiO_3$ solid solutions", *J. Appl. Phys.*, vol. 87, pp. 855–862, 2000.

[149] Adhlakha, N., Yadav, K., "Structural, dielectric, magnetic, and optical properties of $Ni_{0.75}Zn_{0.25}Fe_2O_4+BiFeO_3$ composites", *J. Mater. Sci.*, vol. 49, pp. 4423-4438, 2014.

[150] Palkar, V.R., John, J., Pinto, R., "Observation of saturated polarization and dielectric anomaly in magnetoelectric $BiFeO_3$ thin films", *Appl. Phys. Lett.*, vol. 80, pp. 1628-1630, 2002.

[151] Behera, B., Nayak, P., Choudhary, R.N.P., "Structural and impedance properties of $KBa_2V_5O_{15}$ ceramics", *Mater Res Bull.*, vol. 43, pp. 401-410, 2008.

[152] Plocharski, J., Weiczorek, W., "PEO based composite solid electrolyte containing nasicon", *Solid State Ion.*, vol. 28, pp. 979-982, 1988.

[153] Cao, W., Gerhardt, R., "Calculation of various relaxation times and conductivity for a single dielectric relaxation process", *Solid State Ion.*, vol. 42, pp. 213-221, 1990.

[154] Negi, N.S., Sharma, A.J., Shah, Kotnala, R.K., "Investigation on impedance response, magnetic and ferroelectric properties of $0.20(Co_{1-x}Zn_xFe_{2-y}Mn_yO_4)+0.80(Pb_{0.70}Ca_{0.30}TiO_3)$ magnetoelectric composites", *Mater Chem Phys*, vol. 148, pp.1221-1229, 2014.

[155] Zhang, H., Mak, C.L., "Impedance spectroscopic characterization of fine-grained magnetoelectric $Pb(Zr_{0.53}Ti_{0.47})O_3+(Ni_{0.5}Zn_{0.5})Fe_2O_4$ ceramic composites", *J. Alloys Compd.*, vol. 513, pp. 165-171, 2012.

[156] Kaiser, M., "Electrical conductivity and complex electric modulus of titanium doped nickel-zinc ferrites", *Physica B*, vol. 407, pp. 606-613, 2012.

[157] Choudhary, R.N.P., Pradhan, D.K., Tirado, C.M., Bonilla, G.E., Katiyar, R.S., "Effect of La substitution on structural and electrical properties of $Ba(Fe_{2/3}W_{1/3})O_3$ nanoceramics", *J. Mater. Sci.*, vol. 42, pp. 7423-7432, 2007.

[158] Adler, D., Feinleib, J., "Electrical and optical properties of narrow band materials", *Phys. Rev. B*, vol. 2, pp. 3112-3134, 1970.

[159] Mazumdar, S.C., Khan, M.N.I., Islam, Md. Fakhrul, Hossain, A.K.M. Akther, "Enhanced multiferroic properties in $(1-y)BiFeO_3+yNi_{0.50}Cu_{0.05}Zn_{0.45}Fe_2O_4$ composites", *J. Magn. Magn. Mater.*, vol. 390, pp. 61-69, 2015.

[160] Pattanayak, S., Parida, B.N., Das, P.R., Choudhary, R.N.P., "Impedance spectroscopy of Gd doped $BiFeO_3$ multiferroics", *Appl. Phys. A*, vol. 112, pp. 387-395, 2013.

[161] Reitz, Wayne, "Impedance spectroscopy, theory, experiment, and applications", *Mater Manuf Process*, vol. 21, pp. 425, 2006.

[162] H INABA, "Impedance measurement of single-crystalline and polycrystalline manganese-zinc ferrites with various non-stoichiometries", *J. Mater. Sci.*, vol. 32, pp.1867–1872, 1997.

[163] Anthony, R., West Derek, C., Sinclair, Naohiro Hirose, "Characterization of Electrical Materials, Especially Ferroelectrics, by Impedance Spectroscopy", *J. Electroceram.*, vol. 1, pp. 65–71, 1997.

[164] J.C. Maxwell, "A Treatise on Electricity and Magnetism", Clarendon Press, Oxford, 1982.

[165] Jonscher, A.K., "The 'universal' dielectric response", *Nature*, vol. 267. pp. 673-679, 1977.

[166] Austin, I.G., Mott, N.F., "Polarons in crystalline and non-crystalline materials", *Adv Phys*, vol. 18, pp. 41-102, 1969.

[167] Khandekar, M.S., Kambale, R.C., Patil, J.Y., Kolekar, Y.D., Suryavanshi, S.S., "Effect of calcination temperature on the structural and electrical properties of cobalt ferrite synthesized by combustion method", *J. Alloys Compd.*, vol. 509, pp. 1861-1865, 2011.

[168] Miah, M.J., Khan, M.N.I., Hossain, A.K.M. Akther, "Weak ferromagnetism and magnetoelectric effect in multiferroic $x$Ba$_{0.95}$Sr$_{0.05}$TiO$_3$+ (1-$x$)BiFe$_{0.9}$Gd$_{0.1}$O$_3$ relaxors', *J. Magn. Magn. Mater.*, vol. 401, pp. 600–611, 2016.

[169] Atif, M., Idrees, M., Nadeem, M., Siddique, M., Ashraf, M.W., "Investigation on the structural, dielectric and impedance analysis of manganese substituted cobalt ferrite i.e., Co$_{1-x}$Mn$_x$Fe$_2$O$_4$ (0.0 ≤ x ≤0.4)", *RSC Adv.*, vol. 6, 20876, 2016.

[170] Kadam, S.L., Patankar, K.K., Kanamadi, C.M., Chougule, B.K., "Electrical conduction and magnetoelectric effect in Ni$_{0.50}$Co$_{0.50}$Fe$_2$O$_4$+Ba$_{0.8}$Pb$_{0.2}$TiO$_3$ composites", *Mater Res Bull.*, vol. 39, pp. 2265-2272, 2004.

[171] Buscaglia, V., Viviani, M., Buscaglia, M.T., Nanni, P., Mitoseriu, L., Testino, A., Stytsenko, E., Daglish, M., Zhao, Z., Nygren, M., "Nanostructured barium titanate ceramics", *Powder Technol.*, vol. 148, pp. 24-27, 2004.

[172] Ahad, A., Taher, M.A., Das, Mithun Kumar, Rahaman, M. Zahidur, Khan, M.N.I., "Effect of Y substitution on magnetic and transport properties of Ba$_{0.95}$La$_{0.05}$Ti$_{1-x}$Y$_x$O$_3$ ceramics", *Results in Phys*, vol. 12, pp. 1925–1932, 2019.

[173] Kanamadi, C.M., Kulkarni, S.R., Patankar, K.K., Chuogule, S.S., Patil, S.J., Chougule, B.K., "Magnetoelectric and dielectric properties of Ni$_{0.5}$Cu$_{0.5}$Fe$_2$O$_4$+Ba$_{0.5}$Pb$_{0.5}$Ti$_{0.5}$Zr$_{0.5}$O$_3$ ME composites", *J. material Sci.*, vol. 42, pp. 5080-5084, 2007.

[174] Cai, N., Zahi, J., Nan, C.W., Lin, Y., Shi, Z., "Dielectric, ferroelectric, magnetic, and magnetoelectric properties of multiferroic laminated composites", *Phy Rev B*, vol. 68, 224103, 2003.

[175] Bammannavar, B.K., Naik, L.R., Chougule, B.K., "Studies on dielectric and magnetic properties of ($x$)Ni$_{0.2}$Co$_{0.8}$Fe$_2$O$_4$+(1−$x$)barium lead zirconate titanate magnetoelectric composites", *J. Appl. Phys.*, vol.104, 064123, 2008.

[176] Chavana, Pradeep, Naik, L.R., Belavi, P.B., Chavan, Geeta, Muttannavar, V.T., Bammannavar, B.K., Kotnala, R.K., "Temperature-dependent electric properties and magnetoelectric effects in ferroelectric rich Ni$_{0.8}$Mg$_{0.2}$Fe$_2$O$_4$+BaZr$_{0.2}$Ti$_{0.8}$O$_3$ magnetoelectric composites", *J. Alloys Compd.*, vol.777, pp. 1258-1264, 2019.

[177] Tiwari, Shivangi, Vitta, Satish, "Magnetoelectric and magnetodielectric coupling and microwave resonator characteristics of $Ba_{0.5}Sr_{0.5}Nb_2O_6+CoCr_{0.4}Fe_{1.6}O_4$ multiferroic composite", *Sci. Rep.*, vol. 8, pp. 1-12, 2018.

[178] Momin, A.A., Zubair, M.A., Islam, Md. Fakhrul, Hossain, A.K.M. Akther, "Enhance magnetoelectric coupling in $xLi_{0.1}Ni_{0.2}Mn_{0.6}Fe_{2.1}O_4+(1-x)BiFeO_3$ multiferroic composites", *J Mater Sci: Mater Electron*, vol. 30, pp. 13033–13046, 2019.

[179] Belavi, P.B., Chavan, G.N., Naik, L.R., Mathe, V.L., Kotnala, R.K., "Resistivity and grain size dependent magnetoelectric effect in $(Y)Ni_{0.85}Cd_{0.1}Cu_{0.05}Fe_2O_4+(1-Y)BaTiO_3$ ME composites", *IJSTR*, vol. 2, pp. 298-306, 2013.

[180] Yu, M., Hu, J., Liu, J., Li, S., "Electromagnetic properties of multiferroic magnetoelectric $BaTiO_3+Co_xFe_{3-x}O_4$ core-shell particles obtained by homogeneous coprecipitation", *J. Magn. Magn. Mater.*, vol. 326, pp. 31-34, 2013.

[181] Kumar, P., S.K. Sharma, M. Knobel, M. Singh, "Effect of $La^{3+}$ doping on the electric, dielectric and magnetic properties of cobalt ferrite processed by co-precipitation technique", *J. Alloy. Compd.*, vol.508, pp. 115-118, 2010.

[182] Verma, A., Chatterjee, R. "Effect of zinc concentration on the structural, electrical and magnetic properties of mixed Mn–Zn and Ni–Zn ferrites synthesized by the citrate precursor technique", *J. Magn. Magn. Mater.,* vol 306, pp. 313-320, 2006.

[183] Patil, D.R., Lokare, S.A., Chougule, S.S., Chougule, B.K., "Dielectric and magnetic properties of $xNiFe_2O_4+(1-x)Ba_{0.9}Sr_{0.1}TiO_3$ composites", *Physica B*, vol. 400, pp. 77-82, 2007.

[184] Jia, L.J., Zhang, H.W., Luo, J., Liu, Y.L., Wen, Q.Y., "Effect of MgO additive on the high-frequency properties of Z-type hexaferrite", *J. Magn. Magn. Mater.,* vol. 322, pp. 1934-1938, 2010.

[185] Batoo, K.M. "Study of dielectric and impedance properties of Mn ferrites", *Phys. B*, vol. 406 pp. 382-387, 2011.

[186] Pandian, S. Selvasekara, Vijayakumar, M., "The ac impedance spectroscopy studies on $LiD_yO_2$", *Mater. Chem. Phys.*, vol. 80 pp. 29-33, 2003.

[187] Choudhary, R.N.P., Pradhan, D.K., Tirado, C.M., Bonilla, G.E, Katiyar, R.S., "Effect of La substitution on structural and electrical properties of $Ba(Fe_{2/3}W_{1/3})O_3$ nanoceramics", *J. Mater. Sci.,* vol. 42, pp. 7423-7432, 2007.

[188] Pattanayak, S., Parida, B.N., Das, P.R., Choudhary, R.N.P., "Impedance spectroscopy of Gd doped $BiFeO_3$ multiferroics", *Appl. Phys. A*, vol. 112, pp. 387-395, 2013.

[189] Mazen, S.A., Abu-Elsaad, N.I., "AC impedance studies on $Li_{0.5+0.5x}Ge_xFe_{2.5-1.5x}O_4$ system", *Appl. Phys. A*, vol. 122, pp. 26-31, 2016

[190] Kambale, R.C., Shaikh, P.A., Bhosale, C.H., Rajpure, K.Y., Kolekar, Y.D., "Dielectric properties and complex impedance spectroscopy studies of mixed Ni-Co ferrites", *Smart Mater. Struct.*, vol. 18, pp. 085014-085016, 2009.

[191] Madolappa, Shivanand, Anupama, A V, Jaschin, Pw, "Magnetic and ferroelectric characteristics of $Gd^{3+}$ and $Ti^{4+}$ co-doped $BiFeO_3$ ceramics", *Bull. Mater. Sci.*, vol. 39, pp. 593–601, 2016.

[192] Wang, Y., Wang, Y., Rao, W., Wang, M., Li, G., Li, Y., Gao, J., Zhou, W., Yu, J., "Dielectric, ferromagnetic and ferroelectric properties of the $(1-x)Ba_{0.8}Sr_{0.2}TiO_3+xCoFe_2O_4$ multiferroic particulate ceramic composites" *J. Mater. Sci. Mater. Electron.*, vol. 23, pp. 1064–1071, 2012.

[193] Ma, J., Hu, J., Li, Z., Nan, C.W., "Recent Progress in Multiferroic Magnetoelectric Composites: from Bulk to Thin Films", *Adv. Mater.*, vol. 23, pp. 1062-1087, 2011.

[194] Ramesh, T., Rajendar, V., Murthy, S.R., "$CoFe_2O_4+BaTiO_3$ multiferroic composites: role of ferrite and ferroelectric phases on the structural, magnetodielectric properties", *J Mater Sci: Mater Electron*, vol. 28, pp. 11779-11788, 2017.

[195] Chavan, Pradeep, Naik, L.R., Kotnala, K., "Study of electric, magnetic properties and improvements in ME effects of NMFO+BZT particulate composites", *J. Magn. Magn. Mater.,* vol. 433, pp. 24-28, 2017.

[196] Kunale, R.A., Kadam, R.H., Mane, D.R., "Studies on Magnetoelectric Effect of $Ni_{0.5}Cu_{0.3}Zn_{0.2}Fe_2O_4+BaTiO_3$ ME Composite", *IJOART*, vol. 2, pp. 37-40, 2013.

[197] Rashed, A. Islam, Shashank Priya, "Magnetoelectric properties of the lead–free cofired $BaTiO_3+Ni_{0.8}Zn_{0.2}Fe_2O_4$ bilayer composite", *Appl. Phys. Lett*, vol. 89, 152911, 2006.

[198] Ciomaga, C.E., Airimioaei, M., Nica, V., Hrib, L.M., Caltun, O.F., Iordan, A.R., Palamaru, M.N., "Preparation and magnetoelectric properties of $NiFe_2O_4+PZT$ composites obtained in-situ by gel combustion method", J. *Eur. Ceram. Soc*., vol. 32, pp. 3325-3337, 2012.

[199] Fetisov, Y.K., Kamentsev, K.E., Ostashchenko, A.Y, Srinivasan, G., "Wide-band magnetoelectric characterization of a ferrite-piezoelectric multilayer using a pulsed magnetic field", *Solid State Commun.,* vol. 132, pp. 13–17, 2004.

[200] Thankachan, R.M., Raneesh, B., Mayeen, Anshida, "Room temperature magnetoelectric coupling effect in $CuFe_2O_4+BaTiO_3$ core-shell and nanocomposites", *J. Alloys Compd*., vol. 731, pp. 288-296, 2018.

**Appendices**

## List of peer-reviewed journal articles:

1. Mithun Kumar Das, M. A. Zubair, Hidekazu Tanaka, A. K. M. Akther Hossain, "An experimental insight of the multiferroic properties of magnetoelectrically coupled $x$LNCZFO+(1-$x$)BSTDO composites", Journal of Magnetism and Magnetic Materials, vol. 502, 166449, 2020.

2. Mithun Kumar Das, M. A. Zubair, Hidekazu Tanaka, A. K. M. Akther Hossain, "Study of impedance and magnetoelectric property of lead-free $x$LCNZFO+(1-$x$)BGTDO multiferroic composites", Materials Chemistry and Physics, vol. 255, 123575, 2020.

## List of peer-reviewed conference proceedings:

1. Mithun Kumar Das, Abdulla Al-Momin, A. K. M. Akther Hossain, "Influence of Sintering Temperature on Magnetic Characteristics of Li-Cu-Ni-Zn Ferrite", IEEE Xplore, 2018, http://dx.doi.org/10.1109/ICECE.2018.8 636689.

## List of conference presentation:

1. Mithun Kumar Das, Bablu Chandra Das, A. K. M. Akther Hossain, "Enhancement of electromagnetic and magnetoelectric properties of $x$LCNZFO+(1-$x$)BGTDO multiferroic composites", International Conference on Physics–2020, 05-07 March 2020; Atomic Energy Centre Dhaka, Bangladesh.

2. Mithun Kumar Das, A.A. Momin, A. K. M. Akther Hossain, "Influence of sintering temperature on electromagnetic and magnetoelectric properties of 0.5LCNZFO+0.5BGTDO multiferroic composite", 16th Conference of the Asian Crystallographic Association, 17-20 December 2019, Singapore.

3. Mithun Kumar Das, Bablu Chandra Das, A. K. M. Akther Hossain, "Influence of sintering temperature on electromagnetic and magnetoelectric properties of rare earth substitute multiferroic composite", 16th Conference of the Asian Crystallographic Association, 17-20 December 2019, Singapore.

4. Mithun Kumar Das, A. K. M. Akther Hossain, "Study the effect of sintering temperature on 0.1LCNZFO+0.9BSTDO multiferroic composite", National Conference on Electronics and Informatics-2019, 04-05 December 2019, Atomic Energy Centre, Dhaka, Bangladesh.

5. Mithun Kumar Das, M. N. Hossain, A. K. M. Akther Hossain, "Effect of sintering temperature on magnetic and electrical characteristics of rare earth substitute multiferroic composite", National Conference on Physics–2019, 07-09 February 2019, Dhaka University Dhaka, Bangladesh.

6. Mithun Kumar Das, Abdulla Al-Momin, A. K. M. Akther Hossain, "Influence of Sintering Temperature on Magnetic Characteristics of Li-Cu-Ni-Zn Ferrite", 10th International Conference on Electrical and Computer Engineering, 20-22 December 2018, Department of Electrical and Electronic Engineering, BUET, Dhaka, Bangladesh.

7. Mithun Kumar Das, M. N. Hossain, A. K. M. Akther Hossain, "Temperature Influence on the Electromagnetic Characteristics of $Li_{0.10}Cu_{0.10}Ni_{0.30}Zn_{0.40}Fe_{2.1}O_4$ ferrites", Conference on Weather Forecasting and Advances in Physics, 11-12 May 2018, KUET, Khulna.

8. Mithun Kumar Das, A. K. M. Akther Hossain, "Effect of Sintering Temperature on Structure, Dielectric and Magnetic Properties of $Li_{0.10}Cu_{0.10}Ni_{0.30}Zn_{0.40}Fe_{2.1}O_4$ Ferrites", International Conference on Physics–2018, 08-10 March 2018, Dhaka University, Dhaka, Bangladesh.

9. Mithun Kumar Das, A. K. M. Akther Hossain, "Study of the Structural, Magnetic, Dielectric, Ferroelectric, and Magnetoelectric Property of Lead-Free $x$LNCZFO+(1-$x$)BGTDO Multiferroic Composites", 6th Conference of Bangladesh Crystallographic Association, January 15-16, 2021, Dhaka University, Dhaka, Bangladesh.

Research articles

# An experimental insight of the multiferroic properties of magnetoelectrically coupled $x$LNCZFO + (1 − $x$)BSTDO composites

Mithun Kumar Das[a,*], M.A. Zubair[b], Hidekazu Tanaka[c], A.K.M. Akther Hossain[a]

[a] Department of Physics, Bangladesh University of Engineering and Technology, Dhaka 1000, Bangladesh
[b] Department of Glass and Ceramic Engineering, Bangladesh University of Engineering and Technology, Dhaka 1000, Bangladesh
[c] Institute of Scientific and Industrial Research, Osaka University, Ibaraki, Osaka 567-0047, Japan

ABSTRACT

The conventional solid-state reaction method was used to synthesize the $x$Li$_{0.1}$Ni$_{0.3}$Cu$_{0.1}$Zn$_{0.4}$Fe$_{2.1}$O$_4$ + (1 − $x$) Ba$_{0.95}$Sm$_{0.05}$Ti$_{0.95}$Dy$_{0.05}$O$_3$ multiferroic composites. X-ray diffraction patterns confirmed the coexistence of the constituent phases in the composites. Field Emission Scanning Microscopy images showed that the average grain size increased with the ferrite content in composites. The compositional study confirmed that the proportion of the components is well compatible with their nominal compositions. The real part of the initial permeability was found to increase, but the magnetic loss decreased with ferrite content. The dielectric dispersion was observed at lower frequencies on account of interfacial polarization. The maximum dielectric constant of about 6.7 × 10$^3$ was found for the value of $x$ = 0.60 at 1 kHz. The ac conductivity followed the Jonscher's power law, and the conduction was due to the small polaron hopping. The impedance spectroscopy analysis confirmed that both the grains and grain boundaries affected the conduction for samples with $x$ = 0.40, 0.50 and 0.60, while only grain boundary was the dominating factor for the other samples. Polarization-electric field curves (P-E) confirmed that the samples up to $x$ = 0.20 had a good ferroelectric nature with a maximum saturation polarization of 0.34 μC/cm$^2$ and the rest had lossy behavior. The highest magnetoelectric (ME) voltage coefficient was found to be 170 × 10$^3$ Vm$^{-1}$T$^{-1}$ for $x$ = 0.10.

## 1. Introduction

Multiferroic materials consist of strain-coupled ferromagnetic and ferroelectric phases resulting in ME coupling between the two ferroic orders [1]. This ME coupling in multiferroic materials have gained attention and encouraged a large number of research activities. They were of great interest for their promising technological applications in new multifunctional systems (e.g. microwave phase shifters, multifunctional sensors, data storage, broadband magnetic field sensors, actuators, magnetoelectric memory cells, etc.) [2]. There are two types of multiferroics: single-phase and composite. Natural single-phase multiferroics are rare and their ME coupling response, polarization, magnetization, and transition temperatures are too low for practical applications. Another limitation is that most single-phase materials contain expensive constituent materials and utilize costly processing techniques. Such disadvantages might be overcome by the use of multiferroic composites. Composite materials were extensively used in modern electronic devices with a growing demand for new technology requiring high reliability, limited space, and multifunctional efficiency.

Multiferroic composites are easy to process and have greater ME voltage coefficient compared to single-phase materials such as Cr$_2$O$_3$ by two orders of magnitude [3]. Synthesized multiferroic composites exhibit strong ME effects at ambient temperature, which develop as a product-property of ferroic orders mediated by elastic deformation [2]. This product property is more significant and does not exist in the individual phases. In the presence of the ME coupling, the external magnetic field can trigger electric polarization and the electric field can trigger magnetic order, which makes these materials technologically important. Suitable ferrite and ferroelectric mixture can produce an extremely good ME effect. The high magnetostriction coefficient of the ferrite phase and the prominent piezoelectric coefficient of the ferroelectric phase are fundamental requirements for obtaining a higher ME coefficient for multiferroic composites [4]. Thus, an appropriate combination of two different phases of the material, including magnetostrictive and piezoelectric phases, will result in a widely applicable extrinsic ME voltage coefficient in composites. Multiferroic properties of different composites based on Ni-Cu-Zn and BaTiO$_3$ were reported earlier, such as (1–$x$)NZF + $x$BT [5], (1 − $x$)Ba$_{0.5}$Sr$_{0.5}$Zr$_{0.5}$Ti$_{0.5}$O$_3$ + ($x$)

$Ni_{0.12}Mg_{0.18}Cu_{0.2}Zn_{0.5}Fe_2O_4$ [6], $NiFe_2O_4$-$BaTiO_3$ [7], $Ba_{0.8}Ca_{0.2}TiO_3$-$Ni_{0.2}Cu_{0.3}Zn_{0.5}Fe_2O_4$ [8], $BaTiO_3$-$CoFe_2O_4$ [9], $Ba_{0.6}Sr_{0.4}TiO_3$-$Ni_{0.2}Cu_{0.2}Zn_{0.62}O(Fe_2O_3)_{0.98}$ [10]. To the best of our knowledge, no work has been reported on specific $xLi_{0.1}Ni_{0.3}Cu_{0.1}Zn_{0.4}Fe_{2.1}O_4 + (1-x)$ $Ba_{0.95}Sm_{0.05}Ti_{0.95}Dy_{0.05}O_3$ composites based on literature survey.

In this research, $Li_{0.1}Ni_{0.3}Cu_{0.1}Zn_{0.4}Fe_{2.1}O_4$ (LNCZFO) was chosen as the ferrite phase and $Ba_{0.95}Sm_{0.05}Ti_{0.95}Dy_{0.05}O_3$ (BSTDO) as the ferroelectric phase. The selection of these two materials was made based on the criteria for high ME coefficient mentioned earlier. The $LiNiFe_2O_4$ doped with Jahn-Teller ions such as $Zn^{2+}$, $Cu^{2+}$ had a high magnetostriction coefficient as these ions have a high ME coupling coefficient [11]. Nevertheless, enhanced room temperature (RT) saturation magnetization, complex initial permeability with high cut-off frequency, high relative quality factor, ambient Néel temperature ($T_N$) and large resistivity were also observed in $Li^{1+}$ doped Ni-Cu-Zn ferrites [12,13]. It is therefore quite important to figure out the possible improvements in the different physical properties of the different LNCZFO–BSTDO composites. On the other hand, BSTDO was chosen as a ferroelectric phase because rare earth doped $BaTiO_3$ (BTO) has high dielectric constant, low dielectric loss, high resistance, good thermal stability, low leakage current density, low transition temperature, and high piezoelectric coefficient [14–17]. It was expected that the composites of these two would have good magnetic, electrical and ME properties for RT applications. The structural, magnetic, dielectric, ferroelectric and ME properties of the composites studied are reported in this research. The observed results are thoroughly examined and discussed from an experimental point of view.

## 2. Experimental

### 2.1. Sample preparation

Multiferroic $xLi_{0.1}Ni_{0.3}Cu_{0.1}Zn_{0.4}Fe_{2.1}O_4 + (1-x)Ba_{0.95}Sm_{0.05}Ti_{0.95}$ $Dy_{0.05}O_3$ (where $x = 0.00, 0.10, 0.20, 0.30, 0.40, 0.50, 0.60$ and $1.00$) composites were synthesized by the conventional solid-state reaction technique. High purity $Li_2O$ (99.90%), $NiO$ (99.90%), $CuO$ (99.99%), $ZnO$ (99.90%) and $Fe_2O_3$ (99.98%) powders were used to synthesize the LNCZFO phase. Raw materials of $BaCO_3$ (99.90%), $Sm_2O_3$ (99.90%), $TiO_2$ (99.90%), $Dy_2O_3$ (99.90%) were used to synthesize the BSTDO phase. Stoichiometric amounts of raw materials were mixed with an agate mortar and pestle in an acetone medium. The mixed ferrite and ferroelectric powders were calcined at 973 K and 1273 K, respectively. The ground powders of the constituent phases were then mixed in an acetone medium for 5 h according to the formula $xLNCZFO + (1-x)$ BSTDO with $x = 0.00, 0.10, 0.20, 0.30, 0.40, 0.50, 0.60$ and $1.00$. A granulation binder of 10% polyvinyl alcohol was then mixed into the powders. The mixed powders were uniaxially pressed to make disk- and ring-shaped samples. The optimum properties of the compositions are found at optimum sintering temperatures ($T_s$) which are typically between 1473 and 1573 K. The samples were sintered at various temperatures within this range to determine the optimum $T_s$. The optimum $T_s$ values were obtained as follows: 1573 K for $x = 0.00$, 1523 K for $x = 0.10$, 1498 K for $x = 0.20, 0.30, 0.40, 0.50, 0.60$, and 1473 K for $x = 1.00$.

### 2.2. Characterizations

Phase identification was performed using a Philips PANalytical X'PERT-PRO X-ray diffractometer (XRD) configured with CuKα radiation ($\lambda = 0.15418$ nm). The unit cell parameters of the composites were then calculated from the XRD data. Field Emission Scanning Electron Microscopy (FESEM, model JEOL JSM 7600F) and Energy Dispersive X-ray Spectroscopy (EDS) were used for studying surface morphology and compositional analysis, respectively. The X-ray density ($\rho_x$) of the samples was estimated using the formula:

$$\rho_x = \frac{nM}{N_A V},$$ (1)

where $n$ is the number of atoms in the unit cell, $N_A$ is Avogadro's number, $M$ is the molar mass, and $V$ is the volume of the unit cell. The bulk density ($\rho_B$) of the samples was calculated using the formula:

$$\rho_B = \frac{m}{\pi r^2 t},$$ (2)

where $m$, $r$ and $t$ are the mass, radius and thickness of the pellet, respectively. The porosity ($P$) was calculated using the relation:

$$P(\%) = \frac{\rho_x - \rho_B}{\rho_x} \times 100,$$ (3)

Frequency-dependent magnetic and dielectric properties were measured at RT by impedance analyzer (model-WAYNE KERR 65003). The real part of the initial permeability ($\mu_i'$) was estimated using the relation:

$$\mu_i' = \frac{L_s}{L_0},$$ (4)

where $L_s$ is the self-induction of the winding coil with sample, $L_0$ ($= \frac{\mu_0 N^2 S}{d}$) is the inductance of the coil without sample, $N$ is the number of turns in the coil ($N = 4$), $S$ is the cross-sectional area and $\bar{d}$ is the mean diameter of the sample. The relative quality factor (RQF) was determined using the formula:

$$RQF = \frac{\mu_i'}{tan\delta_M}$$ (5)

where $tan\delta_M$ denotes the loss factor. Samples were coated on both sides with conducting silver paste to ensure better electrical contact for dielectric measurements. The dielectric constant ($\varepsilon'$) was estimated using the relation:

$$\varepsilon' = \frac{Ct}{\varepsilon_0 A},$$ (6)

where $C$, $A$ and $\varepsilon_0$ are the capacitance of the plate, the cross-sectional area of the electrode and the permittivity of free space, respectively. Complex electric modulus ($M^*$) of the composites was calculated using the following equation:

$$M^*(\omega) = \frac{1}{\varepsilon^*} = \frac{1}{\varepsilon' - j\varepsilon''} = \frac{\varepsilon'}{\varepsilon'^2 + \varepsilon''^2} + j\frac{\varepsilon''}{\varepsilon'^2 + \varepsilon''^2} = M'(\omega) + jM''(\omega),$$ (7)

where $\varepsilon^*$ and $\varepsilon''$ represent the complex dielectric constant and imaginary part of complex dielectric constant, respectively.

Simplifying and substituting $\varepsilon''$ by $\varepsilon' tan\delta_E$, we get

$$M^*(\omega) = M'(\omega) + jM''(\omega) = \frac{1}{\varepsilon'(1 + tan^2\delta_E)} + j\frac{tan\delta_E}{\varepsilon'(1 + \tan\delta_E)},$$ (8)

where $M'$ and $M''$ are the real and imaginary parts of $M^*$, respectively.

The ac conductivity ($\sigma_{ac}$) of the compositions was estimated using the formula:

$$\sigma_{ac} = \omega\varepsilon_0\varepsilon'\tan\delta_E$$ (9)

where $\omega$ is the angular frequency. The ME coefficient was measured as a function of the dc magnetic field in the superimposed ac magnetic field on the sample. The electromagnet provided a dc magnetic field of up to 0.7 T. A signal generator (50 Hz) was used to drive the Helmholtz coil to generate the ac magnetic field. The output voltage was measured using a Keithley Electrometer (Model 2000) as a function of the applied dc magnetic field. The ME coefficient ($\alpha_{ME}$) was estimated using the formula:

$$\alpha_{ME} = \left(\frac{dE}{dH}\right)_{H_{ac}} = \frac{V_0}{h_0 t}$$ (10)

where $V_0$ and $h_0$ refer to the ME voltage across the surfaces of the sample and the magnitude of the ac magnetic field, respectively.

## 3. Results and discussion

### 3.1. Phase identification

Fig. 1 shows the X-ray diffraction (XRD) patterns of different $x$LNCZFO + $(1-x)$BSTDO composites. The XRD peaks have been identified with their corresponding Miller indices. The XRD pattern of LNCZFO shown in Fig. 1(a) confirms the single-phase cubic spinel structure, while the pattern of BSTDO shown in Fig. 1(b) is characteristic of the single-phase tetragonal perovskite structure. The positions of all peaks in the XRD patterns match well with previously reported results [12,18]. No third phase is observed in the XRD pattern, indicating that there was no chemical reaction between the two phases. It is seen that, with increasing ferrite content in the composites, the intensity of most of the ferrite peaks increase while perovskite peaks decrease. This implies that intensity of XRD peaks and number of peaks depends on the concentration of constituent phases in the composites. The lattice parameters were calculated by solving different sets of equations related to successive peaks. The values of the lattice parameter obtained for each plane were plotted against the Nelson–Riley function $F(\theta)$ [19].

$$F(\theta) = \frac{1}{2}\left(\frac{cos^2\,\theta}{Sin^2\,\theta} + \frac{cos^2\,\theta}{\theta}\right).$$  (11)

where $\theta$ is Bragg's angle. A straight line fit was obtained and the accurate value of lattice parameter ($a$) was determined from the extrapolation of these lines to $F(\theta) = 0$. It was found that the lattice parameters of the ferroelectric and ferrite phases changed very slightly in the composites. This can be explained by the stress acting between the two phases [20] and the diffusion of a small amount of each phase into the other. The values of the lattice parameter of individual phases and of all the composites are tabulated in Table 1. For 50%LNCZFO + 50% BSTDO composite, the typical lattice parameter for the ferrite phase is $a = 0.85291$ nm and for the ferroelectric phase $a = b = 0.40404$ nm and $c = 0.40150$ nm. These values are well compatible with the values for spinel and perovskite structures reported earlier by other researchers [12,18].

### 3.2. Density and porosity

Fig. 2 demonstrates the variation of $\rho_B$, $\rho_x$ and $P$ as a function of the LNCZFO content. The $\rho_B$ initially increases with the LNCZFO content (for $x = 0.10$) because the small sized grains of BSTDO fill the
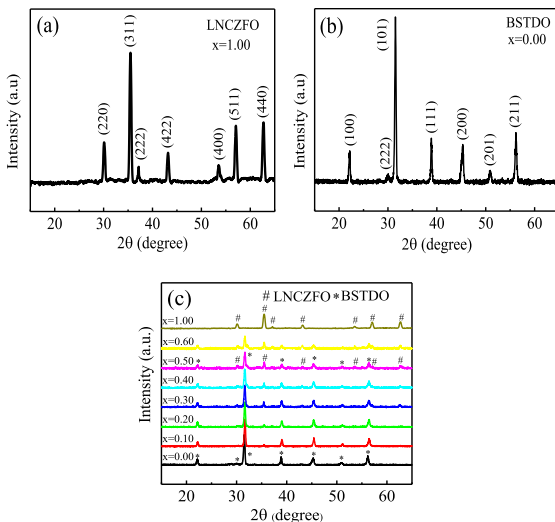
intergranular pores of LNCZFO phase thereby increasing $\rho_B$. Then $\rho_B$ decreases with an increase in the LNCZFO content as the molecular weight of the LNCZFO (232.08 amu) is lower than that of the BSTDO (239.58 amu). The $\rho_x$ decreases almost linearly according to the sum rule. It also appeared that, for all the compositions, the value of $\rho_B$ is lower than the corresponding value of $\rho_x$. This can be explained by the influence of pores that might be created and developed throughout sintering of bulk samples. There are two sources of porosity in ceramic samples: intergranular and intragranular porosity [21]. Thus, total porosity is expressed as,

$$P = P_{inter} + P_{intra.}$$  (12)

As a result of these intergranular and intragranular pores, $\rho_B$ is smaller than $\rho_x$ in the composites.

### 3.3. Surface morphology and energy dispersive X-ray spectroscopy analyses

The microstructure of multiferroic materials plays an important role not only for electrical and magnetic properties but also for the ME coupling. Fig. 3 shows the FESEM images of different $x$LNCZFO + $(1-x)$ BSTDO multiferroic composites. It is observed from the micrographs that the multiferroic composites possess fine crystallite structure. The observed inhomogeneity in the grain size is due to the different growth rates of individual phases in the composites. The average grain diameter ($\bar{D}$) is determined from the FESEM images using the linear intercept method: $\bar{D} = 1.56L$ [22], where $L$ is the average intercept length. With the increase of LNCZFO content in composites, the $\bar{D}$ increased due to a higher $\bar{D}$ of LNCZFO than BSTDO. The increase in $\bar{D}$ with ferrite content may also result in lower stress because of the increased porosity of the composites.

In order to evaluate the chemical composition of different $x$LNCZFO + $(1-x)$BSTDO composites, EDS spectra are recorded from FESEM as depicted in Fig. 4. The EDS spectrum shows that the proportion of the elements in the constituent phases is well compatible with the nominal composition of the composite phases, except for oxygen. This is explained by oxygen deficiency created during the high-temperature sintering process.

### 3.4. Complex initial permeability

Information on the mechanism behind the dynamic magnetic properties of the composites and their capability in high-frequency applications is reflected by the value of $\mu_i'$. Fig. 5 demonstrates the variation of $\mu_i'$ with frequency for different $x$LNCZFO + $(1-x)$BSTDO samples at RT between 10 kHz and 120 MHz. The value of $\mu_i'$ increases with an increase in LNCZFO content in the composites because of high magnetic LNCZFO, while BSTDO exhibits weak ferromagnetic or antiferromagnetic behavior. For $x = 1.00$, the value of $\mu_i'$ is very high compared to the other samples. The $\mu_i'$ of a polycrystalline ferrite is related to two separate processes of magnetization: (i) domain wall motion and (ii) spin rotation [23,24], which is expressed as follows:

$$\mu_i' = 1 + \chi_w + \chi_{spin}$$  (13)

where $\chi_w$ and $\chi_{spin}$ represent the motion of the domain wall and the intrinsic rotational susceptibility of the material, respectively. The $\chi_w$ and $\chi_{spin}$ can be written as:

$$\chi_w = \frac{3\pi M_s^2 \bar{D}}{4\gamma}.$$  (14)

$$\chi_{spin} = \frac{2\pi M_s^2}{K}.$$  (15)

where $M_s$ is the saturation magnetization, $K$ the anisotropy constant, and $\gamma$ the domain wall energy. Therefore, it is seen that the motion of the domain wall is influenced by the $\bar{D}$ and strengthened with the



**Fig. 1.** XRD patterns of (a) LNCZFO (b) BSTDO and (c) various $x$LNCZFO + $(1-x)$BSTDO composites.

**Table 1**

The X-ray density, bulk density, $P$, lattice parameters, $\bar{D}$ and $\mu_i'$ (100 kHz) of various $x$LCNZFO + $(1−x)$BSTDO composites.

| Content ($x$) | Lattice parameter (nm) | | | X-ray density × $10^3$ (kg/$m^3$) | Bulk density × $10^3$ (kg/$m^3$) | $P$ (%) | Average grain size (μm) | $\mu_i'$ at 100 kHz |
|---|---|---|---|---|---|---|---|---|
| | Ferrite $a$ | Ferroelectric | | | | | | |
| | | $a$ | $c$ | | | | | |
| 0.00 | ..... | 0.4041 | 0.4034 | 6.113 | 5.838 | 5 | 0.329 | 25 |
| 0.10 | 0.8760 | 0.4022 | 0.4018 | 6.111 | 5.860 | 4 | 0.387 | 38 |
| 0.20 | 0.8779 | 0.4020 | 0.4017 | 6.100 | 5.705 | 7 | 0.430 | 43 |
| 0.30 | 0.8898 | 0.4023 | 0.4017 | 6.070 | 5.611 | 8 | 0.489 | 45 |
| 0.40 | 0.8529 | 0.4022 | 0.4017 | 6.053 | 5.519 | 9 | 0.521 | 48 |
| 0.50 | 0.8512 | 0.4019 | 0.4015 | 6.038 | 5.402 | 11 | 0.558 | 49 |
| 0.60 | 0.8446 | 0.4020 | 0.4016 | 6.015 | 5.272 | 12 | 0.658 | 54 |
| 1.00 | 0.8405 | ..... | ..... | 5.396 | 5.015 | 14 | 1.597 | 231 |
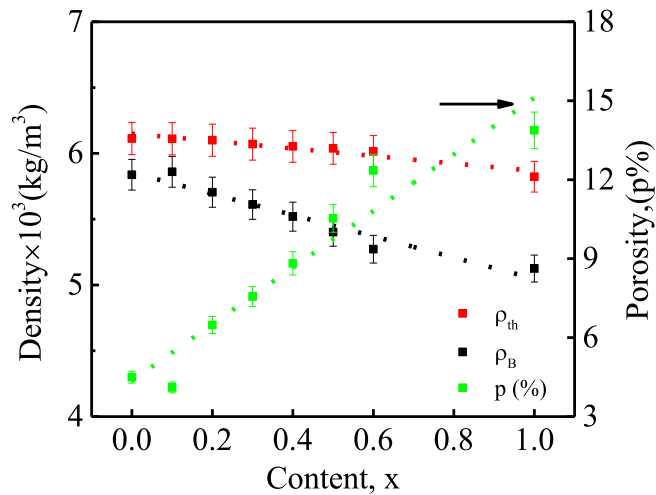


**Fig. 2.** Bulk density ($\rho_B$), X-ray density ($\rho_x$), and porosity ($P$ %) as a function of ferrite content of $x$LNCZFO + $(1−x)$BSTDO composites.



**Fig. 3.** FESEM images of $x$LNCZFO + $(1−x)$BSTDO composites (a) $x$ = 0.00, (b) $x$ = 0.10, (c) $x$ = 0.20, (d) $x$ = 0.30, (e) $x$ = 0.40, (f) $x$ = 0.50, (g) $x$ = 0.60, (h) $x$ = 1.00.

increase of $\bar{D}$. In the case of normal grain growth, the relationship between $\mu_i'$ and $\bar{D}$ is directly proportional. The $\bar{D}$ of $x$ = 1.00 is greater than the other compositions. As a result, the sample with $x$ = 1.00 is much different from the rest. With an increase of frequency, the value of $\mu_i'$ remains almost constant for all compositions up to a certain cut-off frequency $f_r$ and then decreases. The reason for decrease of $\mu_i'$ beyond $f_r$ is the origination of pinning points from intragranular pores and impurities at a higher-frequency on the surface of the sample. This phenomenon obstructs spin rotation and the motion of domain walls and reduces their contribution to $\mu_i'$ [25]. High $\mu_i'$ and high $f_r$ are mutually incompatible, according to the Snoek's relation ($f_r\mu_i'$ = constant) [26]. Therefore, as LNCZFO increases in composites, $f_r$ decreases. No $f_r$ was found for $x$ = 0.00 and $x$ = 0.10 samples in the observed frequency range (inset of Fig. 5) as the cut-off occurs beyond this range. The increase of $\mu_i'$ with an increase of the LNCZFO content is expected as per the sum rule of the composite. The values of $\mu_i'$ are presented in Table 1.

### 3.5. Relative quality factor and magnetic loss tangent

The variation of the RQF as a function of the frequency is demonstrated in Fig. 6(a). The RQF is used as a performance indicator for practical applications. The RQF increases with increase of frequency and peaks at a certain value and then decreases. For LNCZFO, the peak is sharper but broadened by increasing the ferroelectric phase in the composite, increasing the frequency utility range. Fig. 6(b) reveals that the loss of the composites at high-frequency is quite low. This is because of the insulation layers originating from BSTDO enveloping the LNCZFO particles which significantly increase the resistivity of the
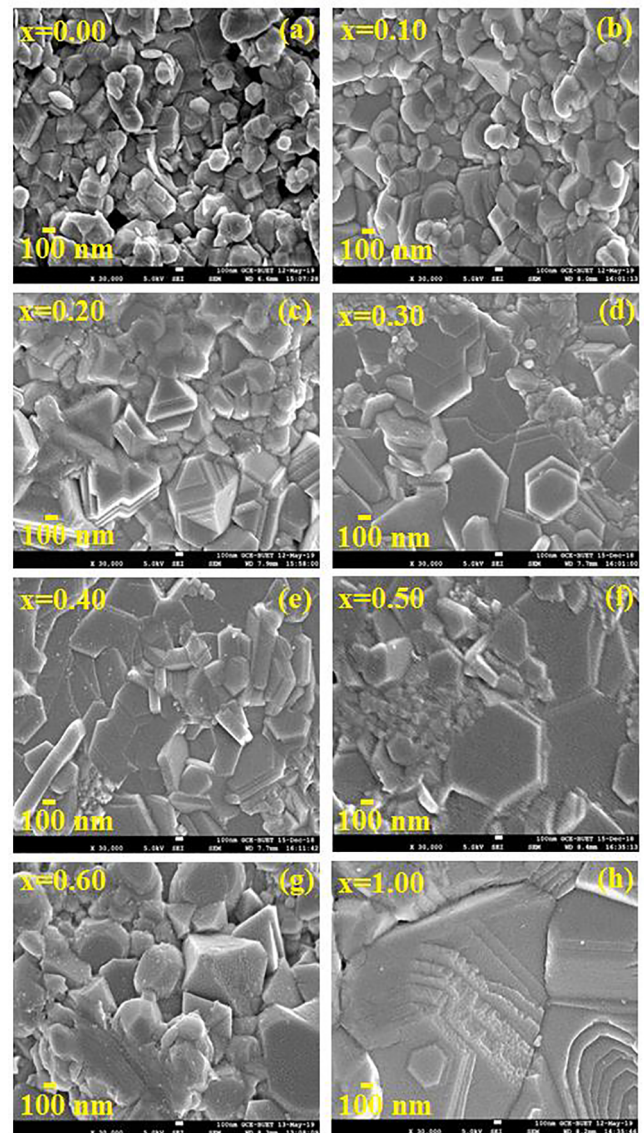
material causing reduction in the eddy current loss [27]. The magnetic loss caused by the latency of domain wall motion with applied ac field is ascribed to various defects, including domain wall bowing, non-uniform and non-repetitive domain wall motion, the variation of
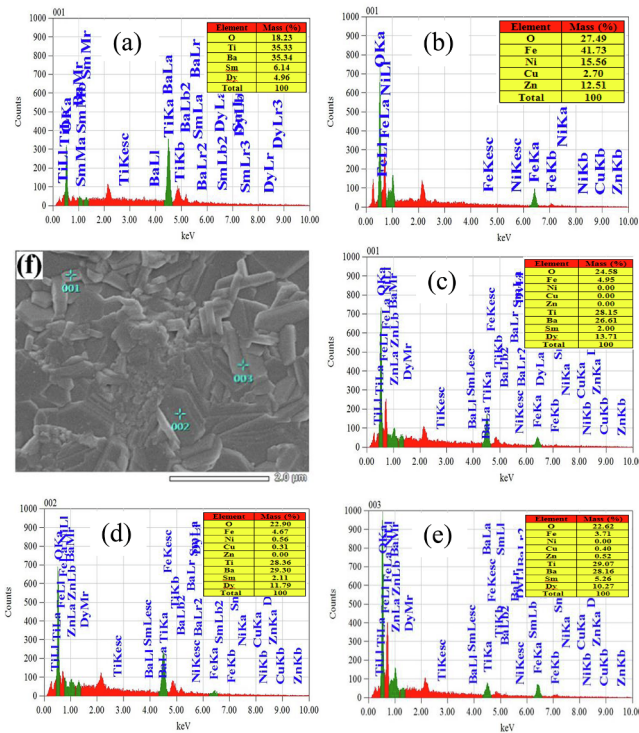
**Fig. 4.** EDS spectrum of (a) BSTDO (b) LNCZFO (c) point 001 (d) point 002 and (e) point 003 of 0.5LNCZFO + 0.5BSTDO composite (f) image used for EDS study of 0.5LNCZFO + 0.5BSTDO composite.
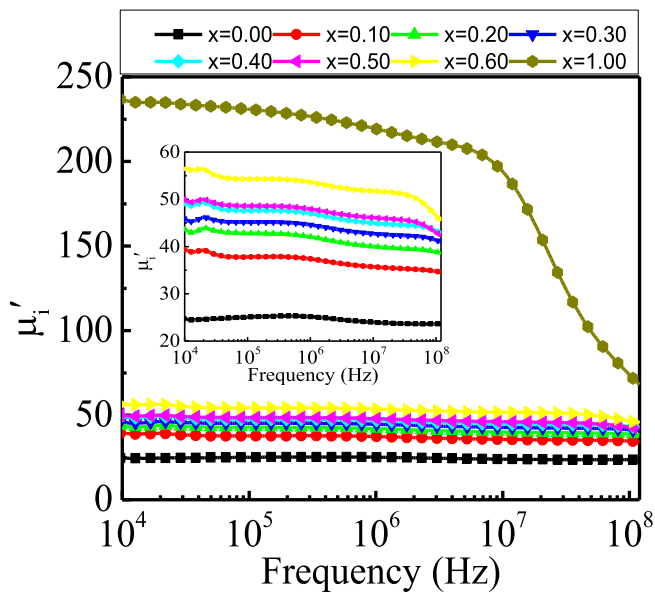


**Fig. 5.** The variation of $\mu_i'$ as a function of frequency for various $x$LNCZFO + $(1-x)$BSTDO composites.

localized flux density, domain wall annihilation and nucleation [28].

### 3.6. Dielectric property

Fig. 7(a) demonstrates the variation of $\varepsilon'$ with frequency. The RT $\varepsilon'$ is investigated within the frequency range from 20 Hz to 10 MHz. It is observed that $\varepsilon'$ decreases with the increase in frequency up to a certain value. Afterwards, it remains almost constant for all compositions. This low-frequency dielectric dispersion results because at low-frequency all types of polarizations (electronic, interfacial, dipolar and ionic) are

present in the samples. However, on increasing frequency some of the polarizations gradually disappear (except electronic and ionic) resulting in a rapid drop of $\varepsilon'$. The $\varepsilon'$ remains almost constant at higher frequencies as the electric dipoles do not get enough time to line up and therefore cannot follow the rapid variation of the applied alternating electric field. In the low-frequency region, the large value of $\varepsilon'$ results from the interfacial polarization suggested by Maxwell–Wagner [29,30]. Interfacial polarization originates from the inhomogeneity of the sample arising from grain structure, impurity, interfacial defects, and porosity. This inhomogeneity is generated in the sample during the process of high-temperature calcination and sintering. The $\varepsilon'$ increases with ferrite content for some of the composites owing to the enlarged $\underline{D}$ of the samples. The grain boundary area decreases as $\underline{D}$ increases. The increase in interfacial polarization also resulted from the heterogeneity of composites [31,32]. These heterogeneities are the interfaces between the ferrite and ferroelectric phases, where the conductivity and permittivity of the constituent phases are different. This gives rise to an interfacial polarization and contribute to $\varepsilon'$ [33]. As a result of the presence of ferrite with large $\underline{D}$ and heterogeneity in the composites, $\varepsilon'$ was increased. In the presented study, an enhanced $\varepsilon'$ was observed for $\underline{D}$ between 0.521 and 0.658 μm and a decreasing trend of $\varepsilon'$ was observed for other values of $\underline{D}$. This is thought to be caused by dilution of a non-ferroelectric grain boundary phase. These results agree with the earlier reports [34,35]. The present composites show an excellent high-frequency constancy of $\varepsilon'$ for a given composition presented at the inset of Fig. 7(a). The absolute value of $\varepsilon'$, however, is decreased with an increase in the ferrite phase for the reason that $\varepsilon'$ is smaller for LNCZFO compared to BSTDO.

Fig. 7(b) reveals the variation of dielectric loss ($\tan\delta_E$) as a function of frequency. This $\tan\delta_E$ is attributed to the resonance of the domain wall [6]. Frequency dispersion $\tan\delta_E$ occurs in both lower and higher-frequency regions. It is observed that the composites exhibit the loss peaks according to the Debye relaxation theory. Such resonance loss peaks arise when the hopping frequency of the electrons between the different ionic states, become almost equal to the frequency of the applied field. That is, when the condition $\omega\tau = 1$ is satisfied [36]. Similar behavior is also reported in earlier studies [6,37]. Composites of $x = 0.40$, 0.50 and 0.60 exhibits large $\varepsilon'$ with low $\tan\delta_E$ compared to both LNCZFO and BSTDO phases as a result of the reduced motion of the charge carriers.

### 3.7. Electric modulus spectra analysis

Fig. 8(a) shows the frequency-dependent $M'$. In the low-frequency region, the value of $M'$ is quite low, indicating the motion of the polaron hopping and the relatively small influence of the electrode impact [38,39]. After a certain frequency, the value of $M'$ increases, because of the inability of some dipoles to follow the alternating electric field at a higher-frequency. The $M'$ significantly increases with frequency for all samples. Fig. 8(b) demonstrates the frequency response $M''$. The region below the peak frequency defines the range of motion of the charge carriers over long distances, i.e. between the grains. Beyond the peak frequency, charge carrier moves within short distances, i.e. within the grains [40]. The region where the peak occurs indicates a shift from long to short-distance mobility. At both ends of the maxima, asymmetrical peak broadening is observed. Asymmetric peak broadening indicates that relaxation times are distributed in different time constants [41].

### 3.8. The ac conductivity

In material science, conductivity is an important topic. Electrical conductivity shows important electrical features and is therefore essential to clarify its mechanism. Fig. 9(a) demonstrates the frequency-dependent $\sigma_{ac}$. The frequency-dependent $\sigma_{ac}$ spectrum shows two
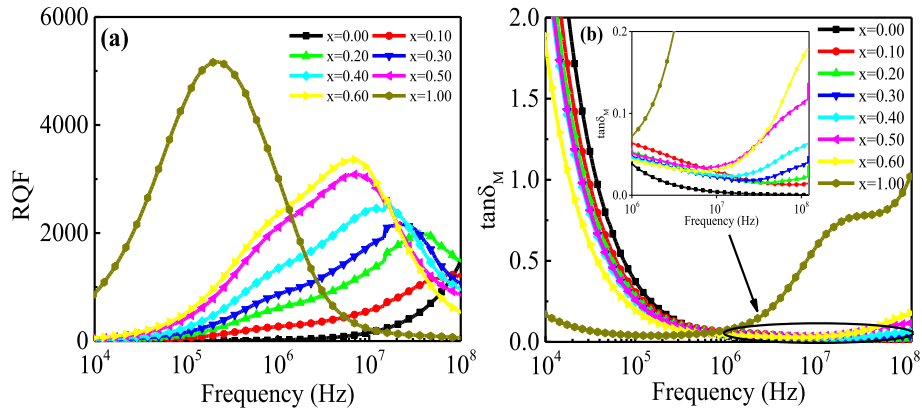
**Fig. 6.** The variation of (a) RQF and (b) $\tan\delta_M$ as a function of frequency for various $x$LNCZFO + $(1-x)$BSTDO composites.

different regions. The conductivity in the lower-frequency region is almost independent of the frequency referred to as dc conductivity ($\sigma_{dc}$), where the resistive grain boundaries are more active for dielectrics according to the Maxwell–Wagner double layer model [30,42]. At the high-frequency region, known as the hopping region, $\sigma_{ac}$ is increasing very rapidly and the transport phenomenon continues with hopping carriers resulting from the constituent elements. Conductive grains become more prominent at higher frequencies, thus increasing the hopping charge carrier and contributing to increased conductivity. Hopping of 3d electrons between $Fe^{2+}$ and $Fe^{3+}$ as well as $Ni^{2+}$ and $Ni^{3+}$ could play a significant role in the conductivity system. The frequency dependent $\sigma_{ac}$ can be written according to the Jonscher's power law [43]:

$$\sigma_{ac}(\omega) = \sigma_{dc} + B\omega^n, \tag{16}$$

where $\sigma_{ac}(\omega)$ is the resultant conductivity, $\sigma_{dc}$ is the dc conductivity, $B$ is the pre-exponential factor, $n$ is the frequency exponent. The exponent $n$ shows the degree to which the moving ions interact with the surrounding lattice. Both $n$ and $B$ depend on materials and temperature. The variation of $\sigma_{ac}$ can easily be explained by the polaron hopping mechanism proposed by Austin and Mott as a function of frequency [44]. In the small polaron model, $\sigma_{ac}$ increases with an increase in frequency, while the $\sigma_{ac}$ decreases with an increase in frequency in the large polaron hopping mechanism [45]. The present investigation is satisfied with the small polaron hopping mechanism. Fig. 9(b) shows the variation of $\log\sigma_{ac}$ as a function of $\log\omega$. The $\log\sigma_{ac}$ increases with an increase in frequency for all samples, indicating the conduction

process in the material is caused by small polaron hopping [46]. The variation of $\log\sigma_{ac}$ with $\log\omega$ should be linear as per Jonscher's law. However, mixed polarons (small/large) conductions are responsible for the slight deviation of some compositions from linearity [47].

### 3.9. Complex impedance spectra

Frequency-dependent resistance ($Z'$) is shown in Fig. 10(a). The graphical representation shows that the magnitude of $Z'$ gradually decreases with an increase in frequency up to a certain value (1 kHz) which confirms the increase of conductivity in the composite. At lower frequencies, the higher value of $Z'$ indicates that relaxors have larger polarization since all types of polarization exist in this region. The plateau-like behavior of $Z'$ at higher frequencies indicates the possible release of space charge polarization at the boundaries of homogeneous phases in composites under the applied external field [48,49]. The obtained results are well compatible with PZT–NZFO and CZFMO–PCT composites [50,51]. The enhanced $Z'$ values are found in the low-frequency region with an increase in the BSTDO content (except for parent compositions, $x = 0.00$ and $1.00$), indicating an increase in the resistive values of the composite. Fig. 10(b) demonstrates the frequency variation of the reactance ($Z''$) following a trend similar to $Z'$.

Polycrystalline relaxors consisting of grains and grain boundaries can be modeled by an equivalent circuit according to the brick-layer model [52] consisting of three parallel RC circuits connected in series (Fig. 11.a). Each RC element of the equivalent circuit contributes a semicircle to the $Z'$ versus $Z''$ graph. A single semicircle indicates grain
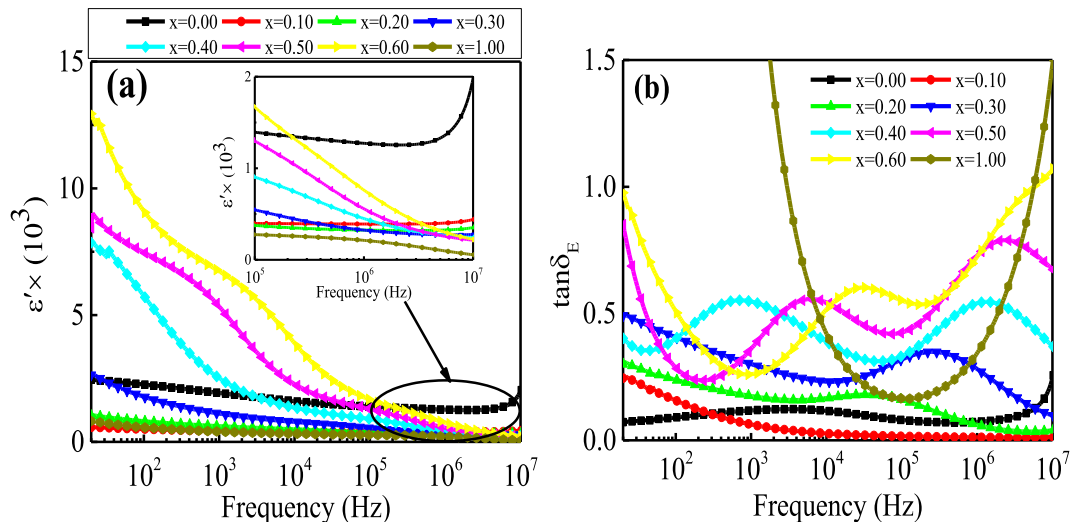


**Fig. 7.** The variation of (a) $\varepsilon'$ and (b) $\tan\delta_E$ as a function of frequency for various $x$LNCZFO + $(1-x)$BSTDO composites.
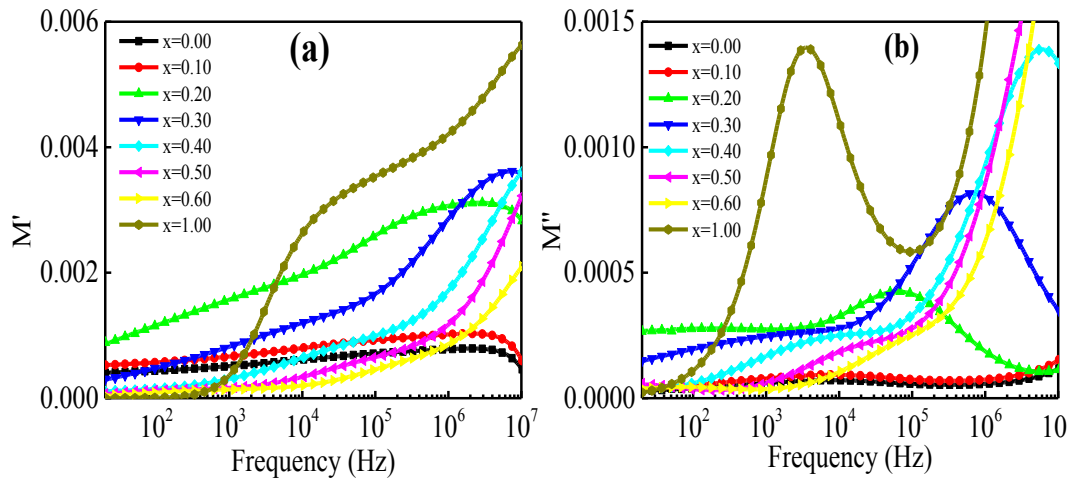
**Fig. 8.** Electric modulus spectra of various $x$LNCZFO + (1 − $x$)BSTDO composites: (a) real part ($M'$) and (b) imaginary part ($M''$).
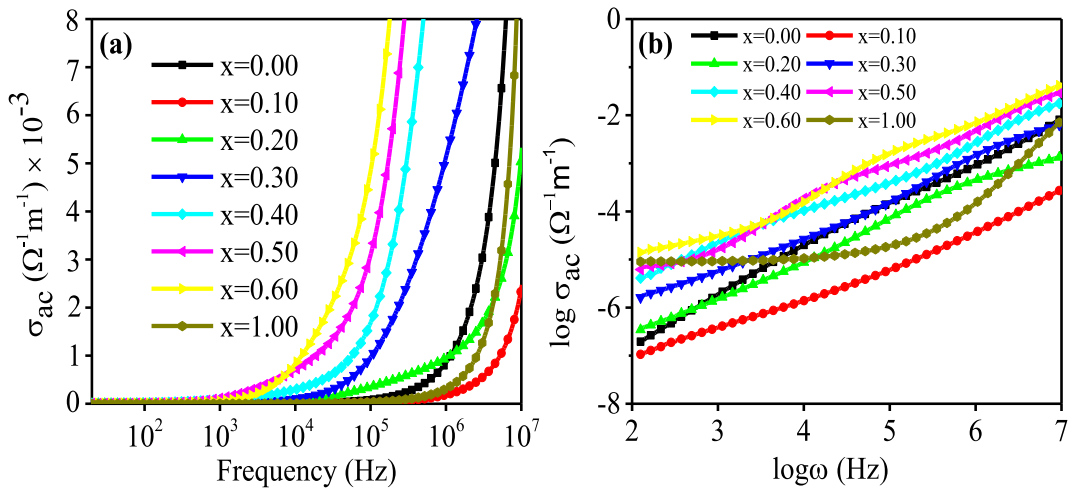


**Fig. 9.** (a) Frequency dependence of $\sigma_{ac}$ and (b) plot of log$\omega$ versus log$\sigma_{ac}$ for various $x$LNCZFO + (1 − $x$)BSTDO composites.

effects and a second semicircle indicates the presence of grain boundary effects. If a third semicircle is present, it indicates the electrode effects. Fig. 11(b-i) demonstrates the Nyquist plot of different compositions taken over a wide range of frequency (20 Hz–120 MHz) at RT. In the impedance spectra, compositions with $x$ = 0.00, 0.10, 0.20, 0.30 and 1.00 have a single semicircular arc, showing excellent uniformity of

conductive and dielectric properties. This suggests that the materials have only a grain boundary effect on the conduction process at RT [53]. The impedance spectra of composites $x$ = 0.40, 0.50 and 0.60 consists of double semicircular arcs. In the high-frequency region, these compositions exhibit an asymmetrical semicircular arc that is caused by the superposition of semicircular arcs of the constituent phases. This may
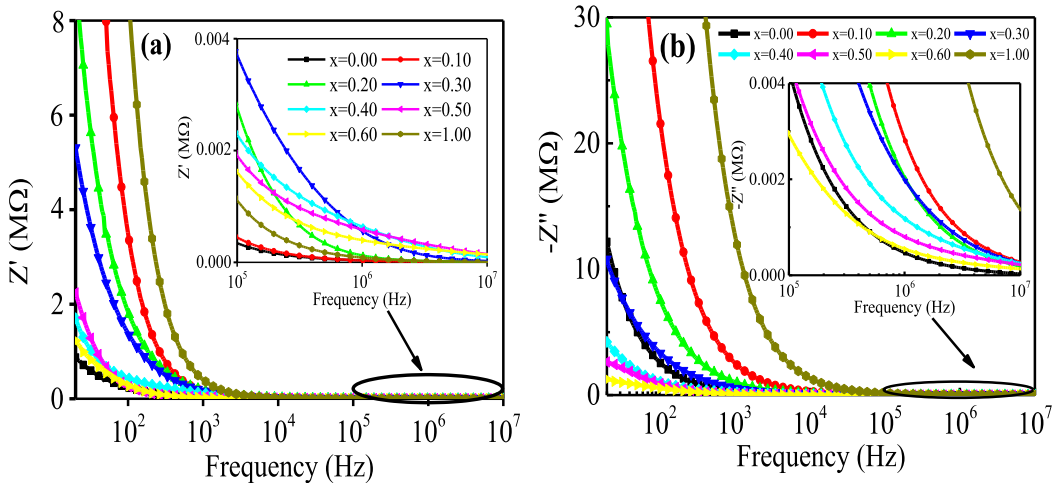


**Fig. 10.** (a) Frequency dependence of $Z'$ and (b) $Z''$ for various $x$LNCZFO + (1 − $x$)BSTDO composites.
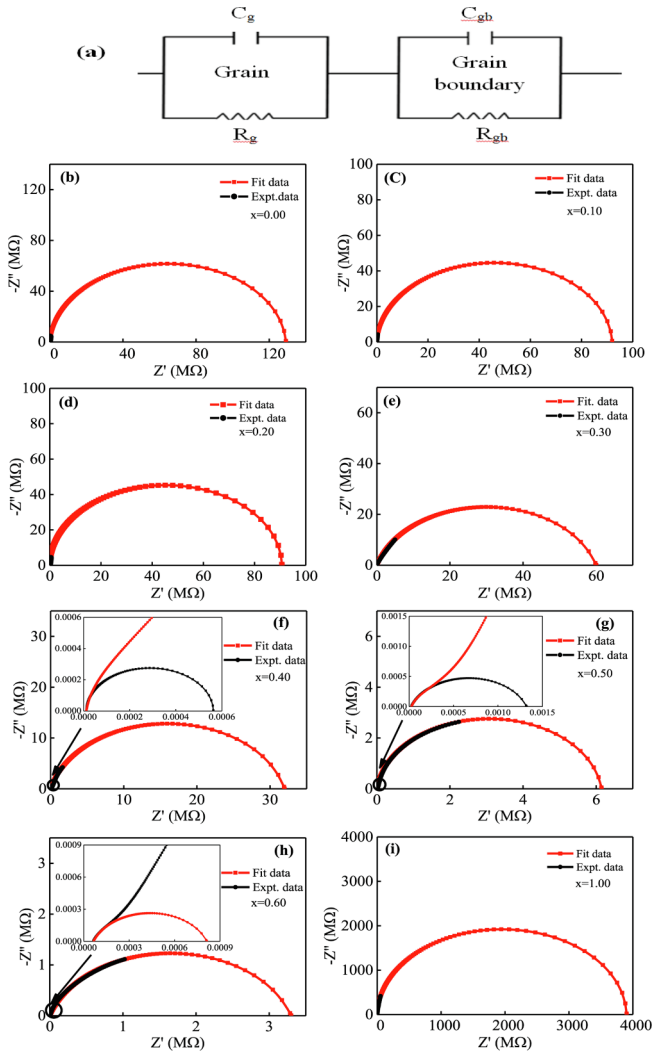
**Fig. 11.** (a) Equivalent circuit model and (b)–(i) show the Cole–Cole plot of complex impedance.

result from a slight difference in relaxation time for grains in the constituent phases. The equivalent circuit consists of two sub-circuits connected in series as shown in Fig. 11(a) can be used to describe this activity. The response of $R_gC_g$ and $R_{gb}C_{gb}$ corresponds to the high and low-frequency semicircular arcs, respectively. Here, $R_g$ and $R_{gb}$ are the grain and grain boundary resistance, $C_g$ and $C_{gb}$ are the grain and grain boundary capacitance, respectively. According to the equivalent circuit, impedance can be evaluated as follows:

$$Z^* = R_g - \frac{1}{i\omega c_g} + R_{gb} - \frac{1}{i\omega c_{gb}}, \tag{17}$$

Non-Debye-type relaxation is found to be present in the studied compositions because each composition exhibit depressed/distorted semicircle. A perfect semicircle with its center at-axis is observed for an ideal Debye-type relaxation [54]. The diameter of the semicircular arcs in the higher-frequency region is quite small compared to the semi-circular arcs in the lower-frequency region, indicating the dominant contribution of the grain boundary to the total resistance. The figure displays that for ferrite content up to $x = 0.60$, the grain boundary resistance decreases. This may be ascribed to the inhomogeneous distribution of grains. The grain boundary resistance is very large for the ferrite phase ($x = 1.00$) as the ferrite grains are less conductive. This large grain boundary resistance also indicates the relatively large porosity of the ferrite sample.
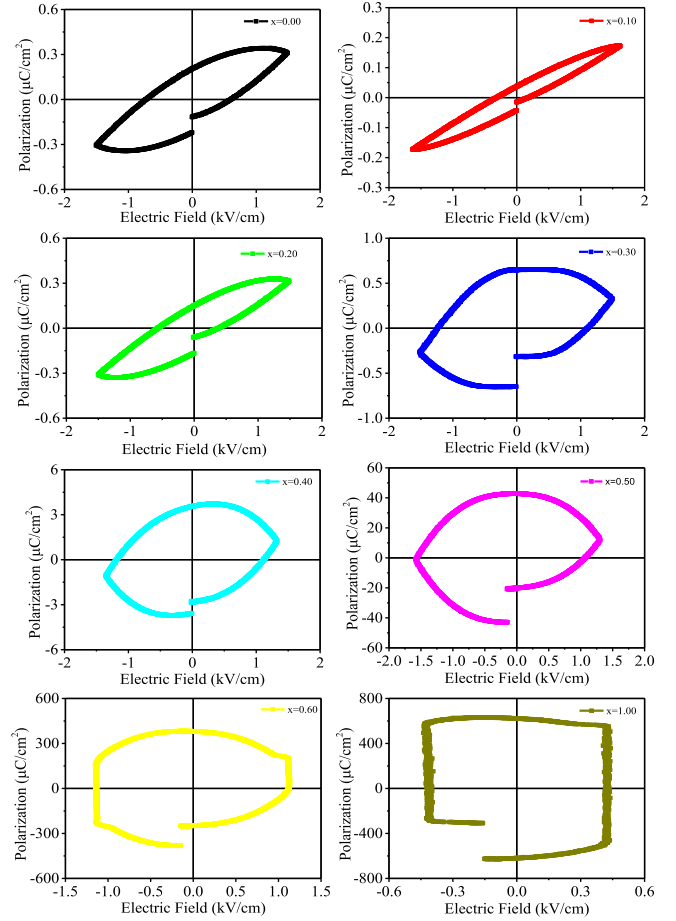


**Fig. 12.** P–E loops of $x$LNCZFO + $(1-x)$BSTDO composites.

### 3.10. Ferroelectric property

P-E curves were evaluated to assess the ferroelectric nature of the composites as shown in Fig. 12. In Fig. 12, samples up to $x = 0.20$ show typical ferroelectric hysteresis, indicating that the samples are polarized spontaneously. The maximum saturation polarization (0.34 μC/cm$^2$) is found for $x = 0.20$ among these compositions. The remnant polarization of these samples is found to be between ranges of 0.035–0.204 μC/cm$^2$, which is quite small. This may be the smallest $\bar{D}$ of the BSTDO phase [55,56]. The ferroelectric behavior of the composites gradually weakens with an increase in ferrite content as LNCZFO ferrite provides a relatively lower electrical resistance than BSTDO perovskite. The P-E loops of the composites with $x = 0.50$ and 0.60 are almost rounded and ferrite phase ($x = 1.00$) illustrates an almost rectangular loop, suggesting a very lossy and lower resistive composition from which nothing could be obtained from the intrinsic ferroelectricity. High leakage charge, inappropriate electrode, and barium volatilization may also be the possible reason for this. Similar behavior has been reported earlier [16]. The ferroelectric coercive field is minimum for $x = 0.10$ composite, which implies that the composite may easily be polarized under the appropriate electric field.

### 3.11. Magnetoelectric coefficient

The strain-mediated ME coupling effect in composites with two ferroic phases depends on the weight proportion of the component phases, the magnetization, polarization and electrical resistivity of the two ferroic orders [57]. The ME effect in multiferroic materials arises from the interaction of the magnetic and ferroelectric domains. Applied magnetic field induces large strain in magnetic domains of the samples,
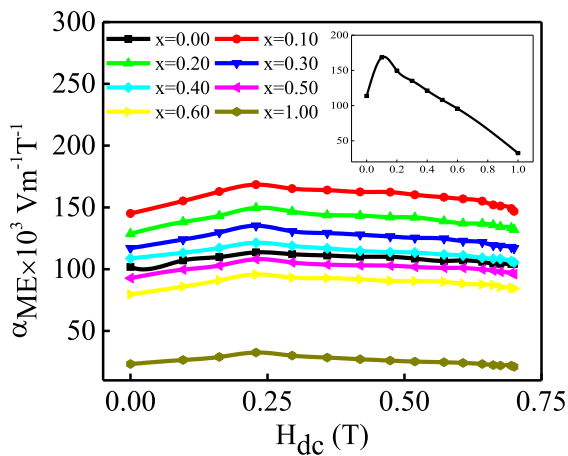
**Fig. 13.** $\alpha_{ME}$ variation with dc magnetic field and $(\alpha_{ME})_{max}$ with the ferrite content (inset) for different $x$LNCZFO$+(1-x)$BSTDO multiferroic composites.

which distort the ferroelectric domains. As a result, charges are induced in the grains. These charges would help to develop more voltage in the grain, which in turn produces a strong ME coupling. The variation of $\alpha_{ME}$ for the compositions as a function of the applied dc magnetic field is demonstrated in Fig. 13. The value of $\alpha_{ME}$ is found to increase with applied dc magnetic field, and gradually decreases after reaching the maximum value. The decrease in $\alpha_{ME}$ with the increase in dc magnetic field is explainable by the fact that the magnetostriction coefficient of ferrite phase reaches its saturation value beyond a certain value of magnetic field. This causes the induced electric field to become constant in the ferroelectric phase, as a result of which, the value of $\alpha_{ME}$ decreases [58]. The variation of maximum $\alpha_{ME}$ with ferrite content is shown in the inset of Fig. 13. The plot reveals that the $(\alpha_{ME})_{max}$ decreases with large grain ferrite content, which is responsible for a significant decrease in composite resistivity. The ME response of the composites depends on the piezoelectricity of the ferroelectric phase and the magnetostriction of the ferrite phase. Smaller grains are more effective in producing both piezomagnetic and piezoelectric coefficients than larger grains [59]. Moreover, to obtain better ME effect in composites, two individual phases should be in equilibrium and mismatch between grains should not be present. Leakage charges are developed through the path of low resistive ferrite grain surrounding the ferroelectric grains. These leakage charges reduce the piezoelectric effect of the ferroelectric phase, which is one of the causes of the $\alpha_{ME}$ decrease. The porosity of the ferrite phase is another possible reason for less ME coupling between the two phases in the composite. The increase in porosity results in a decrease in the net magnetization of the samples, which has a significant effect on the coupling interaction between the two phases. The maximum value of $\alpha_{ME}$ ($170 \times 10^3$ Vm$^{-1}$T$^{-1}$) is found for the 10%LCNZFO$+$90%BSTDO composite. The results of the presented composites are relatively higher than previously reported results by other researchers [60–62].

## 4. Conclusions

Various $x$LNCZFO$+(1-x)$BSTDO multiferroic composites were synthesized by conventional solid-state reaction route and investigation was carried out on their structural, morphological, magnetic properties, dielectric properties, electric modulus, ac conductivity, impedance spectroscopy, ferroelectric property, and ME voltage coefficient. The XRD pattern confirms the existence of both constituent phases without any third phase. The increase in $\mu_i'$ with the concentration of LNCZFO in the composite is attributed to the presence of a strong magnetic phase (LNCZFO) which enhances the consistency and interaction of magnetic grains, leading to an increase in the $\mu_i'$ and reduced loss. As the ferrite content increases, RQF increases and the highest value is obtained for

$x = 1.00$. The typical low-frequency dielectric dispersion behavior of all composites could be explained according to the Maxwell–Wagner interfacial polarization effect. The $\varepsilon'$ remains almost independent in the higher-frequency region, as the electric dipoles with a large relaxation time do not respond to the applied field. The composites exhibit a small tan$\delta_E$ as a result of the reduced mobility of the charge carrier. The modulus and the ac conductivity of the presented composites reveal a polaron hopping conductivity. The conductivity increases with an increase in frequency, which usually results from the inhomogeneity of the composites, possibly induced by the presence of space charge. The linearity of log$\omega$ versus log$\sigma_{ac}$ graphs implies that the conductivity is due to a small polar hopping associated with a lattice strain induced by free charges. The non-Debye type relaxation occurs for all the compositions seeing that each composition has a distorted semicircle in the $Z'$ versus $Z''$ graph. The ferroelectric property of the composites is decreased by adding ferrite of low grain resistance and high leakage current. The $x = 0.10$ composite shows the highest ME voltage coefficient of $170 \times 10^3$ Vm$^{-1}$T$^{-1}$ resulting from uniform grain growth of both phases and the rigidity of the two phases being comparable in magnitude. The results obtained from the present study could be used to manufacture potential multifunctional devices for technological use and to explore the new family of composites.

## Declaration of Competing Interest

The authors declare that they have no known competing financial interests or personal relationships that could have appeared to influence the work reported in this paper.

## References

[1] H. Schmid, Ferroelectrics 162 (1994) 317.
[2] W. Eerenstein, N.D. Mathur, J.F. Scott, Nature 442 (2006) 759.
[3] B.K. Bammannavar, L.R. Naik, Smart Mater. Struct. 18 (2009) 085013.
[4] J. Ryu, S. Priya, K. Uchino, H.-E. Kim, J. Electroceramics 8 (2002) 107.
[5] O.M. Hemeda, A. Tawfik, M.A. Amer, B.M. Kamal, D.E. El Refaay, J. Magn. Magn. Mater. 324 (2012) 3229.
[6] Md.D. Rahaman, S.K. Saha, T.N. Ahmed, D.K. Saha, A.K.M. Akther Hossain, J. Magn. Magn. Mater. 371 (2014) 112.
[7] Prakash Bongurala, Venkataiah Gorige, J. Magn. Magn. Mater. 477 (2019) 350.
[8] K. Sadhan, S.R. Murthy, S. Jie, Y. Xie, Y. Liu, Q. Zhan, R.W. Li, J. Appl. Phys. 113 (2013) 17C731.
[9] K.C. Verma, R.K. Mukhwinder Singh, Navdeep Goyal Kotnala, J. Magn. Magn. Mater. 469 (2019) 483.
[10] L. Su, P. Liu, Y. He, J. Zhou, L. Cai, C. Liu, H. Zhang, J. Alloys Compd. 494 (2010) 330.
[11] R.S. Devan, C.M. Kanamadi, S.A. Lokare, B.K. Chougule, Smart Mater. Struct. 15 (2006) 1877.
[12] M.A. Islam, A.K.M. Mehadi Hasan, Akther Hossain, J. Magn. Magn. Mater. 424 (2017) 108.
[13] Roksana Parvin, A.A. Momin, A.K.M. Akther Hossain, J. Magn. Magn. Mater. 401 (2016) 760.
[14] Lu. Da-Yong, Shu-Zhen Cui, Qiao-Li Liu, Xiu-Yun Sun, Ceram. Int. 42 (2016) 14364.
[15] Manjit Borah, Dambarudhar Mohanta, Appl. Phys. A 115 (2013) 1057.
[16] A. Ahad, M.A. Taher, Mithun Kumar Das, M. Zahidur Rahaman, M.N.I. Khan, Results Phys. 12 (2019) 1925.
[17] Poonam Pahuja, Amit Tomar, R.P. Tandon, Ferroelectrics 516 (2017) 127.
[18] M. Ganguly, S.K. Rout, W.S. Woob, C.W. Ahn, I.W. Kim, Physica B 411 (2013) 26.
[19] J.B. Nelson, D.P. Riley, Proc. Phys. Soc. 57 (1945) 160.
[20] Abdul Samee Fawzi, A.D. Sheikh, V.L. Mathe, Physica B 405 (2010) 340.
[21] A.A. Sattar, H.M. El-Sayed, K.M. El-shookrofy, M.M. El-Tabey, J. Mater. Sci. 40 (2005) 4873.
[22] M.I. Mendelson, J. Am. Ceram. Soc. 52 (1969) 443.

[23] T. Nakamura, J. Appl. Phys. 88 (2000) 348.
[24] T. Tsutaoka, M. Ueshima, T. Tokunaga, T. Nakamura, K. Hatakeyama, J. Appl. Phys. 78 (1995) 3983.
[25] A. Globus, P. Duplex, M. Guyot, IEEE Trans. Magn. 7 (1971) 617.
[26] J.L. Snoek, Physica 14 (1948) 207.
[27] Lu. Xuegang, Liang Gongying, Zhang Yumei, Zhang Wei, Nanotechnology 18 (2007) 015701.
[28] M. Manjurul Haque, M. Huq, M.A. Hakim, J. Magn. Magn. Mater. 320 (2008) 2792.
[29] J.C. Maxwell, A Treatise on Electricity and Magnetism, Oxford University Press, London, 1873.
[30] K. Wagner, J. Ann. Phys. 345 (1913) 817.
[31] S. Upadhyay, D. Kumar, O.M. Parkash, Bull. Mater. Sci. 19 (1996) 513.
[32] V. Kuldeep, O. Subohi, R. Kurchania, Appl. Phys. A 125 (2019) 631.
[33] R. Sharma, P. Poonam, R.P. Tandon, Ceram. Int. 40 (2014) 9027.
[34] T.M. Shaw, S. Trolier McKinstry, P.C. McIntyre, Annu. Rev. Mater. Sci. 30 (2000) 263.
[35] G. Arlt, D. Hennings, G. de With, J. Appl. Phys. 58 (1985) 1619.
[36] Kavita Verma, Ashwini Kumar, Dinesh Varshney, J. Alloys Compd. 526 (2012) 91.
[37] S.C. Mazumdar, M.N.I. Khan, Md. Fakhrul Islam, A.K.M. Akther Hossain, J. Magn. Magn. Mater. 401 (2016) 443.
[38] M. Kaiser, Physica B 407 (2012) 606.
[39] R.N.P. Choudhary, D.K. Pradhan, C.M. Tirado, G.E. Bonilla, R.S. Katiyar, J. Mater. Sci. 42 (2007) 7423.
[40] S. Pattanayak, R.N.P. Choudhary, P.R. Das, S.R. Shannigrahi, Ceram. Int. 40 (2014) 7983.
[41] S. Pattanayak, B.N. Parida, P.R. Das, R.N.P. Choudhary, Appl. Phys. A 112 (2013) 387.
[42] J.C. Maxwell, A Treatise on Electricity and Magnetism, Clarendon Press, Oxford, 1982.

[43] A.K. Jonscher, Nature 267 (1977) 673.
[44] I.G. Austin, N.F. Mott, Adv. Phys. 18 (1969) 41.
[45] M.S. Khandekar, R.C. Kambale, J.Y. Patil, Y.D. Kolekar, S.S. Suryavanshi, J. Alloys Compd. 509 (2011) 1861.
[46] M.J. Miah, M.N.I. Khan, A.K.M. Akther Hossain, J. Magn. Magn. Mater. 401 (2016) 600.
[47] S.L. Kadam, K.K. Patankar, C.M. Kanamadi, B.K. Chougule, Mater Res Bull. 39 (2004) 2265.
[48] B. Behera, P. Nayak, R.N.P. Choudhary, Mater. Res. Bull. 43 (2008) 401.
[49] J. Plocharski, W. Weiczorek, Solid State Ion. 28 (1988) 979.
[50] N.S. Negi, Anshu Sharma, J. Shah, R.K. Kotnala, Mater Chem. Phys. 148 (2014) 1221.
[51] H. Zhang, C.L. Mak, J. Alloys Compd. 513 (2012) 165.
[52] Wayne Reitz, Mater Manuf. Process 21 (2006) 425.
[53] H. Inaba, J. Mater. Sci. 32 (1997) 1867.
[54] R. Anthony, C. West Derek, Naohiro Hirose Sinclair, J. Electroceram. 1 (1997) 65.
[55] Kenji Uchino, Eiji Sadanaga, Terukiyo Hirose, J. Am. Ceram. Soc. 72 (1989) 1555.
[56] V. Buscaglia, M. Viviani, M.T. Buscaglia, P. Nanni, L. Mitoseriu, A. Testino, E. Stytsenko, M. Daglish, Z. Zhao, M. Nygren, Powder Technol. 148 (2004) 24.
[57] C.M. Kanamadi, S.R. Kulkarni, K.K. Patankar, S.S. Chuogule, S.J. Patil, B.K. Chougule, J. Mater. Sci. 42 (2007) 5080.
[58] N. Cai, J. Zahi, C.W. Nan, Y. Lin, Z. Shi, Phys. Rev. B 68 (2003) 224103.
[59] B.K. Bammannavar, L.R. Naik, B.K. Chougule, J. Appl. Phys. 104 (2008) 064123.
[60] Pradeep Chavana, L.R. Naik, P.B. Belavi, Geeta Chavan, V.T. Muttannavar, B.K. Bammannavar, R.K. Kotnala, J. Alloys Compd. 777 (2019) 1258.
[61] Shivangi Tiwari, Satish Vitta, Sci. Rep. 8 (2018) 1.
[62] A.A. Momin, M.A. Zubair, Md. Fakhrul Islam, A.K.M. Akther Hossain, J. Mater. Sci.: Mater. Electron. 30 (2019) 13033.
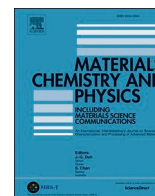
# Study of impedance and magnetoelectric property of lead-free $x$LCNZFO+ $(1\text{-}x)$BGTDO multiferroic composites

Mithun Kumar Das [a],[*],[1], M.A. Zubair [b], Hidekazu Tanaka [c], A.K.M. Akther Hossain [a]

[a] Department of Physics, Bangladesh University of Engineering and Technology, Dhaka, 1000, Bangladesh
[b] Department of Glass and Ceramic Engineering, Bangladesh University of Engineering and Technology, Dhaka, 1000, Bangladesh
[c] Institute of Scientific and Industrial Research, Osaka University, Ibaraki, Osaka, 567-0047, Japan

HIGHLIGHTS

- $x$LNCZFO+$(1\text{-}x)$BGTDO composites were synthesized by a solid-state reaction process.
- Construction of cubic-tetragonal phase coexistence.
- Study the magnetic and dielectric properties of the composite material.
- Impedance and modulus spectroscopy of $x$LNCZFO+$(1\text{-}x)$BGTDO composites.
- The ME coefficient is very high ($\sim 172 \times 10^3$ Vm$^{-1}$T$^{-1}$) for 0.1LNCZFO+0.9BGTDO composites.

ARTICLE INFO

ABSTRACT

Multiferroic $x$LCNZFO+$(1\text{-}x)$BGTDO composites are prepared by the conventional solid-state reaction method. The phase identification of ferrite and perovskite structure is executed by the XRD analysis. The initial permeability enhances with an increment in ferrite content because of high magnetic LNCZFO and a reduction of oxygen vacancies. The dispersive dielectric nature is observed in the low-frequency region due to Maxwell-Wagner interfacial polarization. The sample of $x = 0.60$ is comprised of the maximum dielectric constant of about $1.02 \times 10^4$ at 1 kHz. The ac conductivity results from a small polaron hopping mechanism. The complex impedance spectra of some samples exhibit a single semi-circular arc due to the dominance of grain boundary resistance, whereas other samples show double arcs representing the dominance of grain and grain boundary effect on the conduction mechanism. There is a strong coupling between the two ferroic orders and the optimum magnetoelectric coupling voltage of $172 \times 10^3$ Vm$^{-1}$T$^{-1}$ is obtained for the $x = 0.10$ sample.

## 1. Introduction

Multiferroic materials contain more than one ferroic order at the same phase have recently gained a lot of attention because of their prospective multifunctional application in various devices [1]. There is a strong interaction between the two ferroic phases referred as the magnetoelectric (ME) coupling, which has an extensive application in practical devices along with magnetic sensors, electric field controlled ferromagnetic resonance devices, transducers, actuators, spintronics, phase shifter, data storage and ME memory cells, etc. [1,2]. In multiferroic composites, the strong ME effect is found due to the product properties of the constituent phases [3]. Multiferroics are two forms: single-phase and composite. The combined influence of ferroic orders can easily be seen in a single-phase multiferroic, but in nature, there are a few single-phase materials that can simultaneously possess ferromagnetic and ferroelectric properties. The application of single-phase materials in multifunctional technologies not yet been efficient since it has weak ME influence at room temperature (RT) and Néel or Curie temperatures much beyond RT [4]. Another constraint is that most single-phase components consist of costly materials and require expensive processing technologies. These drawbacks could overcome by the use of multiferroic composites (MFCs). MFCs widely used with the increasing requirement for new technologies to achieve multi-functional performance, high efficiency, and limited space. MFCs are cost-effective

---

and also have a higher ME effect than single-phase multiferroics, including $Pb(Fe_{1/2}Nb_{1/2})O_3$ [5]. Synthesized MFCs have potential ME influences at RT, which develop as a product-property of existing ferroic orders driven by elastic distortions [2]. This potential ME coupling property is highly essential in modern technologies, which are not available in single-phase multiferroics. In the presence of the ME effect, the deformity of the magnetostrictive phase contributes to the polarization of the piezoelectric materials of the composite that may induce the magnetization of the ferromagnetic materials as a result of the mechanical interaction of the two phases, which makes such materials technologically significant. The strong magnetostrictive effect of the piezomagnetic phase and the large piezoelectric effect of the piezoelectric materials are significant parameters for the high ME coefficient ($\alpha_{ME}$) of the MFCs [6]. The present research focuses on the improvement of the ME property of the composites. Therefore, a suitable mixture of magnetostrictive and piezoelectric phases in composites would produce an excellent extrinsic $\alpha_{ME}$. Various ME composites comprised of different ferrites and ferroelectrics have been reported in the literature [7–14]. To the best of our knowledge, no research conducted on particular $xLi_{0.1}Ni_{0.3}Cu_{0.1}Zn_{0.4}Fe_{2.1}O_4+(1-x)Ba_{0.95}Gd_{0.05}Ti_{0.95}Dy_{0.05}O_3$ composites based on a literature survey.

In the present study, $Li_{0.1}Ni_{0.3}Cu_{0.1}Zn_{0.4}Fe_{2.1}O_4$ (LNCZFO) nominated as the ferromagnetic phase and $Ba_{0.95}Gd_{0.05}Ti_{0.95}Dy_{0.05}O_3$ (BGTDO) as the ferroelectric phase. The selection of these phases carried out under the requirements for the high $\alpha_{ME}$. As a magnetostrictive phase, LNCZFO was chosen because of its relatively better magnetic properties. The Li–Ni ferrite doped with Jahn- Teller ions such as $Zn^{2+}$, $Cu^{2+}$, possesses a large magnetostriction coefficient since these ions offer a relatively high $\alpha_{ME}$ [15]. Besides, from the application perspective, Li–Ni ferrite doped with Jahn- Teller ions is one of the most effective and adequate material for general use in both high and low-frequency devices due to its high electrical resistivity (over 107 $\Omega$m), high magnetic permeability, low magnetic loss, good chemical stability, low coercivity, high mechanical hardness, low porosity, reasonable cost, and high Curie temperature [16,17]. Contrarily, BGTDO selected as a piezoelectric phase because of rare earth-substituted $BaTiO_3$ offers good dielectric constant with low loss, minimal leakage current density, high resistance, small transition temperature, good thermal stability, and large piezoelectric effect [18–21]. Therefore, it is quite interesting to find out possible changes in the various physical properties of a class of LNCZFO–BGTDO composites. Once these two-component phases can be successfully incorporated into the composites, it is expected that they might exhibit excellent magnetic, electrical, and ME properties. Lead-free materials used for present MFCs due to the toxicity of lead and associated risks to health and the environment. The lead-free MFCs with the above two ferroic orders expected to become a potential material for modern multifunctional device applications at RT. The results of the structural, morphological, magnetic, dielectric, ferroelectric, and ME properties of $xLNCZFO+(1-x)BGTDO$ composites presented and discussed in detail from the experimental point of view in this paper.

## 2. Experimental

### 2.1. Materials and methods

MFCs $xLi_{0.1}Ni_{0.3}Cu_{0.1}Zn_{0.4}Fe_{2.1}O_4+(1-x)Ba_{0.95}Gd_{0.05}Ti_{0.95}Dy_{0.05}O_3$ (with $x = 0.00, 0.10, 0.20, 0.30, 0.40, 0.50, 0.60$ and $1.00$) were produced using the standard solid-state reaction process. These values of the $x$ parameter were taken for a clear understanding of the real changes in the physical properties of composites with compositional variation according to the literature survey. High-grade $Li_2CO_3$ (99.0%, CAS No. 554-13-2), NiO (99.9%, CAS No. 1313-99-1), CuO (99.99%, CAS No. 1317-38-0), ZnO (99.9%, CAS No. 1314-13-2) and $Fe_2O_3$ (99.5%, CAS No. 1309-37-1) reagents were taken to fabricate the ferromagnetic LNCZFO component. Raw powders of $BaCO_3$ (99.9%, CAS No. 513-77-

9), $Gd_2O_3$ (99.9%, CAS No. 278513-25G), $TiO_2$ (99.9%, CAS No. 13463-67-7), $Dy_2O_3$ (99.9%, CAS No. 1308-87-8) were taken to synthesize the ferroelectric BGTDO phase. The raw elements were mixed in stoichiometric proportions into an acetone solution with an agate mortar and pestle. The mixed powders of ferromagnetic and piezoelectric phases were calcined at 973 K and 1273 K, respectively. The $xLNCZFO+(1-x)BGTDO$ composites were prepared by grinding the LNCZFO and BGTDO powders. Composite powders were combined with 10% polyvinyl alcohol as a binder and then pressed uniaxially to fabricate pellets and toroid samples. The optimum results of the samples are found at optimum sintering temperatures ($T_s$) typically among 1473–1523 K. Fabricated pellets and toroid samples were sintered at different temperatures among this range to evaluate optimum $T_s$. The obtained optimum $T_s$ values were: 1523 K for $x = 0.00$, 1498 K for $x = 0.10, 0.20, 0.30, 0.40, 0.50, 0.60$, and 1473 K for $x = 1.00$.

### 2.2. Characterization

Phase evolution of the synthesized compositions carried out at RT with an X-ray diffractometer (Philips PANalytical X'PERT-PRO) with CuK$\alpha$ radiation ($\lambda = 0.15418$ nm) and 1° per min inspecting rate from 20 to 60°. The lattice constants calculated by X-ray diffraction (XRD) statistics. Field Emission Scanning Electron Microscopy (FESEM, No. JEOL JSM7600F) and Energy Dispersive X-ray Spectroscopy (EDS) used to investigate the surface morphology and elementary distribution of the compositions, respectively. The X-ray density ($\rho_x$) of the materials calculated by the formulation:

$$\rho_x = \frac{nM}{N_A V}, \tag{1}$$

where $n$, $N_A$, $M$, and $V$ are the atoms numbers in a unit cell, Avogadro's number, molar mass, and unit cell volume, respectively. The bulk density ($\rho_B$) of each sample measured by applying the equation:

$$\rho_B = \frac{W_d}{W_d - W_w} \times \rho, \tag{2}$$

where $W_d$, $W_w$ and $\rho$ denote the weight of the pellet in the air, in the water, and density of water, respectively. Porosity ($P$) of the samples determined by the equation:

$$P(\%) = \frac{\rho_x - \rho_B}{\rho_x} \times 100. \tag{3}$$

The frequency response magnetic properties were evaluated at RT within a range of 10 kHz–120 MHz using an impedance analyzer (model-WAYNE KERR 65003). The real part of the initial permeability ($\mu_i'$) calculated by applying the formula:

$$\mu_i' = \frac{L_s}{L_0}, \tag{4}$$

where $L_s$ represents the core self-induction, $L_0$ ($= \frac{\mu_0 N^2 S}{\overline{d}}$) indicates the inductance of the winding coil, $N$ refers to the turns number of the coil ($N = 4$), $S$ reflects the area and $\overline{d} = (d_1+d_2)/2$ is the mean diameter of the toroid-shaped sample, where, $d_1$ and $d_2$ are the inner and outer diameter of the toroid-shaped sample, respectively. For each sample, the relative quality factor (RQF) determined by applying the equation:

$$RQF = \frac{\mu_i'}{\tan\delta_M}, \tag{5}$$

where $\tan\delta_M$ denotes the magnetic loss factor.

Dielectric analyses were conducted at RT within the range of frequencies of 20 Hz–10 MHz using the Impedance Analyzer. Samples coated with silver paste on both ends to facilitate better electrical contacts for frequency-dependent dielectric measurements. The dielectric constant ($\varepsilon'$) calculated by using the following formula:

$$\varepsilon^{'} = \frac{Ct}{\varepsilon_0 A}, \tag{6}$$

where $C$, $A$, and $\varepsilon_0$ ($= 8.85 \times 10^{-12}$ F/m) represent the capacity of the sample, the cross-section of the electrode, and permittivity in free space, correspondingly.

Complex electrical modulus ($M^*$) of the samples evaluated by using the formula:

$$M^*(\omega) = \frac{1}{\varepsilon^*} = \frac{1}{\varepsilon^{'} - j\varepsilon^{''}}, \tag{7}$$

where $\varepsilon^*$ and $\varepsilon^{''}$ signify the complex and imaginary dielectric constant, separately.

The ac conductivity ($\sigma_{ac}$) of the samples assessed by applying the equation:

$$\sigma_{ac} = \omega\varepsilon_0\varepsilon^{'}\tan\delta_E, \tag{8}$$

where $\omega$ and $\tan\delta_E$ signify the angular frequency and dielectric loss, respectively.

The $\alpha_{ME}$ of the samples calculated by applying an ac magnetic field superimposed a dc magnetic field on the sample. An electromagnet used to supply a dc magnetic field of up to 0.7 T. The Helmholtz coil driven by a signal generator operating at 50 Hz frequency to generate an ac magnetic field. The output voltage generated from the sample under investigation was measured using a Keithley electrometer (Model 2000) as a function of the dc magnetic field. The $\alpha_{ME}$ calculated by using the formula:

$$\alpha_{ME} = \left(\frac{dE}{dH}\right)_{H_{ac}} = \frac{V_0}{h_0 t}, \tag{9}$$

where $V_0$ indicates the ME output voltage through the sample and $h_0$ referred to the magnitude of the ac magnetic field.

## 3. Results and discussion

### 3.1. Phase identification

Fig. 1 illustrates the typical XRD patterns of different $x$LNCZFO+(1-$x$)BGTDO composites. The XRD peaks indexed with equivalent Miller indices. No reflections except those relating to a cubic structure of the ferrite material and tetragonal structure of the ferroelectric material detected, indicating that there were no chemical reactions between the two ferroic phases in the final sintering stage [16–19]. No non-indexed peaks correlated with the initial raw materials found that can attribute to the production of impurity. The existence of both phases in the composite with no third phase confirmed the excellence of the manufacturing of composite material. When the ferrite phase increases, the ferrite peaks become more intense, while the perovskite peaks become less intense. The number and intensity of peaks in the XRD patterns depend on the number and quantity of ferroic phases in the composites. Lattice parameters measured by solving different types of equations associated with subsequent peaks. The calculated lattice parameters for every single plane plotted as a function of the Nelson–Riley [22].

$$F(\theta) = \frac{1}{2}\left(\frac{\cos^2\theta}{\sin^2\theta} + \frac{\cos^2\theta}{\theta}\right), \tag{10}$$

where $\theta$ reveals Bragg's angle. The lattice parameters calculated from the extrapolation of the obtained straight lines $F(\theta) = 0$. There is no remarkable distortion in the lattice parameter of the two fundamental
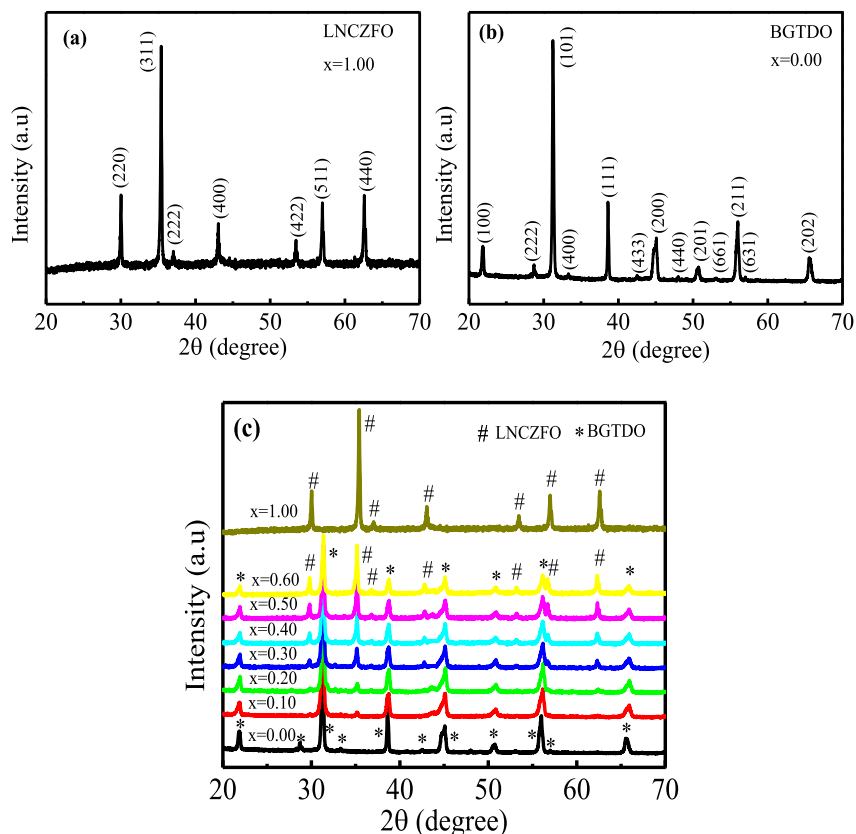


**Fig. 1.** XRD pattern of (a) LNCZFO (b) BGTDO and (c) various $x$LNCZFO+(1-$x$)BGTDO composites.

phases of the composite. Slight changes in the lattice parameters result from the stress between the two ferroic orders [23]. The cubic ferrite material consists of $a = 0.8405$ nm, while $a = b = 0.4028$ nm and $c = 0.4034$ nm for the tetragonal perovskite phase of $x = 0.50$ composite. The results obtained are well satisfied with the results reported earlier [16–19].

### 3.2. Density and porosity

The graphical representation of $\rho_B$, $\rho_x$, and $P$ of the compositions with the ferrite component as depicted in Fig. 2. The $\rho_B$ of all compositions evaluated using the Archimedes principle. The maximum value of $\rho_B$ obtained for $x = 0.10$ samples in the composite, as the small grains of the perovskite material fill the intergranular pores of the composition. The $\rho_B$ decreases above $x = 0.10$ content due to the atomic weight of LNCZFO (232.08 amu) is smaller than the atomic weight of BGTDO (239.92 amu). The $\rho_B$ is lower than $\rho_x$ for all compositions since in the case of $\rho_x$ evaluation, porosity did not consider which can produce and grown well into the bulk samples during the sintering process. The $\rho_x$ declines just about linearly to agree with the mixture rule or the sum rule. In ceramic material, porosity derived from two origins, including intergranular and intragranular porosity [24,25]. The resultant porosity could, therefore, expressed as,

$$P = P_{inter} + P_{intra.} \tag{11}$$

Due to the consideration of the pores referred to above, during the $\rho_B$ measurement, $\rho_B$ is lower than $\rho_x$.

### 3.3. Surface morphology and compositional analysis

The microstructure of MFCs plays an important role in the electric and magnetic behaviors, as well as the ME coupling. The FESEM associated with the EDS carried out the microstructure, surface morphology, and elemental distribution of all samples. The distribution of the grains along with fitted curves as presented in Fig. 3 to evaluate the grain sizes of LNCZFO and BGTDO ferroics in the composites. The two ferroic phases can be easily identified from the FESEM images. From FESEM image analysis it was observed that the relatively larger grains are the ferromagnetic phase. The number of these grains increases as the $x$ value increases. Micrographs exhibit the inhomogeneous grain development in the composites. This inhomogeneity of grain is due to the dissimilar growth of particular phases. The average grain diameter ($\overline{D}$) of the compositions, calculated by fitting the data based on the Gaussian distribution function. The $\overline{D}$ values of the composites in the range of 0.319–1.597 μm were well consistent with the earlier report [26]. The

increase in $\overline{D}$ with an increment in ferrite content in the composite might be the cause of the combination of large ferrite grains with small ferroelectric grains. The $\overline{D}$ value for the different samples presented in Table 1. The porosity of the composites develops with an increment in LNCZFO ferrite, which agreed with the bulk density and porosity measured according to the Archimedes principle. The lower stress created from the high porosity of the ferrite element also leads to an increment in $\overline{D}$ with the ferrite content. The EDS spectra obtained from FESEM to evaluate the atomic percentage of the different $x$LNCZFO+ (1-$x$)BGTDO compositions, as shown in Fig. 4. The EDS spectra confirmed the incorporation of Ni, Cu, Zn, Fe, Ba, Gd, Ti, Dy, and O in the composites. The evaluated quantities of the elements are well-matched with the approximate percentages of the different constituents, excluding oxygen. The oxygen vacancy can create at high temperatures during the sintering.

### 3.4. Complex initial permeability

The $\mu_i'$ represents the stored energy and demonstrates the part of magnetic induction ($B$) in material under the ac magnetic field ($H$). Fig. 5 shows the variation of $\mu_i'$ with a frequency range of 10 kHz–120 MHz for various $x$LNCZFO+(1-$x$)BGTDO compositions. The $\mu_i'$ is almost constant up to a certain frequency for the reason that magnetic moments are capable of following the alternate applied magnetic field in this region through the magnetization process [27]. This frequency independence nature is influential for different applications, including broadband transformer and wideband read-write head for video recording [28,29]. The $\mu_i'$ increases with the ferrite content as the LNCZFO are highly magnetic, whereas the BGTDO is weakly ferromagnetic. The $\mu_i'$ for the ferrite phase is much larger than any of the other compositions. The magnitude of $\mu_i'$ of a ferrite depends on two factors: (i) domain wall motion and (ii) spin rotation [30,31]. For normal grain growth, the domain wall motion is proportional to the $\overline{D}$ of the material. The value of $\overline{D}$ increased by the increase of the domain walls per grain. As the motion of domain walls creates $\mu_i'$, any increase in the number of domain walls may lead to an increase in $\mu_i'$. The $\overline{D}$ for $x = 1.00$ is much larger than the other compositions. That's why $\mu_i'$ for $x = 1.00$ is quite different than the rest of the samples. The $\mu_i'$ decreases in the higher frequencies because of the creation of pinning points on the surface of the sample from impurities and intergranular pores, which obstructs the spin rotation and domain wall motion by lowering the contribution to enhancing $\mu_i'$ [32]. The maximum $\mu_i'$ and the corresponding cut-off frequency ($f_r$) are inversely proportional to each other as per the Snoek ($f_r\mu_i' = $ constant) relationship [33]. Thus, an increase of LNCZFO in composites causes a decrease in the magnitude of $f_r$. Hence, it is possible to control the $\mu_i'$ and $f_r$ of the composites by changing the LNCZFO or BGTDO content. No resonance peak identified in the observed frequency range for $x = 0.00$, 0.20, and 0.30 compositions as above the frequency studied. The $\mu_i'$ increases with LNCZFO content according to the sum rule of the composite and reported in Table 1.

The RQF used as a performance assessment parameter of material for practical applications. Fig. 6(a) represents the frequency-dependent variation of RQF of the samples. The RQF enhances as the frequency increases and then decreases with the additional increment showing a peak. The $Q_{max}$ and $f_r$ shifted to lower frequencies with an increase in the ferrite content. For pure ferrite, the peak is thin but widens by enhancing the ferroelectric component in the composite, which increases the frequency band of the utility. Fig. 6(b) describes the frequency-dependent $\tan\delta_M$ of all compositions. The $\tan\delta_M$ for all samples in high frequency is quite low due to the insulating layer created from BSTDO surrounding the LNCZFO elements, which can significantly enhance the resistive property of the materials and minimize the loss of eddy current [34]. This $\tan\delta_M$ creates from the lack of domain wall motion with the applied ac magnetic field and also attributed to different defects, like non-uniform and non-repetitive domain wall motion and variation of
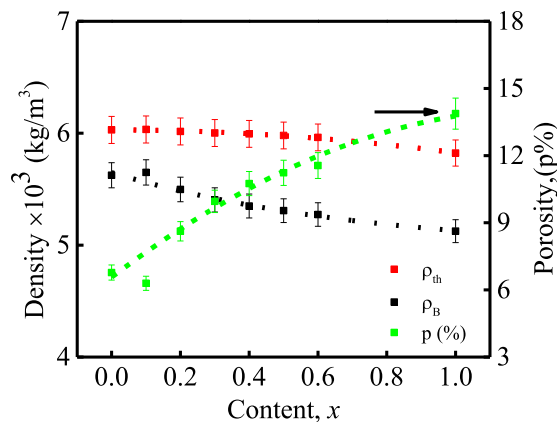


**Fig. 2.** $\rho_B$, $\rho_x$, and $P$ as a function of ferrite content of $x$LNCZFO+(1-$x$) BGTDO composites.
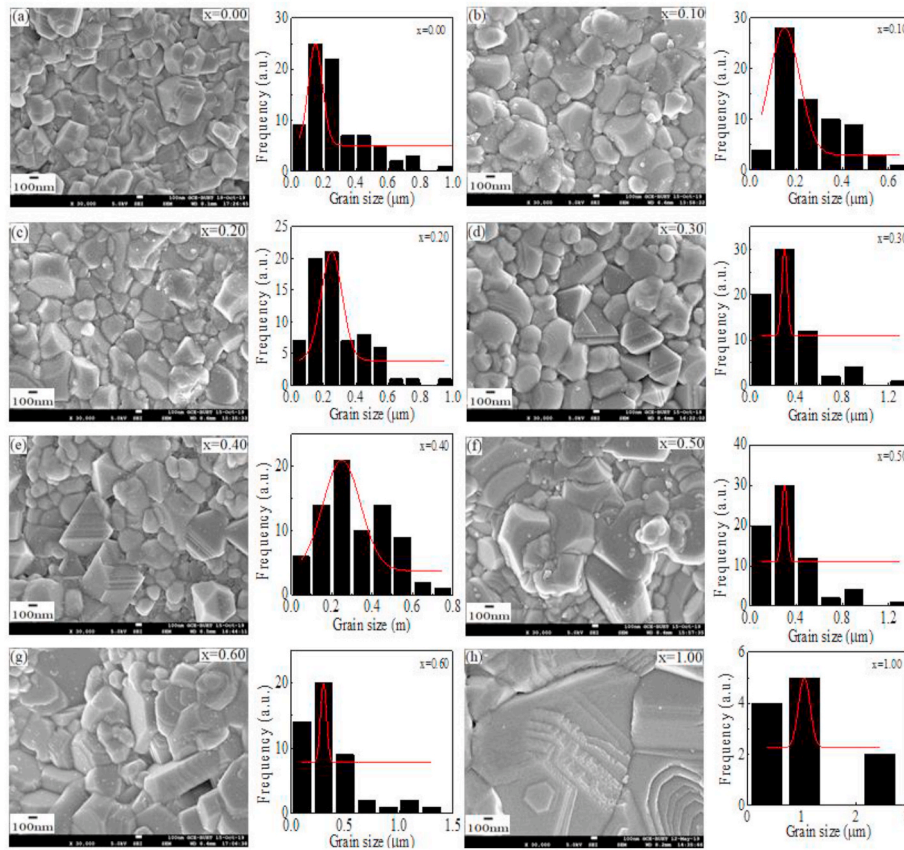
**Fig. 3.** FESEM spectra and corresponding histogram of $x$LNCZFO+(1-$x$)BGTDO composites.

**Table 1**

The lattice parameters, $\rho_x$, $\rho_B$, $P$, $\overline{D}$, and $\mu_i{'}$ of various $x$LCNZFO+(1-$x$)BGTDO composites.

| Content ($x$) | Lattice parameter (nm) | | | $\rho_x \times 10^3 (\text{kg/m}^3)$ | $\rho_B \times 10^3 (\text{kg/m}^3)$ | $P(\%)$ | Average grain size ($\mu$m) | $\mu_i{'}$ at 100 kHz |
|---|---|---|---|---|---|---|---|---|
| | Ferrite $a$ | Ferroelectric | | | | | | |
| | | $a$ | $c$ | | | | | |
| 0.00 | – | 0.4041 | 0.4045 | 6.03 | 5.63 | 7 | 0.319 | 26 |
| 0.10 | 0.8442 | 0.4044 | 0.4039 | 6.04 | 5.65 | 6 | 0.378 | 30 |
| 0.20 | 0.8441 | 0.4029 | 0.4034 | 6.02 | 5.50 | 9 | 0.423 | 32 |
| 0.30 | 0.8451 | 0.4030 | 0.4039 | 6.00 | 5.40 | 10 | 0.478 | 35 |
| 0.40 | 0.8447 | 0.4038 | 0.4033 | 5.99 | 5.35 | 11 | 0.512 | 41 |
| 0.50 | 0.8445 | 0.4028 | 0.4034 | 5.98 | 5.31 | 12 | 0.547 | 45 |
| 0.60 | 0.8447 | 0.4027 | 0.4032 | 5.96 | 5.27 | 13 | 0.635 | 48 |
| 1.00 | 0.8405 | – | – | 5.82 | 5.13 | 14 | 1.597 | 231 |

localized flux density, domain wall bowing [35].

### 3.5. Dielectric property

The dielectric constant, also known as relative permittivity, is a unique parameter used to describe the dielectric behaviors of the materials. The $\varepsilon{'}$ is the amount of energy stored in the material. The frequency-dependent $\varepsilon{'}$ depicted in Fig. 7(a). The $\varepsilon{'}$ decreases to certain values by increasing the frequency. After that, $\varepsilon{'}$ becomes almost constant for all of the compositions. The low-frequency dielectric dispersion occurs since all kinds of polarizations (interfacial, dipolar, electronic, and ionic) are present in the compositions at low-frequency. But, as the frequency increases, some polarizations are significantly disappeared (except for electronic and ion) leading to a sharp fall of $\varepsilon{'}$. The $\varepsilon{'}$ exhibits independent nature at higher frequencies because the electric dipoles do not get sufficient time to align and unable to obey the fast variation of the ac electric field. In the low-frequency region, the high magnitude of

$\varepsilon{'}$ derived from the interfacial polarization proposed by Maxwell-Wagner [36,37]. Interfacial polarization creates from inhomogeneity of the material, results through grain composition, porosity, interfacial defects, charges trapped by the defects at the grain boundaries, oxygen vacancies, and impurity. During the high-temperature calcination and sintering, this inhomogeneity formed in the sample. Besides, space charge polarization could also be caused by the Ba-volatility and the transition from $Fe^{3+}$ to $Fe^{2+}$ in LNCZFO. The $Fe^{3+}$ to $Fe^{2+}$ transition in LNCZFO takes place to maintain a charge balance, which may also contribute to the formation of oxygen vacancies [38]. The $\varepsilon{'}$ for some samples of $x = 0.40$, $0.50$ and $0.60$ enhances with the increase of LCNZFO content because of the large $\overline{D}$ for the ferrite phase as well as the reduction of oxygen vacancy. The area of the grain boundary reduces with the increase of $\overline{D}$. The heterogeneity of the composites also increased the interfacial polarization [39,40]. The difference in conductivities and permittivities of the interface between the constituent phases forms this heterogeneity. When an electric field is implemented
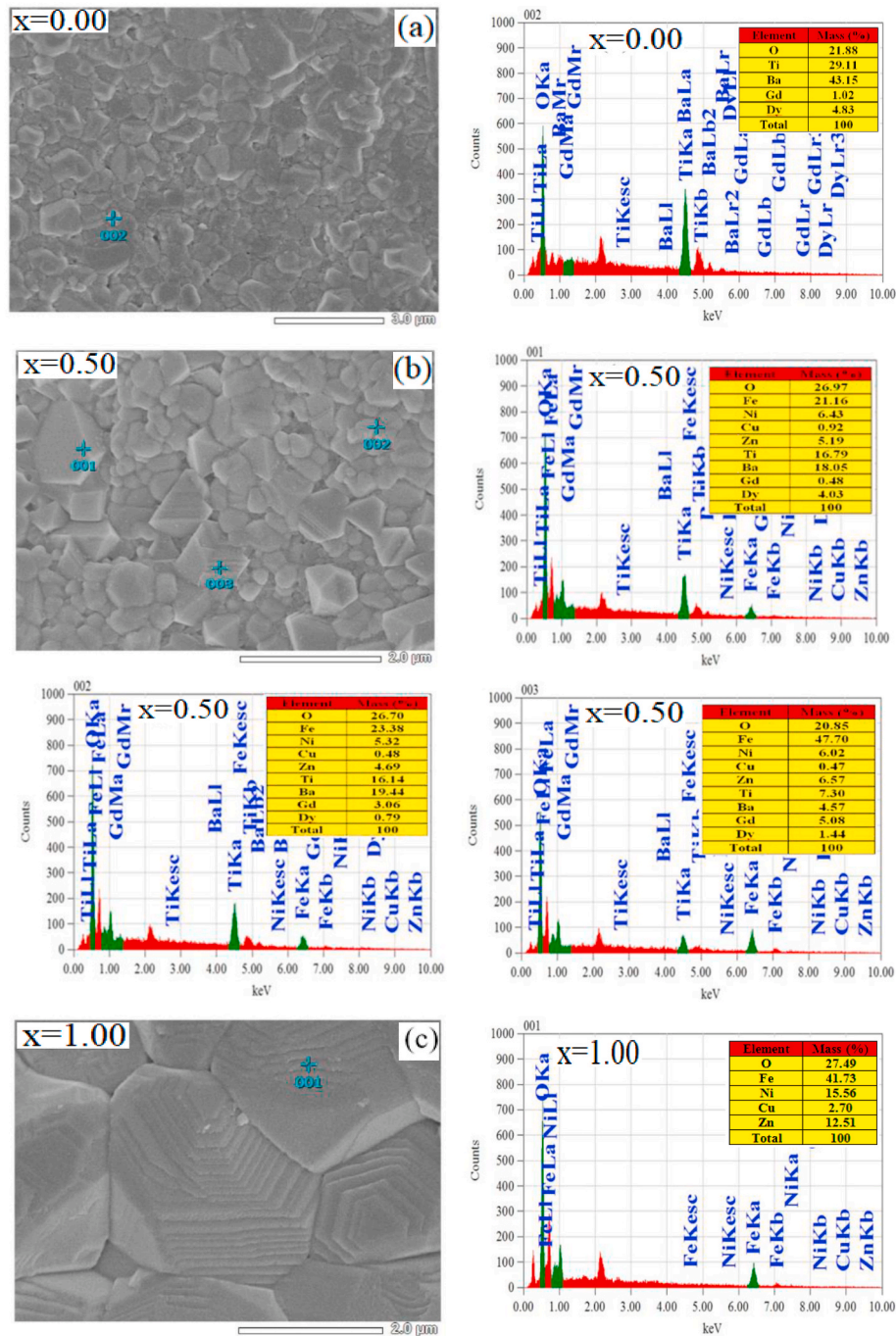
**Fig. 4.** Micrographs and corresponding EDS spectra of (a) BGTDO (b) 0.5LNCZFO+0.5BGTDO (for point 001, 002 and 003) composite and (c) LNCZFO.

to the studied samples, the space charge given by the ferrite phase accumulates at the interface of the two phases as a result of the existence of distinct conductivities and permittivities. It leads to the rise of the interfacial polarization and contributes to the $\varepsilon'$ [41]. The effect of large $\overline{D}$ of ferrite phase and heterogeneity of the composite contribute to an increase of $\varepsilon'$. In this investigation, enlarged $\varepsilon'$ found for samples with $\overline{D}$ values ranging from 0.521 to 0.659 μm and a declining pattern of $\varepsilon'$ observed for all other $\overline{D}$ values. Dilution of the grain boundary of the non-ferroelectric phase usually responsible for such type of behavior. The findings are well agreed with the previous reports [42,43]. The studied composites showed an immense frequency consistency of $\varepsilon'$ presented at the inset of Fig. 7(a). Nevertheless, with an increment in the ferromagnetic phase, the absolute value of $\varepsilon'$ is declined since $\varepsilon'$ is

smaller for LNCZFO than for BGTDO. The tan$\delta_E$ variation, depending on frequency, is presented in Fig. 7(b). This tan$\delta_E$ resulted from the domain wall resonance [8]. The high tan$\delta_E$ of ferrite is due to some ion migrations and, in particular, to the loss of conductivity induced by hopping electrons between $Fe^{3+}$ and $Fe^{2+}$ ions [38]. As mentioned, the grains show higher conductivity than that of the grain boundaries in ferrite, while small grains are efficient for reducing the $Fe^{2+}$ concentration [44]. On the other hand, BGTDO ceramics could cause a decrement in grain size, leading to a decline in conductivity. As a result, we may conclude that tan$\delta_E$ reduces conductivity. In both lower and higher frequency bands, frequency dispersion tan$\delta_E$ occurs. The composites show the loss peaks satisfying to the Debye theory of relaxation. These resonance tan$\delta_E$ peaks resulted while the hopping frequency of electrons from the different ionic elements is approximately equal to the applied electric
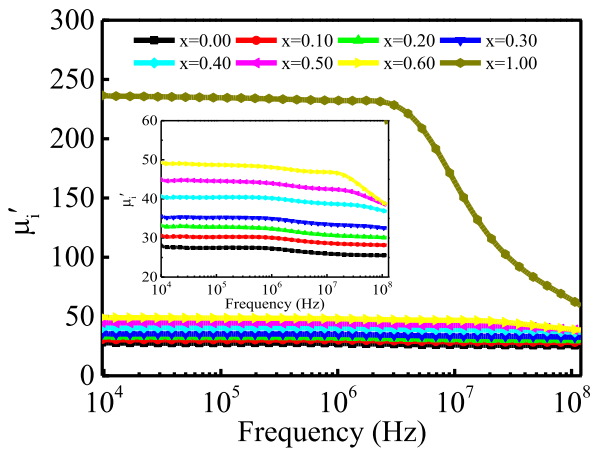
**Fig. 5.** Variation of $\mu_i'$ as a function of frequency for different $x$LNCZFO+(1-$x$) BGTDO composites.
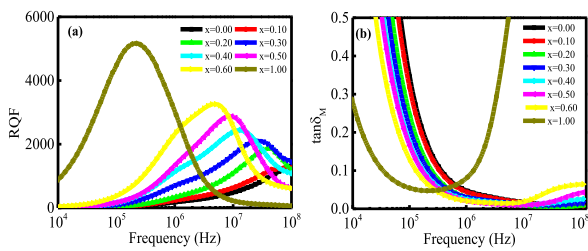


**Fig. 6.** Variation of (a) RQF and (b) $\tan\delta_M$ with frequency for various $x$LNCZFO+(1-$x$)BGTDO composites.
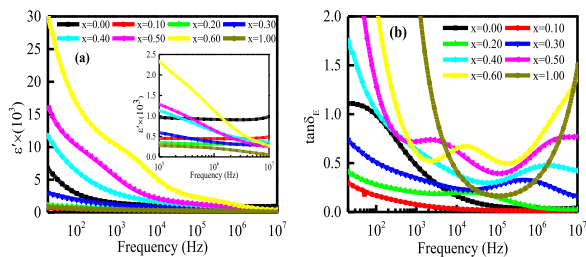


**Fig. 7.** Variation of (a) $\varepsilon'$ and (b) $\tan\delta_E$ with frequency for different $x$LNCZFO+ (1-$x$)BGTDO composites.

field. In other terms, if the state $\omega\tau = 1$ is satisfied [45]. In earlier studies, similar behaviors are also reported [8,46]. The MFCs of $x = 0.40$, 0.50 and 0.60 have enlarged $\varepsilon'$ with a little $\tan\delta_E$ than those of LNCZFO and BGTDO for the decreased mobility of the charge carriers.

### 3.6. The ac conductivity

The measurement of $\sigma_{ac}$ executed in the frequency limit from 20 Hz to 10 MHz. The frequency-dependent $\sigma_{ac}$ of MFCs stated by the polaron hopping mechanism depends on the free charges available in the composites. When the electric field applied, the mobility of negative charges in oxide metals begins to distort or polarize the adjacent lattice to form polarons. If distortions within lattice are of the order of the lattice constant, small polarons developed, while the distortions are above the lattice constant, large polarons created. It is also possible to describe the $\sigma_{ac}$ by the Austin and Mott polaron models [47]. The large polaron

interprets when the $\sigma_{ac}$ decreases as the frequency increases, while the small polaron interprets when the $\sigma_{ac}$ increases with the frequency [48]. Fig. 8(a) illustrates the variation of frequency-dependent $\sigma_{ac}$. There are two different regions in the frequency-dependent $\sigma_{ac}$ spectrum. In the low-frequency region, the conductive behavior is independent of the frequency defined as dc conductivity ($\sigma_{dc}$), in which the grain boundary effect becomes more prominent to dielectrics according to the Maxwell–Wagner double layer model [37,49]. In the high-frequency hopping region, $\sigma_{ac}$ increases rapidly, and hopping carriers from the components are continuing to develop. Conductive grains at higher frequencies become more dominant, increasing the hopping carrier and conductivity. Hopping 3d electrons between $Ni^{2+}$ and $Ni^{+3}$ also between $Fe^{2+}$ and $Fe^{3+}$ might play an influential role in the conduction mechanism. By the power law of Jonscher's [50], the frequency-dependent $\sigma_{ac}$ expressed as

$$\sigma_{ac}(\omega) = \sigma_{dc} + B\omega^n, \tag{12}$$

where $\sigma_{ac}(\omega)$, $B$, and $n$ represent the total conductivity, the pre-exponential factor, and the frequency exponent, respectively. The term $n$ indicates the interaction between the mobile ions and the nearby lattice. Both $n$ and $B$ are dependent on the temperature and intrinsic properties of the material. The value of frequency exponent $n$ can be obtained from the slope of the $\log(\sigma_{ac})$ vs $\log(f)$ curve. The $n$ parameter specifies whereas the conduction is dependent on the frequency ($0 < n < 1$) or independent on the frequency ($n = 0$). The independent nature of $\sigma_{ac}$ at a lower frequency and increasing trend at a higher frequency, indicating the shift of an ion from long-range hopping to short-range ion motion and thereby confirms the establishment of conductivity relaxation. Fig. 8(b) depicts the $\log\sigma_{ac}$ variation with $\log\omega$. The $\log\sigma_{ac}$ enhances with an enhancement of frequency for all compositions, representing that small polaron is responsible for the material conduction process [51]. Fig. 8(b) also demonstrates that the conductivity enhances with the increment of LNCZFO content in composites, which shows a semiconducting behavior rather than an insulating one. The addition of LNCZFO with BSTDO results in a reduction of resistivity of the composites because of the lower resistive value of the LNCZFO phase, which causes an increase in the number of charge carriers that contribute to increasing the conductivity. Depending on the Jonscher Law, the pattern of $\log\sigma_{ac}$ vs. $\log\omega$ should be linear. However, the slight deviation of some samples from linearity caused by mixed polarons (small/large) [52].

### 3.7. Electric modulus spectra analysis

The bulk characteristics evident in the impedance investigation are associated with dipole relaxation and/or long-range conductivity. It is hard to distinguish this bulk characteristic with the help of impedance studies, for which electrical modulus analysis processes used. Electric modulus, depending on the capacitance value, helps to understand the different relaxation and space charge aspects. Fig. 9(a) demonstrates the frequency variation of $M'$. The value of $M'$ is quite low in the lower-frequency region, suggesting the activity of polaron hopping and the
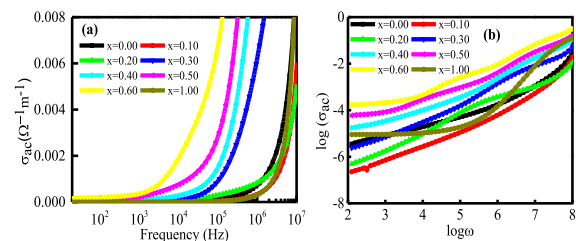


**Fig. 8.** (a) Variation of $\sigma_{ac}$ with frequency and (b) plot of $\log\omega$ vs. $\log\sigma_{ac}$ for different $x$LNCZFO+(1-$x$)BGTDO composites.

relatively small influence of electrode effects [53,54]. The *M′* increases up to a certain frequency since various dipoles cannot follow the ac electric field near a higher frequency. The *M′* significantly enhanced for all samples with frequency and reaching to high-frequency saturation. Dispersion is significant at low frequency, which shifts to higher-frequency for the distribution of relaxation times within the material. The frequency response of *M″* presented in Fig. 9(b). It is evident that *M″* shows the maximum value ($M''_{max}$) at a certain frequency and varies with compositions along with the frequency, confirming the different relaxation times for different samples. Asymmetrical peak broadening found at both ends of the maxima, which indicates that periods of relaxation divided into separate time constants [55]. The peak broadening results due to the spatial distribution of local conductivity and electrical response time as a result of the non-uniform microstructure of the material [56]. The frequency range below the peak specifies the mobility region of charge carrier over long distances, i.e., between the grains. Above the peak frequency, the charge moves within short distances, i.e., within grains [57]. The peak represents the transition from long to short-distance mobility.

### 3.8. Complex impedance spectra

The frequency-dependent nature of *Z′* shown in Fig. 10(a). The value of *Z′* decreases with an increase in frequency to a certain value, indicating that the carrier conductivity is increased up to this limit and then follow the frequency-independent nature. The larger *Z′*-value in the lower-frequency range specifies that the relaxors comprise a higher polarization resulting from all types of polarization. The impedance spectroscopy study revealed that the *Z′*-values initially reduced by an increment in frequency to a certain value of ≤104 Hz and attained a stable state at a frequency of ≥104 Hz. The decline in *Z′* may result from an increase in conductivity due to the presence of space charge polarization in the compositions at higher frequencies [58–61]. The large value of *Z′* at lower frequencies indicate that the polarization in the composites is larger. The merger of *Z′* at higher frequencies indicates the possible release of space charge polarization or accumulation at the boundaries of homogeneous phases in the composites under the applied external field. Additionally, with the increase of LNCZFO content, the values of *Z′* decline in the low-frequency region, and then they appear to merge in the frequency region. This suggests that the frequency at which the space charge becomes free also depends upon the LNCZFO phase. The decreasing trend of *Z′* implies an increasing loss in resistive properties of the composites. This is the typical nature due to the existence of space charge polarization in the material. The findings are well agreed with earlier research [62–64]. The variation of *Z″* at RT with frequency presented in Fig. 10(b). Fig. 10(b) shows the identical variation of *Z″* with frequency as that of *Z′*. The absence of the relaxation phase resulted

from the static relaxation of the electron in the compositions. The frequency-independent nature is attributed to the release of space charges.

### 3.9. Nyquist plots

Impedance spectroscopy is a well-known method used to determine the influence of grain and grain boundary influences on polycrystalline compounds. The Nyquist plots are particularly suitable for materials with one or more different relaxation mechanisms of similar magnitude and following the Cole-Cole functional methods. The equivalent circuit of the brick-layer model [65] with three parallel RC circuits paired in series can explain the relaxors properties of the material containing the effect of grain, grain boundaries, and electrode. Depending on the electrical properties of the composition, the plot may have two semi-circles. The first semicircular arc at the lower frequency range and the second at higher frequency region represents the resistance of grain boundary and grain, respectively [66]. In some cases, a relatively narrow semicircular arc observed at a slightly lower frequency, which may be due to the influence of interfaces or electrodes [67]. The semicircular arc in the intermediate frequency region is due to the dominant grain boundary effect, resulting from the parallel arrangement of the grain resistance and grain capacitance of the material. One the other hand, arcs at larger frequencies reveal the grain influence creating from the parallel arrangement of grain resistance and capacitance of the sample [68]. Fig. 11(b–i) shows the complex impedance plots for all the compositions evaluated in the frequency order 20 Hz-10 MHz at RT. The points in the black line represent the experimental data and points in the red line show the theoretical fit data in Fig. 11. In the present study, samples of *x* = 0.10, 0.20, 0.30, and 1.00 comprise only a single semicircle, suggesting that electrodes and grains do not have much impedance since this would produce an extra semicircular arc. A single semicircle in the impedance spectra demonstrates that only a grain boundary effect is dominant for the conduction of the compositions. The samples of *x* = 0.00, 0.40, 0.50 and 0.60 exhibit double semicircle in their diagram of impedance spectra. The impedance spectra with double semicircular arc reveal the contribution of both grain and grain boundary resistance to the conduction process within the samples. The grain contribution arc usually lies in a frequency region higher than the grain boundary, as the grain boundary relaxation time is higher than the grain and the grain boundaries are also more resistive as well as capacitive than grain. This activity can explain with an equivalent circuit comprising of two sub-circuits linked in series as presented in Fig. 11(a). The magnitude of the complex impedance of the material can be determined using the following equation:
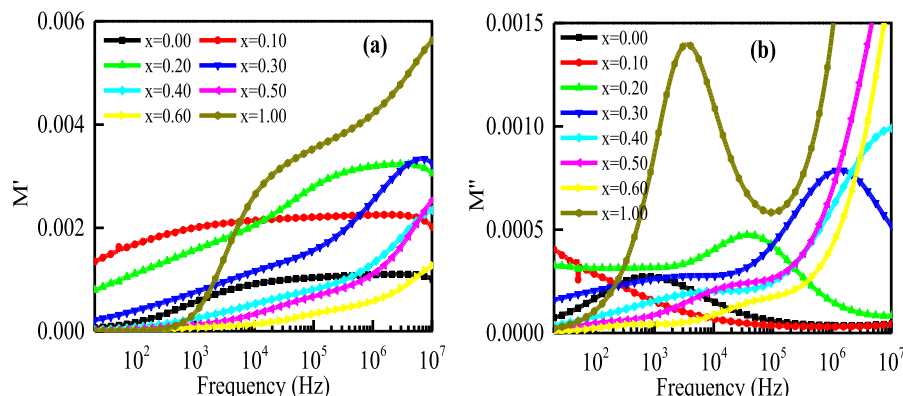


**Fig. 9.** Electric modulus of various *x*LNCZFO+(1-*x*)BGTDO MFCs: (a) real part (*M′*) and (b) imaginary part (*M″*).
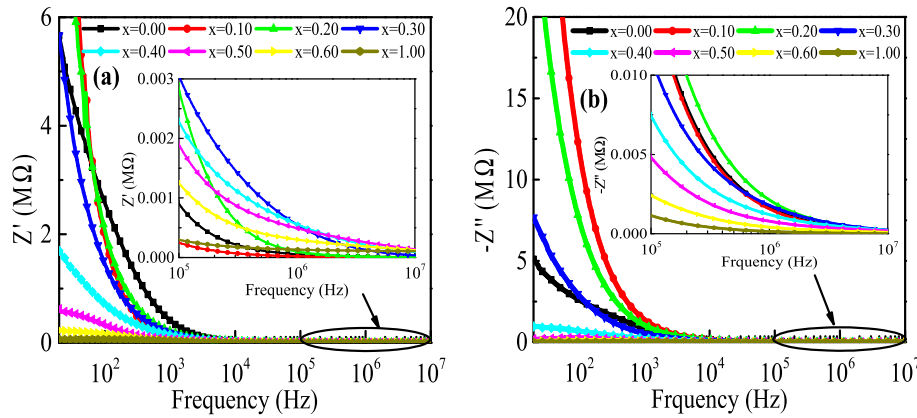
**Fig. 10.** (a) Frequency dependent $Z'$ and (b) $Z''$ for different $x$LNCZFO+(1-$x$)BGTDO composites.

$$Z^* = R_g - \frac{1}{i\omega c_g} + R_{gb} - \frac{1}{i\omega c_{gb}}, \tag{13}$$

where $R_g$ and $R_{gb}$ represent the grain and grain boundary resistance, $C_g$ and $C_{gb}$ reflect the grain and grain boundary capacitance, consequently. If the center of the semi-circular arc lies on the axis, the Deby-type nature relaxation occurs [69]. Relaxation of the non-Debye pattern obtained for the investigated compositions, as each composition produces a depressed/distorted semicircle. The grain boundary resistance is more prominent to the total resistance of the compositions because of the smaller diameter of the grain relative to the grain boundary. The grain and grain boundary resistances obtained from the fit for the studied compositions. The grain boundary resistance of the samples decreases with ferrite content (except $x = 0.10$ and 1.00) due to the enhanced grain inhomogeneity in the compositions. Besides, with an increase in frequency, the values of grain and grain boundary resistance decrease, suggesting that the samples are more conducting with increased frequency. The large grain boundary resistance is found for the pure LNCZFO phase compared to the rest of the samples as a result of large grain diameter and porosity.

### 3.10. Ferroelectric property

The ferroelectric behavior of the composites evaluated by polarization vs. the electric field (*P-E*) curves demonstrated in Fig. 12. Compositions up to $x = 0.30$ show a typical ferroelectric characteristics curve, signifying spontaneous polarization under the applied electric field. These samples display $P$ vs. $E$ hysteresis loop, which is not fully saturated. Besides, the polarization increases with an increase in the ferrite content, and the highest polarization of 0.419 μC/cm$^2$ obtained for $x = 0.30$ of these samples. The remanent polarization increases with an increase in ferrite content. This increase in polarization may be due to the space charge polarization created by the heterogeneity of the interface between the ferrite and ferroelectric phases. The contribution to polarization due to space charge increases with an increase in ferrite content in the composites. Similar results were reported earlier [70,71]. This confirms that the presence of nickel ferrite in the composite has significant effect on the ferroelectric properties of barium titanate phase. The composites of $x = 0.40$ and 0.50 exhibited almost rounded shaped loops, whereas samples of $x = 0.60$ and 1.00 showed a nearly rectangular shaped loop, suggesting a lower resistive and highly lossy samples from which no inherent ferroelectricity can found. The significant reason for the lack of ferroelectricity of the samples could be the high leakage current, improper electrode, and barium volatilization. These findings are well compatible with the results reported earlier [20,26]. The sample of $x = 0.00$ comprises the minimum coercive field, which signifies that the samples can be polarized easily by an adequate electric field.

### 3.11. Magnetoelectric coefficient

The ME effect generated in multiferroic materials by the coupling between the piezomagnetic and piezoelectric domains of the materials. The ME response is an interface that incorporates piezoelectric and piezomagnetic phases by the elastic interactions between them [72]. At RT, the strain-mediated ME response was observed depending on the mole percentage of the constituent phases, polarization, electric resistance, and the magnetization of the ferroic phases [73]. The applied magnetic field and the coupling between piezomagnetic and piezoelectric domains establish strain in magnetic domains, which leads to stress in piezoelectric domains. This stress causes polarization of the ferroelectric domains, resulting in the creation of voltage in the grains. The $\alpha_{ME}$ variation for all samples with the applied dc magnetic field shown in Fig. 13. The figure shows that $\alpha_{ME}$ increases with the applied dc magnetic field reaches a peak and then gradually decreases. A similar result reported by other researchers [74]. The increase in elastic interaction between the ferroic phases may contribute to this initial increase in $\alpha_{ME}$. The highest ME value for all the compositions observed in the 0.3 T dc region, suggesting that the piezomagnetic order has reached a saturation state creating a steady electric field in the BGTDO phase, resulting in a decrement of $dE/dH$ with an increment of the magnetic field [75]. The inset of Fig. 13 demonstrated the variation of the maximum $\alpha_{ME}$ of each sample with ferrite content. The inset figure shows that the $(\alpha_{ME})_{max}$ decreases with an increase in ferrite of large grain owing to a significant reduction in composite resistivity. The $\alpha_{ME}$ depend on the piezoelectricity and the magnetostriction of the ferroelectric and ferromagnetic phases, respectively. Smaller grains are more efficient than larger grains for the enhancement of piezomagnetic and piezoelectric coefficients [76]. However, to achieve a better result in composites, two particular components would be symmetry, and there would be no disparity between grains. The decreasing of the $\alpha_{ME}$ with an increasing concentration of the LNCZFO phase due to the low resistance ferrite provides poor piezoelectricity and also establishes a path for the charges created in the piezoelectric phase. Besides, leakage charges are formed by the low-resistive ferrite grain through the mentioned path, which plays an important role to decrease the $\alpha_{ME}$. Due to the higher porosity of the ferrite phase, the net magnetization of the compositions decreases as the ferrite phase increases, this may be another potential reason for decreasing the $\alpha_{ME}$ with the ferrite content. However, the shift of stress between the piezomagnetic and the piezoelectric orders plays an influential role in obtaining high resistance. The maximum $\alpha_{ME}$ of almost $172 \times 10^3$ Vm$^{-1}$T$^{-1}$ was found for $x = 0.10$ composites at 0.3 T applied dc magnetic field, which is relatively higher than the results reported earlier [77–79].
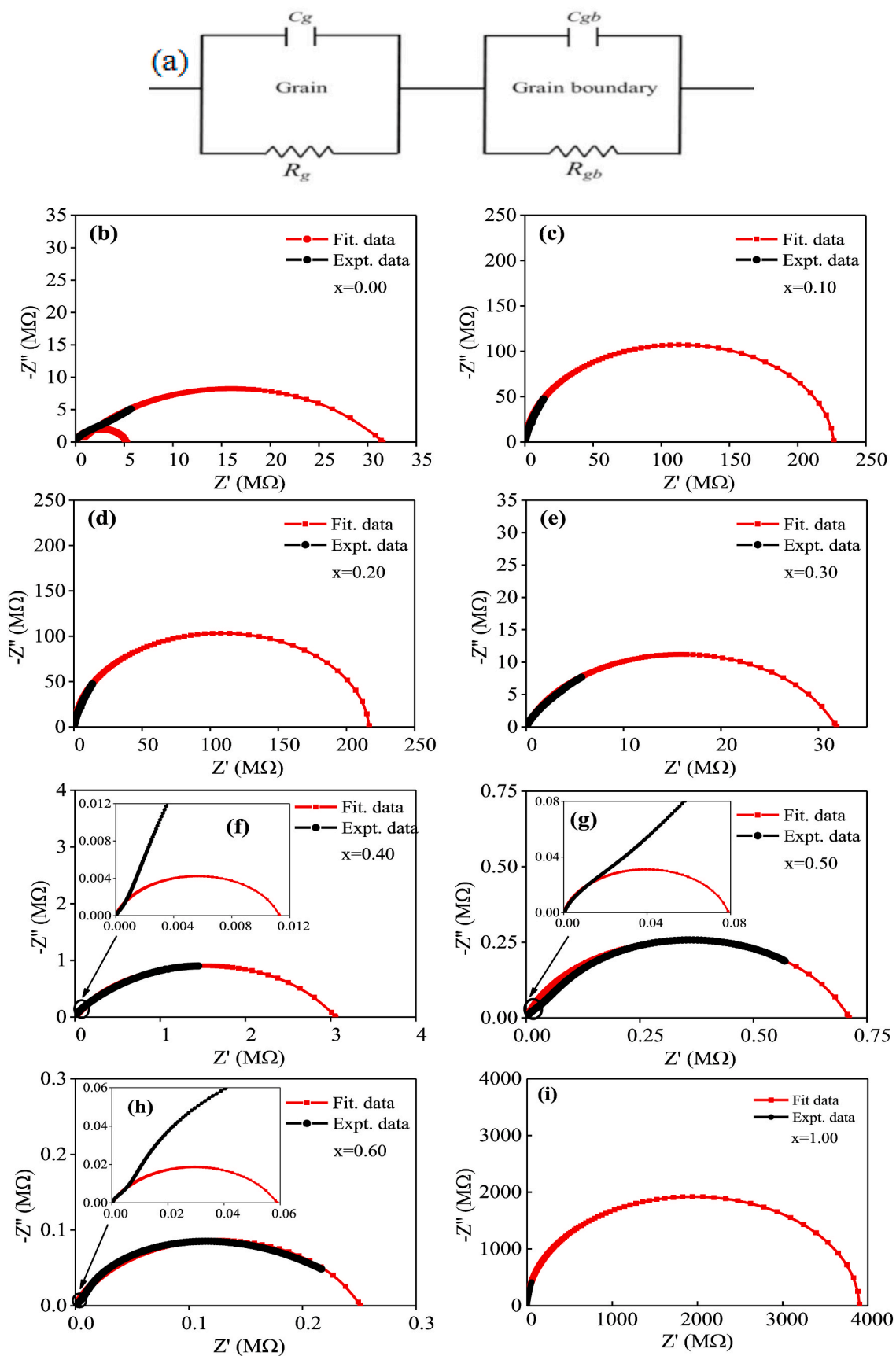
**Fig. 11.** (a) Equivalent circuit and (b)–(i) show the Nyquist plot of complex impedance.
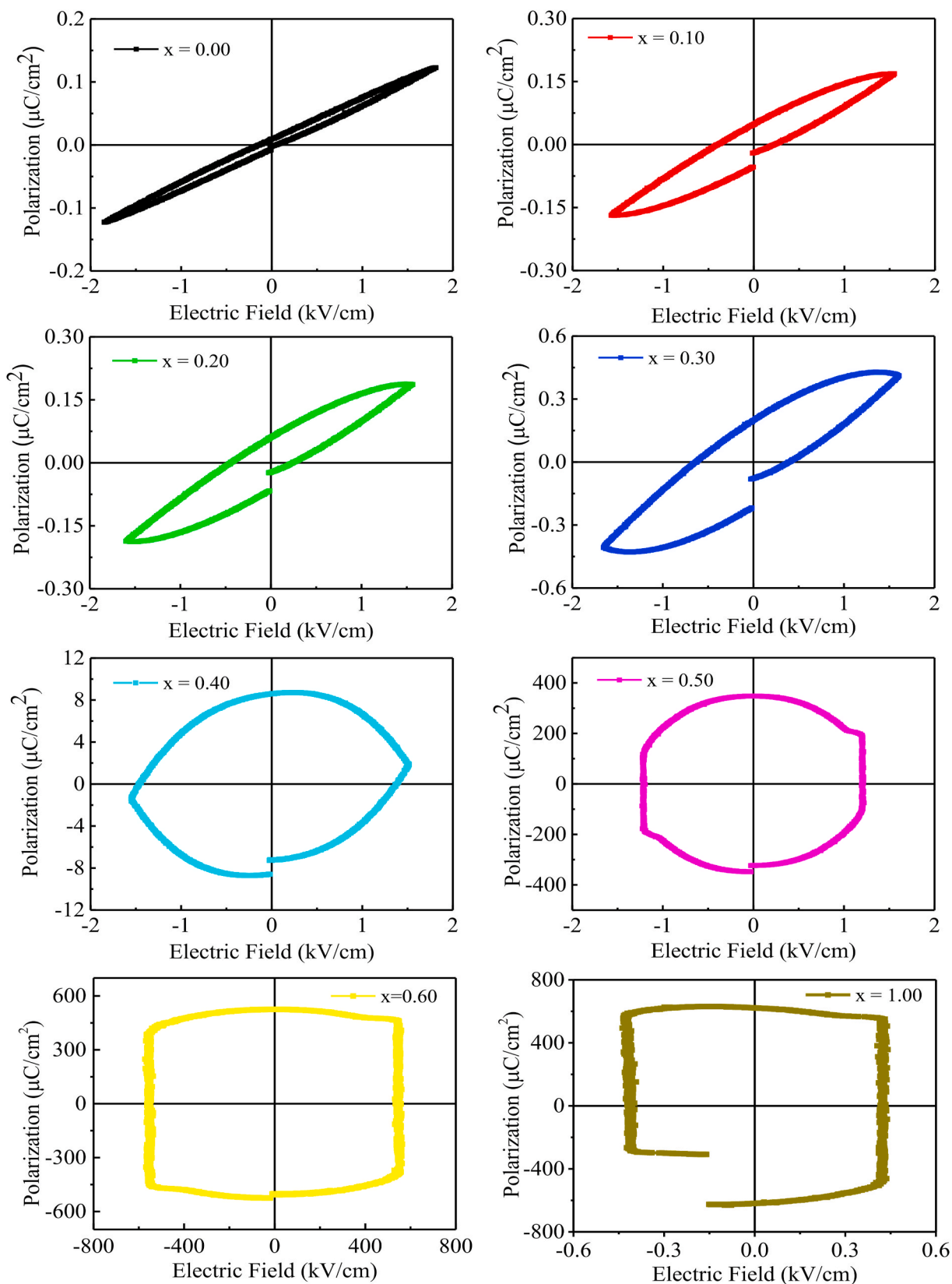
**Fig. 12.** *P–E* plots of different *x*LNCZFO+(1-*x*)BGTDO composites.
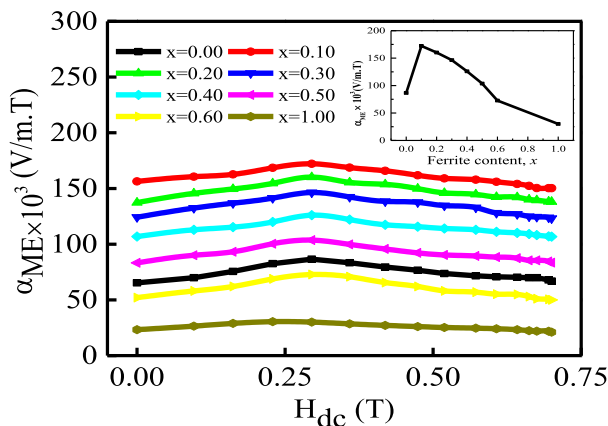
**Fig. 13.** Variation of $\alpha_{ME}$ as a function of dc magnetic field and $(\alpha_{ME})_{max}$ with the ferrite phase (inset) for various $x$LNCZFO+(1-$x$)BGTDO MFCs.

## 4. Conclusions

The standard solid-state reaction technique has been used to synthesize the $x$LNCZFO+(1-$x$)BGTDO MFCs. The XRD and FESEM analyses confirms the coexistence of the two constituent phases with no third phase. The average grain diameter was enhanced by an increase in the LNCZFO phase. On the other hand, the density was decreased with an increment of LNCZFO in MFCs. A significant improvement of $\mu_i$' was observed due to the substitution of BGTDO by strong magnetic LNCZFO. The mechanical barrier for moving domain wall was decreased by decreasing oxygen vacancy, which may also be a possible reason for an increase in $\mu_i$'. The typical low-frequency dielectric dispersal behavior was evident for all samples due to the Maxwell-Wagner interfacial polarization. As a result of a lack of response to the rapid variation of the applied field by the electric dipoles with higher relaxation time, the independent nature of $\varepsilon'$ in the high-frequency region was observed. The frequency variation of the $\sigma_{ac}$ obeyed the Jonscher's power law, and the linearity of the $\log\omega$ vs. $\log\sigma_{ac}$ plots confirmed that the conductivity was for a small polar hopping mechanism. Electrical modulus analysis also verified the presence of polaron hopping type conduction in the present samples. Furthermore, complex impedance spectroscopy has been demonstrated that $x = 0.10$, 0.20, 0.30, and 1.00 samples have only a grain boundary contribution, while $x = 0.00$, 0.40, 0.50 and 0.60 samples have grain and grain boundary effect on the conductivity of the material. Excellent intrinsic ferroelectric properties were identified for samples up to $x = 0.30$. The highest $\alpha_{ME}$ was found to be $172 \times 10^3$ $Vm^{-1}T^{-1}$ for the composite of $x = 0.10$. These results suggest that $x = 0.10$ may be useful for engineering in lead free multifunctional devices in the broad frequency ranges.

## CRediT authorship contribution statement

**Mithun Kumar Das:** Conceptualization, Methodology, Investigation, Formal analysis, Writing - original draft. **M.A. Zubair:** Resources, Investigation. **Hidekazu Tanaka:** Resources, Investigation. **A.K.M. Akther Hossain:** Supervision, Project administration, Writing - review & editing.

## Declaration of competing interest

The authors declare that they have no known competing financial interests or personal relationships that could have appeared to influence the work reported in this paper.

## References

[1] H. Schmid, Multiferroic magnetoelectric, Ferroelectrics 162 (1994) 317–338, https://doi.org/10.1080/00150199408245120.

[2] W. Eerenstein, N.D. Mathur, J.F. Scott, Multiferroic and magnetoelectric materials, Nature 442 (2006) 759–765, https://doi.org/10.1038/nature05023.

[3] J.V. Suchetelene, Product properties: a new application of composite materials, Philips Res. Rep. 27 (1972) 28–37.

[4] J. Ryu, A.V. Carzo, K.J. Uchino, H.E. Kim, Magnetoelectric properties in piezoelectric and magnetostrictive laminate composites, Jpn. J. Appl. Phys. 40 (2001) 4948–4951, https://doi.org/10.1143/jjap.40.4948.

[5] M.H. Lente, J.S. Guerra, G.K.S. Sousa, C.F.V. Raigoza, D. Garcia, J.A. Eiras, Investigation of magnetoelectric coupling in single-phase multiferroic ceramics, Ferroelectrics 368 (2008) 99–106, https://doi.org/10.1080/00150190802368032.

[6] J. Ryu, S. Priya, K. Uchino, H.E. Kim, Magnetoelectric effect in composites of magnetostrictive and piezoelectric materials, J. Electroceram. 8 (2002) 107–119, https://doi.org/10.1023/a:1020599728432.

[7] O.M. Hemeda, A. Tawfik, M.A. Amer, B.M. Kamal, D.E. El Refaay, Structural, spectral and dielectric properties of piezoelectric–piezomagnetic composites, J. Magn. Magn Mater. 324 (2012) 3229–3237, https://doi.org/10.1016/j.jmmm.2012.03.055.

[8] Md D. Rahaman, S.K. Saha, T.N. Ahmed, D.K. Saha, A.K.M. Akther Hossain, Magnetoelectric effect of (1-$x$)Ba$_{0.5}$Sr$_{0.5}$Zr$_{0.5}$Ti$_{0.5}$O$_3$+($x$) Ni$_{0.12}$Mg$_{0.18}$Cu$_{0.2}$Zn$_{0.5}$Fe$_2$O$_4$ composites, J. Magn. Magn Mater. 371 (2014) 112–120, https://doi.org/10.1016/j.jmmm.2014.07.025.

[9] Prakash Bongurala, Venkataiah Gorige, Structural, magnetic and electric properties of multiferroic NiFe$_2$O$_4$-BaTiO$_3$ composites, J. Magn. Magn Mater. 477 (2019) 350–355, https://doi.org/10.1016/j.jmmm.2018.12.014.

[10] K. Sadhan, S.R. Murthy, S. Jie, Y. Xie, Y. Liu, Q. Zhan, R.W. Li, Magnetic field induced polarization and magnetoelectric effect of Ba$_{0.8}$Ca$_{0.2}$TiO$_3$-Ni$_{0.2}$Cu$_{0.3}$Zn$_{0.5}$Fe$_2$O$_4$ nanomultiferroic, J. Appl. Phys. 113 (2013) 17C731, https://doi.org/10.1063/1.4795820.

[11] K.C. Verma, Mukhwinder Singh, R.K. Kotnala, Navdeep Goyal, Magnetic field control of polarization/capacitance/voltage/resistance through lattice strain in BaTiO$_3$-CoFe$_2$O$_4$ multiferroic nanocomposite, J. Magn. Magn Mater. 469 (2019) 483–493, https://doi.org/10.1016/j.jmmm.2018.09.020.

[12] L. Su, P. Liu, Y. He, J. Zhou, L. Cai, C. Liu, H. Zhang, Electrical and magnetic properties of low temperature sintered $x$Ba$_{0.6}$Sr$_{0.4}$TiO$_3$+(1-$x$)Ni$_{0.2}$Cu$_{0.2}$Zn$_{0.62}$O (Fe$_2$O$_3$)$_{0.98}$ composite ceramics, J. Alloys Compd. 494 (2010) 330–335, https://doi.org/10.1016/j.jallcom.2010.01.029.

[13] S.U. Durgadsimi, S.S. Chougule, S.S. Bellad, Electrical and magnetoelectric properties of ($Y$)Li$_{0.5}$Ni$_{0.7}$Zn$_{0.05}$Fe$_2$O$_4$+(1-$Y$)Ba$_{0.5}$Sr$_{0.5}$TiO$_3$ magnetoelectric composites, Appl. Mech. Mater. 592 (2011) 826–830. https://doi.org/10.4028/www.scientific.net/amm.592-594.826.

[14] Bongurala Prakash, Venkataiah Gorige, Structural, magnetic and electric properties of multiferroic NiFe$_2$O$_4$-BaTiO$_3$ composites, J. Magn. Magn Mater. 477 (2019) 350–355, https://doi.org/10.1016/j.jmmm.2018.12.014.

[15] R.S. Devan, C.M. Kanamadi, S.A. Lokare, B.K. Chougule, Electrical properties and magnetoelectric effect measurement in ($x$)Ni$_{0.8}$Cu$_{0.2}$Fe$_2$O$_4$+(1-$x$) Ba$_{0.9}$Pb$_{0.1}$Ti$_{0.9}$Zr$_{0.1}$O$_3$ composites, Smart Mater. Struct. 15 (2006) 1877–1881, https://doi.org/10.1088/0964-1726/15/6/043.

[16] M.A. Islam, Mehadi Hasan, A.K.M. Akther Hossain, Enhancement of initial permeability and reduction of loss factor in Zn substituted nanocrystalline Li$_{0.35-0.5x}$Ni$_{0.3}$Zn$_x$Fe$_{2.35-0.5x}$O$_4$, J. Magn. Magn Mater. 424 (2017) 108–114, https://doi.org/10.1016/j.jmmm.2016.10.030.

[17] Roksana Parvin, A.A. Momin, A.K.M. Akther Hossain, Improvement of microstructure, initial permeability, magnetization and dielectric properties of nanocrystalline Li$_x$Cu$_{0.1}$Co$_{0.1}$Zn$_{0.8-2x}$Fe$_{2+x}$O$_4$, J. Magn. Magn Mater. 401 (2016) 760–769, https://doi.org/10.1016/j.jmmm.2015.10.130.

[18] Da-Yong Lu, Shu-Zhen Cui, Qiao-Li Liu, Xiu-Yun Sun, Dielectric properties and defect chemistry of barium titanate ceramics co-doped R and Dy ions (R = Eu, Gd, Tb), Ceram. Int. 42 (2016) 14364–14373, https://doi.org/10.1016/j.ceramint.2016.05.197.

[19] Manjit Borah, Dambarudhar Mohanta, Effect of Gd$^{3+}$ doping on structural, optical and frequency-dependent dielectric response properties of pseudo-cubic BaTiO$_3$ nanostructures, Appl. Phys. A 115 (2013) 1057–1067, https://doi.org/10.1007/s00339-013-7941-7.

[20] A. Ahad, M.A. Taher, Mithun Kumar Das, M. Zahidur Rahaman, M.N.I. Khan, Effect of Y substitution on magnetic and transport properties of Ba$_{0.95}$La$_{0.05}$Ti$_{1-x}$Y$_x$O$_3$ ceramics, Results Phys. 12 (2019) 1925–1932, https://doi.org/10.1016/j.rinp.2019.01.072.

[21] Noriyuki Inoue, Toshihiro Okamatsu, Akira Ando, Hiroshi Takagi, Takashi Hashimoto, Chikako Moriyoshi, Yoshihiro Kuroiwa, Structural characteristics of (Ba$_{0.94}$Gd$_{0.06}$)(Ti$_{0.97}$Mg$_{0.03}$)O$_3$ in cubic structure determined by

high-energy synchrotron-radiation power diffraction, Jpn. J. Appl. Phys. 48 (2009), 09KF03, https://doi.org/10.1143/jjap.48.09kf03.

[22] J.B. Nelson, D.P. Riley, An experimental investigation of extrapolation methods in the derivation of accurate unit-cell dimensions of crystals, Proc. Phys. Soc. 57 (1945) 160–177, https://doi.org/10.1088/0959-5309/57/3/302.

[23] Abdul Samee Fawzi, A.D. Sheikh, V.L. Mathe, Multiferroic properties of Ni ferrite-PLZT composites, Physica B 405 (2010) 340–344, https://doi.org/10.1016/j.physb.2009.08.090.

[24] A.A. Sattar, H.M. El-Sayed, K.M. El-shookrofy, M.M. El-Tabey, The effect of Al-substitution on structure and electrical properties of Mn-Ni-Zn ferrites, J. Mater. Sci. 40 (2005) 4873–4879, https://doi.org/10.1007/s10853-005-3884-5.

[25] Xuewu Li, Jingsong Liang, Tian Shi, Danni Yang, Xinchun Chen, Chuanwei Zhang, Zhaohui Liu, Dianzi Liu, Qiaoxin Zhang, Tribological behaviors of vacuum hot-pressed ceramic composites with enhanced cyclic oxidation and corrosion resistance, Ceram. Int. 46 (2020) 12911–12920, https://doi.org/10.1016/j.ceramint.2020.02.057.

[26] Mithun Kumar Das, M.A. Zubair, Hidekazu Tanaka, A.K.M. Akther Hossain, An experimental insight of the multiferroic properties of magnetoelectrically coupled *x*LNCZFO+(1-*x*)BSTDO composites, J. Magn. Magn Mater. 502 (2020) 166449, https://doi.org/10.1016/j.jmmm.2020.166449.

[27] M. Yu, J. Hu, J. Liu, S. Li, Electromagnetic properties of multiferroic magnetoelectric BaTiO$_3$–Co$_x$Fe$_{3-x}$O$_4$ core–shell particles obtained by homogeneous coprecipitation, J. Magn. Magn Mater. 326 (2013) 31–34, https://doi.org/10.1016/j.jmmm.2012.08.033.

[28] P. Kumar, S.K. Sharmab, M. Knobel, M. Singh, Effect of La$^{3+}$ doping on the electric, dielectric and magnetic properties of cobalt ferrite processed by co-precipitation technique, J. Alloys Compd. 508 (2010) 115–118, https://doi.org/10.1016/j.jallcom.2010.08.007.

[29] A. Verma, R. Chatterjee, Effect of zinc concentration on the structural, electrical and magnetic properties of mixed Mn–Zn and Ni–Zn ferrites synthesized by the citrate precursor technique, J. Magn. Magn Mater. 306 (2006) 313–320, https://doi.org/10.1016/j.jmmm.2006.03.033.

[30] T. Nakamura, Snoek's limit in high-frequency permeability of polycrystalline Ni–Zn, Mg–Zn, and Ni–Zn–Cu spinel ferrites, J. Appl. Phys. 88 (2000) 348–353, https://doi.org/10.1063/1.373666.

[31] T. Tsutaoka, M. Ueshima, T. Tokunaga, T. Nakamura, K. Hatakeyama, Frequency dispersion and temperature variation of complex permeability of Ni-Zn ferrite composite materials, J. Appl. Phys. 78 (1995) 3983–3991, https://doi.org/10.1063/1.359919.

[32] A. Globus, P. Duplex, M. Guyot, Determination of initial magnetization curve from crystallites size and effective anisotropy field, IEEE Trans. Magn. 7 (1971) 617–622, https://doi.org/10.1109/tmag.1971.1067200.

[33] J.L. Snoek, Dispersion and absorption in magnetic ferrites at frequencies above one Mc/s, Physica 14 (1948) 207–217, https://doi.org/10.1016/0031-8914(48)90038-x.

[34] Xuegang Lu, Gongying Liang, Yumei Zhang, Wei Zhang, Synthesis of FeNi$_3$/ (Ni$_{0.5}$Zn$_{0.5}$)Fe$_2$O$_4$ nano composite and its high-frequency complex permeability, Nanotechnology 18 (2007), 015701, https://doi.org/10.1088/0957-4484/18/1/015701.

[35] M. Manjurul Haque, M. Huq, M.A. Hakim, Influence of CuO and sintering temperature on the microstructure and magnetic properties of Mg–Cu–Zn ferrites, J. Magn. Magn Mater. 320 (2008) 2792–2799, https://doi.org/10.1016/j.jmmm.2008.06.017.

[36] J.C. Maxwell, A Treatise on Electricity and Magnetism, Cambridge University Press, Cambridge, 1873, https://doi.org/10.1017/CBO9780511709340.009.

[37] K. Wagner, Zur Theorie der unvollkommenen Dielektrika, J. Ann. Phys. 345 (1913) 817–855, https://doi.org/10.1002/andp.19133450502.

[38] D.R. Patil, S.A. Lokare, S.S. Chougule, B.K. Chougule, Dielectric and magnetic properties of *x*NiFe$_2$O$_4$+(1-*x*)Ba$_{0.9}$Sr$_{0.1}$TiO$_3$ composites, Physica B 400 (2007) 77–82, https://doi.org/10.1016/j.physb.2007.06.019.

[39] S. Upadhyay, D. Kumar, O.M. Parkash, Effect of composition on dielectric and electrical properties of the Sr$_{1-x}$La$_x$Ti$_{1-x}$Co$_x$O$_3$ system, Bull. Mater. Sci. 19 (1996) 513–525, https://doi.org/10.1007/bf02744823.

[40] V. Kuldeep, O. Subohi, R. Kurchania, Investigations on dielectric, electrical and ferroelectric properties of *x*BaTiO$_3$-(1-*x*)NiFe$_2$O$_4$ multiferroic composite ceramics, Appl. Phys. A 125 (2019) 631, https://doi.org/10.1007/s00339-019-2921-1.

[41] R. Sharma, P. Poonam, R.P. Tandon, Structural dielectric ferromagnetic ferroelectric and ac conductivity studies of the BaTiO$_3$–CoFe$_{1.8}$Zn$_{0.2}$O$_4$ multiferroic particulate composites, Ceram. Int. 40 (2014) 9027–9036, https://doi.org/10.1016/j.ceramint.2014.01.115.

[42] T.M. Shaw, S. Trolier- McKinstry, P.C. McIntyre, The properties of ferroelectric films at small dimensions, Annu. Rev. Mater. Sci. 30 (2000) 263–298, https://doi.org/10.1146/annurev.matsci.30.1.263.

[43] G. Arlt, D. Hennings, G. de With, Dielectric properties of fine-grained barium titanate ceramics, J. Appl. Phys. 58 (1985) 1619–1625, https://doi.org/10.1063/1.336051.

[44] L.J. Jia, H.W. Zhang, J. Luo, Y.L. Liu, Q.Y. Wen, Effect of MgO additive on the high-frequency properties of Z-type hexaferrite, J. Magn. Magn Mater. 322 (2010) 1934–1938, https://doi.org/10.1016/j.jmmm.2010.01.010.

[45] Kavita Verma, Ashwini Kumar, Dinesh Varshney, Dielectric relaxation behavior of A$_x$Co$_{1-x}$Fe$_2$O$_4$ (A=Zn, Mg) mixed ferrites, J. Alloys Compd. 526 (2012) 91–97, https://doi.org/10.1016/j.jallcom.2012.02.089.

[46] Shivanand Madolappa, Swarup Kundu, Rajasekhar Bhimireddi, K.B.R. Varma, Improved electrical characteristics of Pr-doped BiFeO$_3$ ceramics prepared by sol-gel route, Mater. Res. Express 3 (2016), 065009. http://iopscience.iop.org/2053-1591/3/6/065009.

[47] I.G. Austin, N.F. Mott, Polarons in crystalline and non-crystalline materials, Adv. Phys. 18 (1969) 41–102, https://doi.org/10.1080/00018736900101267.

[48] M.S. Khandekar, R.C. Kambale, J.Y. Patil, Y.D. Kolekar, S.S. Suryavanshi, Effect of calcination temperature on the structural and electrical properties of cobalt ferrite synthesized by combustion method, J. Alloys Compd. 509 (2011) 1861–1865, https://doi.org/10.1016/j.jallcom.2010.10.073.

[49] J.C. Maxwell, A Treatise on Electricity and Magnetism, Clarendon Press, Oxford, 1982.

[50] A.K. Jonscher, The 'universal' dielectric response, Nature 267 (1977) 673–679, https://doi.org/10.1038/267673a0.

[51] M.J. Miah, M.N.I. Khan, A.K.M. Akther Hossain, Weak ferromagnetism and magnetoelectric effect in multiferroic *x*Ba$_{0.95}$Sr$_{0.05}$TiO$_3$-(1-*x*)BiFe$_{0.9}$Gd$_{0.1}$O$_3$ relaxors, J. Magn. Magn Mater. 401 (2016) 600–611, https://doi.org/10.1016/j.jmmm.2015.10.083.

[52] S.L. Kadam, K.K. Patankar, C.M. Kanamadi, B.K. Chougule, Electrical conduction and magnetoelectric effect in Ni$_{0.50}$Co$_{0.50}$Fe$_2$O$_4$+Ba$_{0.8}$Pb$_{0.2}$TiO$_3$ composites, Mater. Res. Bull. 39 (2004) 2265–2272, https://doi.org/10.1016/j.materresbull.2004.07.021.

[53] M. Kaiser, Electrical conductivity and complex electric modulus of titanium doped nickel-zinc ferrites, Physica B 407 (2012) 606–613, https://doi.org/10.1016/j.physb.2011.11.043.

[54] R.N.P. Choudhary, D.K. Pradhan, C.M. Tirado, G.E. Bonilla, R.S. Katiyar, Effect of La substitution on structural and electrical properties of Ba(Fe$_{2/3}$W$_{1/3}$)O$_3$ nanoceramics, J. Mater. Sci. 42 (2007) 7423–7432, https://doi.org/10.1007/s10853-007-1835-z.

[55] S. Pattanayak, B.N. Parida, P.R. Das, R.N.P. Choudhary, Impedance spectroscopy of Gd doped BiFeO$_3$ multiferroics, Appl. Phys. A 112 (2013) 387–395, https://doi.org/10.1007/s00339-012-7412-6.

[56] J. Liu, C. Duan, W. Yin, W.N. Mei, R.W. Smith, Hardy, Large dielectric constant and Maxwell–Wagner relaxation in Bi$_{2/3}$Cu$_3$Ti$_4$O$_{12}$, Phy. Rev. B 70 (2004) 144106, https://doi.org/10.1103/PhysRevB.70.144106.

[57] S. Pattanayak, R.N.P. Choudhary, P.R. Das, S.R. Shannigrahi, Effect of Dy-substitution on structural, electrical and magnetic properties of multiferroic BiFeO$_3$ ceramics, Ceram. Int. 40 (2014) 7983–7991, https://doi.org/10.1016/j.ceramint.2013.12.148.

[58] K.M. Batoo, Study of dielectric and impedance properties of Mn ferrites, Phys. B 406 (2011) 382–387, https://doi.org/10.1016/j.physb.2010.10.075.

[59] S. Selvasekara Pandian, M. Vijayakumar, The ac impedance spectroscopy studies on LiDyO$_2$, Mater. Chem. Phys. 80 (2003) 29–33, https://doi.org/10.1016/s0254-0584(02)00510-2.

[60] B. Behera, P. Nayak, R.N.P. Choudhary, Structural and impedance properties of KBa$_2$V$_5$O$_{15}$ ceramics, Mater. Res. Bull. 43 (2008) 401–410, https://doi.org/10.1016/j.materresbull.2007.02.042.

[61] J. Plocharski, W. Weiczorek, PEO based composite solid electrolyte containing nasicon, Solid State Ionics 28 (1988) 979–982, https://doi.org/10.1016/0167-2738(88)90315-3.

[62] Shivanand Madolappa, Bharathi Ponraj, Rajasekhar Bhimireddi, Kalidindi B. R. Varma, Enhanced magnetic and dielectric properties of Ti-doped YFeO$_3$ ceramics, J. Am. Ceram. Soc. (2017) 1–10, https://doi.org/10.1111/jace.14809, 00.

[63] H. Zhang, C.L. Mak, Impedance spectroscopic characterization of fine-grained magnetoelectric Pb(Zr$_{0.53}$Ti$_{0.47}$)O$_3$–(Ni$_{0.5}$Zn$_{0.5}$)Fe$_2$O$_4$ ceramic composites, J. Alloys Compd. 513 (2012) 165–171, https://doi.org/10.1016/j.jallcom.2011.10.013.

[64] Xuewu Lia, Shi Tian, Ben Li, Xinchun Chen, Chuanwei Zhang, Zhiguang Guo, Qiaoxin Zhang, Subtractive manufacturing of stable hierarchical micro-nano structures on AA5052 sheet with enhanced water repellence and durable corrosion resistance, Mater. Des. 183 (2019) 108152, https://doi.org/10.1016/j.matdes.2019.108152.

[65] Wayne Reitz, Impedance spectroscopy, theory, experiment, and applications, Mater. Manuf. Process. 21 (2006), https://doi.org/10.1080/10426910500476796, 425-425.

[66] S.A. Mazen, N.I. Abu-Elsaad, AC impedance studies on Li0$_{.5+0.5x}$Ge$_x$Fe$_{2.5-1.5x}$O$_4$ system, Appl. Phys. A 122 (2016) 26, https://doi.org/10.1007/s00339-015-9554-9.

[67] R.C. Kambale, P.A. Shaikh, C.H. Bhosale, K.Y. Rajpure, Y.D. Kolekar, Dielectric properties and complex impedance spectroscopy studies of mixed Ni-Co ferrites, Smart Mater. Struct. 18 (2009), https://doi.org/10.1088/0964-1726/18/8/085014, 085014-085016.

[68] H. Inaba, Impedance measurement of single-crystalline and polycrystalline manganese-zinc ferrites with various non-stoichiometries, J. Mater. Sci. 32 (1997) 1867–1872, https://doi.org/10.1023/a:1018561024682.

[69] R. Anthony, C. West Derek, Naohiro Hirose Sinclair, Characterization of electrical materials, especially ferroelectrics, by impedance spectroscopy, J. Electroceram. 1 (1997) 65–71, https://doi.org/10.1023/a:1009950415758.

[70] Shivanand Madolappa, A.V. Anupama, Pw Jaschin, K.B.R. Varma, B. Sahoo, Magnetic and ferroelectric characteristics of Gd$^{3+}$ and Ti$^{4+}$ co-doped BiFeO$_3$ ceramics, Bull. Mater. Sci. 39 (2016) 593–601, https://doi.org/10.1007/s12034-016-1176-0.

[71] Y. Wang, Y. Wang, W. Rao, M. Wang, G. Li, Y. Li, J. Gao, W. Zhou, J. Yu, Dielectric, ferromagnetic and ferroelectric properties of the (1–*x*)Ba$_{0.8}$Sr$_{0.2}$TiO$_3$–*x*CoFe$_2$O$_4$ multiferroic particulate ceramic composites, J. Mater. Sci. Electron. 23 (2012) 1064–1071, https://doi.org/10.1007/s10854-011-0548-x.

[72] J. Ma, J. Hu, Z. Li, C.W. Nan, Recent progress in multiferroic magnetoelectric composites: from bulk to thin films, Adv. Mater. 23 (2011) 1062–1087, https://doi.org/10.1002/adma.201003636.

[73] C.M. Kanamadi, S.R. Kulkarni, K.K. Patankar, S.S. Chuogule, S.J. Patil, B. K. Chougule, Magnetoelectric and dielectric properties of $Ni_{0.5}Cu_{0.5}Fe_2O_4–Ba_{0.5}Pb_{0.5}Ti_{0.5}Zr_{0.5}O_3$ ME composites, J. Mater. Sci. 42 (2007) 5080–5084, https://doi.org/10.1007/s10853-006-0594-6.

[74] T. Ramesh, V. Rajendar, S.R. Murthy, CoFe2O4–BaTiO3 multiferroic composites: role of ferrite and ferroelectric phases on the structural, magnetodielectric properties, J. Mater. Sci. Mater. Electron. 28 (2017) 11779–11788, https://doi.org/10.1007/s10854-017-6983-6.

[75] N. Cai, J. Zahi, C.W. Nan, Y. Lin, Z. Shi, Dielectric, ferroelectric, magnetic, and magnetoelectric properties of multiferroic laminated composites, Phys. Rev. B 68 (2003) 224103, https://doi.org/10.1103/physrevb.68.224103.

[76] B.K. Bammannavar, L.R. Naik, B.K. Chougule, Studies on dielectric and magnetic properties of $(x)Ni_{0.2}Co_{0.8}Fe_2O_4+(1−x)$barium lead zirconate titanate magnetoelectric composites, J. Appl. Phys. 104 (2008), 064123, https://doi.org/10.1063/1.2986470.

[77] Pradeep Chavana, L.R. Naik, P.B. Belavi, Geeta Chavan, V.T. Muttannavar, B. K. Bammannavar, R.K. Kotnala, Temperature-dependent electric properties and Magnetoelectric effects in ferroelectric rich $Ni_{0.8}Mg_{0.2}Fe_2O_4+BaZr_{0.2}Ti_{0.8}O_3$ magnetoelectric composites, J. Alloys Compd. 777 (2019) 1258–1264, https://doi.org/10.1016/j.jallcom.2018.10.157.

[78] Shivangi Tiwari, Satish Vitta, Magnetoelectric and magnetodielectric coupling and microwave resonator characteristics of $Ba_{0.5}Sr_{0.5}Nb_2O_6/CoCr_{0.4}Fe_{1.6}O_4$ multiferroic composite, Sci. Rep. 8 (2018) 1–12, https://doi.org/10.1038/s41598-018-30132-2.

[79] A.A. Momin, M.A. Zubair, Md Fakhrul Islam, A.K.M. Akther Hossain, Enhance magnetoelectric coupling in $xLi_{0.1}Ni_{0.2}Mn_{0.6}Fe_{2.1}O_4–(1−x)BiFeO_3$ multiferroic composites, J. Mater. Sci. Mater. Electron. 30 (2019) 13033–13046, https://doi.org/10.1007/s10854-019-01665-7.

# Influence of Sintering Temperature on Magnetic Characteristics of Li-Cu-Ni-Zn Ferrite

Mithun Kumar Das[1, 2*], Abdulla Al-Momin[1], A.K.M. Akther Hossain[1]

[1]Department of Physics, Bangladesh University of Engineering & Technology, Dhaka-1000, Bangladesh

[2]Department of Physics, Comilla University, Comilla-3506, Bangladesh

*e-mail: mkdas.ju@gmail.com

*Abstract*—**The ferromagnetic Li$_{0.10}$Cu$_{0.10}$Ni$_{0.30}$Zn$_{0.40}$Fe$_{2.1}$O$_4$ synthesized by the typical ceramic technique which is sintered at the various temperatures. The formation of single phase cubic spinel structure at varied sintering temperatures (T$_s$) is confirmed by the x-ray diffraction (XRD) analysis. XRD pattern confirms that the T$_s$ does not distress the inner structure of the sample. The bulk density and theoretical density are found to be improved with T$_s$. Due to increasing of T$_s$, a normal fast grain growth happens over the pores volume which reduced the porosity with sample density. The value of relative quality factor (RQF) and initial permeability are also enhanced with T$_s$ because of low porosity and high density. The peaks of the relative quality factor are shifted toward to the left with the T$_s$ which indicates the decreasing trend of the loss factor. The characteristics of structural, density, porosity, relative quality factor, initial permeability and loss factor of the composition are explained here.**

*Index Terms*—**X-ray diffraction, permeability, porosity, sintering.**

## I. INTRODUCTION

Polycrystalline mixed spinel type ferrites have been taken into account as appreciably crucial materials because of its vast applications in almost every electronic device. The high resistivity, high permeability, and low losses make the ferrites applicable in high-quality coils, telecommunication engineering, television and radio transformers [1]. Depending on the cation distribution and various chemical compositions AB$_2$O$_4$ type crystal structure can exhibit antiferromagnetic paramagnetic and ferromagnetic behavior [2]. The physical characteristics of mixed spinel ferrites can be controlled by the quantity of substitution, preparation methods, compositional variation and sintering temperature [3]. Due to very high potential and low-cost the mixed Lithium-ferrites and Lithium-ferrite are the good replacement of garnet in microwave applications. The highly enhanced temperature performance and hysteresis loop squareness prepared them highly auspicious candidates for the microwave devices application [4]. Remarkable relaxation and anisotropic characteristics have been observed in different cations substituted mixed Lithium ferrites [5] [6] it has been reported that Nickel substitution in Lithium-ferrite, Lithium–Zinc ferrite and Zinc substituted Lithium-Nickel ferrite seems to enhance the magnetic properties [7] [8] [9] .however the study of Cu-substituted Lithium-Nickel-Zinc ferrite has not been reported yet in the literature. Therefore the current study is aimed to investigate the influence of sintering temperature on the structural and magnetic properties of the Li$_{0.10}$Cu$_{0.10}$Ni$_{0.30}$Zn$_{0.40}$Fe$_{2.1}$O$_4$ composite.

## II. EXPERIMENTAL

Polycrystalline mixed spinel type ferrite of Li$_{0.10}$Cu$_{0.10}$Ni$_{0.30}$Zn$_{0.40}$Fe$_{2.1}$O$_4$ sample was synthesized by conventional ceramic technique. The stoichiometric amount of commercially available high concentration level chemical elements of LiCO$_3$ (99.9%), CuO (99.9%), NiO (99.9%), ZnO (99.9%) and Fe$_2$O$_3$ (99.9%) were weighed up and ground by hand grinding process for 5h. Calcination of the ground composition was carried out at 973K for 5h in the appearance of air medium. The grinding process was repeated after the calcination, and the fine powders were granulated using a small amount of polyvinyl alcohol (PVA) as a binder. Then the ground powder with PVA was uniaxially constrained into toroid-and disk-shaped materials. At the moment of sintering, PVA disintegrated and abolished from the samples. The desired shaped components were sintered at different temperatures 1273, 1373, 1423, 1473 and 1523K for 6 h in the air. During the entire time of the sintering process, the temperature ramp was 278K min$^{-1}$ for mutually heating and cooling. The structural study was performed by an innovative X-ray diffractometer (model-Philips PANalytical X'PERT-PRO) fortified with CuKα by means of a target (A= 0.1540598 nm). The lattice constant of all samples at various sintering temperature be found with Nelson- Riley function [10]. The theoretical densities (ρ$_{th}$) of all sintered samples were evaluated using the formula: $\rho_{th} = \frac{(8M_A)}{N_A a_0^3}$ ..... (1), where N$_A$ denotes the Avogadro's number, M$_A$ represents the molecular weight and a$_0$ is lattice constant. The bulk density (ρ$_B$) of every sample was deliberately using the formula: $\rho_B = \frac{M}{\pi r^2 t}$ ..... (2), where M, t, and r represent the mass, thickness, and radius of the pellet respectively. Porosity (P) of the investigated materials was determined using the equation $(\%) = \frac{\rho_{th} - \rho_B}{\rho_{th}} \times 100$ ..... (3). The room temperature complex initial permeability (μ$_i$) was performed (frequency range 100Hz-120MHz) with the impedance analyzer (model-WAYNE KERR 65003). The real part of initial permeability (μ$_i$'), and imaginary (μ$_i$") part of initial permeability were calculated using the following formulas: $\mu_i' = \frac{L_s}{L_0}$ .....(4) and μ$_i$" = μ$_i$' × tanδ.....(5) correspondingly, where L$_s$ represents the sample core inductance, $L_0$ $(= \frac{\mu_0 N^2 S}{\bar{d}})$.....(6) represents the winding coil's inductance without sample core[11], and N is the turns of winding coil (N = 4), S denotes cross-sectional area and $\bar{d}$ is the mean diameter of the toroid sample. The value of relative quality factor (RQF) has been determined using the relation: RQF $= \frac{\mu_i'}{\tan\delta}$ ..... (7) [12], where tanδ represents the loss tangent of the material.

## III. RESULT AND DISCUSSIONS

### A. Lattice Constant, Porosity and Density

Fig.1. shows the XRD graph for $Li_{0.10}Cu_{0.10}Ni_{0.30}Zn_{0.40}Fe_{2.1}O_4$ sintered at various $T_s$. The formation of single-phase cubic structure is confirmed by the XRD pattern analysis. All well-defined peaks are indexed as (111), (311), (220), (222), (422), (400), (511) and (440) from the reflections of well-matched XRD reported earlier [13]. The lattice constant of this sample is represented with different $T_s$ in Fig.2. From the change of lattice constant with $T_s$, it is observed that lattice constant decreases with $T_s$.

The density of a sample shows a starring character in controlling the different characteristics of the ferrite material. Fig. 3(a) shows that both the theoretical and bulk density increases in a similar trend with $T_s$. Conversely, porosity decreases with $T_s$ represented in Fig. 3(b). The measured values of $\rho_{th}$, $\rho_B$, and P of the investigated composition with various $T_s$ are presented in Table 1. Thermally generated force during the sintering process affects the grain boundary to grow over pores, which is responsible for reducing in pore size with the enhance of material density. Intergranular porosity and intragranular porosity are the two possible sources of porosity of ceramic materials [14]. Then resultant porosity can be written as P = $P_{intra}$+$P_{inter}$. During the rate of grain growth which is comparatively high, pores may be left in arrears by promptly affecting grain boundaries, causing in pores which are confined into grains. The intragranular porosity is significantly responsible for the small magnetic and mechanical characteristics. The intergranular porosity generally depends on material's grain size [14]. But at very high $T_s$ the driving energy becomes very large which confines the pores inside the material and decreases the bulk density.
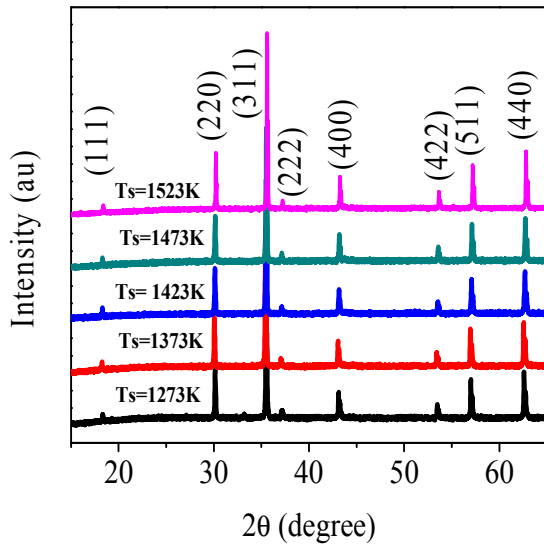


Fig. 1 XRD patterns of the polycrystalline composition at room temperature.
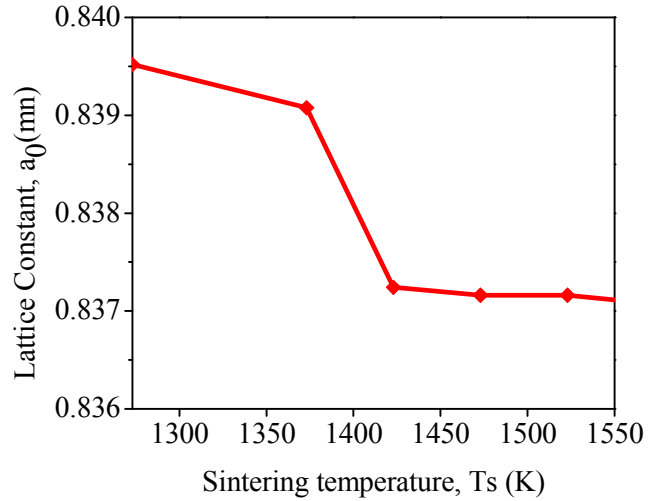


Fig. 2 The variation of the lattice constant of the composition with sintering temperature.
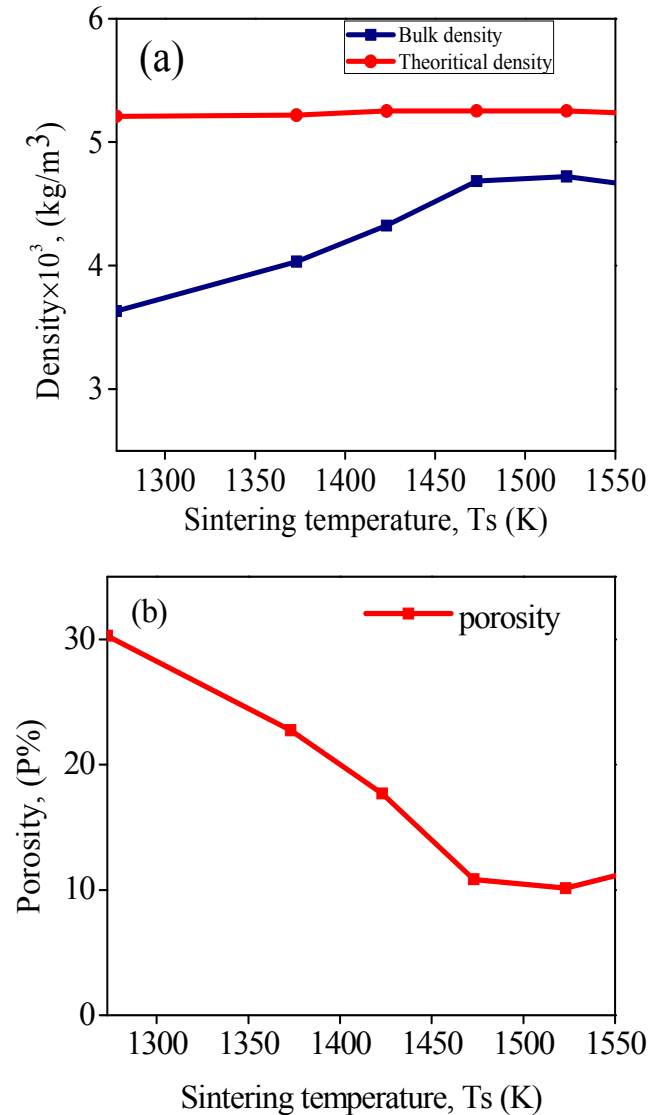


Fig. 3(a) The variation of theoretical density and bulk density and (b) porosity of the composition with sintering temperature.

## B. Complex Initial Permeability

The variation of complex initial permeability for the sample was measured with frequency (100Hz-120MHz). Fig.4(a) and 4(b) shows the change of real part $(\mu_i')$ and imaginary part $(\mu_i'')$ of initial permeability with $T_s$ for the present sample. From the fig.4(a) we observed that the value of $\mu_i'$ enhance with $T_s$ because of the reduction of voids and pores. For all sintering temperatures $\mu_i'$ are observed independent of the frequency lower than a particular value, termed as resonance frequency ($f_r$). Above $f_r$, a sharp fall in $\mu_i'$ and a rapid increase in the $\mu_i''$ is observed. The increase of $\mu_i'$ with a decrease of corresponding $f_r$ value which satisfied Snoeks limit [15]. With the increasing $T_s$, the corresponding $f_r$ decreases which are a characteristic property of a ferrite material. The maximum value of $\mu_i' = |314.30|$ with the corresponding value of $f_r = |3.41MHz|$ is found for the $T_s$=1523K. At the lowest sintering temperature (1273K) the maximum value of $f_r = |45MHz|$ with the corresponding value of $\mu_i' = |88.2|$ is observed for the composition.

## C. Relative Quality Factor and Loss Factor

The RQF is often referred to as a degree of performance of a material for the applications of multifunctional devices. For the present composition, the change of RQF with frequency sintered at different Ts is presented in fig.5(a). The peak value of RQF, decreasing trend is observed below the Ts= 1423K and above these increases with Ts. Due to increasing of Ts a normal fast grain growth occurs over the pores volume which reduced the porosity with increasing composition density. Due to high density and low porosity, the RQF is enhanced with Ts at the higher temperature up to the optimum value. In the present composition, because of the less growth of imperfection and defects, at relatively high Ts, RQF becomes maximum. Fig. 5(b) shows the decreasing inclination of loss with Ts because of the atoms in the materials diffused through the grain boundaries, the peak value of RQF is increased. The maximum value of RQF (= |4841|) is obtained for the sample sintered at 1523K similar trend as μi'. The RQF peak frequency is decreased with Ts due to the soft magnetic material. The maximum value of RQF (Qmax) for different Ts is tabulated in Table-1.
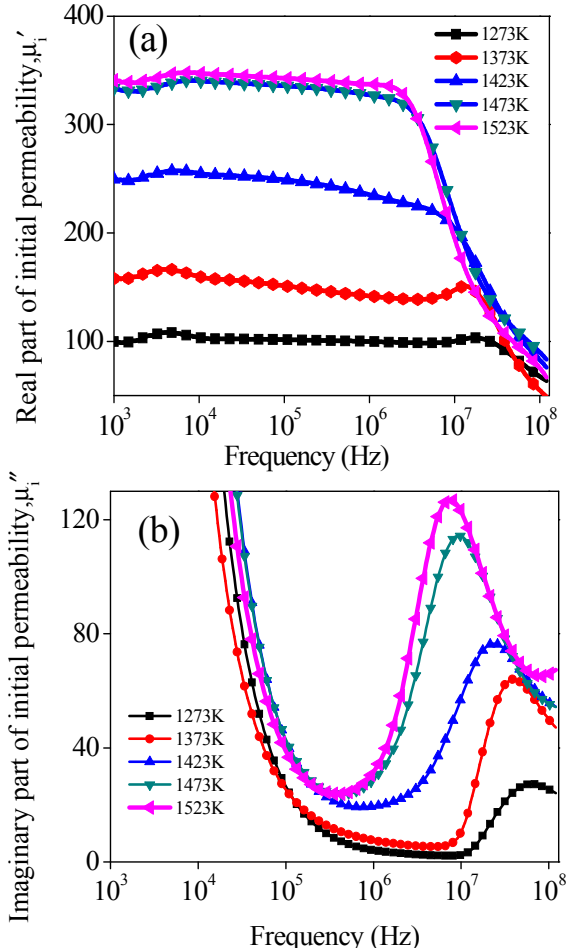


Fig. 4 (a) The real and (b) imaginary initial permeability for of the composition sintered at 1273, 1373, 1423, 1473 and 1523K for 6h in the air.
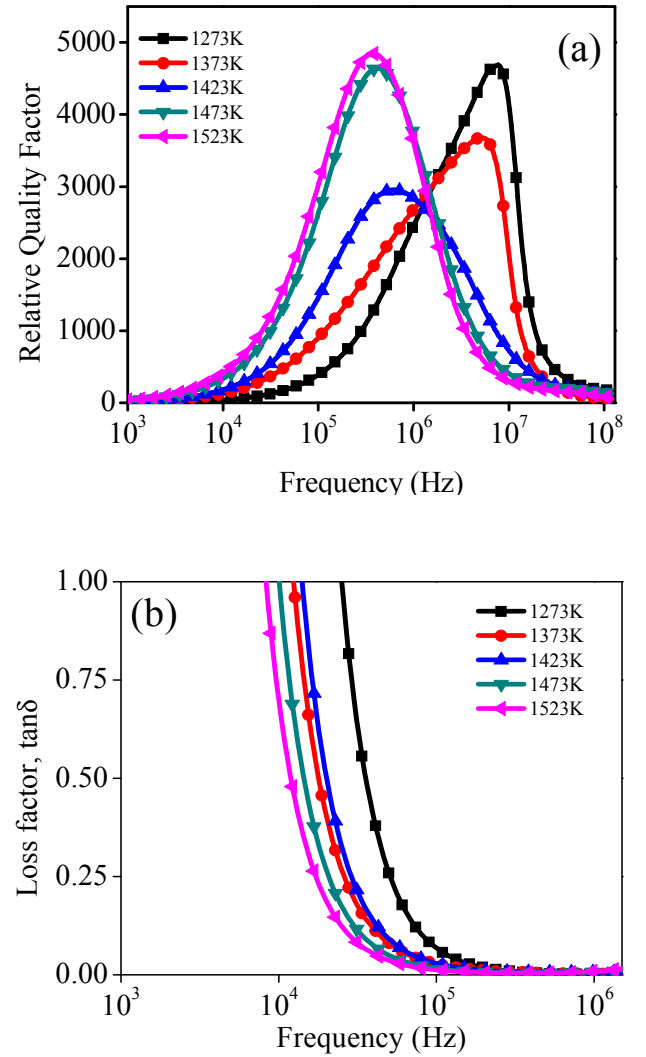


Fig. 5(a) The variation of the relative quality factor and (b) loss factor for the composition with frequency at different sintering temperatures.

TABLE I

The lattice constant, porosity, density, maximum quality factor, resonance frequency, and initial permeability for the composition are sintered at the different temperature

| $T_s$ (K) | $a_0$ (nm) | $\rho_{th}\times10^3$ (kg/m³) | $\rho_B\times10^3$ (Kg/m³) | P (%) | $f_r$ (MHz) | (RQF) $Q_{max}$ | $\mu_i'$ (1MHz) |
|---|---|---|---|---|---|---|---|
| 1523 | 0.8395 | 5.21 | 3.63 | 30 | 28.21 | 4654 | 100 |
| 1373 | 0.8390 | 5.22 | 4.03 | 22 | 16.32 | 328 | 142 |
| 1423 | 0.8373 | 5.25 | 4.32 | 17 | 8.73 | 338 | 236 |
| 1473 | 0.8372 | 5.26 | 4.68 | 11 | 3.41 | 4640 | 328 |
| 1523 | 0.8371 | 5.26 | 4.72 | 10 | 2.50 | 4845 | 338 |

## IV. CONCLUSIONS

Polycrystalline spinel type ferrite of composition $Li_{0.10}Cu_{0.10}Ni_{0.30}Zn_{0.40}Fe_{2.1}O_4$ was synthesized by conventional ceramic techniques. The theoretical and bulk density of the sample increased in a similar trend with the increase of $T_s$. With increasing of $T_s$, porosity is decreased and the sample becomes denser. The $\mu_i'$ enhance with $T_s$ due to reducing of voids and pores. The maximum $\mu_i'$, $f_r$ and RQF is found to be 315, 3.41MHz and 4841, respectively, sintered at 1523K. The investigated spinel ferrite has large permeability with less loss that makes it technologically significant in various practical device applications.

References

[1] J.M. Hasting, L.M. Corliss, "An Antiferromagnetic Transition in Zinc Ferrite," *Phys. Rev.* vol. 102, pp. 1460, June. 1956.

[2] R. Peelamedu, C. Grimes, D. Agrawal, R. Roy, "Synthesis of CuO and Cu2O crystalline nanowires using Cu(OH)2 nanowire templates,"J. Mater. Res. vol. 18, pp. 2756-2759, December 2003.

[3] Yang Bai, Ji zhou, Zhilun Gui, Zhensing yue, Longtu Li, "Preparation and magnetic characterization of Y-type hexaferrites containing zinc, cobalt and copper," *Matter. Sci. Eng.* vol. 99 , pp. 266, May 2003.

[4] G.M. Argetina, P.D. Baba, "Microwave Lithium Ferrites: An Overview," IEEE Trans. *Microphone Tech.* vol. 22 (6), pp. 652-658, June 1974.

[5] C.E. Patton, D.L. Blankenbeckler, C.J. Brower, B.B. Dalton, A.M. Lucero, "Microwave relaxation properties of substituted lithium ferrite*,"* *IEEE Trans. Magn.* vol. 17 (6), pp. 2976, November 1981.

[6] C.J.Brower, C.E. Patton, "Determination of anisotropy field in polycrystalline lithium ferrites from FMR linewidths"*, J. Appl. Phys.* vol. 53, pp. 2104. 1982.

[7] S. Bhatu, V.K. Lakhani, A.R. Tanna, N.H. Vasoya, J.U. Buch, P.U. Sharma, U.N. Trivedi, H.H. Joshi, K.B. Modi, "Effect of nickel substitution on structural, infrared and elastic properties of lithium ferrite", *Ind. J. Pure Appl. Phys.* vol. 45,pp. 597, July 2007.

[8] I. Soibam, S. Phanjoubam, C. Prakash, "Magnetic and Mössbauer studies of Ni substituted Li–Zn ferrite", *J. Magn. Magn. Mater.* vol. 32, pp. 2779, September 2009.

[9] M.A. Islam, Mehadi Hasan and A.K.M Hossain, "Enhancement of initial permeability and reduction of loss factor in Zn substituted nanocrystalline $Li_{0.35-0.5x}Ni_{0.3}Zn_xFe_{2.35-0.5x}O_4$", J. Magn. Magn. Mater., Vol-424, pp 108-114, 2017.

[10] J.B. Nelson, D.P. Riley, "An experimental investigation of extrapolation methods in the derivation of accurate unit-cell dimensions of crystals", *Proc. Phys. Soc. London* vol. 57, pp. 160, 1945.

[11] A. Goldman, *Handbook of Modern Ferromagnetic Materials,* Kluwer Academic Publishers, Boston, U.S.A, 1999.

[12] B.D. Cullity, C.D. Graham, *Introduction to Magnetic Materials*, 2nd ed., Wiley IEEE Press, Hoboken, New Jersey, USA, 2008.

[13] A.K.M. Akther Hossain, M. Seki, T. Kawai, H. Tabata, "Colossal magnetoresistance in spinel type $Zn_{1-x}Ni_xFe_2O_4$", *J. Appl. Phys.* vol. 96, pp. 1273, June 2004.

[14] A.A. Sattar, H.M. El-Sayed, K.M. El-Shokrofy, M.M. El-tabey, "Improvement of the magnetic properties of Mn-Ni-Zn Ferrite by the non-magnetic Al-Ion substitution", *J. Appl. Sci. vol.* 5 (1), pp. 162-168, 2005.

[15] J.L.Snoek, "Dispersion and absorption in magnetic ferrites at frequencies above one Mc/s", *Physica* vol. 14, pp. 207, May 1948.